

RD-R167 318 MIZEX A PROGRAM FOR MESOSCALE AIR-ICE-OCEAN INTERACTION 1/2

EXPERIMENTS IN AR. (U) COLD REGIONS RESEARCH AND

ENGINEERING LAB HANOVER NH P WADHAMS MAY 85

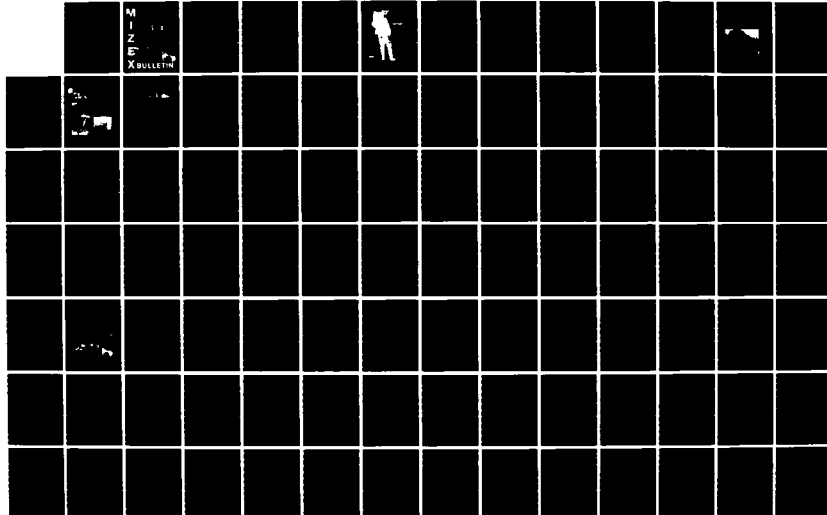
UNCLASSIFIED

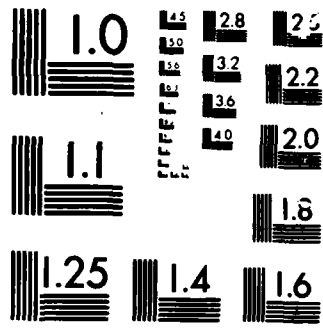
CRREL-SR-85-6

F/G 8/12

NL

M  
I  
Z  
E  
X  
B  
U  
L  
L  
E  
T





MICROCOPI

CHART

VI: MIZEX-WEST

(2)

AD-A167 310

M  
Z

E

DTIC  
ELECTE  
APR 30 1986  
S D  
D

DTIC FILE COPY

Approved for public release by the Defense  
distribution is unlimited



MAY 198

X BULLETIN

86 4 29 047

## MIZEX BULLETIN SERIES: INFORMATION FOR CONTRIBUTORS

The main purpose of the MIZEX Bulletin series\* is to provide a permanent medium for the interchange of initial results, data summaries, and theoretical ideas relevant to the Marginal Ice Zone Experiment. This series will be unrefereed and should not be considered a substitute for more complete and finalized journal articles.

Because of the similarity of the physics of the marginal ice zone in different regions, contributions relevant to any marginal ice zone are welcome, provided they are relevant to the overall goals of MIZEX.

These overall goals are discussed in Bulletin I (Wadhams et al., CRREL Special Report 81-19), which described the research strategy, and Bulletin II (Johannessen et al., CRREL Special Report 83-12), which outlined the science plan for the main 1984 summer experiment. Copies of earlier or current bulletins may be obtained from the Technical Information Branch, USA CRREL.

Persons interested in contributing articles to the bulletin should send copies to one of the editors listed below with figures reproducible in black and white. Proofs of the retyped manuscripts will not be sent to the author unless specifically requested.

### Science Editors:

W.D. Hibler III  
USA Cold Regions Research and  
and Engineering Laboratory  
72 Lyme Road  
Hanover, New Hampshire 03755-1290

### Technical Editor:

Maria Bergstad  
USA Cold Regions Research  
and Engineering Laboratory  
72 Lyme Road  
Hanover, New Hampshire 03755-1290

Peter Wadhams  
Scott Polar Research Institute  
Lensfield Road  
Cambridge CB2 1ER  
United Kingdom

---

\* The MIZEX Bulletin series is funded by the Office of Naval Research.

**MIZEX**  
**A Program for Mesoscale Air-Ice-Ocean**  
**Interaction Experiments in**  
**Arctic Marginal Ice Zones**

**VI: MIZEX-WEST**

**Peter Wadhams, Editor**

**May 1985**

**U.S. Army Cold Regions Research and Engineering Laboratory**  
**Hanover, New Hampshire, USA**

## PREFACE

It was with deepest regret that the polar community learned of the death of Arnold M. Hanson on 2 January 1985. Arne Hanson was one of the great men of the Arctic Ocean. He first went onto the ice with the University of Washington during the International Geophysical Year in 1957, and he subsequently took part in almost every Arctic project mounted by the University. He sailed aboard USCGC *Westwind* on MIZEX-West in the Bering Sea in winter 1983; on *Polarbjörn* during the MIZEX-83 summer experiment in the Greenland Sea; and on *Polar Queen* during MIZEX-84. It was soon after his return from MIZEX-84 that the tumour was diagnosed which so tragically and so rapidly killed him.

Arne was deeply loved by everyone who knew him. He was unfailingly kind, good-humoured, competent and unassuming. He loved being out on the ice, and his cumulative field experience was probably greater than that of any other sea ice researcher. This rich store of experience is now sadly lost. His last paper, submitted to the *MIZEX Bulletin*, was a report on sea ice observations that he made from USCGC *Polar Sea* in 1981 when she was locked in the ice of the Chukchi Sea—characteristically he volunteered to “ride her” southwards (or wherever) as she drifted. We are proud to publish this paper as the introduction to a special issue on the results of the MIZEX-West field experiment of February 1983. The issue, with respect, is dedicated to the memory of Arne Hanson.

PETER WADHAMS  
March 1985



Photograph: A. Heiberg, July 1984, Greenland Sea

**In Memoriam**

**ARNOLD M. HANSON**

May 24, 1928 – January 2, 1985

## CONTENTS

	Page
Preface .....	ii
Observations of Ice and Snow in the Eastern Part of the Chukchi Sea; A Serendipitous Cruise on the <i>Polar Sea</i> .....	1
<i>Arnold M. Hanson</i>	
Introduction to MIZEX-West .....	11
<i>Seelye Martin</i>	
Temperature and Salinity Observations in the Bering Sea Winter MIZ; <i>R.D. Muench, J.L. Newton and R.L. Rice</i>	13
Regional Ice Drift During MIZEX-West,..... <i>R. Michael Reynolds and Carol H. Pease</i>	31
Ice Dispersion in the Bering Sea Marginal Ice Zone..... <i>Seelye Martin and Alan S. Thorndike</i>	38
The Motion of Ice Edge Radar Transponders During MIZEX-West..... <i>Peter Wadhams and Siobhan P. O'Farrell</i>	50
Bottom Ablation Measurements and Heat Transfer Coefficients from MIZEX-West, February 1983:..... <i>Edward G. Josberger and David Meldrum</i>	68
Some Wave Attenuation Results from MIZEX-West..... <i>Vernon A. Squire and Peter Wadhams</i>	73
Further Aircraft Measurements of Air-Ice Drag Coefficients..... <i>James E. Overland and Bernard A. Walter, Jr.</i>	79
Geostrophic Drag of the High Latitude Atmospheric Boundary Layer..... <i>James E. Overland</i>	84
NASA CV-990 Aircraft Observations During MIZEX-West..... <i>D.J. Cavalieri, P. Gloersen and T.T. Wilheit</i>	90
Measurement of the Complex Refractive Index of First-Year Sea Ice and Snow Using a Microwave Untuned Cavity,..... <i>Rodney J. Knight and David T. Llewellyn-Jones</i>	97
Fluctuations of Flow Through Bering Strait..... <i>J.D. Schumacher, A.T. Roach and K. Aagaard</i>	105
Theory of Wind-Driven Coastal Polynyas..... <i>Carol H. Pease</i>	112

# Observations of Ice and Snow in the Eastern Part of the Chukchi Sea: A Serendipitous Cruise on the *Polar Sea*

ARNOLD M. HANSON

Department of Atmospheric Sciences, University of Washington  
Seattle, Washington 98195, USA

## ABSTRACT

Observations of ice and snow conditions were made in the eastern Chukchi Sea during a two-month period in spring 1981 as part of the *Polar Sea* Drift Project. Snow depth was found to depend initially on ice roughness, averaging 5 cm on flat first-year ice and 50 cm in adjacent broken and ridged ice. Whitish bands of snow ice occurred throughout the region and were estimated to comprise from 10% to 25% of the volume of the first-year ice. Darker bands containing sediment and algae were also common in the ice. Algae-coated blocks of loose ice observed bobbing to the surface in newly formed fractures indicated that substantial amounts of unconsolidated rubble were present beneath the floes. The frequency of pressure ridges with sail heights greater than 0.3 m was nearly 20 per kilometer.

## INTRODUCTION

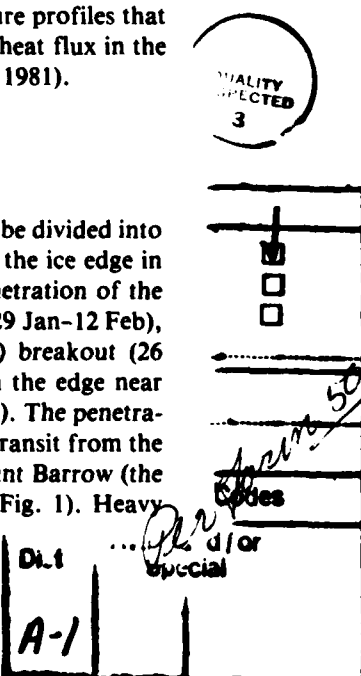
The USCGC *Polar Sea* sailed to the Arctic in January 1981 to test the feasibility of winter transit to Prudhoe Bay, Alaska, under the project name Arctic Winter West 1981 (AWW81) (Shuhy, 1981). Serious damage to the steering gear and loss of use of the port shaft after reaching Point Barrow brought about a condition of besetment (Dirschel, 1981). With the loss of the port shaft on 25 February, it seemed reasonable to assume that extraction of *Polar Sea* from the ice pack would have to await the summer thaw. The scientific community was then invited to utilize the ship as a secure research platform during the enforced drift. Although notice was short, investigators from the National Park Service, the University of Washington, the University of Alaska, and ARCTEC Inc. set up an experimental program, termed the *Polar Sea* Drift Project (PSDP), that

began on 12 March and continued throughout the drift. A summary of planned research activities during PSDP has been given by Shuhy (1981).

Our interest at the University of Washington was in studying the state and structure of the snow and ice cover in a region of predominantly seasonal ice. While a great deal of information regarding perennial ice has been gathered from drifting stations in the central Arctic and recent interest in the marginal ice zone (MIZ) has prompted studies of the ice edge in the Greenland and Bering Seas, conditions in the remainder of the seasonal sea ice zone are not well documented. Our specific plans were to observe spatial and temporal changes in the distribution of brine pockets and air bubbles included in the top layer (10-30 cm) of the ice, to measure physical properties and depth distribution of the snow cover, and to estimate the frequency and height of pressure ridges in the vicinity of the ship. Such information is needed for understanding the interaction of electromagnetic radiation with the ice pack and for interpreting remote sensing data at visible, near infrared, and microwave wavelengths. We also hoped to obtain growth rate data and ice temperature profiles that could be used to infer the oceanic heat flux in the region (McPhee and Untersteiner, 1981).

## THE CRUISE

The 1981 cruise of *Polar Sea* can be divided into five legs: 1) transit from Seattle to the ice edge in the Bering Sea (20-28 Jan), 2) penetration of the ice pack to Point Barrow, Alaska (29 Jan-12 Feb), 3) besetment (13 Feb-25 Mar), 4) breakout (26 Mar-13 May), and 5) transit from the edge near Bering Strait to Seattle (14-22 May). The penetration leg comprised a nearly steady transit from the ice edge on the Bering Strait to Point Barrow (the track from 6 Feb on is shown in Fig. 1). Heavy



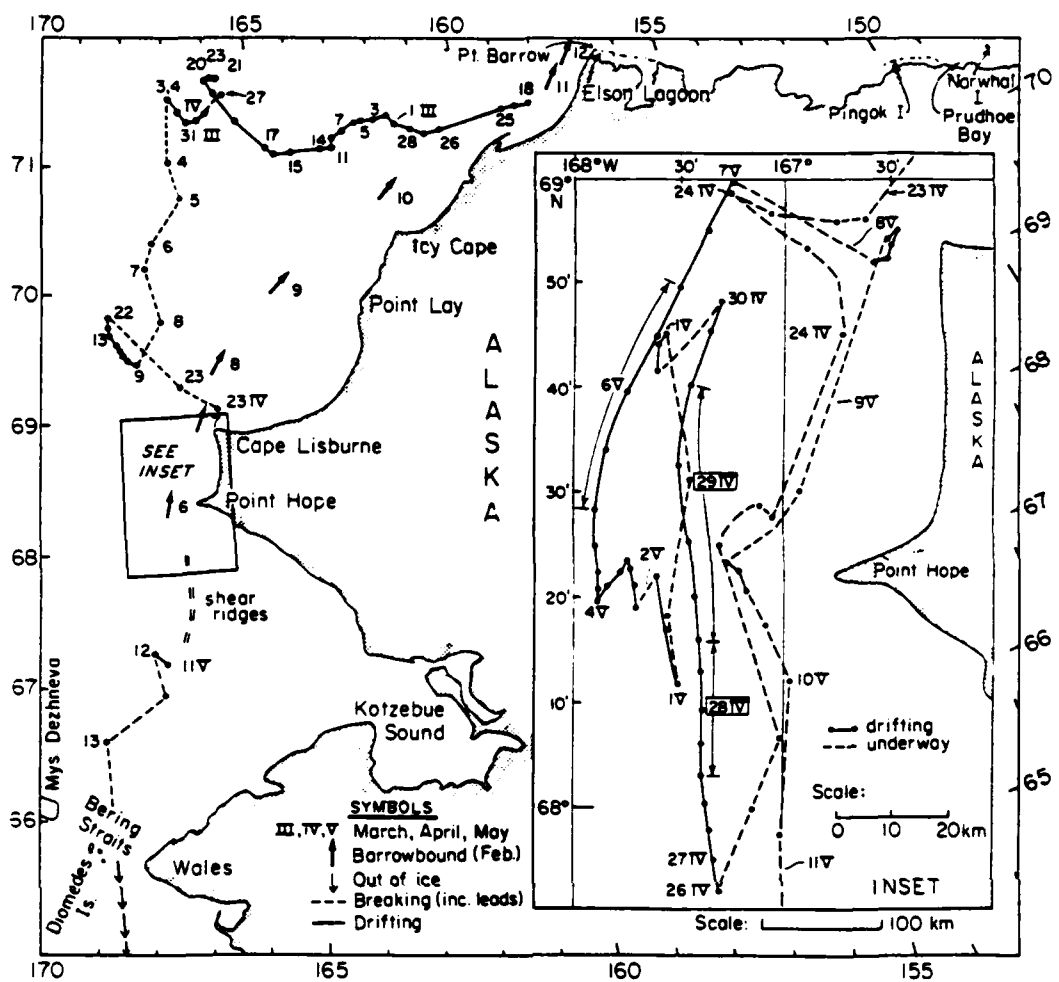


Fig. 1. A smoothed track of *Polar Sea*, 6 February to 13 May 1981 (Transverse Mercator projection). Inset is an approximate rectilinear plan.

multiyear ice encountered off Point Barrow damaged the steering system and brought this leg to an end. Besetment began on 13 February and by 26 March the ship had drifted nearly 300 km to the west. While there were brief periods when the ship was underway, the distance traveled during these periods was small compared to that drifted. Scientific observations were begun on 12 March, about two weeks before the breakout leg. The strategy adopted during the breakout leg was to travel southward in favorably oriented leads or lead systems whenever possible, and to lay-to when the ice pack closed. Because of the ship's frequent movement during the breakout phase, it was not possible to follow temporal changes in the state of the ice cover at a particular site; hence the scientific program was forced to concentrate on spatial variations.

A particularly favorable lead system was en-

countered during 3–9 April when over 200 km of southward progress was made. The multiyear ice was left behind during this period and the ship entered a region of strictly first-year ice. Another large move was made between 22 and 26 April, allowing *Polar Sea* to round Point Hope (see inset, Fig. 1). However, the ice then closed and a northward drift of more than 100 km began a fortnight of disappointments. Winds during this period were generally southeasterly. Discovery by aerial reconnaissance of a lead adjacent to a lengthy shear ridge provided the final pathway from the ice. Nearly half the distance from Point Hope to the Bering Strait was accomplished by running along this great fault. Thereafter the ice encountered was thinner and less compact and presented no further obstacles. The ice edge was passed north of Bering Strait on 13 May and only scattered patches were seen in the northern part of Bering Sea.

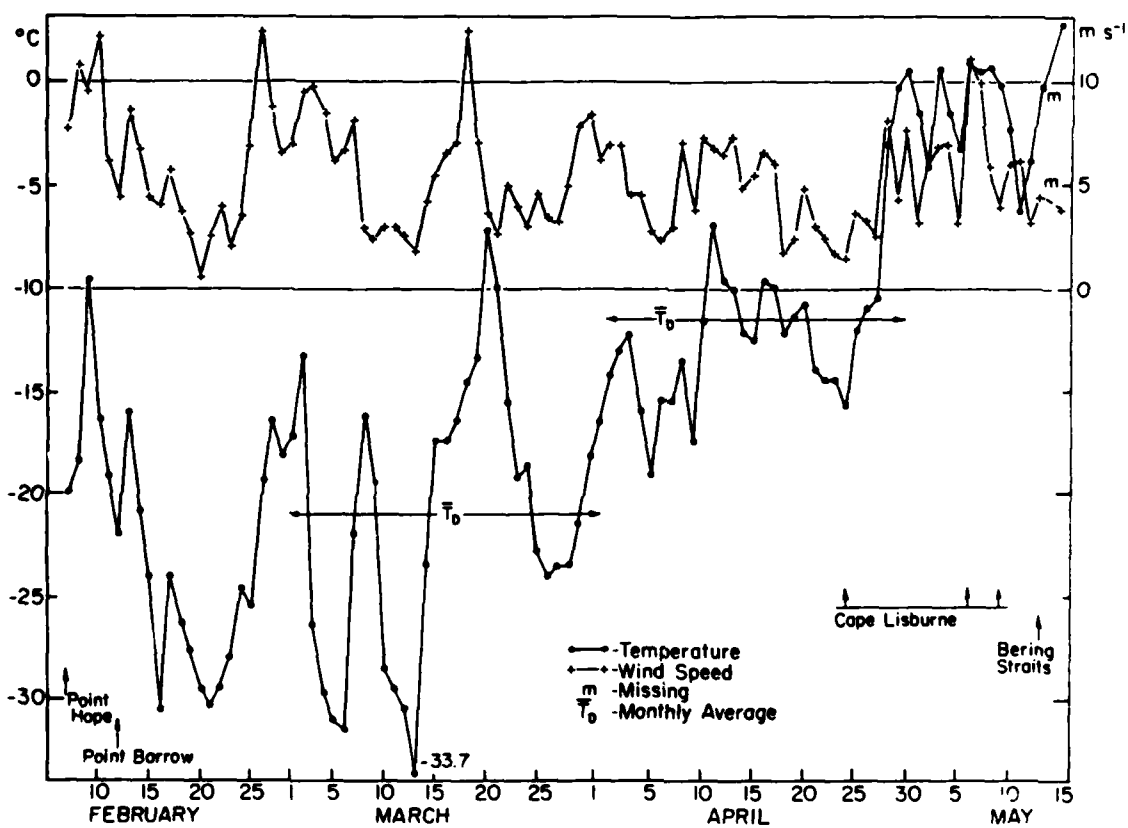


Fig. 2. Graph of temperature and wind speed. Daily averages were calculated from 6-hourlies (7 Feb to 1 Mar) and 3-hourlies (2 Mar to 15 May). Arrows indicate days when Polar Sea was at or near the named geographic features.

## WEATHER

Routine weather observations (pressure, wet and dry bulb temperatures, wind speed and direction, visibility, clouds, and weather type) were made at six-hour intervals prior to 2 March, after which time they were made hourly. Temperature and wind data were measured from the helicopter flight deck, about 9 m above the waterline. No attempt has been made to take into account the "heat island effect" of the ship, so it should be kept in mind that the recorded air temperatures (Fig. 2) are likely to be somewhat higher than would have been observed at a standard thermometer screen placed on nearby ice. Air temperatures during February and March were usually in the  $-15^{\circ}$  to  $-30^{\circ}\text{C}$  range. The day with the lowest average temperature ( $-33.7^{\circ}\text{C}$ ) was 13 March, when the ship was drifting about a hundred kilometers northwest of Icy Cape, Alaska. Temperatures moderated rapidly following the 13 March extreme, with a general warming trend evi-

dent throughout the remainder of the cruise. Snowfall was reported in 23% of the observations, while fog occurred only about 8% of the time (Table 1). Conditions with blowing snow or rain were each reported less than 2% of the time. Days with the greatest drift of the ship (up to  $2\text{ km hr}^{-1}$ ) were those with southeasterly winds, generally in excess of  $10\text{ m s}^{-1}$ .

## SNOW AND ICE OBSERVATIONS

Snow may fall on any day of the year in this region. Because snow depth is so variable in space, accurate estimates of total amount require measurements at a large number of points. Snow depth determinations during the cruise were made using an  $11 \times 11$  rectangular sampling array with a grid spacing of 3 m. In practice it is useful to distinguish between snow cover on "smooth" ice and "rough" ice (Hanson, 1980). Smooth ice can be either flat first-year ice or multiyear ice with a

**Table 1. Frequency of weather element (ww) of the synoptic reports from *Polar Sea* for 2 March through 13 May from 3-hourly observations.**

ww	No. of reports	Percent of total	Comments
00	91	15.6	Clear
01	90	15.4	Clearing
02	97	16.6	No change
03	107	18.2	Increasing clouds
05	9	1.5	Haze
07	1	0.2	Distant storm
23	1	0.2	Snow, ended last hour
28	1	0.2	Storm, ended last hour
36	1	0.2	
38	4	0.7	Blowing snow
39	4	0.7	
40	3	0.5	
41	1	0.2	
42	3	0.5	
43	6	1.0	Fog (variable amount)
44	5	0.9	
45	9	1.5	
46	5	0.9	
47	9	1.5	
51	1	0.2	Drizzle
66	1	0.2	
68	5	0.9	Rain and snow
69	2	0.3	
70	34	5.8	
71	67	11.5	
72	3	0.5	
73	14	2.4	Snow (various intensities)
77	8	1.4	
79	2	0.3	
87	1	0.2	

gently undulating surface. On rough ice substantial areas of the surface are covered by upthrust blocks, rubble piles, or pressure ridges. Snow surveys were carried out on 13 April over flat first-year ice and adjacent rough ice. The *Polar Sea* was then at latitude 69.7°N and longitude 168.3°W, approximately 125 km northwest of Cape Lisbourne, Alaska. The mean snow depths were 5.0 and 49.3 cm for the smooth and rough categories, respectively. Snow depth statistics are given in Table 2; also included in Table 2 for comparison are several earlier snow depth surveys from the Alaskan coastal region. Depths observed during PSDP probably represent five to six months' accumulation since the thickness of the flat first-year ice was between 1.2 and 1.4 m, roughly the total ice growth expected between fall freezeup and early spring. It is clear, however, that there must have been considerable horizontal transport of snow from smooth areas to rougher ones.

The snow cover was frequently found to contain significant amounts of salt. Values as high as 22.7% were observed. Table 3 lists measurements made at three different sites. The highest salinity sample appears to represent a crust formed from efflorescent crystals with an admixture of wind-transported snow, a situation that is probably common in the region. The 27 April samples unexpectedly showed a higher salinity in the upper part of the snow than in the lower. This was again probably the result of wind transport, but in this case it was the salt of the efflorescent crystals on the thin ice of nearby leads which must have been blown over existing snow at the site sampled. The

**Table 2. Results of snow cover depth surveys.**

Sample date	N*	$\bar{z}^{\dagger}$	S†	T**	Comment
13 Apr 81	138	5.0	4.2	5.5	Chukchi Sea smooth fyi, †† 9-m grid
13 Apr 81	104	49.3	45.1	5.5	Chukchi Sea rough fyi, 9-m grid
18 May 79	121	17.8	7.9	7.3	Elson Lagoon, 9-m grid
29 Apr 79	132	6.9	3.6	7.0	Narwhal Island smooth, 10-m grid
29 Apr 79	93	25.7	23.9	7.0	Narwhal Island rough, 10-m grid
29 Apr 79	225	22.7	22.7	7.2	Narwhal Island, 1 km E, rubble-free

\* Number of measurements.

† Mean and standard deviation in centimeters.

\*\* Estimated period of accumulation in months.

†† fyi = first-year ice.

**Table 3. Snow salinities from the Chukchi Sea.**

Sample date	Snow layer	Salinity	Comments
31 Mar	2-4 cm deep	22.7	Ice thickness about 1 m
27 Apr	0-5 cm deep	8.7	Top half of snow layer
27 Apr	5-11 cm deep	5.7	Bottom half of snow layer
3 May	top 3-4 cm	0.0	Wet drift, 0°C, thawing
3 May	mid 4-6 cm	0.0	had begun
3 May	low 3-5 cm	0.2	

presence of salt in the snow will tend to advance the onset of snowmelt and promote the formation of liquid water within the snow cover. In an active region where winter lead formation is frequent, nearby multiyear and first-year ice are both likely to accumulate layers of salty snow. With the onset of spring warming, this salt may act to blur the distinction between microwave emission from first-year and multiyear ice.

A striking feature of the first-year ice in the Chukchi Sea was the presence of more or less continuous horizontal bands oriented roughly parallel to the ice/water interface. A dark band of algae, 1-5 cm thick, was often present either at or near the bottom of the ice, while extensive whitish bands were evident at higher levels within the ice. Ridge blocks usually displayed portions of these white bands (e.g. Fig. 3). These bands frequently



*Fig. 3. Block of snow-capped first-year ice with snow-ice forming the portion above the dark band (arrows).*

maintained a nearly uniform thickness over tens of meters in the horizontal. Samples of the band material were examined in thin section and appeared to be essentially homogeneous. The darker band (arrows, Fig. 3) contained submillimeter sized bits of sediment trapped in the ice. Thin bands below the dark band are more or less parallel with the upper surface, suggesting ordinary growth as described by Bennington (1963). The whitish bands were probably formed when snow fell or was blown onto areas of thin ice or fell directly into an open water area. Snow already deposited could also be blown onto thin ice or into open leads where the water-saturated mass would eventually freeze. These processes appear to be of major importance in the eastern Chukchi Sea, where 10% to 25% of the ice cover south of 69°N may be made up of this "snow-ice."

The ice pack in the vicinity of the ship at the onset of our observations (17 March) was a mixture of roughly 40% first-year ice and 60% multiyear ice. This ratio persisted until 6 April when the ship reached a region that was essentially all first-year ice. Accompanying the change in age and thickness was a change in the color of the ice as a result of increased sediment loading and algae content. The relatively large amount of sediment incorporated into the surface layer was presumably a result of formation in shallow water in the presence of turbulence. As the ship moved south, there was a gradual increase in the amount contained within the ice. Whether this increase was a result of actual spatial variations in the amount of algae or whether it was a temporal change due to the increasing insolation cannot be determined from these observations.

A particularly interesting ice feature was observed near the ship during the period of besetment. This was a very thick old floe of the type referred to as "paleocrystic" (Moss, 1878). Such floes are characterized by well-rounded hummocks and probably represent the remains of an exceptionally thick hummock field. The highest elevation on this floe reached approximately 16 m above water level. The ice thickness at a distance of 50 m from the peak was in excess of 9 m (B. Smith, personal communication). Except for the "hills" on ice island ARLIS II, this appears to be the largest weathered hummock ever reported.

When the ship was breaking ice, fractures ran outward from the bow in a fan-shaped pattern. These fractures often bifurcated, splitting off new ice blocks. In addition to the new blocks, there were numerous blocks coated with algae and having a weathered appearance. The weathered

blocks bobbed up from where they had been lodged on the underside of the floes. These observations suggest the existence of a large amount of loose rubble beneath the ice pack in the Chukchi Sea. This material is undoubtedly generated during episodes of ice deformation and transported various distances by currents beneath the ice.

The *Polar Sea* sometimes encountered lanes of open water where it was able to proceed at a relatively steady rate for a sufficient distance to obtain data on pressure ridge frequency. Distance to within  $\pm 15\%$  was obtained by use of a Doppler radar speedometer. Sails of pressure ridges were counted if their heights were estimated to be 0.3 m or greater. Since many ridges had multiple peaks, separate counts were made of peaks and ridges. The tallest sail in these samples was an estimated 5 m high. The average distance between ridges was about 50 m. A summary of the ridge data is presented in Table 4.

The number of ridges per kilometer was as much as an order of magnitude greater than counts obtained from submarine profiles (Hibler et al., 1972; Williams et al., 1975; Wadhams and Horne, 1980). This is probably due to the higher spatial resolution possible with direct visual observation as compared to even narrow-beam sonar measurements. The visual counts may thus include a large number of small ridges that would be missed by the sonar. However, it is also possible that the ridge density in the thinner ice of the eastern Chukchi Sea may be much greater than in the thicker ice of the Central Arctic Basin where much of the submarine data were gathered.

The shape of many of the ridge sails was not simply pyramidal in cross section, but consisted rather of a number of separate peaks. About 36% of the ridges sampled had such multiple peaks. On

Table 4. Counts of pressure ridges in the Chukchi Sea, 7 April 1981.

Sample	1	2	3	4	5
Period (min)	24	30	8	30	30
Latitude (north)	70.3	70.2	70.1	70.0	69.7
Longitude (west)	167.5	167.5	167.5	167.5	167.3
Length (km)	4.4	8.3	2.2	8.7	7.4
Peaks (N)	106	26	47	319	296
Ridges (n)	—	180	22	178	167
B	18	38	13	57	53
N km <sup>-1</sup>	24	32	21	37	40
n km <sup>-1</sup>	—	22	10	20	23
N n <sup>-1</sup>	—	1.48	2.14	1.79	1.77
M	—	3.26	2.92	3.47	3.43

M = (N + B - n)/B, B = count of multipeaked ridges.

the average, such ridges had slightly more than three peaks each.

In addition to ice deformation produced by the ship, several interesting natural events were observed. The most dramatic took place in 1.5- to 2.0-m-thick snow-covered ice during a "crossover" between adjacent leads. While stopped in the crossover, *Polar Sea* was subjected to compressive ice stresses on the port side, which forced ice under the ship and caused a ridge to form on the starboard side. The screws were enmeshed with ice blocks, and the rudder pushed to 19° starboard angle. Off the bow an overthrust between 80 and 100 m in length doubled the ice thickness, while at the same time the 25-m-wide track of rubble in the wake completely vanished. The relative motion of the ice during this event was slow and in pulses averaging between 0.5 and 1.0 cm s<sup>-1</sup>.

A particularly striking deformational feature was a shear ridge system encountered to the south of Point Hope (Fig. 4). A shear ridge is produced by strike-slip faulting with enough compression across the fault plane to break and pile up the ice at the fault. In the Point Hope system, ice to the east of the primary fault (see Fig. 1) remained stationary, while ice to the west was able to move in the north-south direction. The relative motion that formed these ridges was probably synchronous with the several periods of northward drift between 26 April and 8 May. If this is the case, then the minimum offset involved in the formation of these ridges can be estimated from the northward drift of the ship and must have been greater than 170 km. This entire offset did not, of course, take place along a single fault, but rather along a series of parallel faults spaced a few meters apart. The surface of the most recent fault nearly always tilted away from the vertical on both sides, but a small amount of overhanging wall was also observed.

Ice samples were obtained during periods when the ship lay to (e.g. 22 and 23 March, 7, 13, 15 and 27 April, 8 May). Horizontal and vertical thin sections were cut from these samples, smoothed and thinned by melting on a flat surface, then photographed between crossed polarizing filters using a high speed 35-mm color film. Additional exposures were also taken in reflected light and black and white prints made for study purposes. Preliminary examination of the photographs indicates: 1) the thickness of the consolidated layer of frazil crystals (the loose ice crystals which form when seawater initially freezes) varied between 1 and 20 cm, 2) layering was clearly evident in nearly all thrust blocks examined (e.g. Fig. 5), 3) the fre-

quency of occurrence of bubbles was directly related to their diameter, 4) there were few bubbles larger than 1 mm in diameter and these were generally irregular in shape (e.g. Fig. 6), 5) the number concentration of bubbles was typically 200-400 per cm<sup>3</sup> but dropped to less than 100 per cm<sup>3</sup> in a few cases, and 6) there was a tendency for the number of bubbles to decrease with increasing depth in the ice.

## DISCUSSION

Most of the available surface weather observations from the Chukchi Sea have been taken during short-duration cruises along the coast during the shipping season, generally August and September. Some observations during other parts of the year were made by expeditions in the western part of the Chukchi Sea, notably *Jeannette* (1879-80) and *Maud* (1920). A number of drifting ice stations have also transited the northern part of the Chukchi Sea (most recently NP-22 in winter 1978-79), but they produced no information on conditions over the younger ice in the southern Chukchi. With maritime data being extremely sparse and seasonally biased, observations such as those from *Polar Sea* are a welcome addition to the meager data base.

Our observations indicate that significant amounts of snow are incorporated into the ice cover during the formation of snow-ice bands, and also mixed into ice piles and pressure ridges during deformation. Snow depth surveys thus reveal only part of the total mass deposition, making it difficult to infer seasonal snowfall totals from snow depths alone. Unfortunately, direct measurements of snowfall are also subject to considerable error (Black, 1954) as a result of wind effects. Nevertheless, it is possible to get a rough estimate of seasonal snowfall ( $\bar{z}$ ) in the region from observations made during the cruise. If  $z_s$  is the mean snow depth measured on a smooth floe, one would expect a relationship between  $\bar{z}$  and  $z_s$  to have the form

$$\bar{z} = \rho_s z_s / \rho_0 \quad (1)$$

where  $\rho_s$  is the observed snow density and  $\rho_0$  is the initial density of freshly fallen snow. The cruise observations have shown, however, that much of the snowfall in the region is incorporated in the snow-ice. To take this into account, eq 1 must be modified:

$$\bar{z} = (\rho_s z_s + \rho' z_i) / \rho_0 \quad (2)$$

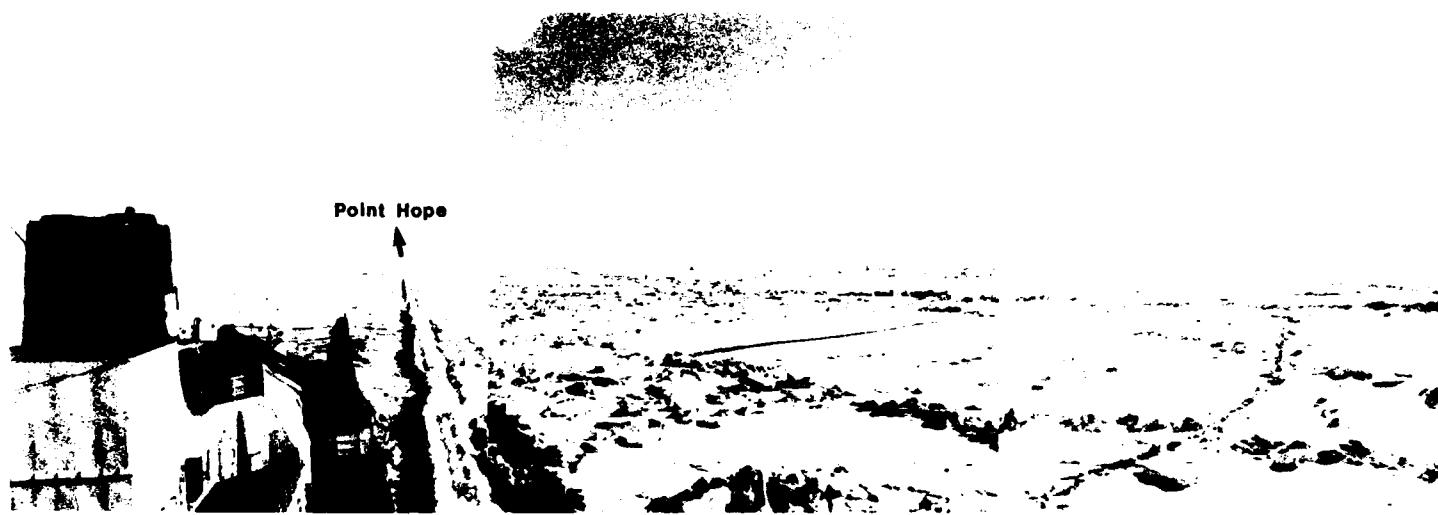


Fig. 4. Panoramic view with six photographs of a shear ridge, 11 May 1981.

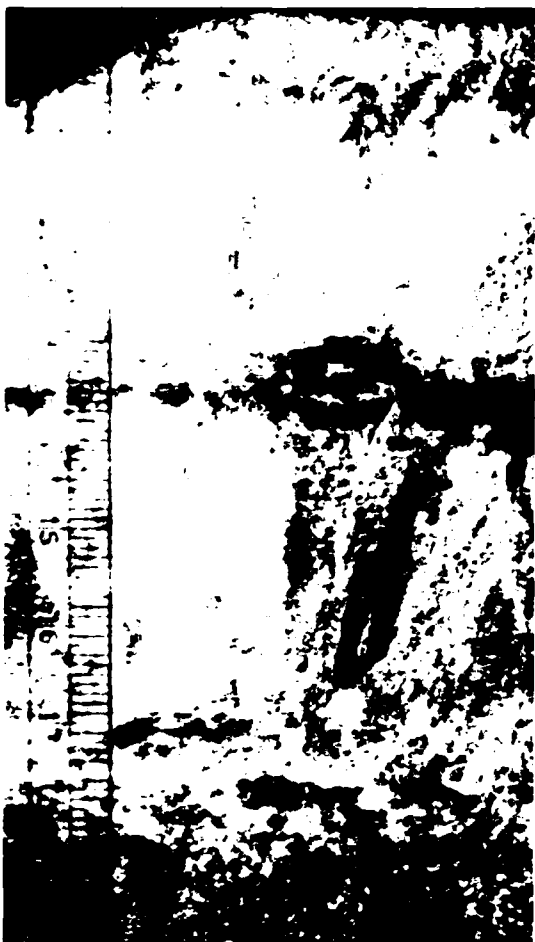


Fig. 5. Triple-stacked thrust structure. The vertical thin section was photographed in color with crossed polarizers (millimeter scale at left). The central layer may be inverted.

where  $z_s$  is the average thickness of the snow-ice layer and  $\rho_s'$  is the density of the snow within the snow-ice. Because of the differences in snow accumulation on smooth and rough ice,  $z_s$  should be treated as an area-weighted average, i.e.

$$\bar{z} = [\rho_s(Rz_s + Sz_s) + \rho_s'(z_s)]/\rho_s \quad (3)$$

where  $R$  and  $S$  are the fractional areas of rough and smooth ice, and  $z_s$  and  $z_s'$  are mean snow depths on rough and smooth areas respectively.

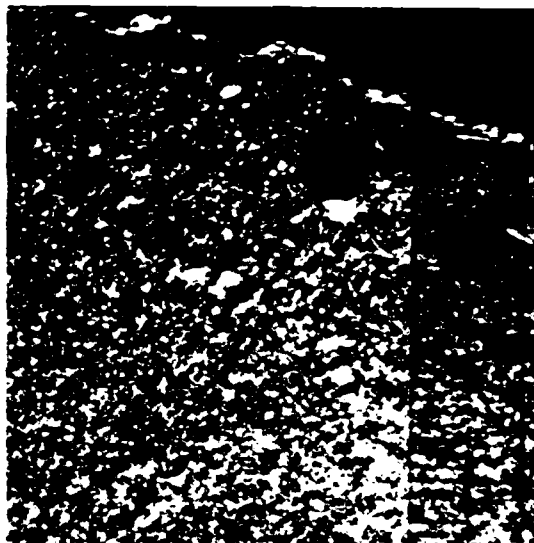


Fig. 6. Vertical section of surface layer of multi-year ice showing typical irregular shaped (sub-rounded) bubble (millimeter scale at right). From an Ektachrome slide.



$R + S$  is assumed to be unity. Hanson (1980) has pointed out that a significant portion of the snow cover on sea ice is due to frost accumulation. If we let  $\beta$  represent this fraction, then

$$\bar{z} = [\varrho_s(1 - \beta)(Rz_s + Sz_s) + \varrho_s' z_s]/\varrho_s. \quad (4)$$

The area of smooth ice in the Chukchi Sea was roughly twice as large as that of rough ice, with  $z_s = 50$  cm and  $z_r = 5$  cm. Thickness of the ubiquitous snow-ice layer reached 50 cm but was more typically about 20 cm. Frost deposition was assumed to account for 20% of the snow cover (Hanson, 1980). Initially, snow density was taken to be  $0.1 \text{ g cm}^{-3}$ , about one-third the value observed for the old snow. The value of  $\varrho_s'$  depends on whether the snow-ice was derived from wind-blown snow or freshly fallen snow. Both types undoubtedly contributed to snow-ice production in the Chukchi, with an average  $\varrho_s'$  somewhere between  $0.1$  and  $0.3 \text{ g cm}^{-3}$ . For the calculations which follow, we simply took  $\varrho_s' = 0.2 \text{ g cm}^{-3}$ . With these values eq 4 gives  $\bar{z} = 88 \text{ cm}$ . Considering that the surveys were carried out on 5- to 6-month-old ice, this snowfall calculation amounts to approximately 2 cm water equivalent per month, consistent with other precipitation data from the western Arctic.

Weeks and Lee (1962) have documented the existence of substantial vertical and horizontal salinity variations in a first-year sea ice cover. The ice samples taken more or less at random during the cruise of the *Polar Sea* show that there are similar differences in ice structure and bubble density,

complicating the interpretation of many types of remote sensing data.

In regard to ice movement, it is clear from the shear ridge shown in Fig. 5 that ice to the southeast of Point Hope behaved like fast ice and did not drift northward. While the *Polar Sea* was drifting northward, there was little evidence of ice movement east of Point Hope. Thus it appears that the best strategy for southbound ships is to round Point Hope toward Kotzebue to take advantage of the relatively stagnant ice there.

Although our plans to monitor temporal changes in the state of the ice at specific locations were stymied by the continued efforts to make southward progress, the icebreaker proved to be a useful platform for gathering data on ice conditions over a wide area. In very active areas where long-term camps would have a high probability of being destroyed, such a platform is the only practical means for observing deformational processes. Research efforts in the marginal and seasonal ice zones need this type of support, and it is expected that increasing use will be made of icebreakers or ice-strengthened ships for scientific purposes in the future.

#### ACKNOWLEDGMENTS

Funding for this research was provided by Office of Naval Research Contracts N00014-76-C-0234 and N00014-81-K-0460. ARCTEC Inc. furnished transportation for the author from Barrow to the *Polar Sea*. My thanks to the crew members of the *Polar Sea* who provided necessary services

too numerous to mention. T.C. Grenfell and G.A. Maykut provided critical comments on the original version of this paper.

## REFERENCES

**Bennington, K.O.**, Some crystal growth features of sea ice, *J. Glaciol.*, 4, 669-688, 1963.

**Black, R.F.**, Precipitation at Barrow, Alaska, greater than recorded, *Trans. AGU*, 35, 203-206, 1954.

**Dirschel, J.J., Jr.** Report of Arctic Winter West 1981 and Polar Sea Drift Project 1981, USCGC *Polar Sea*, Seattle 84 pp., 1981.

**Hanson, A.M.**, The snow cover of sea ice during the Arctic Ice Dynamics Experiment, 1975 to 1976, *Arctic Alpine Res.*, 12, 215-226, 1980.

**Hibler, W.D. III, W.F. Weeks and S.J. Mock**, Statistical aspects of sea-ice ridge distributions, *J. Geophys. Res.*, 77, 5954-5970, 1972.

**McPhee, M.G. and N. Untersteiner**, Using sea ice to measure vertical heat flux in the ocean, *J. Geophys. Res.*, 87, 2071-2074, 1981.

**Moss, E.L.**, *Shores of the Polar Sea*, London, Marcus Ward & Company, 83 pp., 18 chromographs, folio edition, 1878.

**Shuhy, J.L.**, USCGC *Polar Sea* Drift Project '81, *Arctic*, 34, 377-378, 1981.

**Wadhams, P. and R.J. Horne**, An analysis of ice profiles obtained by submarine sonar in the Beaufort Sea, *J. Glaciol.*, 25, 401-424, 1980.

**Weeks, W.F. and O.S. Lee**, The salinity distribution in young sea ice, *Arctic*, 15, 92-108, 1962.

**Williams, E., C. Swithinbank and G. de Q. Robin**, A submarine sonar study of arctic pack ice, *J. Glaciol.*, 15, 349-362, 1975.

## Introduction to MIZEX-West

SEELYE MARTIN

*Experiment Chief Scientist*

*School of Oceanography WB-10, University of Washington  
Seattle, Washington 98195, USA*

The MIZEX-West field experiment took place in the Bering Sea during February 1983. The experiment involved two ships, the Coast Guard ice-breaker *Westwind* and the NOAA ship *Discoverer*; two aircraft, the NASA Convair-990 and the NOAA P-3; a set of over-winter moored current meters; and the Scanning Multichannel Microwave Radiometer (SMMR) on board the Nimbus-7 satellite. Arctic Programs, Office of Naval Research, provided core support for the program; additional support came from the National Aeronautics and Space Administration, the National Oceanic and Atmospheric Administration, the National Science Foundation, the Alaska Oil and Gas Association, the United States Geological Survey, and the British Natural Environment Research Council. The experiment had three purposes: to study the microwave radiometric properties of sea ice with the purpose of improving our use of satellite instruments to determine sea ice concentration; to study the oceanic, atmospheric, and sea ice processes which control the ice motion; and to determine the ice edge position.

The experiment took place as follows: the *Westwind* steamed about 150 km into the ice and deployed an array of satellite- and ship-tracked position and meteorological buoys. The *Westwind* then drifted with the surrounding ice over a 16-day period as the ice moved from the interior toward the ice edge. As the ship drifted, investigators carried out a variety of oceanographic, meteorological, and remote sensing surface observations. At the same time, the *Discoverer* carried out a similar set of measurements at the ice edge. The two aircraft, which were based in Anchorage, carried out several overflights of the experimental region. The NASA aircraft, which was equipped with several passive microwave radiometers, as well as a version of the radar altimeter planned for the European Space Agency satellite ERS-1, carried out six high-level mosaic overflights of the experimental region. The NOAA P-3, which was equipped with gust probes, a SLAR, a laser profilometer, and

temperature sensors, carried out five low-level overflights, in the course of which they flew several experimental stacks over each ship.

The MIZEX-West experiment produced a variety of results on the radiometric properties of the Bering Sea ice cover and on the use of satellite data to determine the ice edge position, the location of polynyas within the ice cover, and the ice concentration as a function of position and time. In addition, the experiment produced a quantitative description of the sea ice, the oceanography, and the meteorology of the Bering Sea MIZ during the observation period. To summarize these results and to compare them with the results from the Greenland Sea, we first note that in contrast to the Greenland Sea, the ice cover in the Bering Sea forms over a continental shelf with depths of 50 to 100 m. Further, the predominant ice drift is toward the ice edge rather than, as occurs in the Greenland Sea, parallel to the ice edge. The control of the ice edge position appears to be a thermal balance between the advection of ice floes southwestward by the northeast winds, and the heat flux from the warm Pacific water at the ice edge. The oceanographic observations show that a 100-km-wide front separates the cold, less-saline shelf water and the warm, saline North Pacific water. Associated with this front is a northwestward-flowing geostrophic current, which apparently leads to the ultimate transport of North Pacific water into the Gulf of Anadyr, around the west side of St. Lawrence Island, then through the Bering Strait.

The experiment further showed that the amount of open water in the form of leads and polynyas increases as we move from the consolidated pack across the MIZ into open water. The meteorological observations show that this increase has a strong effect on the atmospheric boundary layer, in that the increased heat flux from the open water combined with an ocean-swell-induced increase in ice roughness, reduces the thickness of the atmospheric boundary layer and causes a wind acceleration. The ice floe behavior near the ice edge is also

complicated. First, there is a turbulent dispersion of ice floes apparently caused by the turbulent ocean eddies. Second, the ice floes tend to be organized into ice bands, which are accelerated into the warmer water away from the ice edge. Associated with this transport into warm water is a very rapid ice ablation, with measured vertical ablation rates of  $0.7 \text{ m day}^{-1}$ .

As the following papers show, we now have considerable knowledge and data regarding the environmental behavior of the Bering Sea ice

cover. The job remains to use these data in a unified theory of the response of the ice cover to winds and storms.

The author gratefully acknowledges the support of the Office of Naval Research under Task NR 083-012 and contract number N00014-84-C-0111. The author and the other MIZEX-West investigators especially thank Dr. Leonard Johnson for his personal and institutional support of this experiment. Without it, MIZEX-West would not have taken place.

## Temperature and Salinity Observations in the Bering Sea Winter MIZ

R.D. MUENCH

*Science Applications International Corporation  
Bellevue, Washington*

J.L. NEWTON

*Polar Research Laboratory  
Carpinteria, California*

R.L. RICE

*Geo-Ocean Horizons  
Snohomish, Washington*

### INTRODUCTION

An intensive study of physical processes was carried out in the Bering Sea marginal ice zone (MIZ) during winter 1982-1983. A descriptive overview of the experiment and summary of its major results has been presented by the MIZEX-West Study Group (1983). A primary goal of this experiment was to obtain information on oceanographic processes associated with the pronounced ocean frontal system which underlies the MIZ. This frontal system was detected in winter 1979 (Pease, 1980) and was further documented in winter 1981 by Muench (1983). It typically is associated with, and underlies, the MIZ during mid-winter (February-March) when the Bering Sea winter ice cover is at its position of greatest southward advance. The persistent features of this front can be described, with reference to the schematic depiction shown in Fig. 1, as follows:

1. A 100- to 200-km-wide band of two-layered water underlies the MIZ, and the seaward or southern extreme of this band coincides approximately with the ice edge. The layered structure consists of cold, low-salinity water overlying warmer, more saline water. The upper layer is continuous with shelf water to the north, and the lower layer is continuous with oceanic water to the south. The upper layer is less dense than the lower.
2. The interface between these two layers steepens sharply and intersects the sea surface at the ice edge, forming a front there which coincides

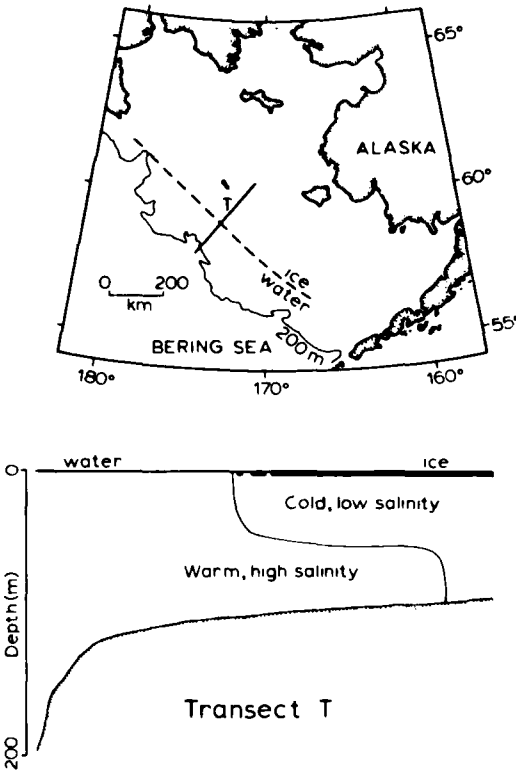


Fig. 1. Conceptualization showing the approximate geographical location and extent of the ice edge front, and its relation to the ice edge (upper). The vertical section (lower) illustrates the ocean structure that typifies the front along cross-frontal transect T.

with the ice edge. Consistent with the thermal stratification across the interface, cold near-surface water is present north of the front and warmer water occurs south of the front.

3. The interface slopes gradually downward toward the north, then steepens and intersects the seabed in the vicinity of the 100-m isobath. Bottom water seaward of this isobath is relatively warm and saline, while water north of it is colder and less saline. North of about the 100-m isobath the water is vertically homogeneous.

Oceanographic conditions associated with the MIZ have been analyzed, using the winter 1983 data, by Muench and Schumacher (1985). They support and further document the above description of MIZ oceanic structure and describe in addition a northwestward current which underlay the ice edge. They conclude that the ice edge location reflects a balance between the heat lost to

melting ice and heat input to the region by a northward flow of relatively warm oceanic water. Hendricks et al. (1985) constructed a more detailed oceanic heat balance for the ice edge. They reaffirm that the balance is dominated by ice melting and northward oceanic heat advection, and they also estimate the magnitudes of vertical and lateral diffusive fluxes and of heat loss to the atmosphere. They derive vertical and lateral eddy diffusivities of approximately  $4 \text{ cm}^2 \text{ s}^{-1}$  and  $3 \times 10^5 \text{ cm}^2 \text{ s}^{-1}$ , respectively, which are similar to those which have been determined for other shelf regions.

Both Muench and Schumacher (1985) and Hendricks et al. (1985) presented specific temperature and salinity data products as called for by their analyses. A significant proportion of the winter 1983 temperature and salinity data have, however, not been shown. It is the purpose of this report to

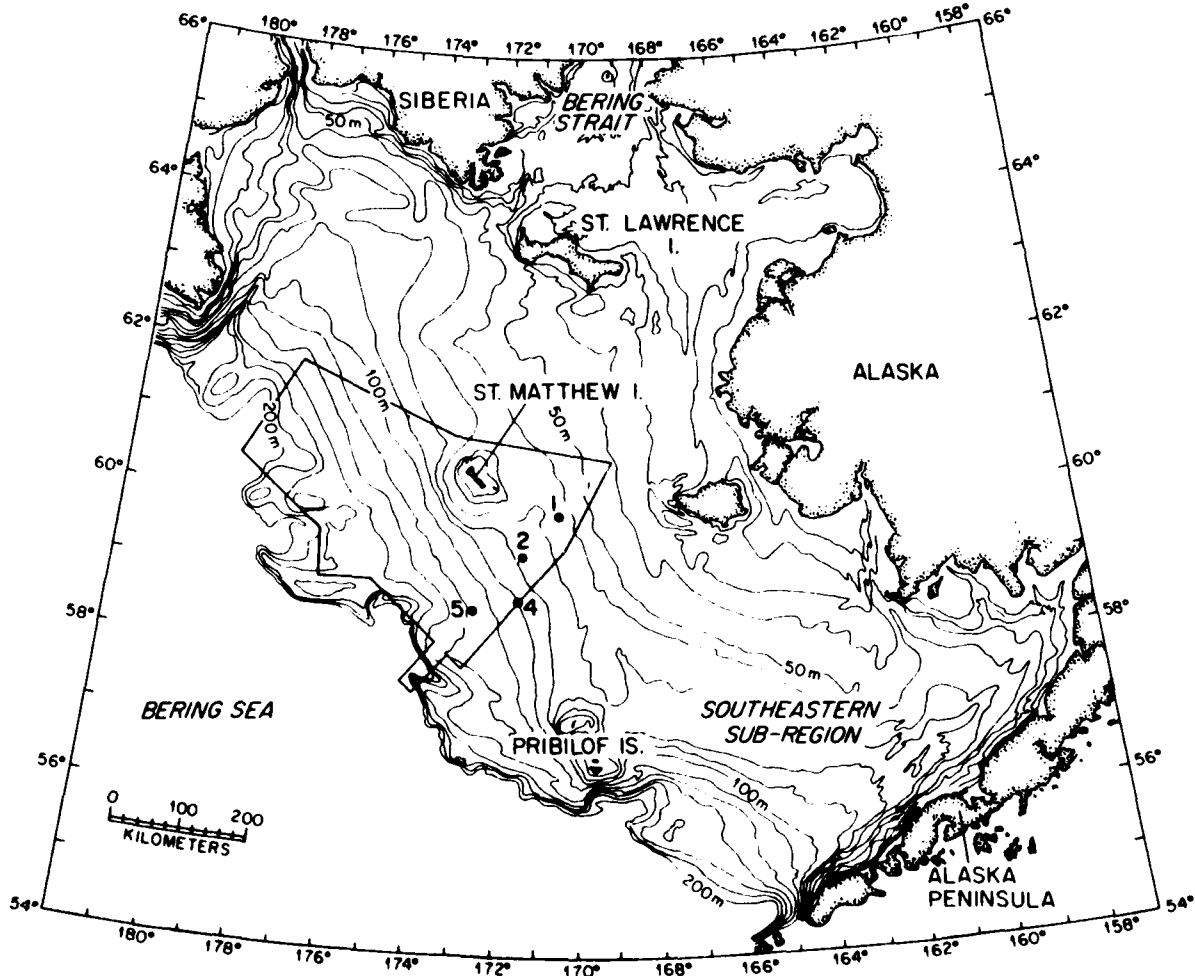


Fig. 2. Geographical location of the winter 1983 Bering Sea Marginal Ice Zone Experiment (MIZEX-West). The area enclosed in the polygon was included in the winter CTD survey. Numbered dots indicate the locations of moorings which were in place over winter 1982-1983. Specific information on the moorings is given in Table 1.

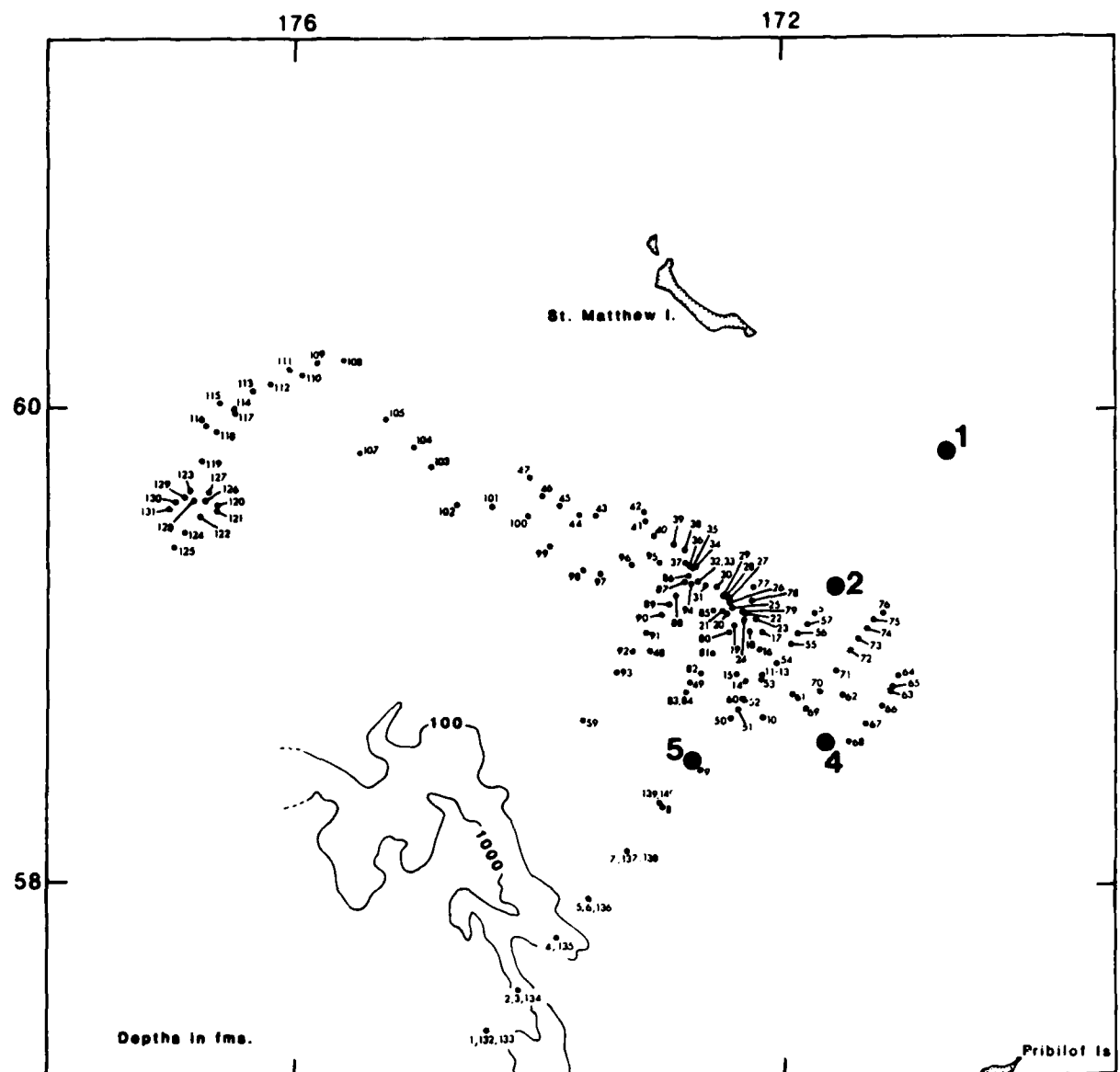


Fig. 3. Geographical locations of CTD casts occupied by the NOAA ship Discoverer during MIZEX-West.

provide a reasonably complete representation of these data accompanied by summary descriptions and discussion.

#### THE FIELD PROGRAM

The 1983 field program was carried out in the central Bering Sea MIZ (Fig. 2). A major goal of this experiment was to better define the temperature and salinity, and associated density, properties of the MIZ oceanic front described above. Two coordinated observational approaches were used to accomplish this:

1. Vertical profiles of temperature and salinity were obtained with CTDs from three vessels that operated in the MIZ over the mid-winter (February–March) period.
2. Taut-wire moorings were deployed in October 1982, at locations projected to underlie the MIZ. These moorings were recovered in May 1983. Their primary function was to measure currents; these data were analyzed and discussed by Muensch and Schumacher (1985) and Hendricks et al. (1985). The moorings also measured temperature and salinity over the entire winter deployment period. Table 1 summarizes pertinent information on the moorings.

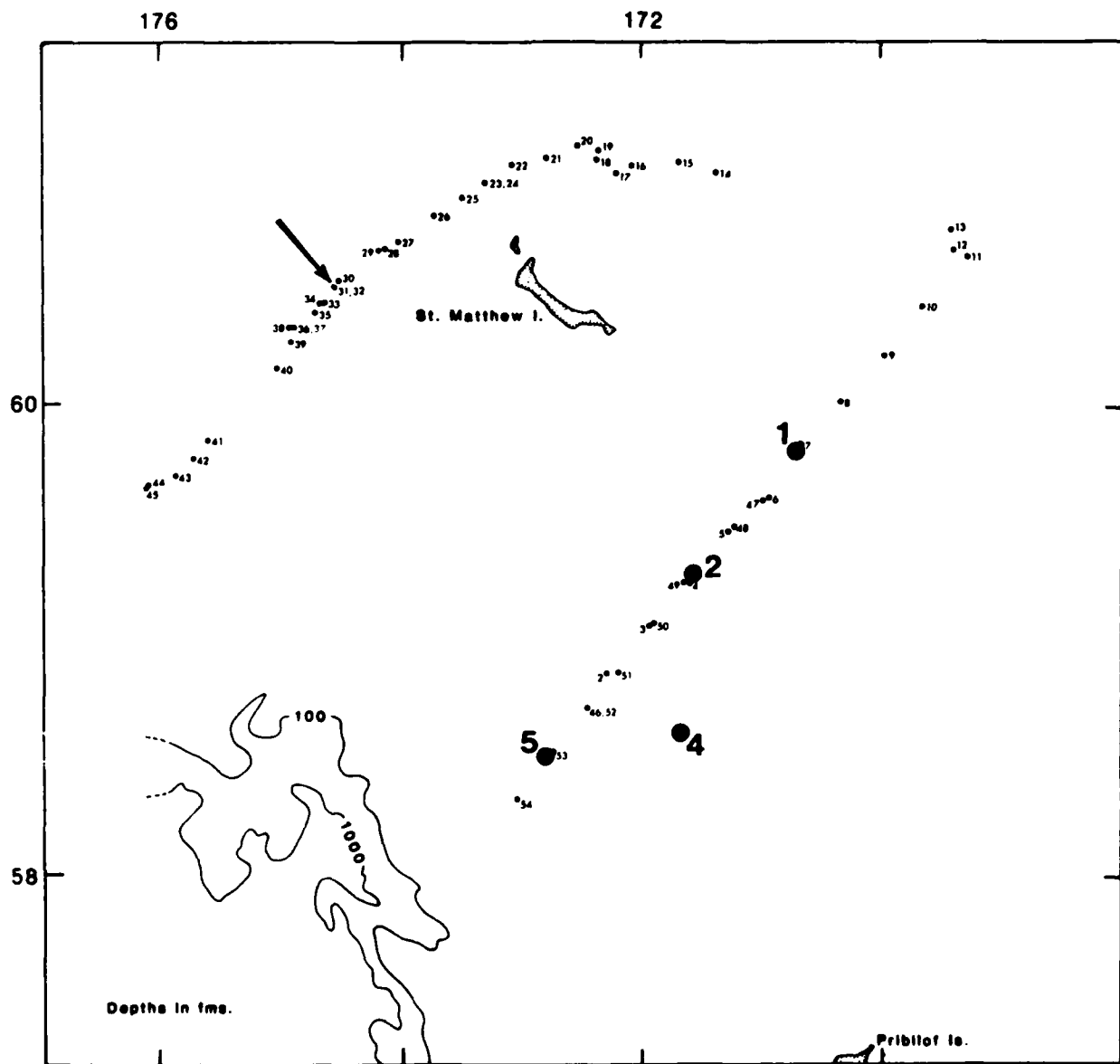


Fig. 4. Geographical locations of CTD casts occupied by the USCG icebreaker Westwind during MIZEX-West. The arrow indicates the time-series cast (32) which was used to construct Fig. 20.

#### Shipboard observations

The mid-winter 1983 shipboard temperature and salinity observation program consisted of the following:

1. The NOAA ship *Discoverer* occupied 138 CTD stations at the ice edge and in the open water seaward of the edge on 5-27 February. Her ice-strengthened hull allowed penetration into the loose, broken ice near the edge but not into the more solid pack well north of the edge. A Grundy CTD system was used which recorded on magnetic tape and also provided a near-real-time readout. Locations of the stations occupied by *Discoverer* are shown in Fig. 3.

2. The USCG icebreaker *Westwind* occupied 53 stations on 6-27 February. These stations were taken within the pack ice north of the edge, utilizing the full icebreaking capability of the vessel. The data were taken using a Neil Brown Instrument Systems Mark III CTD system, which had been modified for arctic use by a specially made sensor head designed to protect the sensors against ice damage. The data were recorded digitally on a Hewlett-Packard 85 microcomputer and as audio signals on a Teac cassette deck. Real-time data printouts were also provided. Locations of the *Westwind* CTD stations are shown in Fig. 4.

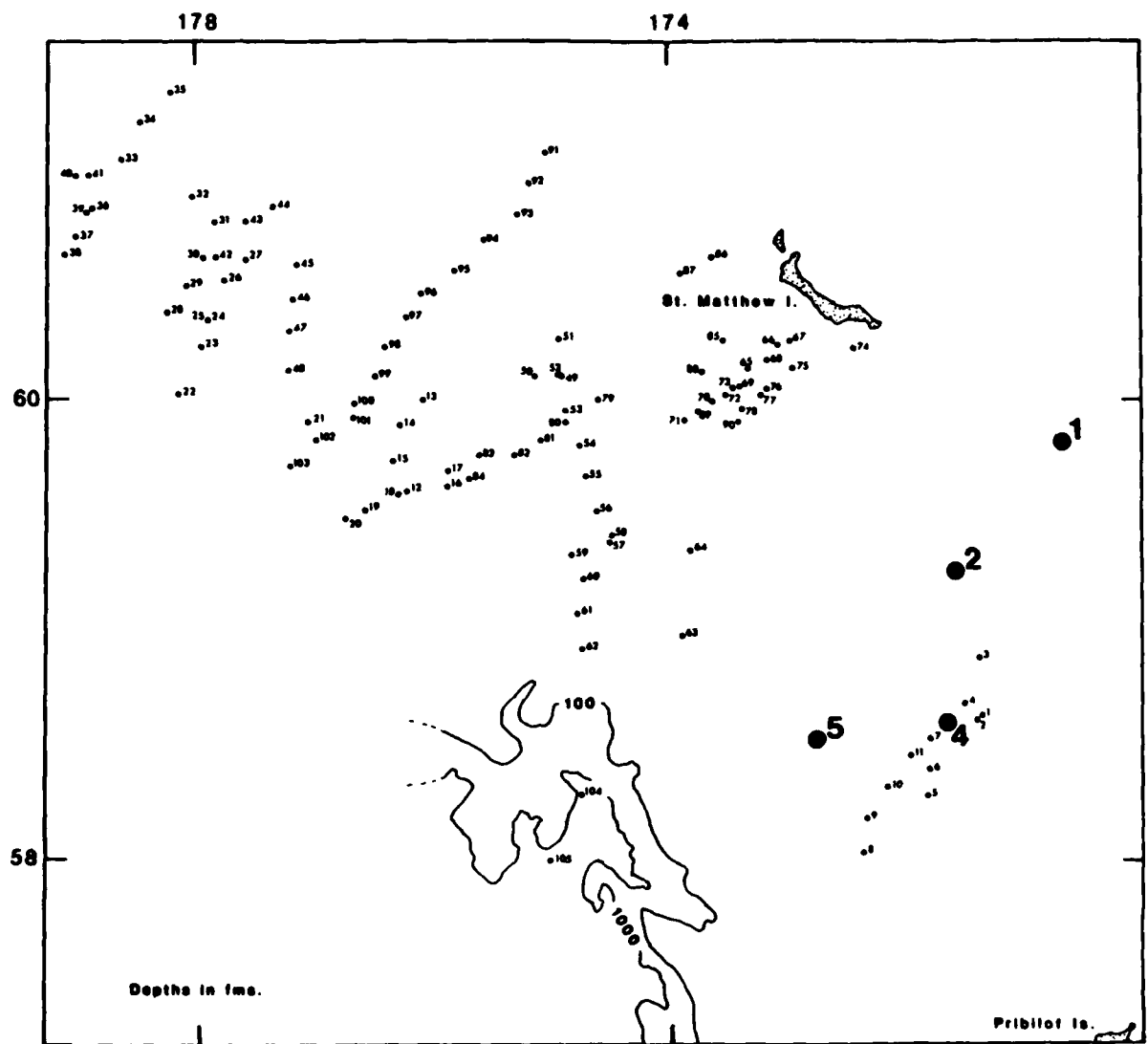


**Fig. 5. Geographical locations of CTD casts occupied by the USCG icebreaker Polar Sea during MIZEX-West.**

**Table 1.** Temperature and salinity data obtained from moorings during the winter 1982-83 MIZEX-West program. Geographical locations are indicated schematically in Figure 2.

<i>Mooring</i>	<i>Lat. (N)</i>	<i>Long. (W)</i>	<i>Bottom depth (m)</i>	<i>Instrument depth (m)</i>	<i>Date in</i>	<i>Date out</i>	<i>Parameter</i>
1	59°50.23'	170°41.06'	66	45	23 Oct 82	10 May 83	<i>T</i>
2	59°15.99'	171°34.98'	78	14 36 62	22 Oct 82	10 May 83	<i>T</i> <i>T,S</i> <i>T</i>
4	59°37.09'	171°39.85'	92	12 39	22 Oct 82	9 May 83	<i>T</i> <i>T,S</i>
5	58°32.09'	172°45.44'	108	12 45 85	21 Oct 82	9 May 83	<i>T</i> <i>T,S</i> <i>T</i>

3. The USCG icebreaker *Polar Sea* occupied 105 CTD stations over a broad area extending from seaward of the ice edge to well inside the solid pack north of the edge. These stations overlapped only partly in time with those taken on *Discoverer* and *Westwind*; they were taken on 20 February–18 March, so that only about the first half of the cruise coincided with operations by the other two vessels. The *Polar Sea* data were obtained with a prototype fine structure sampling CTD system on loan from the Applied Physics Laboratory of the University of Washington. Locations of the CTD stations are shown in Fig. 5.

Particular care was taken to ensure that the temperature and salinity data were of the best quality obtainable. Calibration data were taken at about every fifth cast on each vessel using a rosette sampler or Nansen water sampling bottle and deep-sea reversing thermometers. The resulting salinity samples were analyzed aboard ship using laboratory salinometers. In addition, intercalibration casts were carried out between the ships *Discoverer* and *Westwind* at the start and finish of the joint 6–27 February field program. No significant problems were encountered with any of the CTD systems. The resulting temperature and salinity data are believed accurate, based upon sensor specifications and comparisons between sensors and the calibration data, to within  $\pm 0.02^{\circ}\text{C}$  and  $\pm 0.02\text{‰}$  respectively. The derived density data, presented below as sigma- $t$ , are of the same accuracy.

#### The moored observations

The overwinter moorings utilized both Neil Brown Instrument Systems acoustic current meters and Aanderaa RCM-4 current meters to record temperature at all sampled locations and depths and salinity at selected locations and depths (see Table 1). These instruments were calibrated just prior to deployment. CTD casts were taken adjacent to each mooring both upon deployment and recovery, and the CTD data were used to check the calibrations. All of the instruments performed satisfactorily. Based upon the sensor specifications and comparisons with the CTD calibration data, the temperature and salinity data from the moorings are believed accurate to  $\pm 0.1^{\circ}\text{C}$  and  $\pm 0.1\text{‰}$ , respectively.

#### OBSERVED TEMPERATURE AND SALINITY CONDITIONS

The temperature and salinity data are presented as vertical transects of temperature, salinity and density (expressed as sigma- $t$ ) (Fig. 6–16), as horizontal maps of temperature (Fig. 17), and as temperature and salinity time series from the moorings (Fig. 18–20).

#### Large-scale features

The three-dimensional temperature, salinity and density structure of the ice edge front can be clearly seen by inspection of the vertical transects (Fig. 6–16), with reference to the station location figures (Fig. 3–5) and the horizontal temperature distributions described below. Four of the transects encompassed all or nearly all of the frontal structure and show its cross-frontal extent (Fig. 6, 9, 10 and 16). The general nature of the front varied little over the 5 February–17 March duration of the field program, and its large-scale features qualitatively resembled those depicted schematically in Fig. 1. Lower-layer temperatures and salinities were higher than those in the upper layer, though considerable variations were present within each layer. The lower layer was always several tenths of a sigma- $t$  unit denser than the upper.

The horizontal distributions of near-surface temperature for two different time periods, 5–16 February and 20 February–18 March, are shown in Fig. 17. It was impossible to combine the data from these two periods on the same plot because the ice edge and its associated frontal structure had advanced about 80 km seaward between the two periods in response to strong northeasterly winds. The frontal advance can be easily seen along an imaginary transect drawn through moorings 1, 2 and 5 (compare also Fig. 6 and 10), as well as in Fig. 17. A similar wind-driven advance was observed in winter 1981 (Muench, 1983). The sharp curvature or “kinking” of isotherms in the earlier period is an artifact resulting from tidal excursion coupled with a relatively slow occupation of the transects. The later distribution was far more complete and suggests an exceedingly regular frontal structure with no apparent wave-like or eddy-like features.

The greatest cross-frontal temperature gradients during both periods were associated with about the  $-0.5^{\circ}\text{C}$  isotherm. Seaward of this isotherm

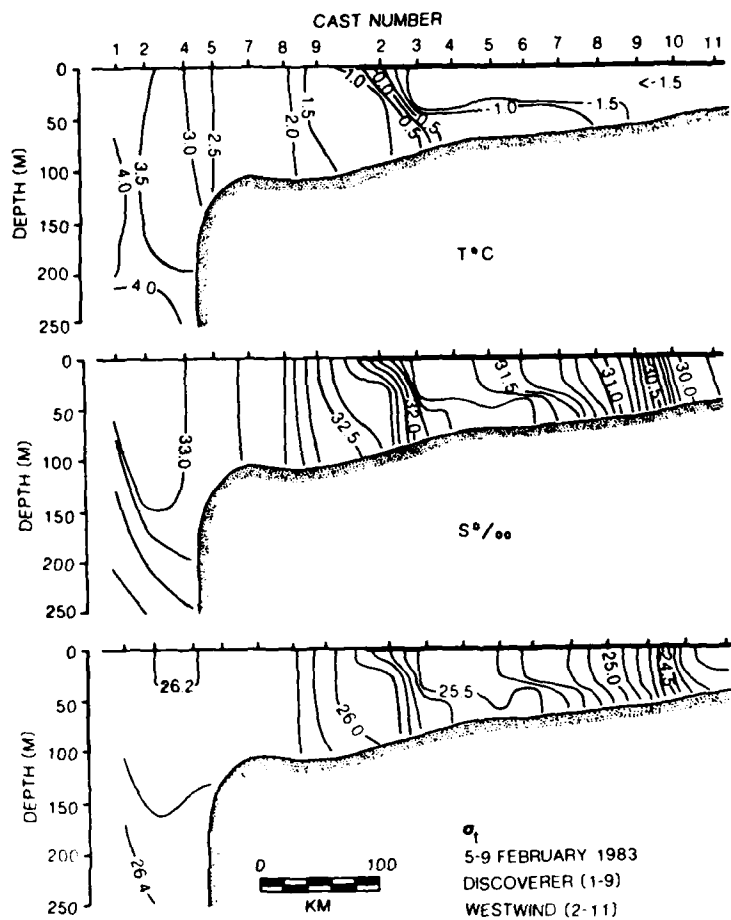


Fig. 6. Vertical distributions of T, S and  $\sigma_t$  along a 5-9 February transect; CTD cast locations are shown in Fig. 3 and 4.

near-surface temperatures increased monotonically to more than  $3.0^{\circ}\text{C}$  over the continental slope. Temperatures decreased sharply, north from the ice edge, to the freezing point and remained at the freezing point as far north as observations were obtained.

The near-bottom temperature data were adequate to define only a relatively short segment of the intersect between the  $-0.5^{\circ}\text{C}$  isotherm and the seabed. However, this segment was long enough to clearly indicate, by comparing locations of the surface and bottom intersects, the width of the band occupied by the two-layered structure. Similarly to the near-surface waters, near-bottom temperatures increased monotonically southward from the seabed intersect and were at the freezing point north of the intersect.

Significant time variations occurred in the detailed frontal structures. The most apparent of these was the frontal advance noted above. The cross-frontal gradients were strongly sharpened

concurrently with this advance, and the two-layered structure became more pronounced (compare Fig. 6 and 10). This more strongly developed structure was still present by 17 March (Fig. 16) and so persisted until the end of the winter field program. Hendricks et al. (1985) applied heat budget arguments to the observed frontal advance and demonstrated a feedback mechanism which limits seaward ice advance. Seaward migration of the ice edge and its underlying front requires that warmer water, which lies seaward of the front, be entrained. The heat contained in this warmer water is then available to melt the ice. Hendricks et al. demonstrated that the heat entrained by the observed frontal advance was approximately equal to that required for melting the ice that moved seaward over the same period.

#### Small-scale features

The shorter transects document various portions of the cross-frontal structure. Most cross the

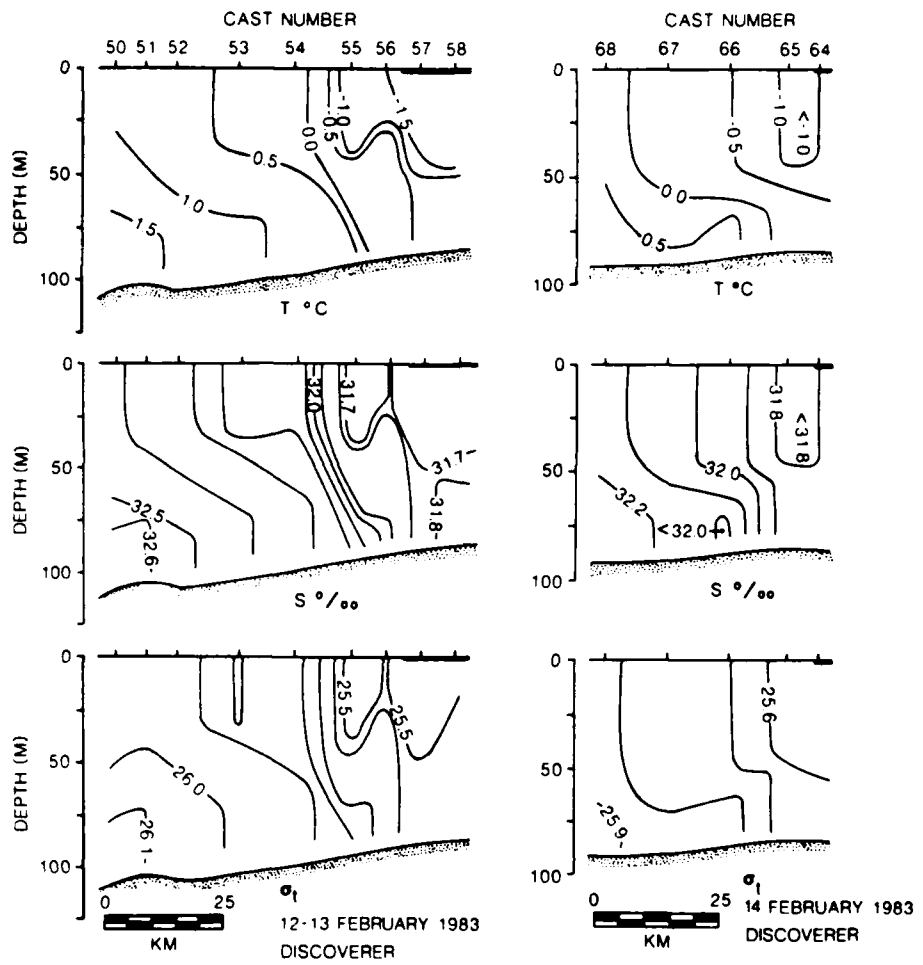


Fig. 7. Vertical distributions of T, S and  $\sigma_t$  along 12-13 and 14 February transects; cast locations are shown in Fig. 3.

ice edge, though two (in Fig. 13 and 15) were taken in completely ice-covered water. Station spacing was often much less on the short transects (5-10 km) than on the longer ones (20-30 km), and in some cases this close station spacing allowed detection of locally increased horizontal temperature and salinity gradients. Such increases were evident, for instance, between casts 54 and 55 on 12-13 February (Fig. 7) and between casts 78 and 81 on 15 February (Fig. 8). Hendricks et al. (1985) defined a "typical" cross-frontal temperature gradient to be  $10^{-4}$  deg m $^{-1}$  and use this to estimate a horizontal eddy conductivity of about  $3 \times 10^5$  cm $^2$  s $^{-1}$ . Locally large horizontal temperature gradients might reflect small-scale (5-10 km) processes along the ice edge.

The vertical gradients of temperature, salinity and density across the interface between layers are of particular interest. Stegen et al. (1985) and

Hendricks et al. (1985) have demonstrated that significant upward heat transfer can occur across this interface through double diffusion. Hendricks et al. (1985) derived a "mean" vertical eddy diffusion coefficient of about 3 cm $^2$  s $^{-1}$ . This occurs because the interfacial stratification of cold, low-salinity water overlying warmer, more saline water is unstable to double-diffusive convection as discussed for example by Turner (1973). Inspection of the transects indicates that vertical interfacial gradients varied widely with both space and time. Hendricks et al. (1985) demonstrated that upward heat flux can also vary widely, depending on these gradients. As for the subfrontal scale variations in horizontal gradients, variability in vertical interfacial gradients can affect smaller scale processes along the ice edge. In general, these gradients were stronger later in the field program following the seaward advance of the front.

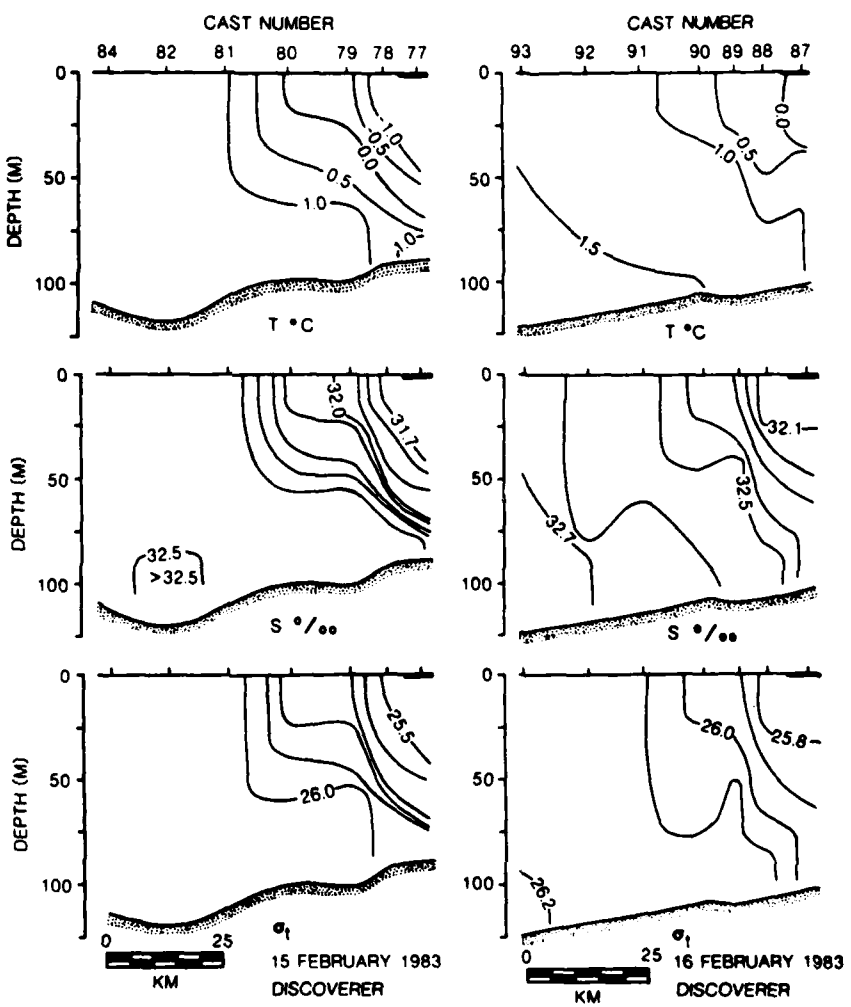


Fig. 8. Vertical distributions of T, S and  $\sigma_t$  along 15 and 16 February transects; cast locations are shown in Fig. 3.

#### Seasonal change

The temporal development of typical midwinter stratification can be seen from the time series records of temperature and salinity that were obtained from the moorings (Fig. 18 and 19). Over about the first half of the record the upper layer was warmer than the lower (Fig. 18). The upper layer cooled continuously during this period until by sometime in January the upper and lower layers were at the same temperatures. Upper layer cooling continued, and the greatest cooling occurred during two episodes. The first of these episodes occurred in late January; following this event the mid-winter stratification of cooler water overlying warmer was present at the northern three moorings (1, 2 and 4). A second cooling event occurred in mid- to late February and ex-

tended the winter layered structure south past mooring 5. This second event coincided with the wind-driven southward migration, described above, of the ice edge and associated front. The mid-winter thermal stratification persisted in the region until mid-April, by which time upper layer warming had commenced.

In contrast to the temperatures, salinity did not show an unambiguous seasonal cycle (Fig. 19). At the northernmost moorings (2 and 4) it increased slightly until about late December, then decreased to relatively low values, which persisted through winter until mid-April when it began to increase again. At the southern mooring (5) salinity increased monotonically throughout the observation period, with some temporary decreases, such as that in January, superimposed on this increase.

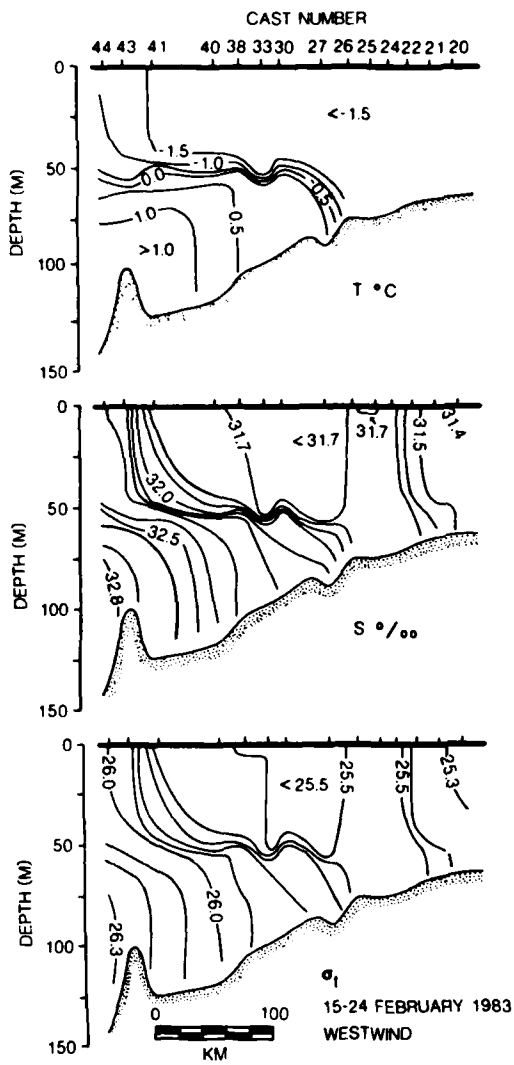


Fig. 9. Vertical distributions of  $T$ ,  $S$  and  $\sigma_t$  along a 15-24 February transect; cast locations are shown in Fig. 4.

The January salinity decrease was apparent at all three moorings and corresponded with the temperature decrease. The sudden late-February decrease at moorings 4 and 5 coincided with the sharp drop in temperature which was observed at those locations.

#### Internal waves

The sharp density interface underlying the MIZ can provide an excellent medium for internal wave propagation. Muench et al. (1983) hypothesized that such internal waves can be generated in the MIZ by interactions between winds and a moving ice cover. Undulations suggestive of interfacial internal wave motions were not, however, common-

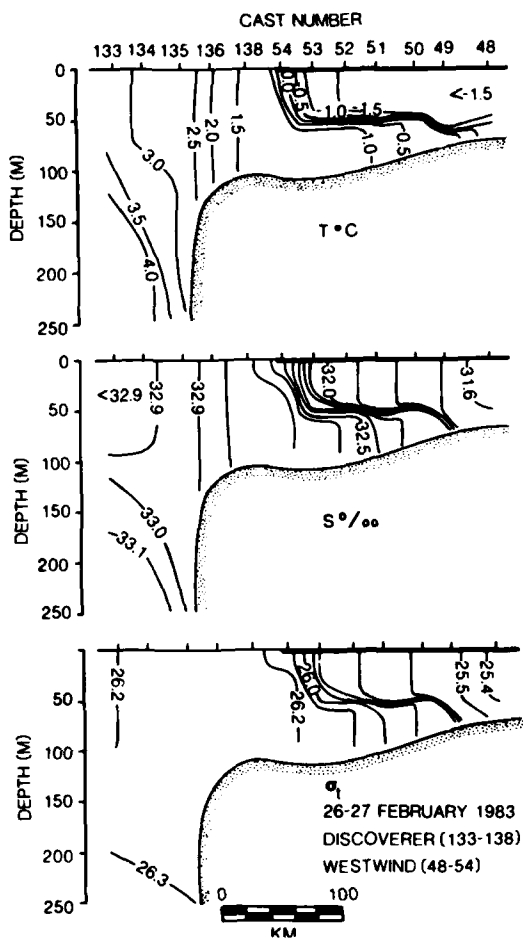


Fig. 10. Vertical distributions of  $T$ ,  $S$  and  $\sigma_t$  along a 26-27 February transect; cast locations are shown in Fig. 3 and 4.

ly observed during the winter 1983 Bering Sea experiment. The best-defined such undulations occurred on 16-17 March (Fig. 16) with amplitudes of 10-20 m and about a 50-km spacing between "crests." However, because two days were required to occupy this transect it is impossible to realistically assign a wavelength to these features. They serve only to indicate the presence of vertical displacements of the interface.

The temperature and salinity time series (Fig. 18 and 19) are both characterized, at times when the interface passed through or nearly through the instruments, by rapid fluctuations which suggest that vertical interfacial oscillations were present. Similar features were noted in winter 1981 moor-

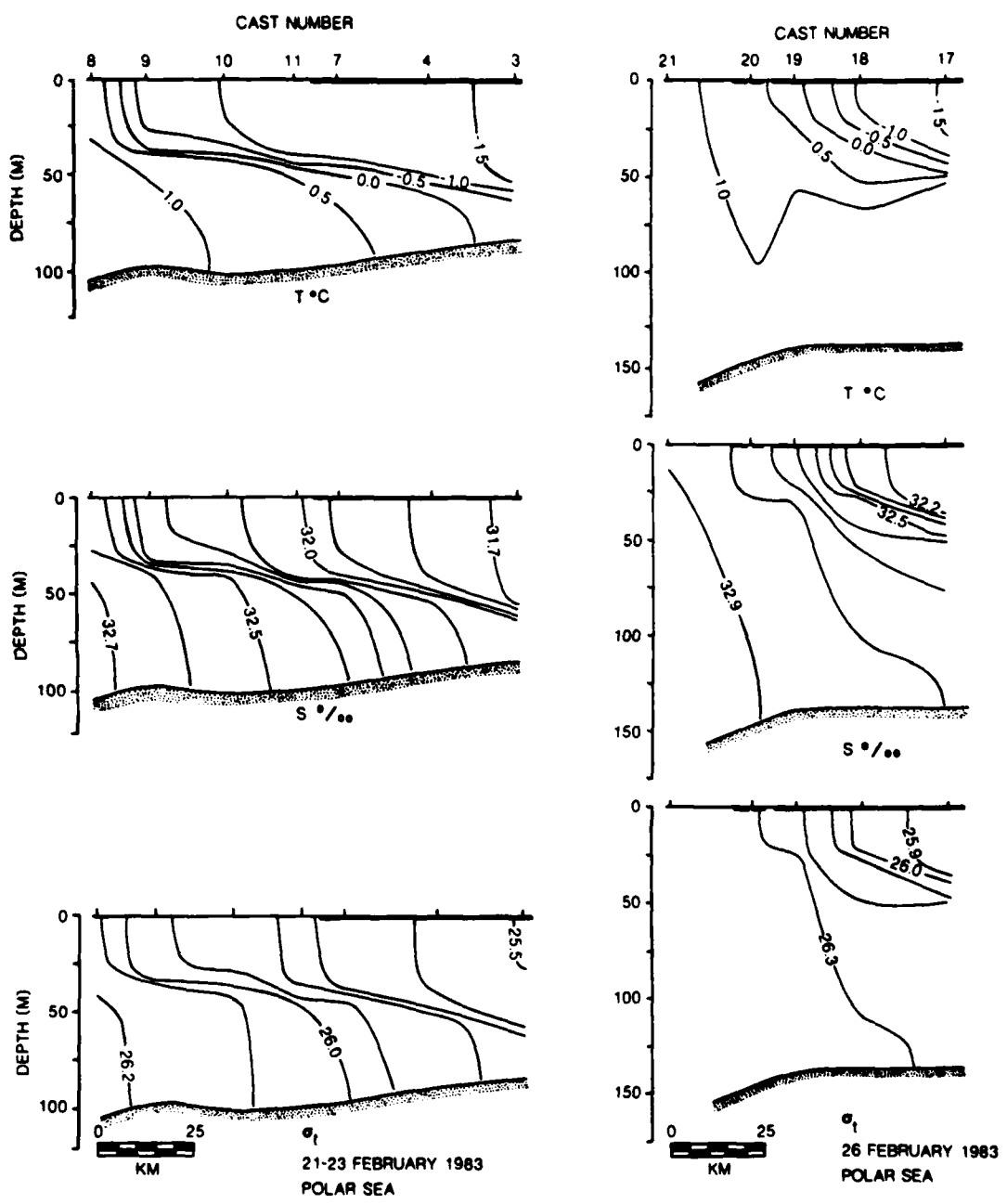


Fig. 11. Vertical distributions of  $T$ ,  $S$  and  $\sigma_1$  along 21-23 and 26 February transects; cast locations are shown in Fig. 5.

ing temperature records by Muench et al. (1983). The sampling intervals used by the moored instruments were between 30 and 60 minutes, however, and were too long to allow definition in time of the interfacial displacements.

Two attempts were made in February 1983 to obtain shipboard CTD time-series observations adequate to detect interfacial internal waves. These observations were carried out from the

Westwind at the locations indicated in Fig. 4. The vessel was held at a fixed geographical location during these observations, i.e. was not allowed to drift with the ice. The CTD was then suspended in the strongest part of the interface between layers and allowed to record. The first of the two experiments was inconclusive, as the CTD was suspended at a depth too far below the interface and so did not register  $T$  and  $S$  fluctuations. The second ex-

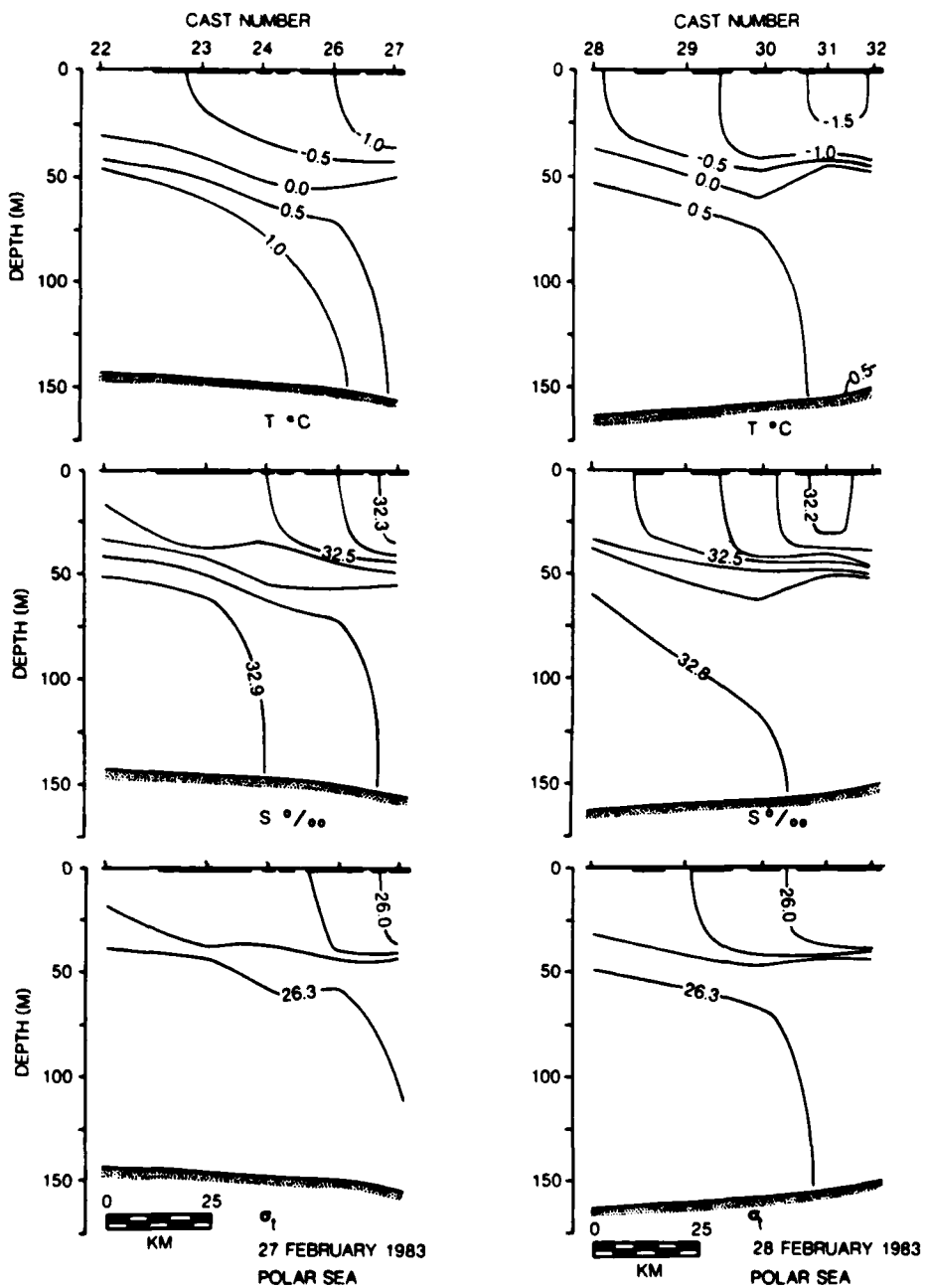


Fig. 12. Vertical distributions of  $T$ ,  $S$  and  $\sigma_t$  along 27 and 28 February transects; cast locations are shown in Fig. 5.

periment showed  $T$  and  $S$  (and consequently sigma- $t$ ) fluctuations in time over about a 45-minute period (Fig. 20). Interference of drifting ice with the CTD cable made it impossible to continue the observations over a longer period. The record obtained clearly indicates, however, that vertical interfacial motions adequate to displace the interface vertically past the CTD were

present. The record suggests a 30-minute time scale for the fluctuations but is too short to define a period.

#### Upwelling

Wind-driven upwelling has recently been hypothesized to occur along the ice edge in the southeastern Bering Sea and to contribute to biological

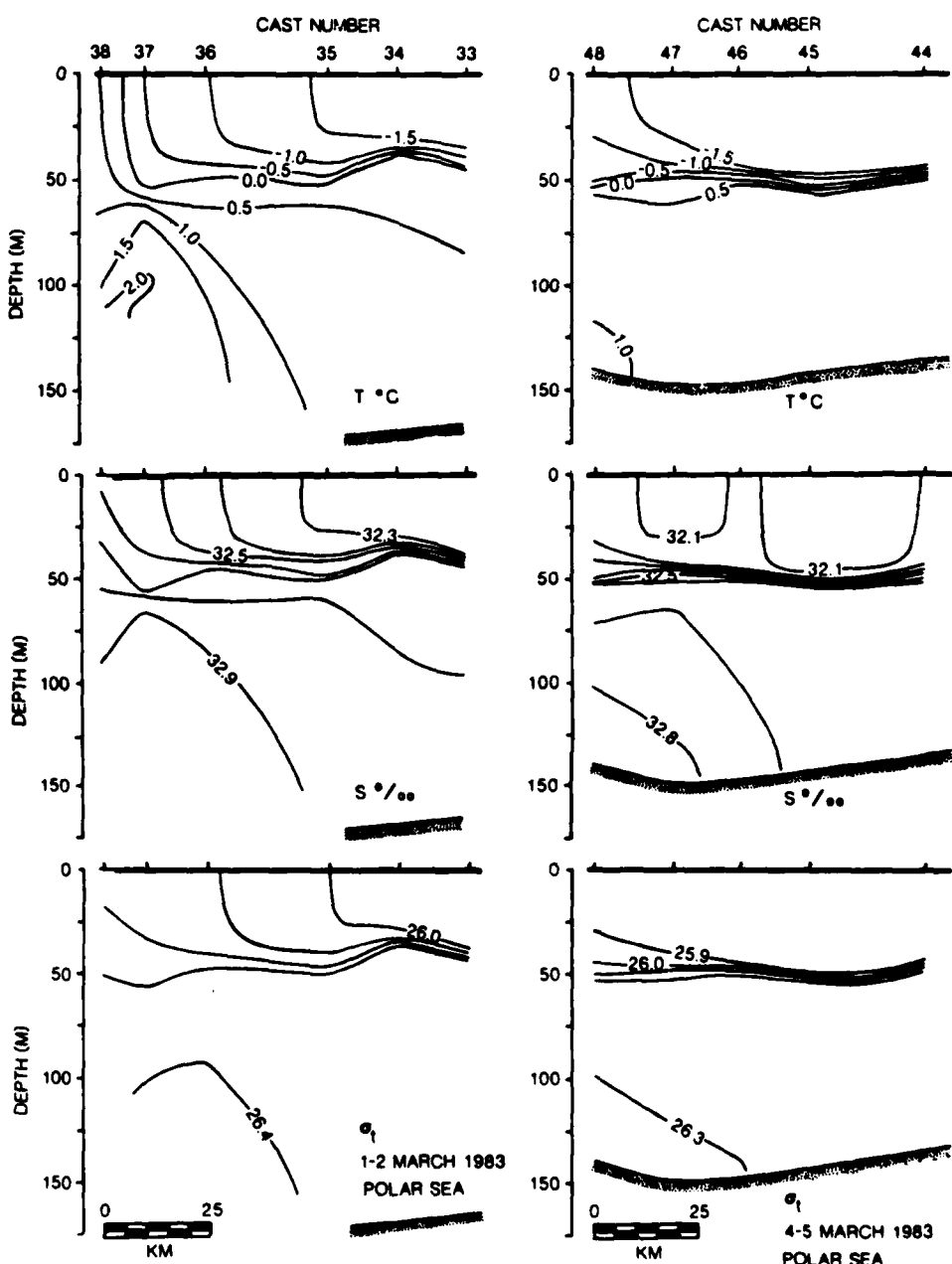


Fig. 13. Vertical distributions of T, S and  $\sigma_t$  along 1-2 and 4-5 March transects; cast locations are shown in Fig. 5.

productivity there (Alexander and Niebauer, 1981). Numerical models have predicted the occurrence, given specific wind and ice cover conditions, of such upwelling (e.g. Røed and O'Brien, 1983). It is therefore of interest to examine the temperature and salinity data for evidence of wind-driven ice edge upwelling along the winter 1983 Bering Sea ice edge.

None of the observed temperature or salinity features suggested convincingly that wind-driven ice edge upwelling was occurring. The transects occupied on 12-13 February (Fig. 7) and 16 February (Fig. 8) showed some upward bowing of temperature or salinity isopleths at mid-depths or near bottom just seaward of the ice edge. These features did not attain the surface, and they occurred

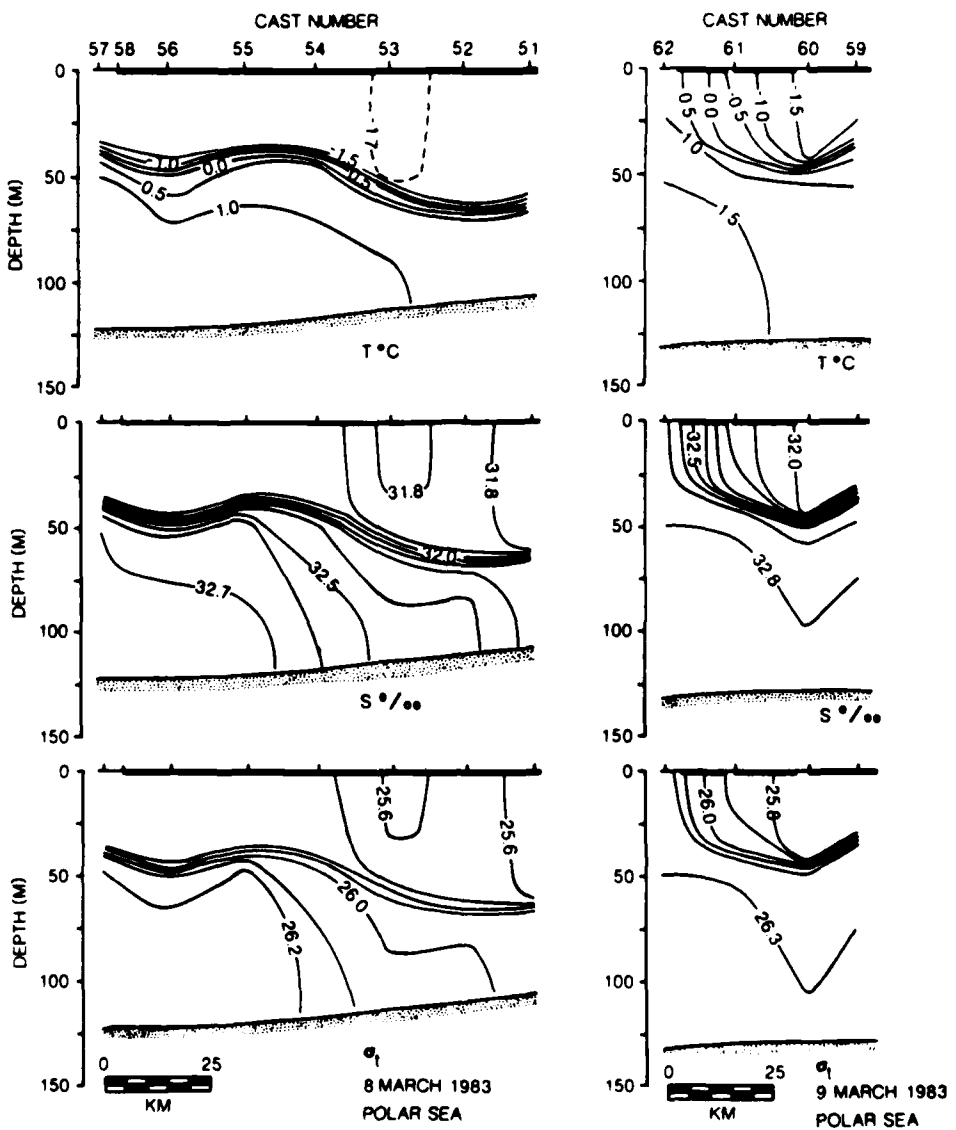


Fig. 14. Vertical distributions of  $T$ ,  $S$  and  $\sigma_t$  along 8 and 9 March transects; cast locations are shown in Fig. 5.

at times when local winds were weak, variable and on-ice so they would not have been upwelling-favorable. No other transects suggested upward bowing of isopleths, which might have indicated upwelling.

The apparent lack of upwelling may be due to the character of the Bering Sea ice coupled with the nature of the wind field. The ice near and along the edge is entirely first-year ice and is unconsolidated. Heavily fractured, primarily by incoming ocean swell, it presents a rough and mobile hydrodynamic interface between surface

winds and the underlying water. The ice edge upwelling mechanism requires a wind-stress divergence across the edge. In the Bering Sea the ice was observed to initiate its breakup and transition from solid pack into individual floes at distances of 50–100 km inward from the edge. Any wind-stress-induced divergence would have been spread out over this considerable distance. In addition, the ice near the edge was highly mobile and attained seaward speeds at times exceeding  $50 \text{ cm s}^{-1}$  in response to northerly winds. As an additional complication, the system was decidedly not

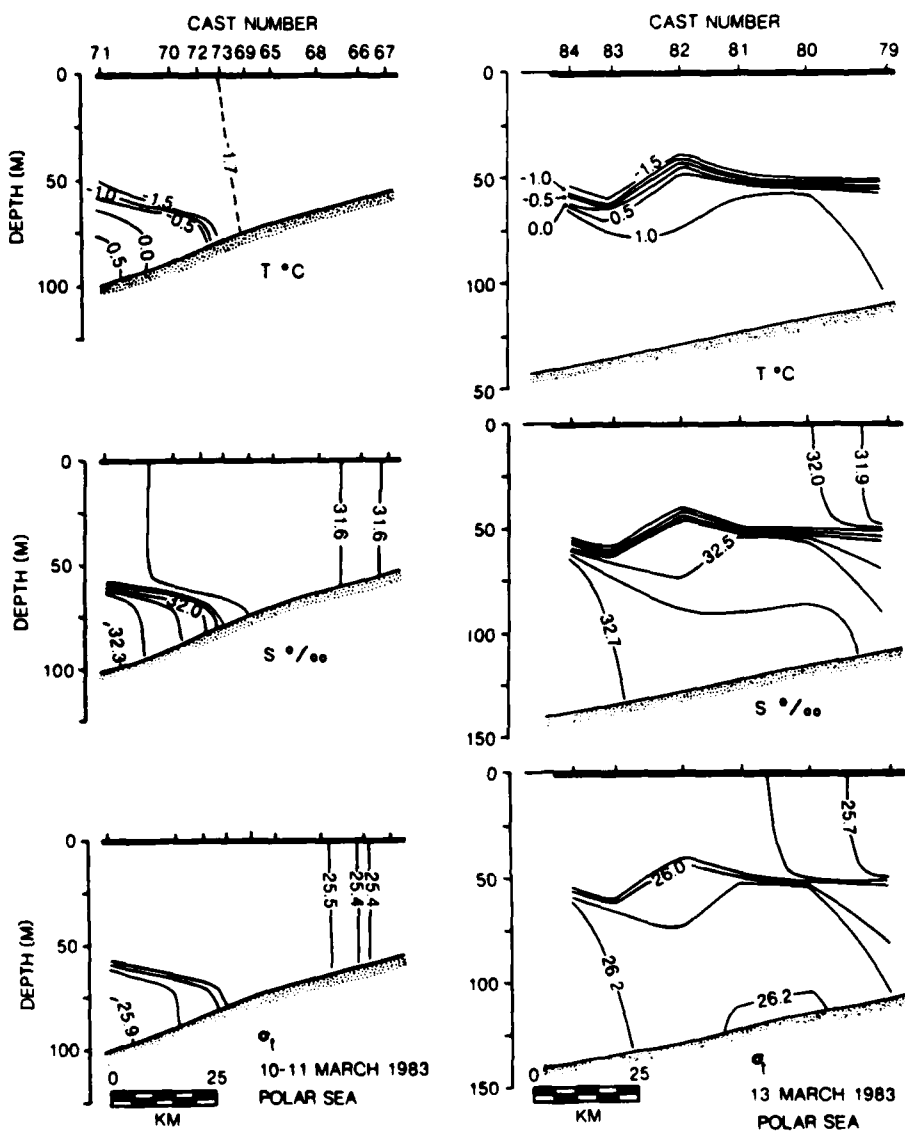


Fig. 15. Vertical distributions of T, S and  $\sigma_t$  along 10-11 and 13 March transects; cast locations are shown in Fig. 5.

steady-state. The wind field fluctuated in speed and, within the northeasterly quadrant, in direction throughout most of the experiment.

While significant upwelling was not evident in the winter 1983 data, a region of vertical homogeneity was present at the shelf break well seaward of the ice edge. This feature was present at casts 5, 7 and 8 on 5-9 February (Fig. 6) and casts 136 and 138 on 26-27 February (Fig. 10), i.e. in all cases where the data extended seaward past the shelf break. Such homogeneity suggests that vertical density stratification at the shelf break was insuf-

ficient to prevent vertical mixing. Such mixing might be driven, in this region, by winds and the turbulence derived from mean and tidal currents. Examination of the mixing mechanism is beyond the scope of this paper; however, the mixing itself can provide a means for transporting dissolved matter such as nutrients upward into the near-surface layers. Muench and Schumacher (1985) show that mean currents in the central Bering Sea MIZ have a significant on-ice component, hence nutrients mixed upward to the surface layer will ultimately be transported toward the ice edge.

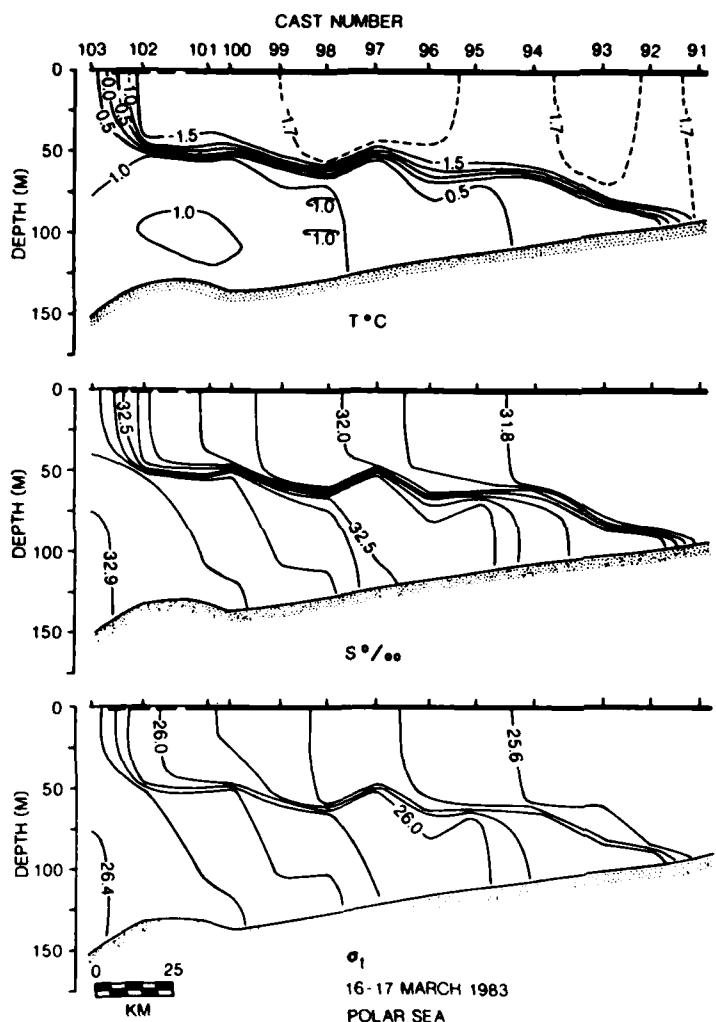


Fig. 16. Vertical distributions of T, S and  $\sigma_t$  along a 16-17 March transect; cast locations are shown in Fig. 5.

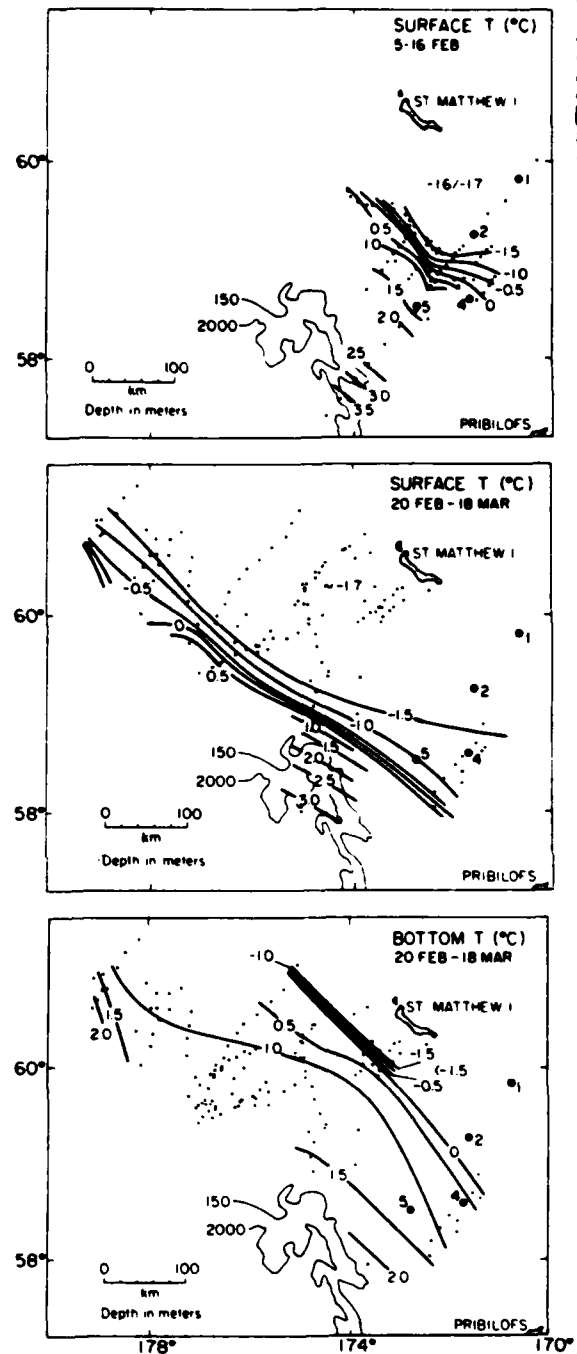


Fig. 17. Horizontal distributions of near-surface temperature on 5-16 Feb (upper) and on 20 Feb-18 Mar (middle), and distribution of near-bottom temperature on 20 Feb-18 Mar (lower). Numbered dots show mooring locations, and small unnumbered dots indicate locations of CTD casts used in constructing the plots.

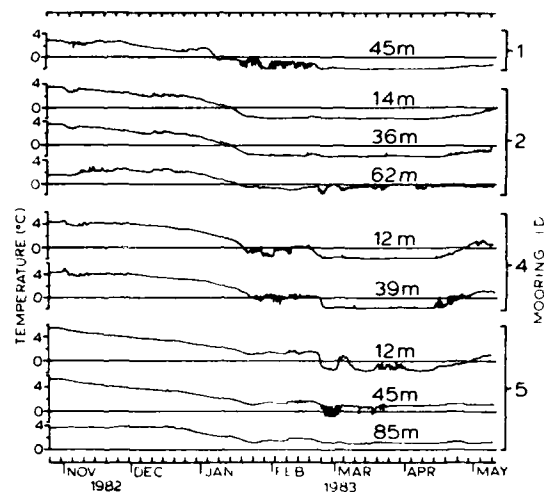


Fig. 18. Temperatures derived from the over-winter moorings and plotted against time. Mooring locations are shown schematically in Fig. 2 and 17, and a list of particulars is provided in Table 1. Mooring ID's are shown in the right-hand margin, and the depths shown along the time axes indicate the depths from which observations plotted on each axis were obtained.

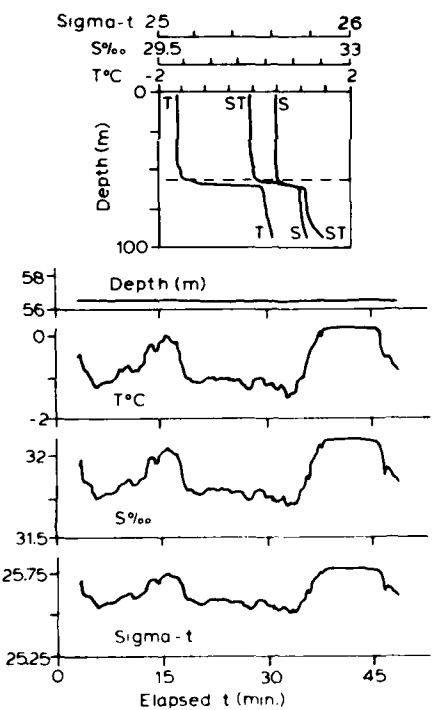


Fig. 20. Short-term time-series of temperature, salinity and  $\sigma_t$  plotted against time (lower). Upper part of figure shows vertical distributions of temperature, salinity and  $\sigma_t$  at the site of the time-series observations. These data were obtained from CTD cast 32 (see Fig. 4 for location) on 20 February.

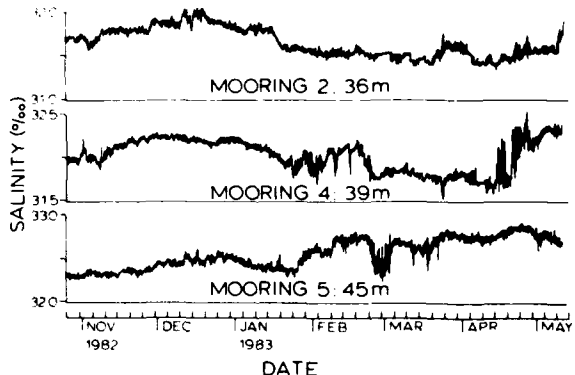


Fig. 19. Salinities derived from the over-winter moorings and plotted against time as for Fig. 18. Mooring ID and sample depth are indicated above the time axis for each plot.

## SUMMARY

The winter 1983 temperature and salinity data from the Bering Sea MIZ provided the most detailed information to date on the oceanic frontal structures there. Examination of these data has shown that:

1. A two-layered band of water underlies the MIZ throughout the February–March field season. This structure was bounded on the south by intersection of the between-layer interface with the surface at the ice edge, and on the north by its intersection with the seabed.
2. A major southward advance of the frontal system and the ice edge occurred in response to persistent, vigorous northerly winds. Cross-frontal gradients in temperature and salinity increased during this advance, but the general structure of the frontal system remained unchanged.
3. Horizontal and vertical temperature and salinity gradients varied over distances of 5–10 km in a small number of cases, suggesting that such spatial variability occurs but is not especially widespread. This observation was supported by the regularity in near-surface temperatures.
4. Both the vertical transects and the time-series data showed fluctuations which were consistent with the presence of interfacial internal waves. These data were, however, inadequate to test for the presence of such waves.
5. There was no evidence that wind-driven ice edge upwelling was occurring. However, a vertically homogeneous region near the shelf break,

south of the ice edge, may indicate vertical mixing processes there that could provide deeper water to the upper layers in the MIZ.

## ACKNOWLEDGMENTS

This work has been funded by the Office of Arctic Programs, Office of Naval Research, under contract N00014-82-C-0064 to Science Applications International Corporation. This is SAIC contribution No. 995-47 and MIZEX contribution No. 078.

## REFERENCES

**Alexander, V. and H.J. Niebauer**, Oceanography of the eastern Bering Sea ice-edge zone in spring, *Limnol. Oceanogr.*, 26, 1111-1125, 1981.

**Hendricks, P.J., R.D. Muench and G.R. Stegen**, A heat balance for the Bering Sea ice edge, *J. Phys. Oceanogr.*, 15, submitted, 1985.

**MIZEX-West Study Group**, MIZEX West—The Bering Sea marginal ice zone experiment, *EOS*, 64, 578-579, 1983.

**Muench, R.D.**, Mesoscale oceanographic features associated with the central Bering Sea ice edge: February-March 1981, *J. Geophys. Res.*, 88, 2715-2722, 1983.

**Muench, R.D., P.H. LeBlond and L.E. Hachmeister**, On some possible interactions between internal waves and sea ice in the marginal ice zone, *J. Geophys. Res.*, 88, 2819-2826, 1983.

**Muench, R.D. and J.D. Schumacher**, On the Bering Sea ice edge front, *J. Geophys. Res.*, 90, 3185-3197, 1985.

**Pease, C.H.**, Eastern Bering Sea ice processes, *Mon. Wea. Rev.*, 108, 2015-2023, 1980.

**Røed, L.P. and J.J. O'Brien**, A coupled ice-ocean model of upwelling in the marginal ice zone, *J. Geophys. Res.*, 88, 2863-2872, 1983.

**Stegen, G.R., P.J. Hendricks and R.D. Muench**, Vertical mixing on the Bering Sea Shelf, *Proc. Symposium on Wave Breaking, Turbulent Mixing and Radio Probing of the Ocean Surface*, Sendai, Japan, in press, 1985.

**Turner, J.S.**, *Buoyancy Effects in Fluids*, Cambridge Univ. Press, 1973.

## Regional Ice Drift During MIZEX-West

R. MICHAEL REYNOLDS AND CAROL H. PEASE  
*Pacific Marine Environmental Laboratory/NOAA*  
*Seattle, Washington 98115, USA*

A marginal ice zone experiment (MIZEX-West) took place in the southern Bering Sea in February 1983. In the original plan, the U.S. Coast Guard icebreaker *Westwind* was to push 100 km into the ice and deploy an array of instrumentation at a position of approximately 59°N, 171°W. The NOAA research ship *Discoverer* would occupy stations at the ice edge and wait for the array and the icebreaker to drift out to meet her. In keeping with the plan, both ships met for a pre-experiment intercomparison of common instrumentation at 59°2.1'N, 172°4.0'W on 6 February. On 7 February the *Westwind* headed northeast into the ice pack looking for ice that was thick enough to support instrumentation. The ice to the east of St. Matthew Island was thin (< 0.5 m) and laced with leads and large areas of open water. For this reason, the ship steamed much further into the ice than originally planned. Finally, ice of sufficient thickness was found, and the array was deployed. The *Discoverer* remained at the ice edge making measurements of density structure, ice edge dynamics and wave-ice interaction until 18 February.

Eight Argos-tracked transponders were placed on the ice in the vicinity of 61°N, 170°W and were tracked westward, then southward around St. Matthew Island until 28 February when the last transponder broke out of the ice and ceased transmitting (Fig. 1). The tracked floes were numbered 1 to 8. Seven of the transponders were deployed on 10 February by helicopters from *Westwind*. Floe 7 was instrumented two days later over the side of the ship.

Meteorological stations were deployed on floes 2 and 7. These stations measured mean winds and temperature for 10 minutes every half hour at a height of 3 m, and mean ocean currents and temperature at -2 m under the ice. Floe rotation was monitored once an hour with a magnetic compass. Floe 7, the main camp, also had a precision pressure sensor, a Loran receiver, and additional current meters at -2 and -6 m. The Loran receiver

gave position fixes every hour, which increased tracking accuracy and resolution.

The wind acceleration at the ice edge is a result of reduced friction and baroclinic forcing in keeping with the theory of Overland et al. (1983) and Reynolds (1984). As a typical example, at 1200 GMT on 19 February, winds accelerated from 7 m s<sup>-1</sup> to 12 m s<sup>-1</sup> over a distance of 122 km.

The weather during the period is summarized by Fig. 2 (Wilson et al., 1984). On 3 February a region of low pressure was centered in the Aleutian Islands. The stationary low generated a swell from the southeast, but in the region of St. Matthew Island the isobars were oriented east-west and produced northeasterly winds. By 10 February the low had filled and moved to the northwest. Isobars were from the southeast direction, and winds were easterly. By 15 February, the low had almost disappeared and the pressure gradient in the Bering Sea was weak. However, its westerly position was sufficient to kink the isobars in the vicinity of St. Matthew Island and produce southerly winds. Finally, by 19 February, a high pressure region developed over Siberia which coupled with a low pressure region in the Gulf of Alaska to produce strong northeasterly winds in the study area. These winds remained from the north or northeast during the remainder of the experiment and accounted for the significant portion of the ice advance.

A summary of the surface winds and temperatures (Fig. 3) agrees well with the synoptic scale weather patterns. Even when reduced to a 3-m height, winds at the *Discoverer* were stronger than those at either ice camp. Winds on floe 2, a large, smooth floe, were 17% stronger than those at the main camp, which was located on an old, rough floe. Wind directions were well correlated, and differences can be explained by the large separation between the ship and camps. This is especially evident on 14 February when the *Discoverer* operated southeast of St. Matthew Island while the array was northwest of the island. The shift to

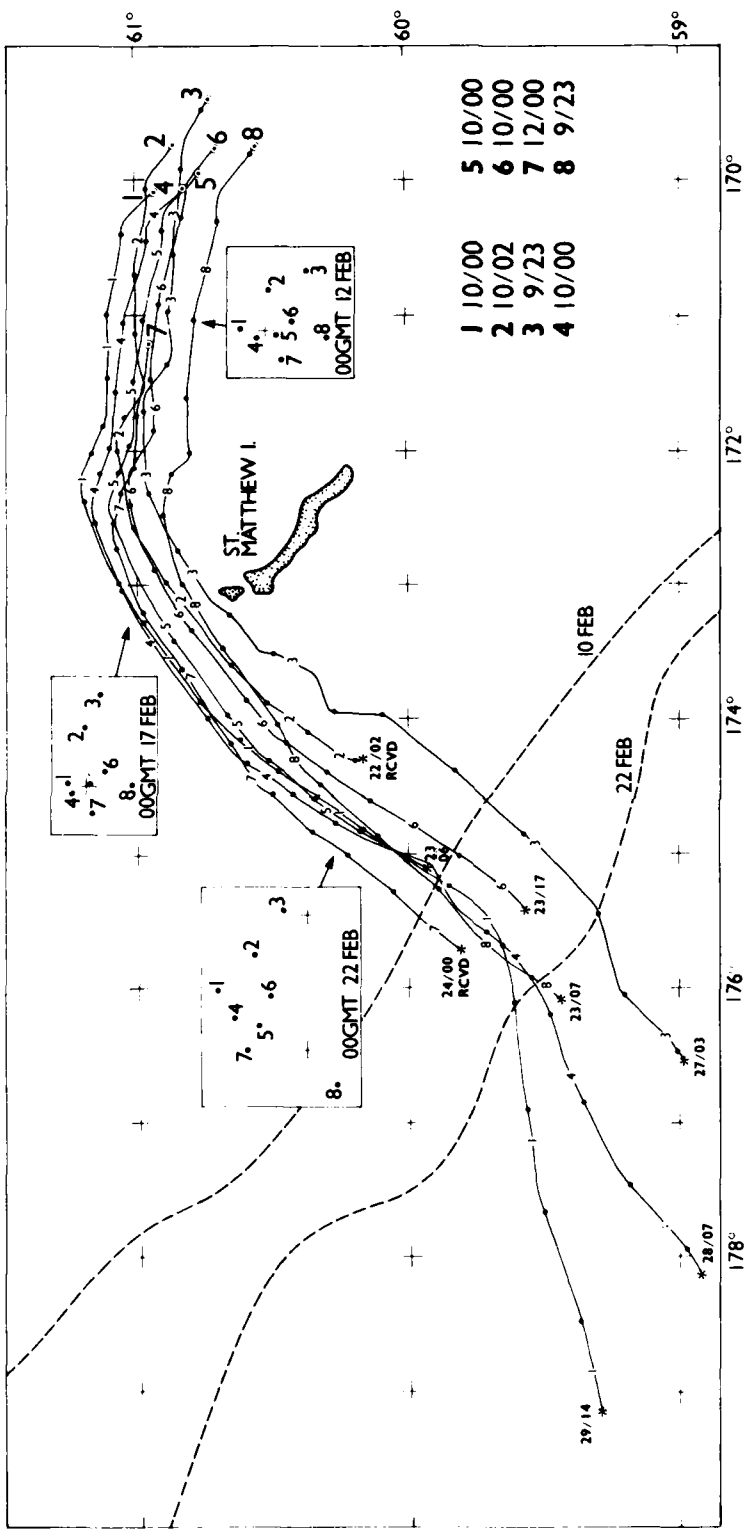
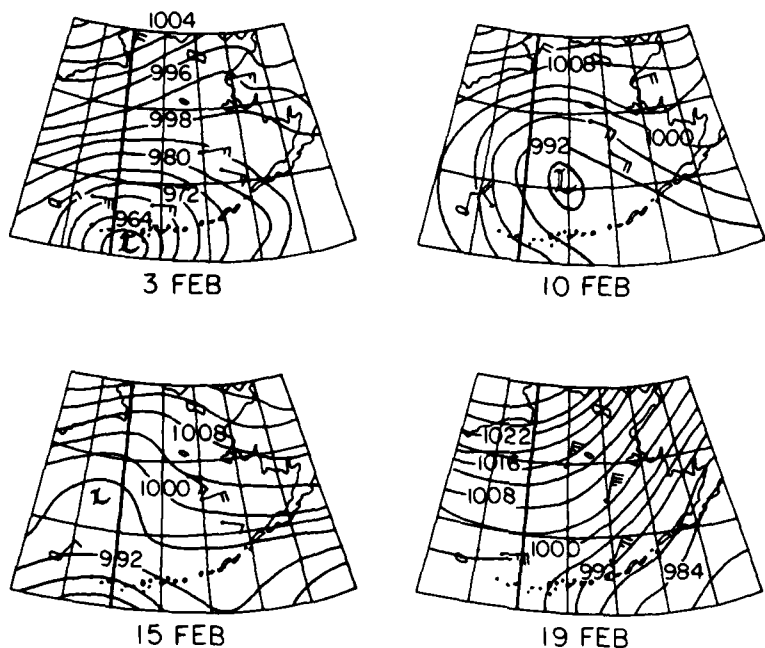
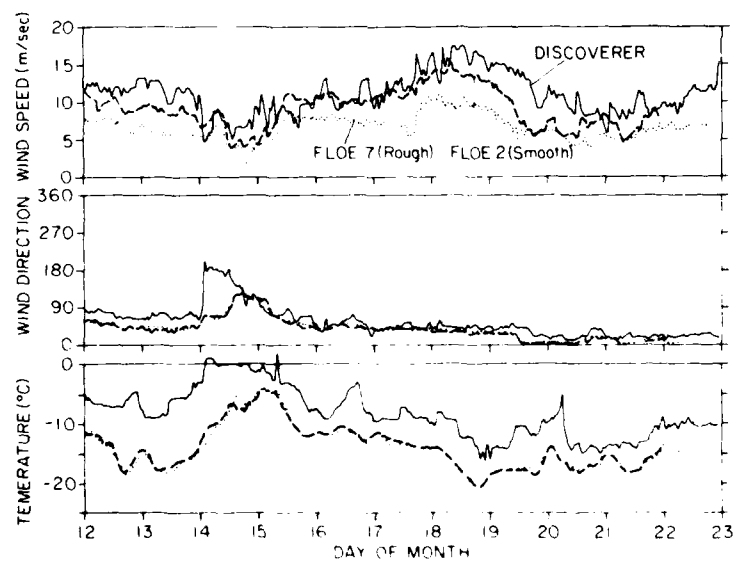


Fig. 1. A detailed map of the ice-buoy tracklines. Floes are numbered from 1 to 8. Meteorological and oceanographic measurements were taken on floes 2 and 7. The Westwind operated near floe 7 while the Discoverer operated near the ice edge—from 6 to 17 February to the south of St. Matthew Island, and after that to the southwest.



*Fig. 2. Summary of synoptic-scale weather during the experiment. Maps are for 0000 GMT on the days shown.*



*Fig. 3. Raw wind speeds measured at the remote stations at nodes two and seven, and from the Discoverer. Measurement height at the remote stations was 3 m, and on the Discoverer it was 30 m, but those winds and temperatures were reduced to 3 m by adiabatic surface layer correction.*

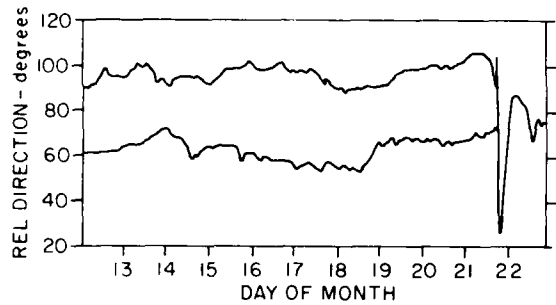


Fig. 4. Raw compass measurements from floes 2 (lower curve) and 7 (upper curve). The measurements were taken every hour at the end of the wind sampling period. Shifts in the compass direction were used to correct wind directions. The sudden onset of motion at the end of the camp 7 series occurred at the same time as a sudden opening of leads. This is believed to be the beginning of the MIZ.

southerly winds occurred first at the ship, then retrograded westward, reaching the camp 12 hours later. Temperatures at the ship were generally 5°C higher than at the array. The difference is observed to decrease later in the experiment as their physical separation decreased.

Winds at floe 2 were stronger than those measured at floe 7, which implies a difference in surface roughness at the two sites. As Fig. 1 plainly shows, aside from a small amount of dispersion the array maintained its original shape over the entire period of 10–22 February. Thus there is less variability in the wind stress between the floes because the change in roughness is offset by a reduction in wind speed.

The compass measurements are shown in Fig. 4. The floes maintained their initial orientation surprisingly well, even though their velocity vector direction underwent strong tidal and longer-term changes.

The measured currents 2 m below the ice, relative to the ice motion, are shown in Fig. 5. Again, floe 2 registered stronger relative currents. The current speeds were more variable than the corresponding winds and showed a great deal of short-term variability. On scales greater than a day, the

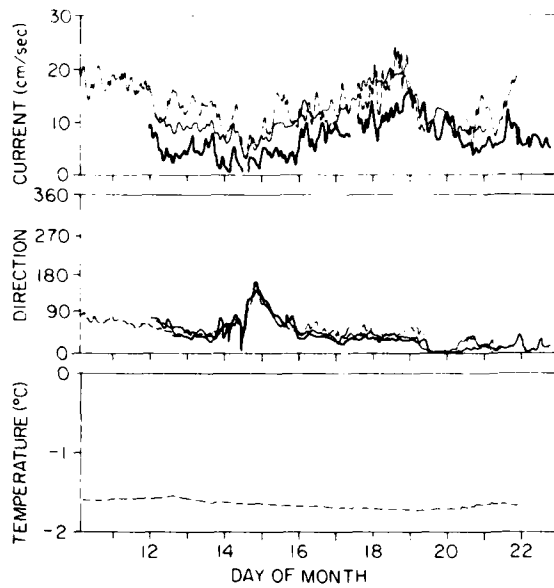


Fig. 5. Currents relative to the ice measured under the ice. The heavy solid line is from floe 7 at -2 m, the thin solid line from floe 7 at -6 m. The dashed line is from floe 2 at -2 m.

current directions are very well correlated with the wind directions and nearly colinear. It should be emphasized that each plotted point in Fig. 5 represents two 10-minute vector averages taken at 30-minute intervals over the hour. It is uncertain whether the speed variability should be attributed to instrumental error or sampling problems. Further, sudden changes in wind speed (e.g. 0600 on 15 February, or 2000 on 17 February) do not produce correlated changes in relative current speed. The wind speed maximum on 18 February and minimum on 14 February have excellent counterparts in the current record.

The current meter at -6 m below the ice registered stronger currents than the -2-m observations, as is expected in a frictional boundary layer. The directions were nearly identical, which is indicative of a well mixed or neutral layer. The small-scale variance at -2 m is much stronger than that at -6 m, although the two signals appear correlated on scales longer than a few hours. The observations are consistent with under-ice measurements by Smith (1974), which show a rapid decrease in turbulent intensity from -2 to -6 m.

The observed motion of ice floe 7 as deduced from Loran is shown in Fig. 6. The relative cur-

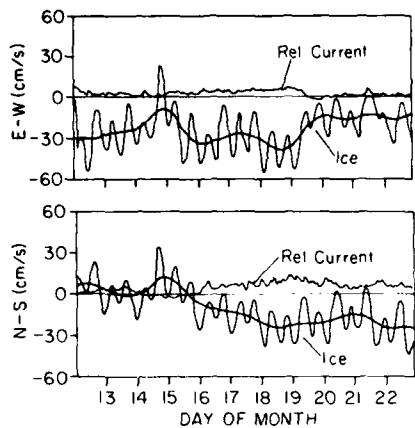


Fig. 6. Vector components of ice velocity and relative currents at  $\sim 2$  m for floe 7. The detided (24-hour low pass filter) ice velocity curve is shown superimposed on the raw signal.

rents at  $\sim 2$  m are repeated here for comparison. Ice motion is dominated by semi-diurnal tidal motion. Tidal oscillations show amplitudes from  $0.01$  m  $s^{-1}$  to  $0.4$  m  $s^{-1}$  and average approximately  $0.15$  m  $s^{-1}$ . Trends in the ice velocity components reflect concurrent trends in wind and relative water current components. However, small-scale oscillations in ice motion are not as apparent as they are in the relative currents; perhaps they are present but are masked by the large-amplitude tidal signal.

Detailed plots of winds, floe velocity and relative current for the period of 0000 GMT 14 February to 1200 GMT 15 February (Fig. 7) show the salient observable characteristics of the measurements; again, the small-scale ( $\frac{1}{2}$ - to 3-hour) variations in winds and relative currents are not correlated. Longer period variations in wind are revealed in the relative current but a response time of about 6 hours is evident. There is no obvious tidal signal in the relative current.

Power spectral estimates for the Loran-deduced ice velocity are given in Fig. 8 (upper panel). The ordinate is plotted as  $\log$  (base 10) of the power spectral density of the velocity components. The diurnal and semi-diurnal peaks dominate the spectrum, and energy drops almost three orders of magnitude immediately outside these bands. The background level of noise is of the order of  $10^{-3}$  m $^2$   $s^{-2}$  hr. If we consider this to be a uniform noise background over the entire frequency band of 0 to  $0.5$  hr $^{-1}$ , we would predict a standard deviation of

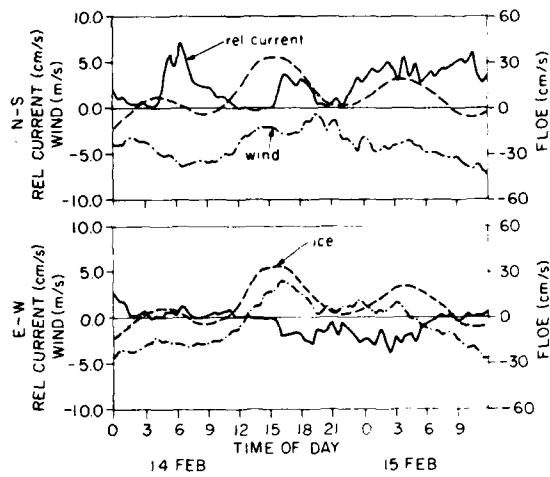


Fig. 7. Detailed plot of wind, relative current, and ice velocity for a period of time when the wind changed abruptly. Wind and current plots are from raw half-hourly data and ice velocity is from raw hourly data.

the noise to be  $0.022$  m  $s^{-1}$ . This level is above the theoretical ideal noise level of  $0.006$  m  $s^{-1}$  and is probably real. The power spectra of the  $\sim 2$  m water velocity components (lower panel) are broad, nearly white and have no discernible tidal peaks. The background level is approximately the same as that of the tidal flow,  $0.02$  to  $0.03$  m  $s^{-1}$ . All the above data imply that energy is transferred slowly from the air to the water, a weak coupling, whereas the coupling of the ice to the current is strong. The floe can be considered to be "frozen" into the water currents, whose time scales are several hours or more.

The current meter variability is due to either turbulence under the ice or random motion of the floes. In either case, the measurements are badly aliased. We expect turbulence on much smaller scales. That this much variation is evident after a 10-minute average is surprising until we consider that the differential current is of the order of  $0.1$  m  $s^{-1}$  and a 10-minute sample average smooths over length scales to  $60$  m. It is easy to imagine turbulent eddies of that size. Any future current-sampling schemes should take this motion into account and use a more rapid measurement.

An overview of the response of floe 7 to winds is given in Fig. 9, which shows the drift angle and drag colinearity, the wind factor, and the ratio of air/ice to ice/water drag coefficients. The ice velocity used to compute drift angle and ice factor was the Loran-computed velocity smoothed by a 24-hour wide modified-Daniell smoothing kernel

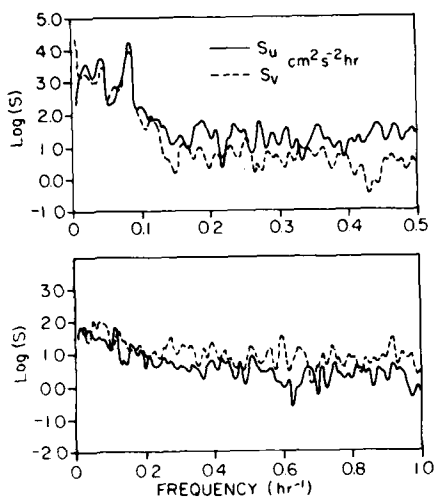


Fig. 8. Power spectra of the ice velocity components  $S_u$  (east-west),  $S_v$  (north-south) are dominated by tidal oscillations and drop rapidly to a background density of about  $10^{-3} \text{ m}^2 \text{ s}^{-2} \text{ hr}$  while the relative current has no discernible tidal peaks and a lower background noise level.

(Bloomfield, 1976). This filter is almost perfectly tuned to the diurnal and semi-diurnal tides and removed them almost entirely (Fig. 6). The wind and current data were block-averaged into hourly estimates to agree with the Loran data, and the final curves were smoothed with a 6-hour averaging kernel.

The plotted variables demonstrate how closely the floe response agreed with free-drift theory. With the exception of the wind shift period that occurred on 14 February, the drift angle  $(\theta_i - \theta_0)$  stayed in the range of  $20^\circ$  to  $50^\circ$  with a mean of  $33^\circ$ , and the ice factor  $(v_i/v_0)$  averaged slightly over 4%. However, the colinearity angle of relative winds and currents was consistently less than  $180^\circ$  with the exception of the period of frontal passage and at the very end of the experiment. This indicates that a force such as bow form drag counters the Coriolis force. We note that the colinearity angle is an extremely difficult measurement as it is a small difference. There are a variety of external and unknown factors that can cause errors of this magnitude. One potentially large possibility of error is the effect of large keels on the mean flow. Over much of the experiment the floe

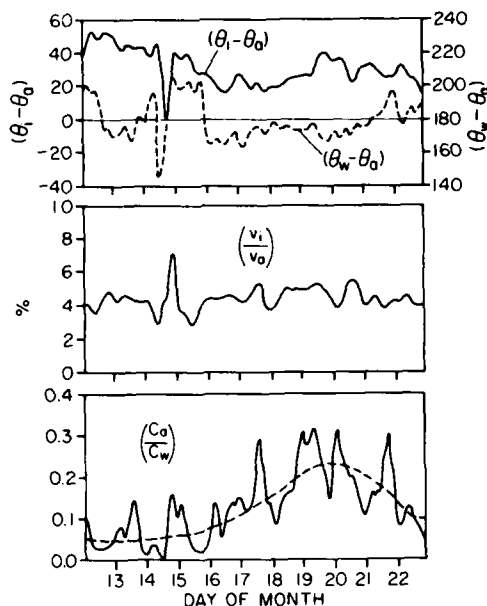


Fig. 9. Important steady-state free drift parameters for floe 7. The drift angle  $\alpha$  and colinearity angle  $\beta$  are shown in the top diagram; the ice factor is shown in the middle diagram; and the drag ratio is shown in the lower diagram. The dashed line in the latter is a visual estimate of a mean value of drag ratio.

motion and orientation were steady. A large keel nearby could distort the flow in the vicinity of the meter, thereby producing an angular difference of this magnitude. Instrumental errors, especially in field alignment, could be present.

The drag coefficient ratio  $C_d/C_w$  computed for quadratic stress laws relative to  $+3 \text{ m}$  and  $-2 \text{ m}$  (Pease et al., 1983) shows high variability. Since this term is proportional to the square of the ratio of water to air velocities, it will be strongly affected by the almost white variability of the observed water currents. A mean trend of the ratio (dashed line) shows a definite increase in  $C_d/C_w$  to a value of about 0.2 on 20 February, then a dramatic decrease to 0.08 at the end of the experiment. A physical explanation for the increase in  $C_d/C_w$  from 15 to 20 February could be a reduction in  $C_w$  due to melting and stratification of the water as the ice works its way to the edge. The drop at the end is not so easy to explain. It occurred at the same time as a sudden increase in floe rotation (Fig. 4), which is indicative of entry into the outer MIZ. There was no perceptible increase in the surface roughness of the floe or any of the surrounding area.

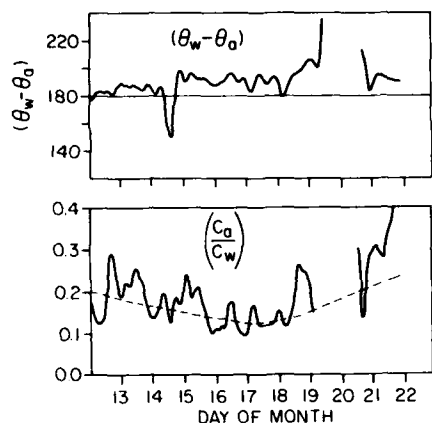


Fig. 10. Colinearity angle and drag ratio for floe 2; the smoother floe shows somewhat different and physically more reasonable behavior.

The sudden shift in wind direction that occurred at 1300 GMT 14 February provides an excellent case study in the response characteristics of the floe. From Fig. 9 we see that  $(\theta_w - \theta_o)$  dropped suddenly as the wind shifted but the water was not affected immediately. The water direction slowly followed the wind but reached its maximum at 2200 GMT, 9 hours after the wind.

A similar plot of the colinearity angle and drag coefficient ratio for floe 2 is shown in Fig. 10. This floe was large and almost perfectly flat so we expect flow distortion from keels to be a minimum. Indeed, the colinearity angle was generally greater than  $180^\circ$  in accordance with simple free-drift theory. The ratio of drags begins at a value of 0.2, decreases slightly (in the mean), then apparently increases to the end of the series. The drop in

$C_o/C_w$  after 20 February that was observed for floe 7 was not apparent in this record.

MIZEX-West shows that ice drift in the southern Bering Sea comprises almost a solid body motion in response to tidal currents and the synoptic scale winds, but with considerable high-frequency motion present.

This paper is a contribution to the Marine Services Project at PMEL and was funded in part by the Arctic Program of the Office of Naval Research. This is Contribution Number 765 from the Pacific Marine Environmental Laboratory.

## REFERENCES

Bloomfield, P., *Fourier Analysis of Time Series: An Introduction*, John Wiley and Sons, New York, 258 pp., 1976.

Overland, J.E., R.M. Reynolds and C.H. Pease, A model of the atmospheric boundary layer over the marginal ice zone, *J. Geophys. Res.*, 88, 2836-2840, 1983.

Pease, C.H., S.A. Salo and J.E. Overland, Drag measurements for first-year sea ice over a shallow sea, *J. Geophys. Res.*, 88, 2853-2862, 1983.

Reynolds, R.M., On the local meteorology of the marginal ice zone of the Bering Sea, *J. Geophys. Res.*, 89, 1984.

Smith, K.E., Turbulent structure of the surface boundary layer in an ice-covered ocean, *Rapp. P.-V. Reun. Cons. int. Explor. Mer.*, 167, 53-65, 1974.

Wilson, J.G., A.L. Comiskey, R.W. Lindsay and V.L. Long, Regional meteorology of the Bering Sea during MIZEX-West, February and March 1983, NOAA-PMEL Special report, 115 pp., 1984.

# Ice Dispersion in the Bering Sea Marginal Ice Zone

SEELYE MARTIN

*School of Oceanography, University of Washington  
Seattle, Washington 98195, USA*

ALAN S. THORNDIKE

*Department of Physics, University of Puget Sound  
Tacoma, Washington 98416, USA*

## ABSTRACT

This paper calculates the relative diffusion of ice in the Bering Sea from the motion of a set of 12 satellite- and radar-tracked buoys that were mounted on ice floes. To calculate the diffusivity of the marked floes, we look at the statistics of the difference between the mean-square separation of pairs of buoys over a time delay  $\tau$ . The short and long time delay results compare well with the theoretical predictions of Batchelor. We also find that the ice diffusivity is non-Fickian, in that the two-particle diffusion increases according to the 1.8 power of the separation between the ice floes. Comparison with other data sets shows that the ice floe diffusivity is about an order of magnitude smaller than temperate ocean measurements, and about an order greater than ice floe diffusion in the Beaufort Sea.

## 1. INTRODUCTION

This paper derives the relative diffusivity of sea ice from a particular geophysical data set, namely the motion of 12 satellite- and radar-tracked buoys located on ice floes in the Bering Sea during the period 9 February–3 March 1983. Our results show that the ice floe diffusivity has a Richardson-like behavior, in that the diffusivity increases according to the 1.8 power of the separation between floes.

Historically, the experiments and theory of Richardson (1926), Richardson and Stommel (1949), and Stommel (1949) suggest that the relative diffusion of particles on the ocean surface and in the atmosphere is governed by a  $1/r$ -dependence of diffusivity on particle separation. They also show that this  $1/r$  power follows from a similarity

solution to the Kolmogorov energy spectrum. Batchelor (1950) carried out a critique of the Richardson and Stommel work, and showed that their theory is misapplied to their data. Batchelor's critique was redone by Kraichnan (1966), and is summarized in the present paper.

In the following, Section 2 describes our experiment and Section 3 summarizes the relevant molecular and turbulent diffusion theory. Section 4 describes our data reduction techniques, and compares our results to the theoretical predictions of Batchelor (1952). Section 4 also compares our data to Okubo's (1971) compilation of temperate ocean diffusion, calculates the normal and parallel diffusion components, which we compare with Kraichnan's (1966) results, and compares our results to Thorndike's (1985) Beaufort Sea data.

## 2. THE EXPERIMENT

The 12 buoys were deployed and monitored from the U.S. Coast Guard icebreaker *Westwind* during 10–28 February 1983. Fig. 1 shows a chart of the region with the buoy positions marked at 4-day intervals. In the figure, the letters A–D identify the radar buoys, the positions of which were recorded on the ship at 0.5-hour intervals, and the letters F–K identify the satellite-tracked Argos buoys, the positions of which were recorded about 18 times per day. One satellite buoy, E, is not shown because it was located on the same floe as radar buoy A. Dr. M. Reynolds and Ms. C. Pease of the NOAA Pacific Marine Environmental Laboratory (PMEL) carried out the design and deployment of the Argos array.

Fig. 1 shows the westward, then southwestward movement of the buoy array around St. Matthew Island under the influence of the prevailing winds.

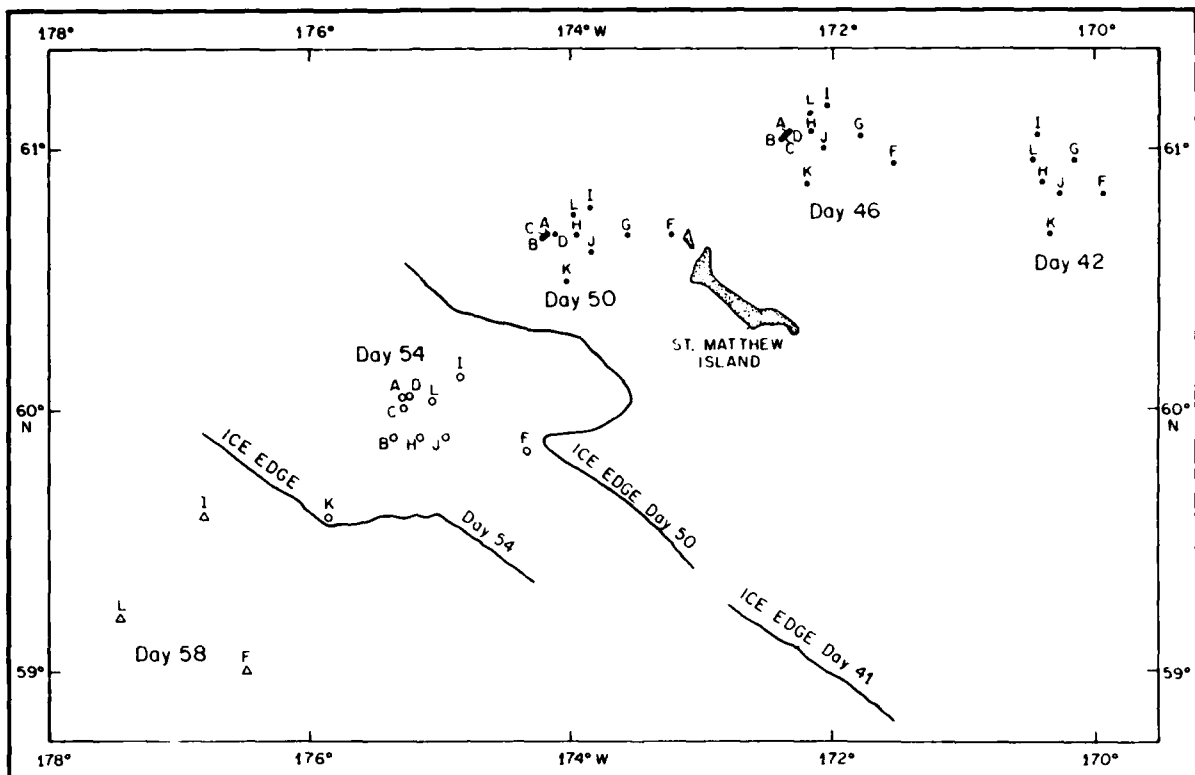


Fig. 1. A chart of the experimental study region with the buoy positions shown at 4-day intervals. The chart also shows the ice edge positions for days 41, 50 and 54 taken from air and satellite images. See text for additional description.

As the buoys approached the ice edge, certain buoys were recovered, some melted through the ice, and others were left to continue the drift. At the beginning of the experiment, we deployed the buoys both by helicopter and from the ship within solid ice cover at a distance of approximately 100 km from the ice edge. The deployment began on days 40-41, where day 40 corresponds to 9 February 1983, with establishment of the satellite buoy array, and was completed on day 45, when the four radar buoys became operational. The ship was then allowed to freeze into the ice and drift with the array.

The ice on which the radar buoys were deployed consisted of small ridged floes, with sizes between  $30 \times 30$  m and  $100 \times 100$  m. The level portions of these floes had thicknesses between 1.3 and 2 m; the floe ridge heights were 1 to 2 m. The maximum ridging in the vicinity of the ship was 2 m; the ridged ice was generally silty, suggesting the ridges had formed from the wind forcing the ice against a coast in shallow water. From aerial surveys, the ice containing the array at the beginning of the experiment was nearly compact, with little open

water. Between days 50 and 54 the ice became less compact as we drifted out toward the ice edge. Large leads and polynyas appeared within the ice cover, and two of the buoys, B and K, moved away from their neighbors under the action of wind and radiation stress across these leads. On day 54 we recovered radar buoy B and satellite buoy G. The other radar buoys, A, C and D, were recovered on day 55.

The forces acting on the ice are the atmospheric winds and temperatures, the ocean currents and tides, and the ocean thermohaline circulation. The results of the shipboard observations and the GOES weather stations deployed at stations A and G by Dr. M. Reynolds of PMEL\* show that the ice drift (Fig. 1) was in response to strong mean winds. The data show that for most of the deployment the winds, adjusted to a 10-m height, aver-

\* The weather, buoy and oceanic data are available from the National Snow and Ice Data Center (c/o Dr. Richard Armstrong, NSIDC, CIRES Campus Box 449, University of Colorado, Boulder, Colorado 80309; or on GTE Telemail: To: NSIDC, Subject: Attn Richard Armstrong).

aged  $10 \text{ m s}^{-1}$ . The wind direction was primarily from the northeast quadrant; from days 41–45, the wind direction was  $60\text{--}90^\circ$ ; from days 46–58, the direction was  $0\text{--}45^\circ$ . The periods of strongest sustained winds were days 46–50 and 53–55, when the mean speeds were  $13\text{--}15 \text{ m s}^{-1}$ , with gusts as high as  $25 \text{ m s}^{-1}$ . The air temperatures during this period were well below freezing, with a maximum of  $-5^\circ\text{C}$ , a minimum of  $-20^\circ\text{C}$ , and a mean of  $-10^\circ\text{C}$ .

Pearson et al. (1981) discussed the tides of the continental shelf to the east of St. Matthew Island, and Muench and Schumacher (1985) discussed the oceanography of the region as observed during the present experiment. The major short period tidal

component in the buoy drift region is the M2 tide (12.42 hours); this period is visible both in the drift tracks (not shown) and in the separation between certain buoy pairs (Fig. 2d, days 44–50). These tides, then, contribute to the fluctuations in the mean square separation.

Muench and Schumacher show that ocean salinity and temperature structure divides into three parts. First, inside the ice edge region and over the continental shelf the vertical water structure is uniform, consisting of low salinity ( $30 \text{ g kg}^{-1}$ ) water near its freezing point of  $-1.7^\circ\text{C}$ . Second, southwest of the ice edge and off the continental shelf, the surface waters are much warmer and saltier at  $33 \text{ g kg}^{-1}$  and  $+4^\circ\text{C}$ . Third, under the ice edge

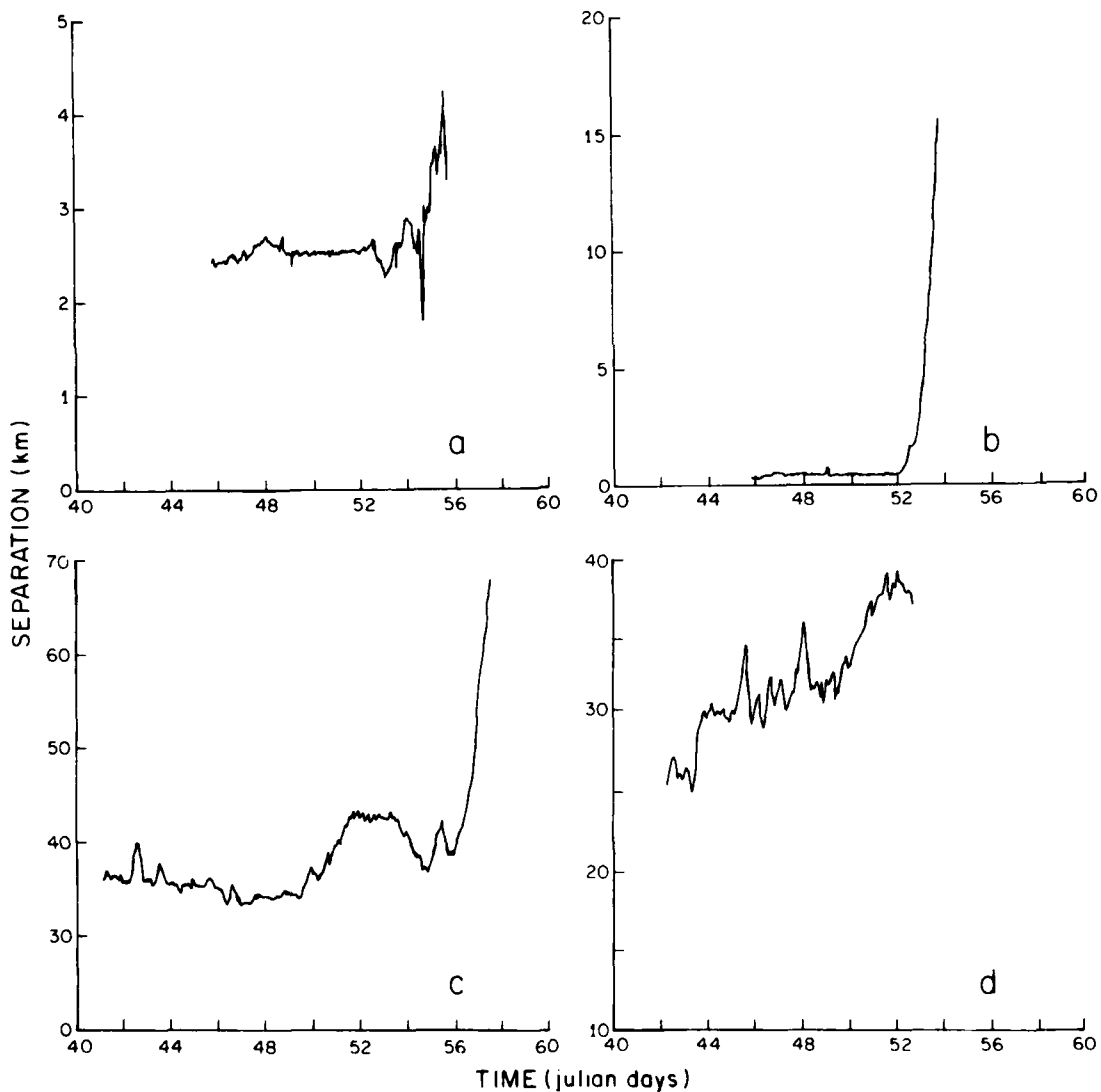


Fig. 2. Plots of the absolute separation between pairs of buoys: (a) buoy pair A and D; (b) B and C; (c) F and I; (d) A and G. See text for additional description.

there is a frontal system between the two water types, where the warm, more saline water intrudes under the cold, less saline shelf water.

As the wind advects the ice floes across this front, the ocean surface temperature increases and the ice floes melt, thus contributing to the cold, low salinity surface layer, and causing the frontal system to advance southwest. This front also generates a broad geostrophic flow to the northwest, with characteristic velocities of 0.05 to 0.10 m s<sup>-1</sup>. In the drift experiment, the buoys entered the frontal region about day 52 and remained over it for the remainder of the experiment. Once the floes moved over the front, the ice floes making up the previously solid ice cover melted and diverged, so that large areas of open water appeared within the previously consolidated pack.

To give some specific examples of the behavior of buoy pairs, Fig. 2 shows four plots of relative separation versus time for initial buoy separations ranging from 0.4 to 40 km. Fig. 2a shows, for the separation between buoys D and A, the characteristic behavior of the small-scale radar buoy separation; this behavior consisted of a period of relatively small excursions up to day 52, followed by large excursions. As another radar buoy example, Fig. 2b shows the separation between buoys B and C; these buoys remained within 400 m of each other up to day 52, then rapidly separated as buoy B moved across an adjacent polynya. For the larger buoy separations, Fig. 2c shows that the separation between buoys F and I had initial fluctuations between 30 and 40 km, followed by an increase similar to that shown in Fig. 2b; and Fig. 2d shows that the separation between buoys A and G had periodic fluctuations caused by the M2 tide, as well as non-periodic fluctuations.

### 3. THEORETICAL BACKGROUND

#### 3.1. Fickian diffusion

Following Csanady (1973, Chapter 1), Fick's law states for the molecular diffusion of a solute such as salt with concentration  $s$  in water that the flux  $F$  of  $s$  is

$$F = -x \nabla s \quad (1)$$

where  $x$  is the molecular diffusivity, and the time and distance scales of the observed process are large compared to the molecular collision time and the mean free path. Combination of eq 1 with the continuity equation yields the familiar diffusion equation.

From the diffusion equation, if the solute is released in a point discharge at the origin at time  $t = 0$ , then the mean-square distance  $\sigma^2$  to which the solute has diffused is proportional to  $t$ , as

$$\sigma^2 = 2x t. \quad (2)$$

This holds for both the one-dimensional and axisymmetric cases. For Fickian diffusion, the time-derivative of  $\sigma^2$  is a constant, so that

$$\frac{\partial}{\partial t} \sigma^2 = 2x. \quad (3)$$

Csanady (Chapter 2) also showed that the above solutions follow from consideration of the Brownian motion of particles in solution, where random collisions cause particle dispersion from the origin. In this case, the mean-square displacement of a single particle from the origin is given by

$$\frac{\partial}{\partial t} \overline{x^2} = \frac{\partial}{\partial t} \overline{r^2} = 2x \quad (4)$$

where the overbars indicate an ensemble average and  $x$  and  $r$  are the particle displacements from the origin. Therefore Brownian motion can be viewed as a molecular mechanism for Fickian diffusion.

Given this short review, we next examine the turbulent diffusion of single particles and pairs of particles to show how a turbulent diffusivity  $x_t$  is derived by analogy to eq 4.

#### 3.2 Turbulent diffusion

The derivation of a turbulent diffusivity from single particle diffusion follows from G.I. Taylor's theorem (Csanady, §2.3, 3.5). In Taylor's theorem, the mean-square single particle displacement is proportional to the time integral of the velocity autocorrelation  $R(\tau)$ , where  $\tau$  is the time delay. For small values of  $\tau$ , the velocities are highly correlated, so that  $R(\tau) \approx 1$ , and

$$\frac{\partial}{\partial t} \overline{x^2} \approx \tau. \quad (5)$$

For large  $\tau$ , the velocities are uncorrelated, and  $R(\tau) = 0$ , so that if the integral is finite,

$$\frac{\partial}{\partial t} \overline{x^2} = 2x_t, \quad (6)$$

where  $x_t$  is a constant, called the turbulent diffusivity. Therefore, for particle motion in a turbulent flow to be described by a diffusivity, the observa-

tion time scale must be greater than the velocity correlation time, which is analogous to the molecular collision time in Fickian diffusion.

As Csanady (Chapter 4) discusses, particularly when a mean flow advects a system of diffusing particles, there are advantages to studying the relative diffusion of particle pairs. For Fickian two-particle diffusion, if the particle separation is greater than the mean free path so that the particle velocities are uncorrelated, then the rate at which the mean-square separation between the particles increases is independent of the separation. From Csanady (Chapters 2 and 4) one may easily show that for two particles separated by a distance  $y$ ,

$$\frac{\partial}{\partial t} \overline{y^2} = 4x \quad (7)$$

where  $x$  is again the molecular diffusivity. Comparison of eq 7 with eq 4 shows that two particles separate at twice the rate that a single particle separates from the origin.

The turbulent dispersion of two particles is discussed theoretically by many authors, including Batchelor (1952), Roberts (1961), Kraichnan (1966) and David (1983). These theories assume that the particles are embedded in a stationary, homogeneous, isotropic flow, and that the energy-containing eddies have a maximum length scale  $L$ . When the particle separation exceeds  $L$ , the particles move independently so that the time derivative of their mean-square separation equals twice the single particle separation.

For separation scales less than  $L$ , the two particles behave in a way first described by Richardson (1926). Namely, suppose that the initial particle separation  $\ell_0$  is less than  $L$ , but much greater than the short length scales where molecular processes dominate. For this case, Csanady (§4.3) shows that it is those eddies with length scales of order  $\ell_0$  that cause the two particles to diffuse. Eddies that are much smaller than  $\ell_0$  have little effect on the particle separation, and eddies much larger than  $\ell_0$  advect both particles without changing their relative separation. Furthermore, since the particle separation increases with time, progressively larger eddies act on the particles so that two things happen. First, the relative diffusivity increases with separation up to the scale  $L$  because the larger eddies cause larger root-mean fluctuations; second, for separations less than  $L$  the relative diffusivity is a function of both time and separation.

Batchelor (1952) gives solutions for the short and long time behavior of diffusing particle pairs. To describe these solutions, we first define as in

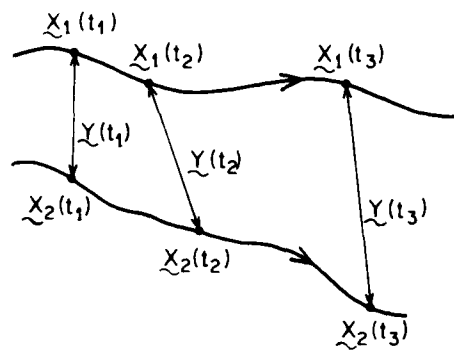


Fig. 3. A definition figure showing for a particle pair  $X_1$ ,  $X_2$ , the absolute displacement  $X$ , and the relative displacement  $Y$ .

Fig. 3 the absolute displacement of two particles by  $X_1(t)$  and  $X_2(t)$  and their relative displacement by  $Y(t)$ . Then the mean-square separation of two particles is

$$\overline{Y_i(\tau) Y_j(\tau)} = \overline{Y_i(0) Y_j(0)} + \int_0^\tau \int_0^\tau \overline{V_i(t') V_j(t'')} dt' dt'' \quad (8)$$

where the overbars again denote an ensemble average, the  $V_i$  are the components of the relative velocity of the two particles, the subscripts on  $Y$  and  $V$  denote the vector components, and  $\tau$  is the elapsed time.

To describe the small time behavior of the mean-square separation, if we choose  $\tau$  small enough in eq 8 so that  $V_i(0)$  and  $V_i(\tau)$  are nearly equal, then for small  $\tau$

$$\overline{Y_i(\tau) Y_j(\tau)} - \overline{Y_i(0) Y_j(0)} \approx \tau^2 \overline{V_i(0) V_j(0)} \quad (9)$$

For small  $\tau$ , then, the mean-square separation increases as  $\tau^2$ . Alternatively, if we write the left-hand side of eq 9 as  $\Delta \overline{Y_i(\tau) Y_j(\tau)}$ , then

$$\frac{\Delta \overline{Y_i(\tau) Y_j(\tau)}}{\tau} = \tau \overline{V_i(0) V_j(0)} \quad (10)$$

so that for small  $\tau$ , the time derivative in difference form of the mean-square separation increases linearly with  $\tau$ .

For large times, which are those times large enough that the particle separation exceeds the

energy containing eddy scale  $L$ , the particles wander independently. For this case, as Batchelor explicitly shows,

$$\overline{V_i(t')V_j(t')} = 2 \overline{U_i(t')U_j(t')} \quad (11a)$$

where  $U_i$  is the absolute velocity. Therefore,

$$\Delta \overline{Y_i(\tau)Y_j(\tau)} = 2\Delta \overline{X_i(\tau)X_j(\tau)} \quad (11b)$$

where the subscripts on  $X$  refer to the vector components of a single particle displacement. From eq 11, the time derivative in difference form is

$$\frac{\Delta \overline{Y_i Y_j}}{\tau} = 2 \frac{\overline{X_i X_j}}{\tau} = 4x_{ijT}, \quad (12)$$

where  $x_{ijT}$  is the constant turbulent diffusivity in component form.

In the next section, we carry out the above analysis for the scalar case of two particles separated by a distance  $r$ , and for the intrinsic coordinate case of the components of  $Y$  normal and parallel to the initial separation  $Y(0)$ .

#### 4. DATA DISCUSSION

This section describes our data analysis techniques, shows how our technique is related to the theoretical analysis described in the previous section, then states our results. In our analysis, we follow the scheme suggested by Richardson and Stommel (1949) and Stommel (1949).

##### 4.1 Method of analysis

In our scheme, we examine the behavior of the parallel, normal, and radial differences of the two-particle separation  $Y$ . Fig. 4 shows our notation. If we have two vectors,  $Y(0)$  and  $Y(\tau)$ , with the magnitudes  $\ell_0$  and  $\ell(\tau)$ , then we write  $r_p$  as the component of the vector difference parallel to  $Y(0)$ ,  $r_n$  as the normal component of the vector difference, and  $r$  as the difference of the magnitudes  $r = \ell(\tau) - \ell_0$ .

In our numerical calculation we examine the radar and Argos buoy time series at 1.5-hour intervals. The other time interval used in the analysis is  $\tau$ , the time separation used in the calculation of the mean-squares in eq 8-11. In the calculations we set  $\tau = 1.5, 3, 6, 12, 24, 48, 72$  and 96 hours. Then, for each value of  $\tau$  and each buoy pair, fol-

lowing Fig. 4, we calculate the initial and final separations  $\ell_0$  and  $\ell(\tau)$  and the quantities

$$r_n^2(\tau), r_p^2(\tau), r^2(\tau), \text{ and } r_n(\tau)r_p(\tau). \quad (13)$$

We do this beginning at time  $t_0$ , then repeat the calculation at  $t_0 + \Delta T$ , and so forth.

We then bin the four terms in eq 12 into 1-km-wide bins defined by the average separation

$$\ell_a = \frac{\ell_0 + \ell(\tau)}{2}. \quad (14)$$

For example, the first bin includes all values of  $\ell_a$  in the range 0 to 0.99 km, the second, 1 to 1.99 km, and so forth out to 60 km. We then count the number of terms in each bin and group the bins such that there are greater than 300 points in each bin. This binning scheme corresponds to the convention of Richardson and Stommel (1949); it differs slightly from the convention of Batchelor described in the previous section, which groups the data according to  $\ell_0$ . We find some differences between the results of the two conventions for  $\tau > 48$  hours.

The estimates calculated from the contents of each bin have an associated error variance which we must remove. This error variance has two factors. First, it depends on the relative number in each bin of the three possible buoy pairs, radar-radar, radar-satellite, and satellite-satellite; second, as Jenkins and Watts (1968, Chapter 3) showed, it is a linear combination of the radar and satellite buoy position error variances.

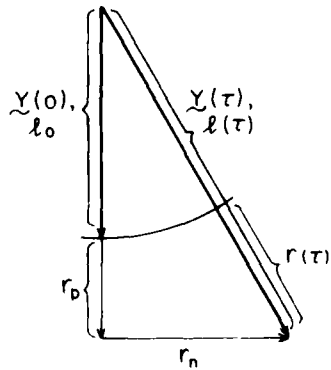


Fig. 4. A pictorial description of the scalars and vectors used in the discussion of our binning scheme. See text for further description.

We determined the radar buoy position error from calculation of the variance in relative displacement of buoys B and C during a 4-day quiescent period. This calculation yields a radar buoy standard deviation in position of  $\pm 25$  m. To determine the satellite buoy position error, we used the fact that up to day 52 the satellite buoy E and the radar buoy A were located 10 m apart on the same ice floe; following day 52 the floe split apart and the two buoys slowly separated. For these two buoys, calculation of the variance in relative position preceding day 52 and use of the radar buoy standard deviation yields a satellite buoy standard deviation of  $\pm 175$  m. This number is slightly smaller than the value of  $\pm 300$  m reported by Thorndike and Colony (1980) as the satellite buoy reading error in absolute position.

Given these error variances, we calculate the corrected mean-square estimates for the quantities (eq 13) in each bin as, for example,

$$\overline{r^2(\tau)} = \frac{1}{n} \sum_{i=1}^n \{r_i^2(\tau)\} - (\text{reading error variance}) \quad (15)$$

where  $i$  sums over the number of points  $n$  in each bin. On the assumption that the flow is stationary, eq 15 is equivalent to an ensemble average.

Batchelor (1950, §6) discusses the conditions under which the Richardson-Stommel formulation is equivalent to the left-hand side of eq 9. He shows that if  $\overline{Y(\tau)} = 0$ , then the mean-square quantities as in eq 15 and the bin definition in eq 14 reduce to his formulation. Given that we wish to compare our field results with Batchelor's predictions, we next show that for our specific experiment, the quantities in eq 13 and 15 approximately equal Batchelor's definitions.

Our binning technique as described in the paragraph containing eq 14 is roughly equivalent to defining an average  $\bar{r}$ . We show next that this bin definition is equivalent to binning particles on their initial separation. From Fig. 4, we write

$$\frac{\bar{r}}{l_0} = 1 + \frac{1}{2} \bar{\alpha}, \quad (16a)$$

where

$$\bar{\alpha} = \frac{\overline{r(\tau)}}{l_0}. \quad (16b)$$

Examination of our data shows that  $\frac{1}{2} \bar{\alpha} \leq 10^{-1}$

for all bins and all values of  $\tau$ . Therefore

$$\bar{r} \approx l_0, \quad (16c)$$

and eq 14 is consistent with Batchelor's formulation.

Similar arguments hold for the mean-square quantities. First for the mean-square radial displacement  $\overline{r^2}$ , where we drop the  $\tau$  for clarity,

$$\overline{r^2} = \overline{(r - l_0)^2} = \overline{r^2} + \overline{l_0^2} - 2\bar{r}l_0. \quad (17a)$$

From eq 16b,

$$\frac{\bar{r}}{l_0} = 1 + \bar{\alpha}. \quad (17b)$$

Our data show that for all bins and  $\tau \leq 48$  hours,  $\bar{\alpha} \leq 10^{-1}$ ; and that for all bins and  $\tau \leq 96$  hours,  $\bar{\alpha} \leq 2 \times 10^{-1}$ . Therefore,

$$\overline{r^2} \approx \overline{r^2} - l_0^2, \quad (17c)$$

and our formulation is approximately equal to Batchelor's.

For the normal component  $\overline{r_n^2}$ , since

$$\overline{Y_n(0)} = 0, \overline{r_n^2} = \overline{Y_n^2(\tau)}. \quad (18)$$

For the parallel and cross components  $\overline{r_p^2}$  and  $\overline{r_n r_p}$ , we also find from our data that

$$\overline{r_p^2} \approx \overline{Y_p^2} - l_0^2, \quad (19a)$$

and

$$\overline{r_n r_p} \approx \overline{Y_n Y_p}, \quad (19b)$$

to the same order of accuracy as eq 17c. Given the above discussion, our estimates approximately equal Batchelor's definitions, so that the long and short time behavior of our estimates should follow eq 10 and 12.

#### 4.2 Comparison of $x_\tau$ with theory

To show that the  $\tau$ -behavior of our estimates agrees with Batchelor's predictions, we next examine a plot of  $x_\tau$  derived from  $r^2(\tau)$ , where  $x_\tau$  is approximately given by

$$4x_\tau = \frac{r^2(\tau)}{\tau}. \quad (20)$$

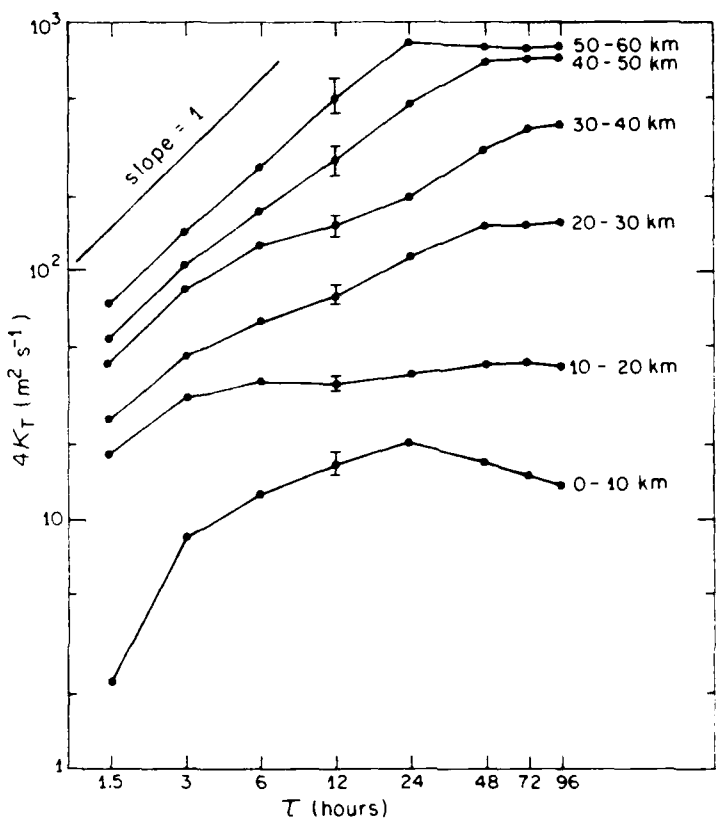


Fig. 5. Plots of  $4x_t$  versus  $\tau$  for the 10-km-wide bins. The line with slope 1 is for reference only.

Fig. 5 shows a plot of  $x_t$  versus  $\tau$  for the choice of 10-km-wide bins. These bins run from 0 to 9.99 km, 10 to 19.99 km, and so forth out to 59.99 km. We chose these wide bins to avoid clutter on the graph, while still presenting the behavior of  $x_t$  for small and large separations. On the curves, the vertical cross bars at 12 hours show the 95% confidence limit for all of the points on the particular curve based on the number of estimates in each bin, which ranged from a minimum of 300 points for the 50-60 km bin to a maximum of 1800 for the 10-20 km bin.

For the two largest bins, 50-60 km and 40-50 km, the behavior of  $x_t$  agrees with Batchelor's prediction. Namely, for small  $\tau$ ,  $x_t$  increases linearly, and for large  $\tau$ ,  $x_t$  is nearly constant with a value of  $200 \text{ m}^2 \text{ s}^{-1}$ . Fig. 5 also shows for the other smaller bins, with the exception of the 0-10 km bin, that  $x_t$  also increases linearly for small  $\tau$ , followed by a leveling-off at large  $\tau$ . From this large  $\tau$  behavior, we can estimate the dependence of  $x_t$  on separation. Table 1 lists these values of  $x_t$  versus the bin centerpoints; examination of the table and of Fig. 5 shows the rapid increase of  $x_t$  with in-

creasing separation, whereas we show below that  $x_t$  increases with the 1.8 power of separation. Qualitatively, our observations of a rapid increase in diffusivity with separation are consistent with Richardson's model. Our 1.8 power-law dependence, however, is greater than his and Stommel's values of 1.3 to 1.4.

Finally, we show that the values of  $x_t$  listed in Table 1 are consistent with the dispersion of the

Table 1. The turbulent diffusivity  $x_t$  versus the center points of the 10-km-wide bins (from Fig. 5).

Separation (km)	$x_t$ ( $\text{m}^2 \text{ s}^{-1}$ )
5	4
15	10
25	40
35	100
45	175
55	200

buoy array in Fig. 1. On day 42, the buoy array has an approximate diameter of 45 km. Substitution of  $x_0 = 175 \text{ m}^2 \text{ s}^{-1}$ , the 16-day time period from Fig. 1, and  $\bar{y} = 45 \text{ km}$  into eq 7 shows that after 16 days a buoy array with an initial root-mean-square diameter of 45 km increases in diameter to 55 km. This slow growth of the array over 16 days is consistent with Fig. 1.

#### 4.3 Comparison of $x_T$ with Okubo's data

For comparison of the values of  $x_T$  in Table 1 with other ocean surface data, we compare these data with those of Okubo (1971). Okubo gives a compilation of 19 different temperate ocean surface experiments on the diffusion of dye patches. For each spill, he lists the root-mean-square radius of the patch with time. For non-circular patches characterized by root-mean-square major and minor axes  $\sigma_{maj}$  and  $\sigma_{min}$ , he defines the mean-

square radius as

$$r^2 = 2\sigma_{maj} \sigma_{min}. \quad (21)$$

He takes his diffusivity as  $x_0 = r^2/4t$ , where the time  $t$  is measured from the initiation of the spill, then plots  $x_0$  versus a length scale to find a 1.1 power-law dependence of diffusivity on patch size. The factor of 4 in his definition is so that, as in our eq 20,  $x_0$  reduces to the Fickian value for molecular diffusion.

To compare Okubo's data with our results, we reanalyze the data in his Table 1 according to the following difference form of eq 3:

$$\frac{\partial}{\partial t} r^2 \approx \frac{\Delta r^2}{\Delta t} = \frac{r_1^2 - r_0^2}{t_1 - t_0}, \quad (22)$$

where the subscripts 1 and 0 refer to different

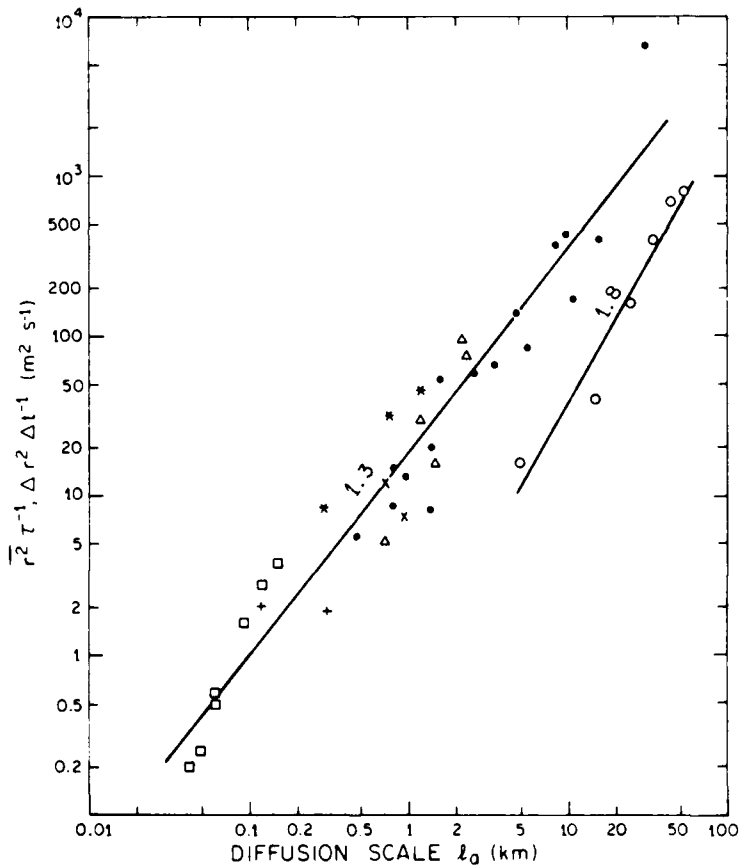


Fig. 6. Plots of  $\Delta r^2 \Delta t^{-1}$  for the Okubo data set, and of  $\bar{r}^2 \bar{t}^{-1}$  for our data versus mean separation or bin. The symbols are defined as follows: our data: o—Okubo's data: •—North Sea; Δ—Cape Kennedy; +—Banana River; ×—Manokin River; \*—New York Bight; □—Southern California. The solid lines show the least-square fit to the two data sets with slopes as marked.

times. In Fig. 6, we then plot  $\Delta r^2/\Delta t$  versus the mean patch radius  $\ell_a$  defined by

$$\ell_a = \frac{r_1 + r_0}{2}. \quad (23)$$

Fig. 6 shows a plot of  $\Delta r^2/\Delta t$  from the reanalyzed Okubo data, and our values of  $\overline{r^2}/\tau$  from Table 1 plotted versus the midpoints of each bin. The solid lines running through the data points are the least-square fits; the numbers above these lines indicate the slope. Examination of the figure shows that, in spite of the very different methods of observing and calculating the diffusivities, the diffusion estimates from the temperate ocean are about an order of magnitude greater than the estimates obtained in our ice-covered region.

The figure also shows that our estimates have a steeper slope than Okubo's. Using orthogonal estimates of the slope and coefficient (Jenkins and Watts, 1968, §4.3.4), a least-square fit of the Okubo data gives

$$\frac{\Delta r^2}{\Delta t} = 19 \ell_a^{1.27 \pm 0.16}, \quad (24a)$$

where  $\ell_a$  has units of km, the equation has units of  $\text{m}^2 \text{s}^{-1}$ , 0.16 is the 95% confidence limit on the slope, and the 95% limit on the coefficient 19 extends from 6 to 60.

Similarly, our six diffusion estimates yield

$$\frac{\Delta r^2}{\Delta t} = 0.16 \ell_a^{1.8 \pm 0.8}, \quad (24b)$$

where the 95% limit on the coefficient 0.16 extends from  $10^{-2}$  to 2. These results suggest that the ice floe diffusion is about an order smaller and has a steeper slope than the temperate ocean diffusion curve.

#### 4.4 The normal and parallel components

Examination of the behavior of  $\overline{r_n^2}$  and  $\overline{r_p^2}$  yields further information about the flow behavior. In this subsection we first discuss some of the theoretical predictions, then discuss our experimental observations.

For the special case of a homogeneous, isotropic, non-divergent turbulent flow, Batchelor (1952) and Roberts (1961) show that

$$\overline{r_n^2} = \overline{r_p^2} + \frac{\ell}{2} \frac{\partial}{\partial \ell} \overline{r_p^2}. \quad (25)$$

For the further restriction of a Kolmogorov spec-

trum, Batchelor (1950) states, and Kraichnan (1964) derives, the behavior of  $\overline{r_n^2}$  and  $\overline{r_p^2}$  for small and large  $\tau$ .

For small  $\tau$ ,

$$\overline{r_n^2} = \frac{4}{3} \overline{r_p^2}, \quad (26a)$$

and

$$\overline{r_n^2} \sim \overline{r_p^2} \sim \overline{r^2} \sim \ell^{2/3}. \quad (26b)$$

For large  $\tau$ ,

$$\overline{r_n^2} = \frac{5}{3} \overline{r_p^2}, \quad (27a)$$

and

$$\overline{r_n^2} \sim \overline{r_p^2} \sim \overline{r^2} \sim \ell^{5/3}. \quad (27b)$$

The large  $\tau$  solution leads to the  $4/3$ -power similarity solution for  $r(\ell)$  discussed by Richardson and Stommel (1949), Stommel (1949), and Csanady (1973).

As examples of our observed small and large  $\tau$  behavior, Fig. 7 shows  $\overline{r_n^2} \tau^{-1}$  and  $\overline{r_p^2} \tau^{-1}$  plotted versus separation for  $\tau = 1.5$  and 72 hours. To obtain a greater spatial resolution than Fig. 5, we use the binning scheme listed in Table 2, and plot the estimates versus the bin center points. We choose 72 hours as our large  $\tau$  for later comparison with Thorndike's Beaufort Sea data.

In Fig. 7, the solid lines show the least-squares fits to the data sets and the vertical crossbars show the maximum 95% confidence intervals of the data points for the two  $\tau$  values. Table 3 lists for these regression lines the slope, the coefficient, and the 95% confidence limits from orthogonal estimates of these terms. Because, as Table 3 shows, the fit to the two 1.5-hour data sets is nearly identical, we show only one curve for this case. Examination of the figure and Table 3 shows that for small  $\tau$ ,  $\overline{r_n^2} \approx \overline{r_p^2}$ , and that the regression lines for the parallel and perpendicular case are nearly coincident, with a slope of 1.1. Because this number is much larger than the  $4/3$  Kolmogorov prediction, our flow does not appear to be governed by a Kolmogorov energy spectrum.

Even if the Kolmogorov spectrum does not govern the flow, the flow can still be homogeneous, isotropic, and non-divergent. We can test for this condition at  $\tau = 1.5$  hours. First, examination of our data shows that the cross-product  $\overline{r_n r_p}$  is at least an order of magnitude smaller than  $\overline{r_n^2}$  or  $\overline{r_p^2}$ . Second, substitution of  $\overline{r_p^2} \sim \ell^{1.1}$  into eq 25 shows that for the flow to be isotropic, homogeneous,

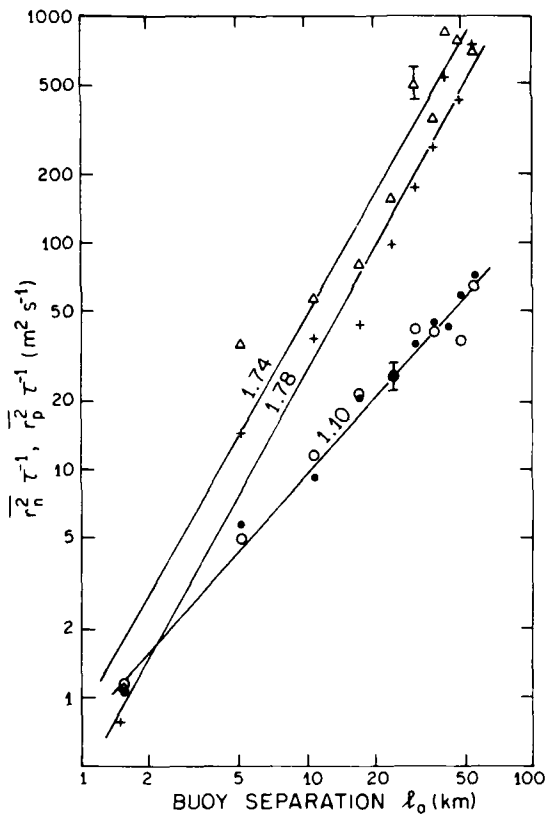


Fig. 7. Plots of  $\bar{r}_n^2 \tau^{-1}$  and  $\bar{r}_p^2 \tau^{-1}$  versus the center of the bins for  $\tau = 1.5$  and 72 hours. For  $\tau = 1.5$  hours,  $\circ$  is  $\bar{r}_n^2 \tau^{-1}$  and  $\bullet$  is  $\bar{r}_p^2 \tau^{-1}$ . For  $\tau = 72$  hours,  $\Delta$  is  $\bar{r}_n^2 \tau^{-1}$ , and  $+$  is  $\bar{r}_p^2 \tau^{-1}$ . The solid lines are the least-square fits of the data; see text for additional discussion.

and non-divergent, not only must  $\bar{r}_n \bar{r}_p = 0$ , but also

$$\bar{r}_n^2 \approx 1.6 \bar{r}_p^2. \quad (28)$$

Although the listings in Table 3 show that eq 28 is possible within our 95% confidence limits, examination of Fig. 7 suggests that eq 28 is unlikely.

For the 72-hour case, we found that  $\bar{r}_n \bar{r}_p$  was about 20% of  $\bar{r}_n^2$  and  $\bar{r}_p^2$ . Table 3 also shows that  $\bar{r}_p^2 \approx \ell^{1.8}$ ; for this, eq 25 predicts

$$\bar{r}_n^2 \approx 1.9 \bar{r}_p^2. \quad (29)$$

From Table 3, our observed ratio of the parallel and perpendicular terms is also 1.9. However, our observations of the large amounts of open water that appeared within the pack near the ice edge suggest that the flow was divergent; because the theory depends on the assumption of non-di-

Table 2. The bins and the number of points in each bin used in Fig. 7.

Bin definition (km)	No. of points
0-3	300
3-7	300
7-14	1100
14-20	1600
20-27	1200
27-33	700
33-39	800
39-44	300
44-50	300
50-60	300

Table 3. The parameters and 95% confidence intervals of the least-square power-law fit to the points in Fig. 7 for separation in km.

Case	Slope	Coefficient (Confidence interval)
$\tau = 1.5$ hr		
$\bar{r}_n^2 \tau^{-1}$	$1.07 \pm 0.17$	0.91 (0.5-1.5)
$\bar{r}_p^2 \tau^{-1}$	$1.12 \pm 0.12$	0.81 (0.6-1.2)
$\tau = 72$ hr		
$\bar{r}_n^2 \tau^{-1}$	$1.74 \pm 0.42$	0.93 (0.3-3.4)
$\bar{r}_p^2 \tau^{-1}$	$1.78 \pm 0.30$	0.49 (0.2-1.2)

vergent motion, the agreement of eq 29 with observation is probably coincidental.

#### 4.5 Comparison with Beaufort Sea data

Finally, we compare the 72-hour results from Fig. 7 with Thorndike's (1985) Beaufort Sea data set. From two Seasat SAR tracks, measuring 1500 km long in the Beaufort Sea and separated in time by 3 days, Thorndike calculates the variance of the parallel and perpendicular components of the ice displacement. For our case, the variance of the estimates is of the same order as the mean-square estimates. If we assume that this is also the case for Thorndike, then we can compare the two cases.

Using a similar binning scheme, Thorndike found that the variance of the normal component is proportional to the 1.1 power of separation, and that the variance of the perpendicular component is proportional to the 1.3 power, where, for separations of 10-60 km, the magnitude of the nor-

mal component variance is about 5 times that of the parallel component. If for a separation of 40 km we convert his numbers into our units, then his parallel component variance has a magnitude of  $5 \text{ m}^2 \text{ s}^{-1}$ , and his normal component a magnitude of  $30 \text{ m}^2 \text{ s}^{-1}$ . For the same approximate separation, our work gives  $\overline{r_n^2} \tau^{-1} \sim \overline{r_p^2} \tau^{-1} = 600 \text{ m}^2 \text{ s}^{-1}$ , which is about an order of magnitude greater than Thorndike's results. This rough comparison suggests that the diffusion processes that occurred in the Beaufort Sea are 10–100 times smaller than our observations.

## ACKNOWLEDGMENTS

The authors thank the officers and crew of the U.S. Coast Guard Cutter *Westwind* for making it possible for us to gather these data. We also thank Carol Pease and Dr. Michael Reynolds for the use of their Argos buoy data. Peter Kauffman, Imants Virsnieks, and David Thoreson worked on the gathering of the radar buoy data; we are grateful for their effort. We also thank Esther Muñoz, who patiently carried out most of the data processing described herein; and Dr. Steven Riser, for many helpful conversations and references. We gratefully acknowledge the support of the Office of Naval Research under Task NR 083-012 and contract number N00014-84-C-0111; and the support of the National Science Foundation under contract number DPP-8217594. This is contribution No. 1443 of the School of Oceanography, University of Washington.

## REFERENCES

**Batchelor, G.K.**, The application of the similarity theory of turbulence to atmospheric diffusion, *Quart. J. R. Met. Soc.*, **76**, 133–146, 1950.  
**Batchelor, G.K.**, Diffusion in a field of homogeneous turbulence: II. The relative motion of particles, *Proc. Cam. Phil. Soc.*, **48**, 345–362, 1952.

**Batchelor, G.K.**, *The Theory of Homogeneous Turbulence*, 197 pp., Cambridge University Press, 1960.  
**Csanady, G.T.**, *Turbulent Diffusion in the Environment*, 248 pp., D. Reidel Pub. Co., Boston, 1973.  
**Davis, R.E.**, Oceanic property transport, Lagrangian particle statistics, and their prediction, *J. Mar. Res.*, **41**, 183–194, 1983.  
**Jenkins, G.M. and D.G. Watts**, *Spectral Analysis and Its Applications*, 525 pp., Holden-Day, San Francisco, 1968.  
**Kraichnan, R.H.**, Dispersion of particle pairs in homogeneous turbulence, *Phys. Fluids*, **9**, 1937–1943, 1966.  
**Muench, R.D. and J.D. Schumacher**, On the Bering Sea ice edge front, *J. Geophys. Res.* (in press), 1985.  
**Okubo, A.**, Oceanic diffusion diagrams, *Deep-Sea Res.*, **18**, 789–802, 1971.  
**Pearson, C.A., H.O. Mofjeld and R.B. Tripp**, Tides of the eastern Bering Sea shelf, in *The Eastern Bering Sea Shelf: Oceanography and Resources, Volume I* (D.W. Hood and J.A. Calder, Ed.), U.S. Dept. of Commerce, 625 pp., 111–130, 1981.  
**Richardson, L.F.**, Atmospheric diffusion shown on a distance-neighbor graph, *Proc. Roy. Soc. London (A)*, **110**, 709–737, 1926.  
**Richardson, L.F. and H. Stommel**, Note on eddy diffusion in the sea, *J. Meteor.*, **5**, 238–240, 1949.  
**Roberts, P.H.**, Analytical theory of turbulent diffusion, *J. Fluid Mech.*, **11**, 257–283, 1961.  
**Stommel, H.**, Horizontal diffusion due to oceanic turbulence, *J. Marine Res.*, **8**, 199–225, 1949.  
**Thorndike, A.S. and R. Colony**, *Arctic Ocean Buoy Program Data Report, 19 January 1979 to 31 December 1979*, 131 pp., Polar Science Center, University of Washington, Seattle, Washington 98195, 1980.  
**Thorndike, A.S.**, Sea ice kinematics, in *Geophysics of Sea Ice* (N. Untersteiner, Ed.), Plenum Press (in press), 1985.

## The Motion of Ice Edge Radar Transponders During MIZEX-West

PETER WADHAMS AND SIOBHAN P. O'FARRELL

*Scott Polar Research Institute, University of Cambridge  
Cambridge, CB2 1ER, England*

### 1. INTRODUCTION

In this report we present and discuss ice floe displacement data obtained from the deployment of radar transponders near the ice edge during the MIZEX-West experiment in the Bering Sea (February 1983). Six separate arrays were deployed during the experiment (coded drift 1-drift 6); the first was set out from USCG icebreaker *West-*

*wind*, then tracked from the NOAA ship *Discoverer*, while drifts 2-6 were set out and tracked from *Discoverer*. Each transponder site (Fig. 1) comprised an X-band Motorola radar transponder mounted inside a plastic tube (of the type described by Martin et al., 1983), which also contained a battery pack, a radar reflector on a sectioned aluminum pole, and a Seadisc one-dimensional telemetering wave buoy mounted on the floe to moni-

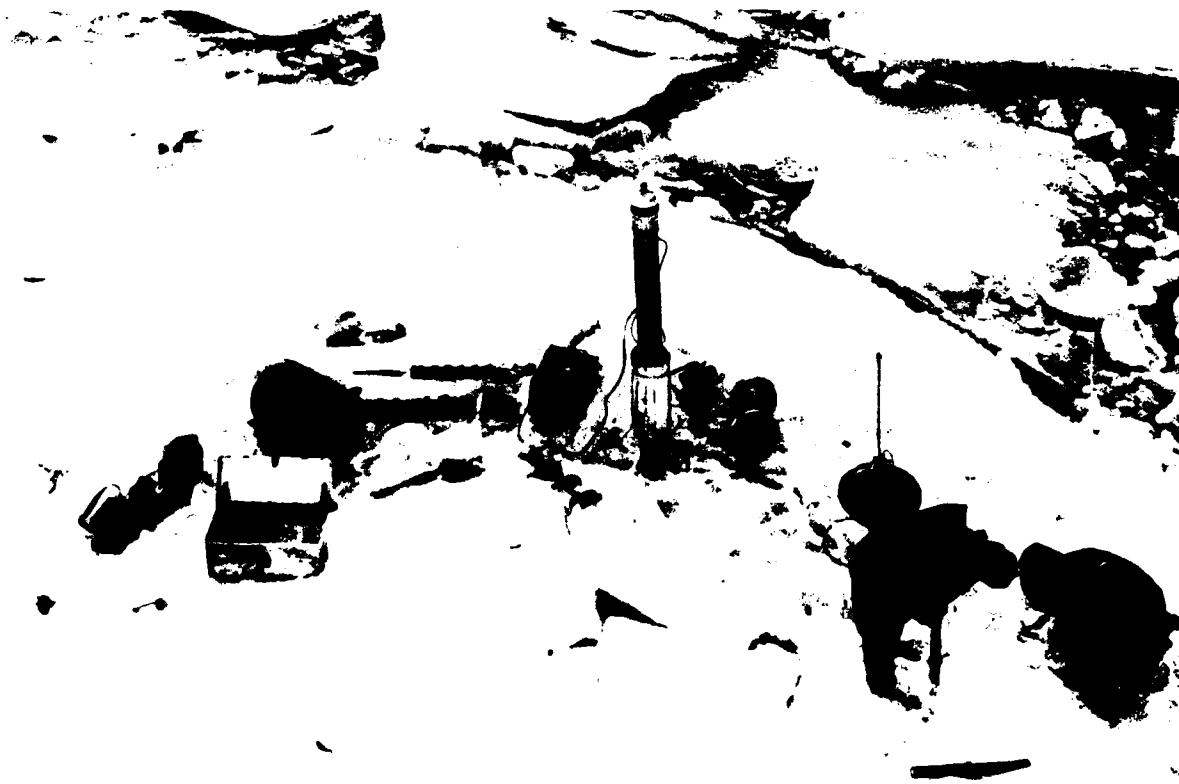


*Fig. 1. Setting up a transponder site for the drift 2 experiment. The radar transponder and Seadisc are installed, and a radar reflector is being set up. Note raised rims around ice cakes in background and rafting on experiment floe.*

**Table 1. Ice-tracking experiments conducted during MIZEX-West.**

Sequence	Date of deployment	Days of drift	Number of transponders	Supporting data
1	7 Feb	5	4	Waves, CTDs, photography, currents (fixed array)
2	17 Feb	2	2	Waves, CTDs, currents (fixed array)
3	18 Feb	1	1	Waves, CTDs, currents
4	21 Feb	2	3	Waves, CTDs, currents, ablation
5	24 Feb	1	2	Waves, CTDs, currents, laser profiles
6	25 Feb	1	2	Waves, CTDs, currents

tor vertical heave. The tracking was accomplished by manual range-bearing measurements taken off the ship's PPI display at 10- to 20-minute intervals, and by semiautomatic computer plotting using a radar image display system (RIDS) rented from Intera Technologies Ltd.

Table 1 summarizes the experiments, and lists other data sets collected during the same periods that may be relevant in interpretation.

The current data were measured by a fixed array of current meter moorings that were in place throughout the winter season in the same general region as the drift experiments (Muensch and Schumacher, 1985). The ablation data during drift 4 were obtained by E. Josberger from the underside of one of the transponder sites (Josberger and Meldrum, 1985). The laser profile was obtained by a NOAA P-3 during drift 5. The photography of drift 1 was carried out by Andrew Cowan (SPRI) using a vertical Vinten F95 70-mm camera from one of *Westwind*'s helicopters. On drifts 2-6 *Westwind* was too far from *Discoverer* to permit aerial photography.

The larger arrays (drift 1 and drift 4) were designed to measure drift and deformation in the ice edge region. The smaller arrays (drifts 2, 3, 5 and 6) were designed to study the anomalous motion of ice edge bands.

## 2. DATA PROCESSING

The raw data set used in the drift track analysis consisted of the range and bearing of the individual transponders measured from the ship's radar. Additionally, the ship's on-board computer logged the ship's coordinates calculated from the Loran-C navigation system every minute, along with winds which were sampled every 10 seconds from an anemometer on the ship's mast installed

by PMEL (Pacific Marine Environmental Laboratory).

During the first drift experiment the data were sampled at approximately 20-minute intervals using a combination of the bridge radar and the RIDS. In the shorter experiments that followed, the sampling interval was reduced to approximately 10 minutes.

When the transponder site was being tracked the position of the reflector was used if visible, but at long ranges the first or second pulse had to be tracked, necessitating a correction for the time delay. The data series was interpolated to produce a 10-minute sampling interval. The resulting time series showed some slight discontinuities, which could represent either small jerks in the floe movement or observer error. Because of the rapid range and bearing changes in this region we estimate the standard deviation in relative position as being somewhat greater than the  $\pm 25$  m found by Martin and Thorndike (1985) in the interior pack. To remove this noise contribution the data are filtered before further analysis. The algorithm used was a maximally flat, symmetric, non-recursive, low pass digital filter given by Kaiser (1979), where the half gain point was set at 40 minutes for this data set. This filtering is sufficient to smooth out the noise level of the data without seriously affecting the ice dynamics. None of the time series was long enough for operating a 35-hour tidal filter. The dominant forcing of the ice motion was the wind, which changes on a more rapid time scale than the tidal signal; hence the use of such a filter would remove the short-term ice dynamics. Values of wind response were formed by comparing 10-minute averages of the 10-second winds with the velocity vectors calculated from the differences between successive transponder positions. The shipboard anemometer was at 30 m elevation; no correction has been applied for this.

Table 2. Transponder sites for drift 1.

Transponder	Floe size (m)	Estimated thickness (m)	Snow depth (m)	Time and position of first fix
1	20 x 10	1.0	0.12	38/2140, 59°09.1'N, 172°06.8'W
2	22 x 15	0.7	0.12	38/2230, 59°11.3'N, 172°03.9'W
3	18 x 10	1.0	0.60	38/2350, 59°12.6'N, 173°01.4'W
4	25 x 20	0.9	0.12	39/0040, 59°08.5'N, 172°04.6'W

### 3. OBSERVATIONS

Throughout the discussion time is given in Julian day of the year and GMT. Local time lagged GMT by 11 hours.

#### 3.1 Drift 1

##### Chronology

The radar transponders used in the experiment were initially placed aboard *Westwind*. On Day 38 (7 February) *Westwind* carried out a helicopter survey that showed the ship to be situated in a large ice edge massif, of 9 to 10/10 cover, with dimensions 45 km in a northeast-southwest direction and 95 km in a northwest-southeast direction. The massif was separated from the main ice cover by 30 km of open water. Within the massif freezing conditions prevailed, with space between floes filled by frazil ice and slush. It was decided to deploy the first array in this massif. Four transponder sites (Table 2) were installed from the ship during the period up to 0100 GMT on Day 39. Site 1 was about 5 km from the outer ice edge. The geometry of sites 1-3 and the shape of the ice massif are as shown in Fig. 1 of Squire and Wadhams (1985).

Tracking continued from *Discoverer* through Days 39 and 40. By the end of Day 41 the wind rose to 15 m s<sup>-1</sup> from the east, and the whole pack began to move faster to the west-northwest, with much grinding and rafting of floes observed. At the beginning of Day 42 transponder 1 went onto a timing cycle. (Each transponder had external auto batteries that operated it continuously, and internal batteries that could operate it via a timing circuit.) An intermittent return on the radar screen was a warning of either a dead battery or a broken connection. *Discoverer* approached site 1 to find the equipment scattered among several floe fragments in an ice edge band only 7 km x 1.5 km in size, composed of small wave-washed cakes em-

bedded in brash and slush and with ice fragments rafted onto their surfaces. After recovery of site 1, transponder 4 also ceased transmitting and was found in a similar state. At 42/1340 transponder 2 ceased transmitting, but could not be recovered immediately because of darkness and could not later be found. Finally, transponder 3 was recovered safely on 42/2100.

It is clear that during the later stages of the drift the transponder sites were steadily moving towards the ice edge, which was being stripped away in the form of small bands. Each band had a very short lifetime once it separated from the main ice edge, since wave pounding caused the floes in it to fragment, followed by rapid melting and disintegration in the warmer surface water into which the band was moving. Thus the effect of a strong wind from this quarter is to generate rapid wind drift of floes along the ice edge, with progressive erosion of the ice edge through band separation and destruction by the wind-induced sea state.

##### Results

Fig. 2 shows the drift tracks of the four transponders. During the first part of the drift (Days 39-40) under a moderate wind, the tracks meander, with evidence of response to a rotary tidal current. When the tidal current (of order 25 cm s<sup>-1</sup>) opposes the wind stress, the array almost stops moving in a northwest direction. The baroclinic mean surface current in this region is about 5 cm s<sup>-1</sup> to the west-northwest (Muench and Schumacher, 1985), as deduced from the dynamic topography at 75 dbar, calculated from the CTD station grid. This early portion of the drift therefore shows a wind response that is superimposed on a geostrophic current in a similar direction, modified by a tidal current. From Day 41 onwards the wind increase causes the drift to become much faster and the buoy tracks straighter; clearly the wind response now dominates the tidal current.

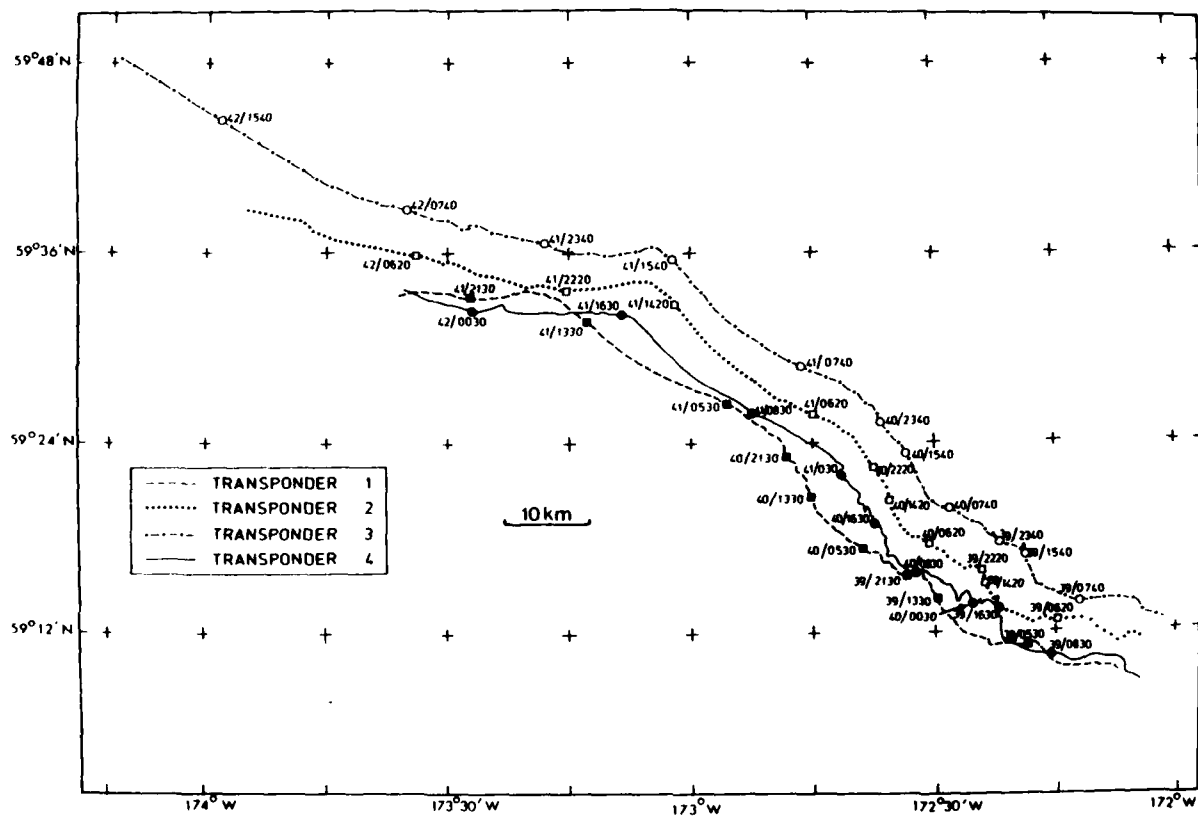


Fig. 2. Drift 1—tracks of the four radar transponders.

Fig. 3 demonstrates the relative drift and deformation by showing the array quadrilateral plotted at 4-hour intervals. During Days 39–40 most of the array (transponders 1, 3 and 4) behaves almost as a rigid body that rotates slightly so as to maintain the same aspect relative to its direction of motion. Transponder 2, however, behaves anomalously in falling behind the rest of the array. For instance, during the 48 hours from 39/0400 to 41/0400 the downstream distances made good by 1, 2, 3 and 4 respectively are 44.1 km, 36.5 km, 41.3 km and 42.1 km. There is thus some shear occurring across the ice edge region, with drift velocities declining in sequence 1 > 4 > 3. However, 2 lies to seaward of 3 yet moves significantly more slowly. From Day 41 onwards, however, this anomaly disappears. Distances made good from 41/0000 to 42/0000 are 46.5 km, 53.2 km, 44.4 km and 46.4 km for 1, 2, 3 and 4 respectively. Note that the ice is moving about twice as fast as during the previous two days and accelerates even more during the decay/recovery period.

A possible explanation of these anomalies lies in the ice roughness. A very approximate force balance, which considers only air stress and water

drag and neglects Coriolis force, internal stress, sea surface tilt and the ice velocity itself, gives in a wind  $U_w$  a steady drift  $U_d$ :

$$\rho_a C_a U_w^2 W^2 + \frac{1}{2} \rho_a h_w W C_d U_d^2 = \rho_a C_w U_d^2 W^2 + \frac{1}{2} \rho_a h_w W C_d U_d^2. \quad (1)$$

This force balance attempts to split the drag forces into skin friction drag coefficients  $C_a$ ,  $C_w$  on the ice surface and underside; and a form drag coefficient  $C_d$  for the leading edges of the floes.  $W$  is the width of the floe,  $W^2$  is assumed to be its area,  $h_w$  is its freeboard and  $h_d$  its draft. It is difficult to assign values to  $C_a$ ,  $C_w$  and  $C_d$  since all experimental values are for the total drag. However, we can try the lowest recorded values for  $C_a$  and  $C_w$  as being the likely flat plate contributions, giving

$$C_a = 1.4 \times 10^{-3} \text{ (Banke et al., 1976)}$$

$$C_w = 3.4 \times 10^{-3} \text{ (McPhee and Smith, 1973).}$$

Arya (1973) found a  $C_d$  of 0.4 for model ice sails

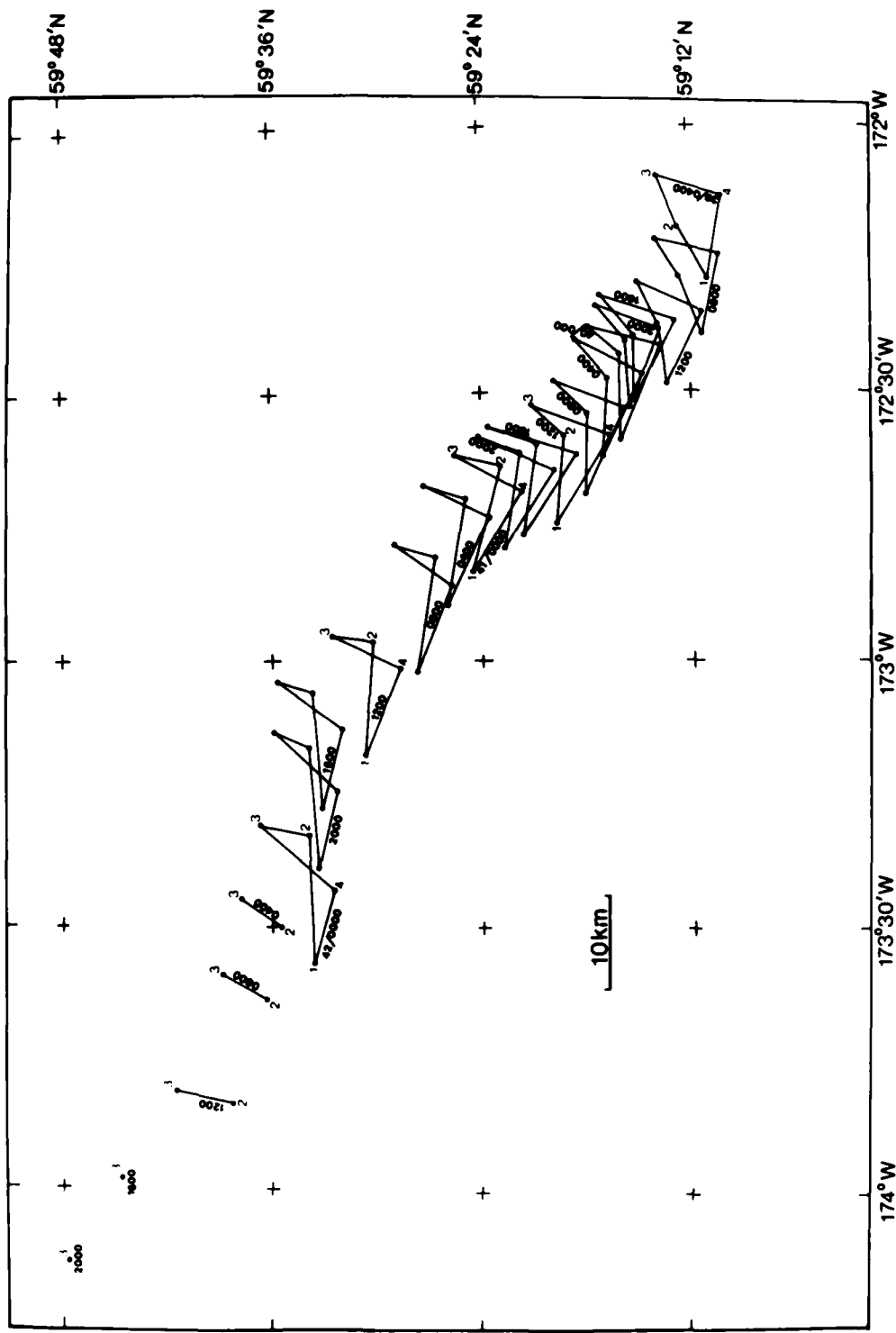


Fig. 3. Drift 1—the array plotted at 4-hourly intervals, showing deformation.

in wind tunnel experiments, which lies within the range 0.1–0.6 observed by Banke and Smith (1975) for sails in the field. Here, most of the form drag arises from floe edges (immersed or above-water) as opposed to ridges on the floe surfaces. A suitable  $C_d$  might be the 0.6 used by Weeks and Campbell (1973) for iceberg walls. In this calculation we use a  $C_d = 0.4$  and using  $\rho_w = 1025 \text{ kg m}^{-3}$  and  $\rho_s = 1.3 \text{ kg m}^{-3}$ , we obtain from eq 1:

$$\frac{U_f^2}{U_a^2} = \frac{0.00182 + 0.26(h_a/W)}{3.485 + 205(h_a/W)}. \quad (2)$$

For small floes (i.e. small height/width ratios) the disproportionate contribution of form drag is now very clear, and it is important that  $h_a$  and  $h_w$  are measured accurately in the field. If we begin by using the mean of the two floe dimensions for  $W$ , and calculate  $h_a$  and  $h_w$  by assuming that sea ice density is  $900 \text{ kg m}^{-3}$  and snow density  $300 \text{ kg m}^{-3}$ , we obtain the results shown in Table 3. Typically, small floes near the ice edge have a rim of rafted brash around their edges, which gives them a greatly increased cross section facing the wind while adding little to their draft. In the last column of Table 3 we have considered the effect

Table 3. Calculated drift speed ratios for drift 1.

Floe	W (m)	$h_a$ (m)	$h_w$ (m)	Speed ratio	Ratio with $\Delta h_a = 0.5$
1	15	0.21	0.91	0.019	0.030
2	18.5	0.17	0.65	0.020	0.032
3	17.5	0.55	1.05	0.025	0.033
4	22.5	0.20	0.82	0.019	0.030

of adding 0.5 m to the effective freeboard without increasing the draft. It is clearly dramatic. Our conclusion must be that apparent anomalies in the drift speed of floes near the ice edge may simply be due to differences in the amount of rafted material on the floes' rims, rather than to any more subtle factor. This also suggests, of course, that a floe in an advanced stage of destruction (i.e. in a disintegrating band) will move even faster as  $h_a/W$  increases due to the piling of rafted fragments onto its shrinking surface. Fig. 1 shows some typical floes with raised rims in the background, and a floe with significant rafting in the foreground.

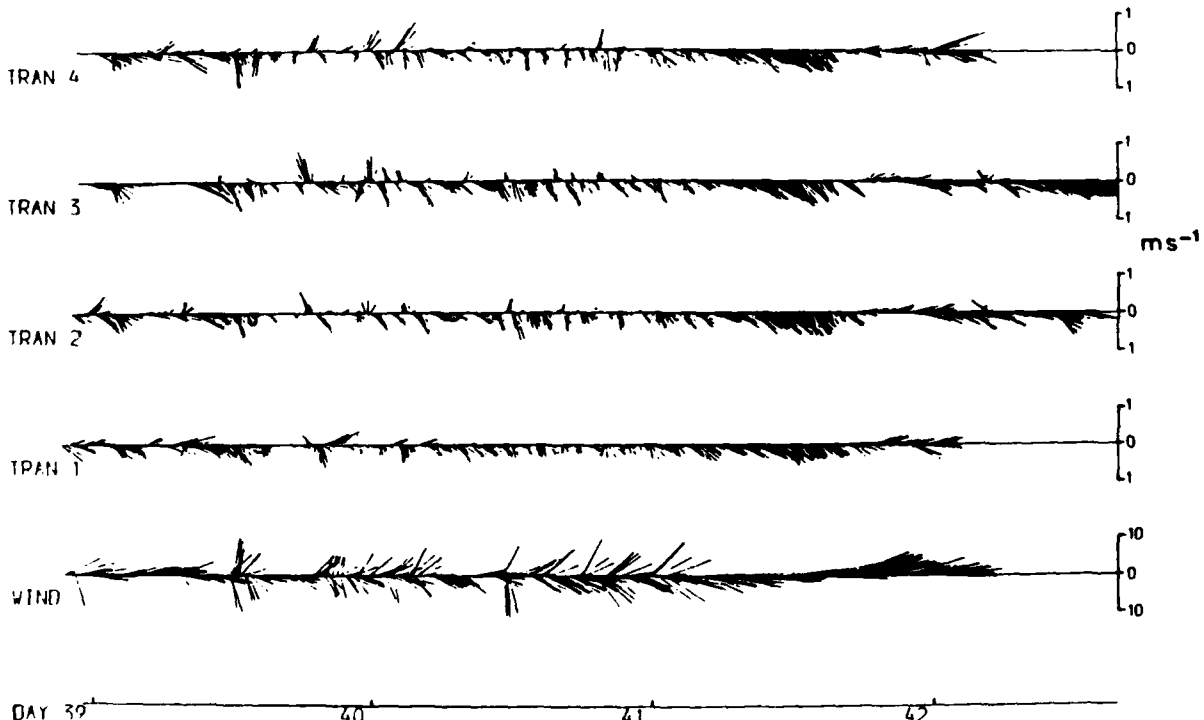


Fig. 4. Drift 1—velocities of the four transponders and wind velocity, at 10-minute intervals. Motion is towards the end of the stick that lies on the axis, with north upwards.

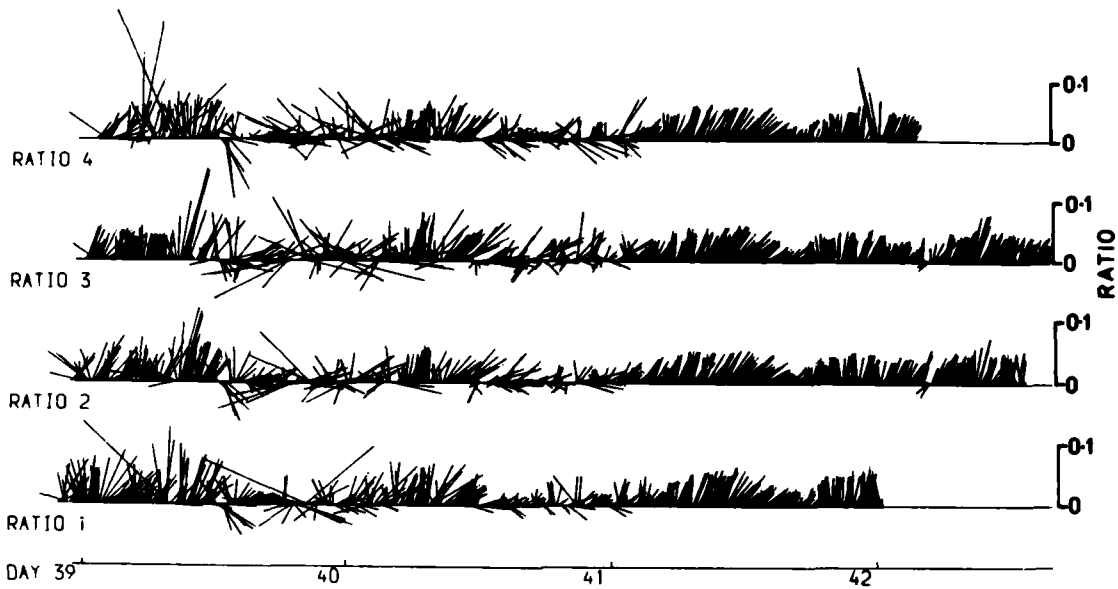


Fig. 5. Drift 1—wind response at 10-minute intervals. The length of the stick is the ratio of ice drift speed to wind speed. The orientation of the stick is the turning angle, vertical implying zero and a lean to the right implying an ice drift to the right of the wind.

Fig. 4 shows the wind velocities and the ice drift velocities of the transponders, computed from the smoothed positions at 10-minute intervals. The vectors are displayed in the meteorological sense, i.e. the wind motion and the ice motion are both directed towards the end of the stick that lies on the axis. North is upwards.

Fig. 5 shows the ratio of the drift vectors to the wind speed, and the turning angle between wind and ice. An upright stick corresponds to a zero turning angle; a stick that “leans” to the right represents ice motion to the right of the wind. Here it is very clear that at the beginning of the experiment, and from Day 41 onwards, the motion of the ice is mainly wind-driven, because of the steadiness of the ratio and turning angle, whereas during Day 40 there is much less correlation between wind and ice motion, indicating an important contribution from other factors. If we consider only the period from Day 41 until the recovery of transponder 1, we obtain the mean values for ratio and turning angle given in Table 4.

There is no significant difference between the speed ratios, nor the turning angles, with the possible exception of transponder 4. The ice moves to the right of the wind. The ratios are higher than those computed in the simple calculation, but this is to be expected since the equation ignores many forces and is merely meant as an exploration of the form drag effect.

### 3.2 Drift 2

#### Chronology

Early on Day 48 (17 February), a few hours after a NOAA P-3 overflight, *Discoverer* deployed a transponder in close pack, as far in from the ice edge as the ship could reach. A strong wind ( $18 \text{ m s}^{-1}$ ) was blowing from the northeast, and it was hoped that the transponder would trace the motion of a newly separating band. At the place of deployment a number of narrow parallel leads, a few hundred meters apart, were seen running perpendicular to the wind direction, but no bands as such. The chosen floe was small in diameter (9 m) but lay high out of the water and was more than 1 m thick, being composed of a “floe sandwich” of two or more rafted layers with additional rafting on top. The floe is shown in Fig. 1.

Table 4. Mean speed ratios and turning angles for drift 1.

Transponder	Speed ratio	Turning angle
1	$0.0402 \pm 0.0015$	$25.7 \pm 3.4^\circ$
2	$0.0383 \pm 0.0020$	$33.4 \pm 4.8^\circ$
3	$0.0391 \pm 0.0018$	$29.4 \pm 3.6^\circ$
4	$0.0429 \pm 0.0023$	$38.6 \pm 4.3^\circ$

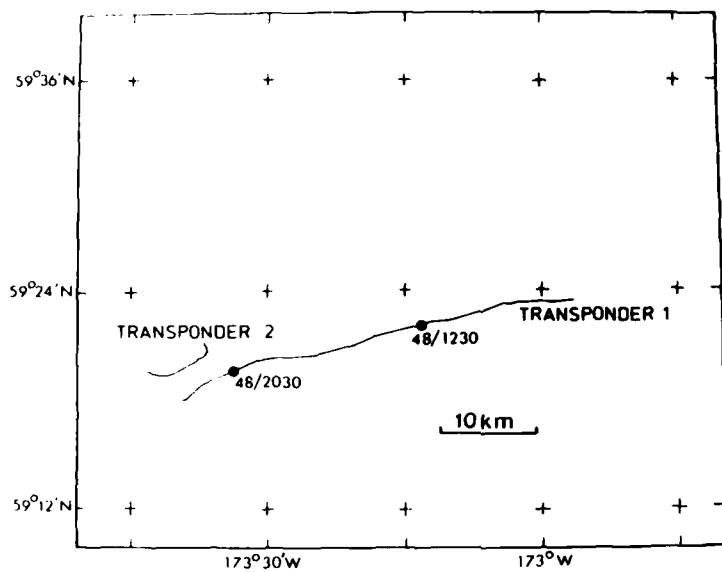


Fig. 6. Drift 2—radar transponder tracks.

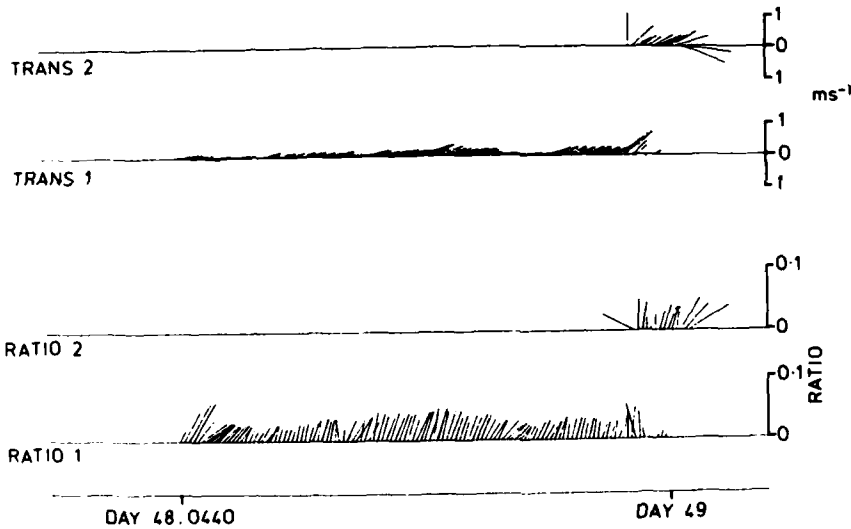


Fig. 7. Drift 2—transponder velocities and wind response.

Tracking continued overnight. Morning revealed that the transponder lay in a narrow (300–500 m) ice band of length about 15 km, completely separated from the main pack, with its long axis perpendicular to the wind. Ice in the band consisted of small, awash, wave-swept rafted cakes. A second (NOAA) radar transponder was deployed in the band, to measure relative motion within the band, but after a short period recovery was necessary because of damage to the equipment as the band completely disintegrated. Surface water tem-

perature as the ice crossed the frontal region had risen to 0.65°C.

#### Results

Fig. 6 shows the drift tracks of transponders 1 and 2. Fig. 7 shows the drift velocities measured between 10-minute positions, and the ratio of drift vectors to the wind. It is clear that the motion is almost a free wind-driven drift, with almost a constant speed ratio and turning angle, which display only a mild modulation due presumably to a tidal

current. The 105 values for speed ratio and turning angle calculated from 17½ hours of motion of transponder 1 before deployment of transponder 2 give the following averages:

Speed ratio  $0.0432 \pm 0.0011$

Turning angle  $23.1^\circ \pm 1.1^\circ$ .

These values are consistent with those of the wind-driven phase of drift 1.

Only 1½ hours of concurrent data were obtained from transponders 1 and 2. Mean wind responses during this period were:

Transponder 1: speed ratio  $0.027 \pm 0.010$ ,  
turning angle  $23 \pm 13^\circ$

Transponder 2: speed ratio  $0.045 \pm 0.007$ ,  
turning angle  $-12^\circ \pm 12^\circ$ .

Clearly, transponder 2 was moving in an anomalous direction, to the left of the wind, indicating strong relative motion within the band. However the joint data set is too short to permit further conclusions.

### 3.3 Drift 3

#### Chronology

A radar transponder was deployed at 49/2300 (18 February) and tracked for 6½ hours until 50/0530. On this day both the NOAA P-3 and the NASA Convair 990 made overflights, and revealed that *Discoverer* lay in a wide band that was over 30 km from the main ice edge, and with no other bands to seaward. Since we had crossed several bands during the previous night to reach this position, it was clear that band disintegration and destruction were proceeding at a rapid rate. The experimental floe was larger than usual (50 m diameter) and 90 cm thick. The transponder was recovered before nightfall to avoid destruction.

#### Results

Fig. 8 shows the relatively simple drift track of the floe. Fig. 9 shows the drift velocities and the velocity ratios. Once again a consistent wind response is seen, with average values of

Speed ratio  $0.0470 \pm 0.0018$

Turning angle  $25.3^\circ \pm 1.9^\circ$ .

The speed ratio is somewhat higher than for drifts 1 and 2, and we suspect the additional driving force of wave radiation pressure may be significant here (Wadhams, 1983). Wave energy was measured concurrently by a Seadisc, and in a forthcoming publication we will analyze the drift more closely in terms of the wave spectrum.

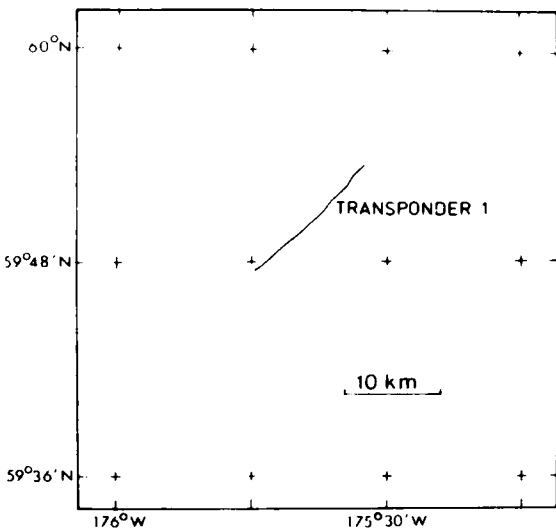


Fig. 8. Drift 3—transponder track.

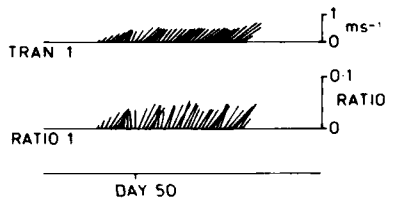


Fig. 9. Drift 3—transponder velocity and wind response.

### 3.4 Drift 4

#### Chronology

On Day 52 (21 Feb) a transponder was deployed on a large, thick floe (28 m  $\times$  20 m), which was also extensively instrumented with a Seadisc, ablation sensors (Josberger and Meldrum, 1985), and a current meter and temperature sensor 2.5 m below the ice. The floe (site 1) had a mean thickness of 132 cm (from 37 measurements). The floe bottom was quite rough, as observed by divers from *Discoverer*, with rafted layers underneath yielding a maximum thickness of 305 cm. The upper surface was, however, smooth. Fig. 10 shows the thickness contours of the floe, which was drilled at 10-ft intervals on a square grid (by D. Egging and W. Culton of Exxon Research). A rafted cake underlying one corner increased the thickness abruptly from 1 m to more than 2 m. The ice pack had a  $\frac{1}{10}$  cover with apparently random open water

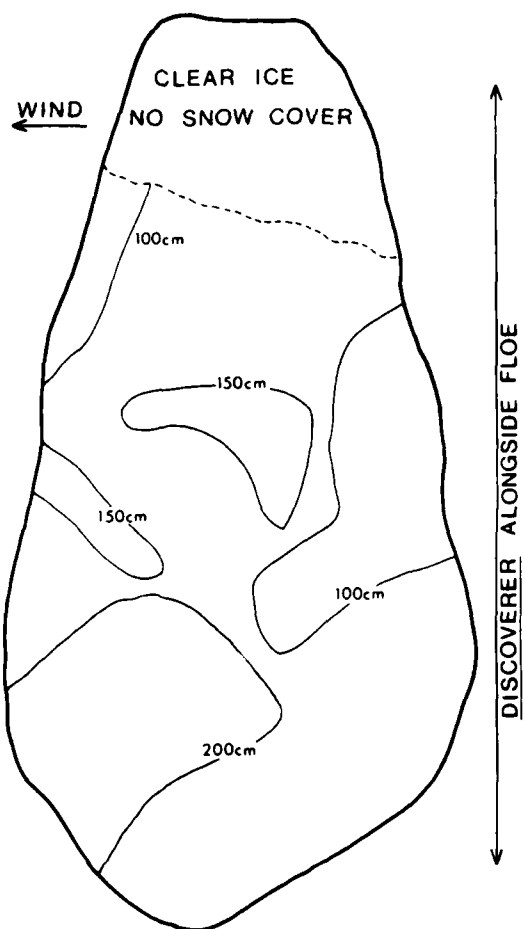


Fig. 10. Drift 4—thickness contours for the floe used for transponder 1. The abrupt transition to 2 m + thickness in the bottom left corner is due to an ice cake completely rafted under the floe, according to a diver's report.

spaces and no organization into bands. Two more transponders were set out on floes nearby. The general nature of the ice edge region was given by the CV 990 imagery (Cavalieri et al., 1985).

Tracking continued through the following day, during which, as in all previous drifts, the array moved seaward under an off-ice wind and the sea surface temperature rose to  $0.3^{\circ}\text{C}$  after the ice edge front was crossed. Transponder 3 was found to be in a band surrounded by rotting floes, so was recovered (53/0330) and redeployed (53/0550) close to transponder 1, and in the same band as transponder 1 was now embedded in. Tracking then continued through the night. Transponder 1 was recovered next morning, its floe being on the edge of a band and in an advanced state of destruction by waves. Transponder 3 was now in a

separate band, a distance of 5 km away from transponder 1 (0.9 km at installation). The two bands were connected by only a narrow, discontinuous ice streamer, whereas the previous evening the two sites were on a single coherent band. Finally, transponder 2 was recovered from a disintegrating floe.

#### Results

Fig. 11 shows the drift tracks of the transponders, "transponder 4" being the track of transponder 3 after repositioning close to transponder 1. Fig. 12 shows the array polygons at 4-hourly intervals. Transponder 1 was moving faster than nearby transponder 2 despite originally being positioned further into the pack ice. Before 3 is repositioned it can be seen that the array is deforming, with 3 moving relatively to the southward, a possible consequence of the effect described by Overland et al. (1983), whereby an off-ice wind increases in velocity in the vicinity of the ice edge when a stable atmospheric boundary layer is present. In the latter stages of the drift, 1 moves relatively faster southward, while the gap between 1 and 4 opens. The overall pattern is of an elongation in the downwind direction, with the floe that is currently furthest to the south moving fastest. Fig. 13 shows the extent of this elongation; transponders 2 and 3 are separating at a steady rate of  $11.3 \text{ cm s}^{-1}$  during the interval plotted.

Fig. 14 shows the floe velocities and the wind vectors measured at the ship. The wind slowly increases during the experiment (the ship stayed in the middle of the array) but remains in the same direction. The floe velocities appear to be strongly modulated by the tidal current. The modulation, at a 12-hour period, is also clearly seen in Fig. 15, which shows the ratios of ice to wind velocities. By averaging over several tidal cycles, we can compute mean wind responses of the floes as shown in Table 5.

Floes 1 and 2 respond with identical speed ratios to the wind, but 2 moves further to the right than 1, an effect which when integrated over the whole drift produces the position changes shown in Fig. 11. Floe 3 moves faster than 1 or 2, although with the same turning angle, while floe 4 also moves fast but with a much smaller turning angle. During the shorter drift of floe 4 (16 hours) the tidal signal may be causing the low turning angle, but it is more likely that wave radiation pressure or even the unbalanced orientation of form drag features on the floe's surface can account for the radically different drift direction.

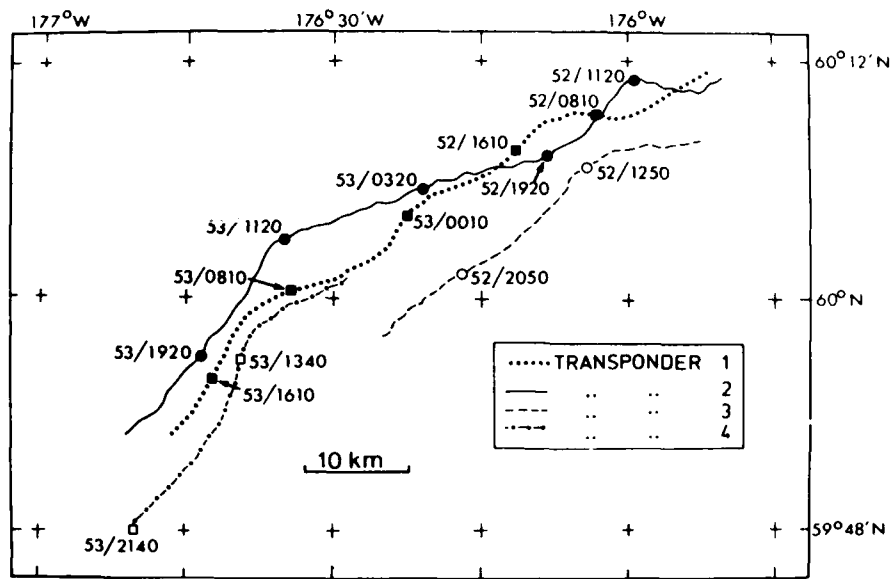


Fig. 11. Drift 4—transponder tracks. The track listed as “transponder 4” is transponder 3 after repositioning.

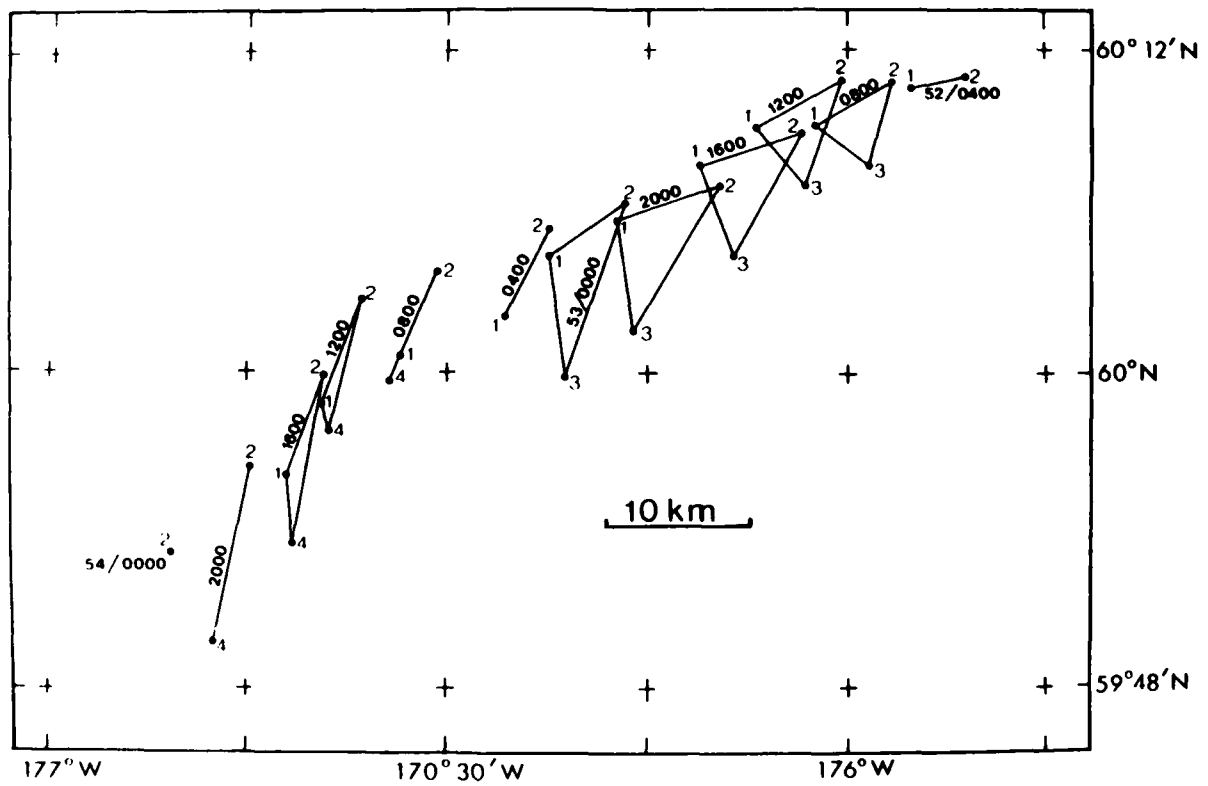


Fig. 12. Drift 4—the array plotted at 4-hourly intervals.

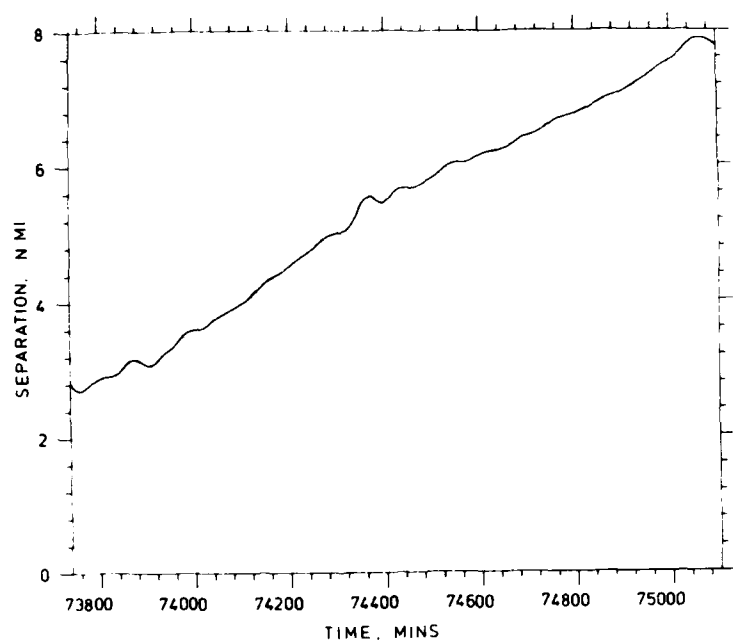


Fig. 13. Drift 4—separation between transponders 2 and 3. Horizontal scale is minutes since beginning of year.

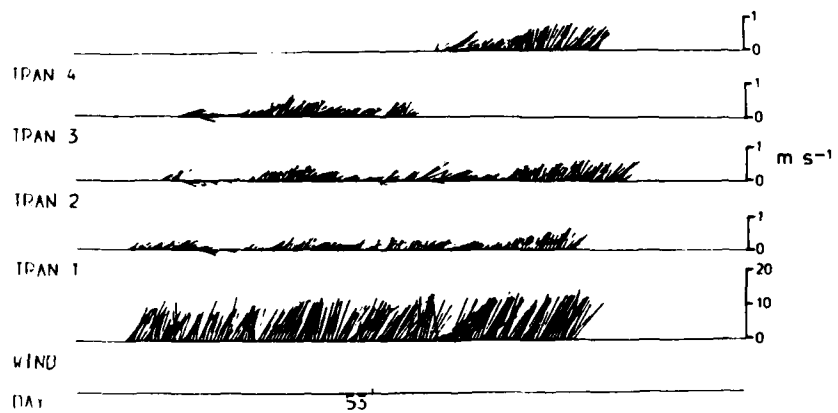


Fig. 14. Drift 4—transponder velocities and wind velocity.

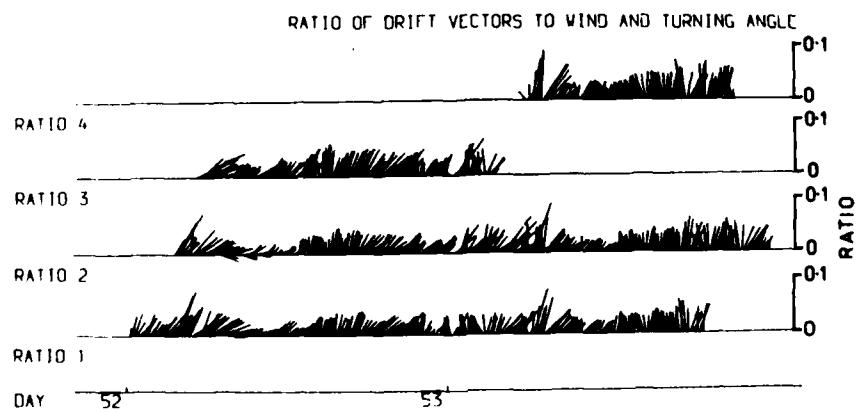


Fig. 15. Drift 4—wind response.

**Table 5. Mean speed ratios and turning angles for drift 4.**

Transponder	Speed ratio	Turning angle
1	$0.0359 \pm 0.007$	$29.1 \pm 1.6^\circ$
2	$0.0361 \pm 0.007$	$34.1 \pm 1.6^\circ$
3	$0.0412 \pm 0.010$	$31.5 \pm 2.2^\circ$
4	$0.0414 \pm 0.011$	$6.9 \pm 2.6^\circ$

### 3.5 Drift 5

#### Chronology

At the beginning of Day 55 (24 Feb) the NOAA P-3 flew over *Discoverer*, finding that the ship lay in the centre of a series of bands. The ship entered a band composed of large floes that were subject to linear rafting features that resembled pressure ridges except that they involved a single thickness of floe. Two transponders were deployed in the same band, with an initial separation of 2.8 km. Each floe was drilled through, giving thicknesses of 99 cm and 73 cm for sites 1 and 2. Tracking continued through the night, during which the two floes moved closer together. The two transponders were recovered the next day. Site 2 was still on its original floe, which had, however, split during the night and was now 60 m from the edge of the band

instead of being near the band centre. Transponder 1 was floating in slush and brash at the edge of the band. (In this experiment we mounted Vega transponders belonging to NOAA on a buoy constructed of a cable reel and plastic floats, so that in the event of a floe breakup the transponder would safely float away.)

#### Results

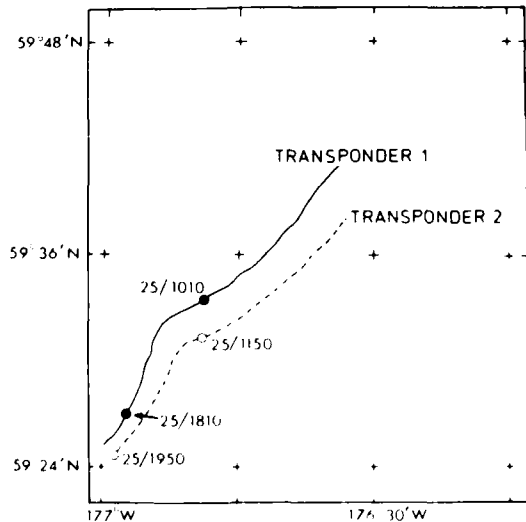
Fig. 16 shows the drift tracks of the transponders, with their steady convergence and a looped motion indicating a response to the tidal current. The convergence is shown more clearly by Fig. 17, which shows the separation of the transponders at 4-hourly intervals, and Fig. 18, which shows the distance between the transponders. The mean velocity of approach over the period of the experiment was  $4.8 \text{ cm s}^{-1}$ .

Fig. 19 shows the wind and ice velocity vectors of the transponders and their wind response. A calculation based on the 15 hours, 40 minutes during which the two transponders were deployed simultaneously yields the following values for the mean wind response:

Transponder 1: speed ratio  $0.0371 \pm 0.0009$ , turning angle  $11.8^\circ \pm 2.3^\circ$

Transponder 2: speed ratio  $0.0361 \pm 0.0011$ , turning angle  $16.5^\circ \pm 2.0^\circ$ .

It can be seen that the relative motion of the two transponders is due more to a difference in turning angle than to any difference in speed ratio.



**Fig. 16. Drift 5—transponder tracks.**

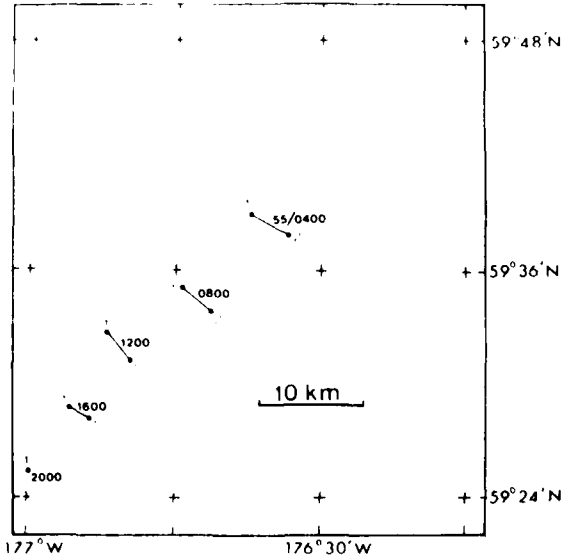


**Fig. 17. Drift 5—transponder positions plotted at 4-hourly intervals.**

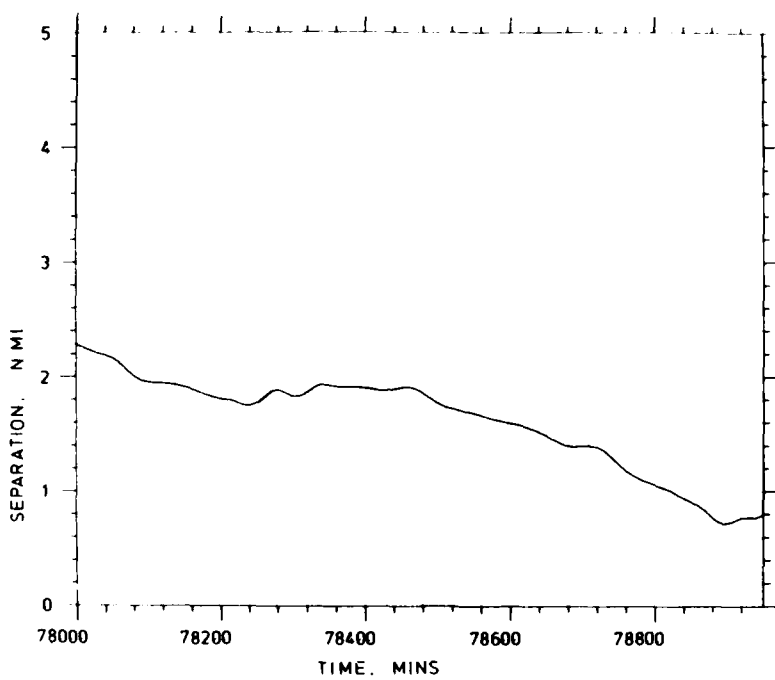


Fig. 18. Drift 5—separation between the transponders.

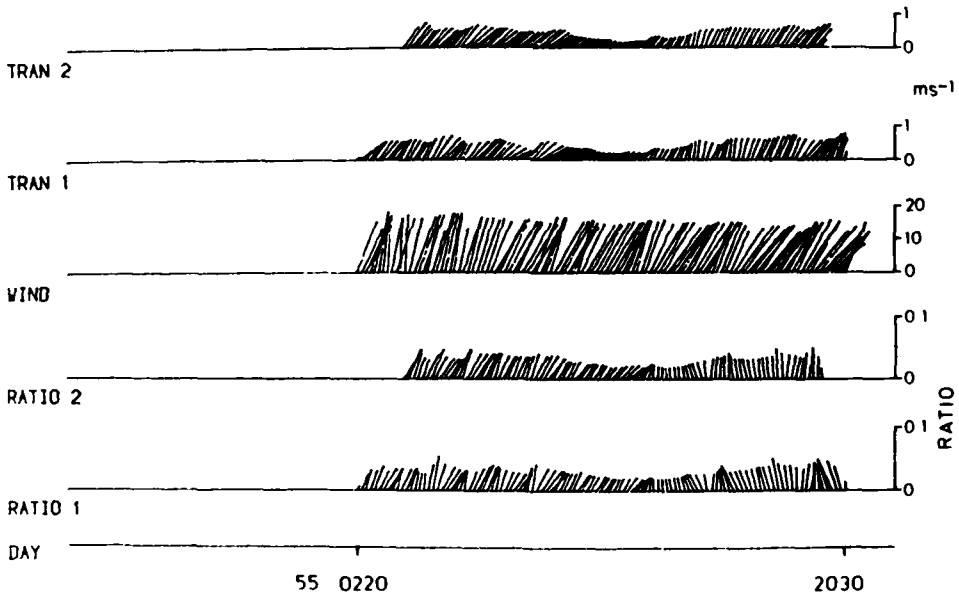


Fig. 19. Drift 5—transponder and wind velocities, and wind response.

### 3.6 Drift 6

#### Chronology

On Day 56 (25 Feb) *Discoverer* again sailed as deeply into the ice as possible, passing several bands. She deployed a NOAA transponder and a Seadisc on a floe, which was also cored (thickness

43 cm), then a second transponder about 2.8 km away in the same band (106 cm thick). The band had dimensions of about 9 km by 0.9 km, with a regularly scalloped edge of wavelength about 0.9 km. Tracking continued overnight, and the transponders were recovered the next day, transponder 1 being found in a small streamer that was separat-

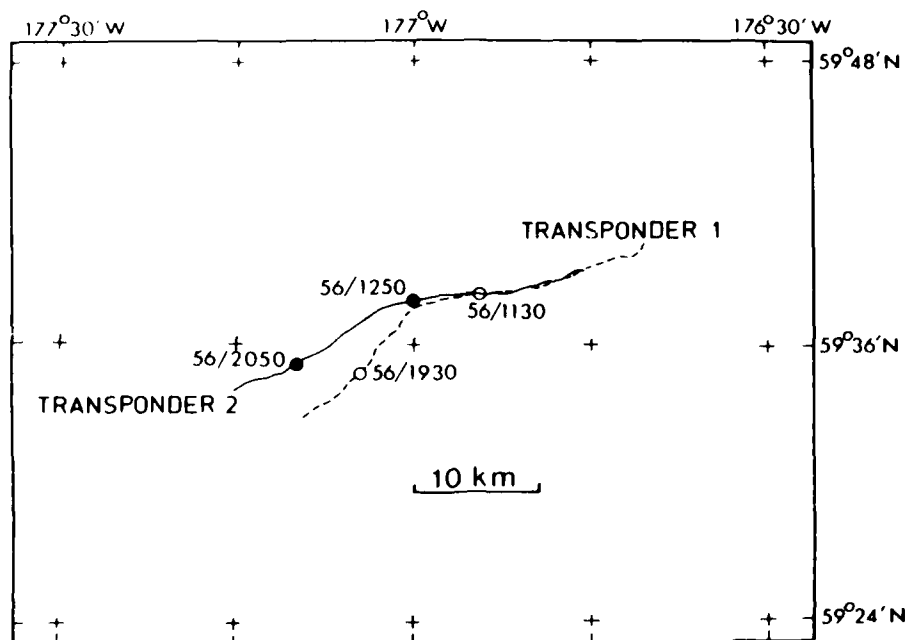


Fig. 20. Drift 6—transponder tracks.

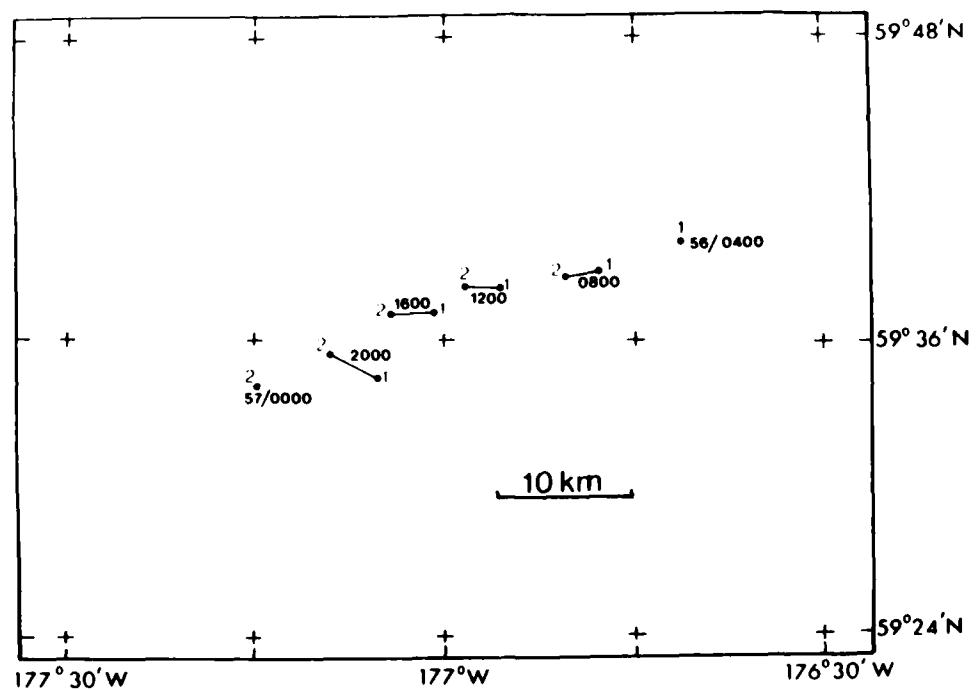


Fig. 21. Drift 6—transponder positions plotted at 4-hourly intervals.

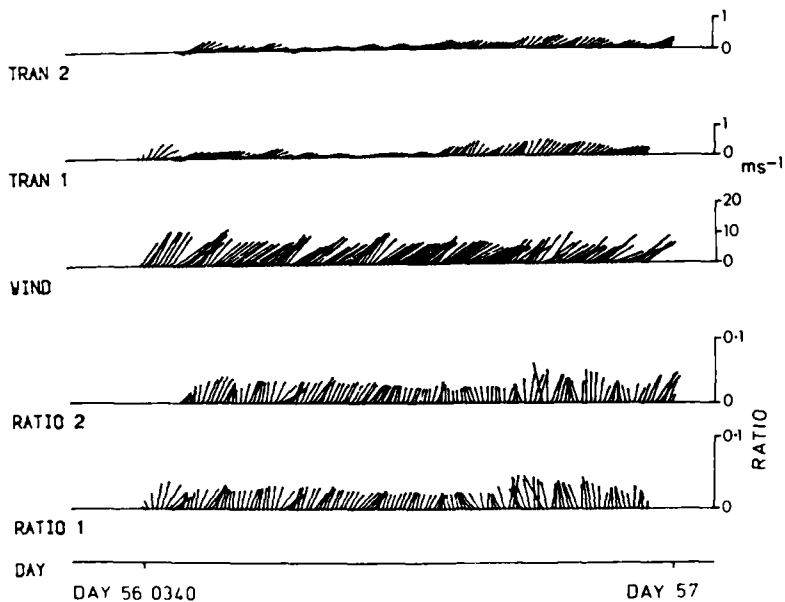


Fig. 22. Drift 6—transponder and wind velocities, and wind response.

ing from the band. After recovery a wave experiment was carried out, with wave buoys deployed upwind and downwind of the band. Results will be reported in a future paper.

#### Results

Fig. 20 and 21 show the drift tracks of the transponders and the deformation of the line joining them. Unlike drift 5, the two transponders moved further apart during the experiment, though their relative orientation varied. Fig. 22 shows the wind and ice velocity vectors and the wind response. The wind was strong and comparatively steady from the northeast, the "normal" quarter for most of these experiments. The drift velocities appear to have passed through about one cycle of modulation by the tidal current. Again, averaging over the whole period when the transponders were simultaneously deployed (18 hours, 20 minutes) yields the following mean response factors:

Transponder 1: speed ratio  $0.0392 \pm 0.0009$ ,  
turning angle  $8.2^\circ \pm 2.0^\circ$

Transponder 2: speed ratio  $0.0372 \pm 0.0010$ ,  
turning angle  $15.8^\circ \pm 1.6^\circ$ .

The speed ratios agree quite well with those of drift 5, but as in the case of drift 5 a difference in turning angle is the cause of the relative motion of the floes, in this case moving them apart rather than together.

#### 4. DISCUSSION

If we combine the wind responses of all the experiments (neglecting the last part of drift 2, with its high variance), we obtain the results shown in Fig. 23. The speed ratios are remarkably consistent over all the experiments, and a best value based on the unweighted mean of the 14 transponder drifts is  $0.0396 \pm 0.0009$ . This is in good agreement with results from the pack interior (Reynolds and Pease, 1985). The turning angles, however, appear to fall into two well-defined groups, one set (group 1) in the region of  $23\text{--}28^\circ$ , the other (group 2) in the range  $7\text{--}16^\circ$ . Examination of the drift tracks shows that the group 2 drifts have in common the fact that the major part of each drift lies to the west of  $176^\circ 30' \text{W}$ , whereas the group 1 drifts lie to the east of this. It is possible that the westerly experiments took place in a region with a lower mean current to the northwest. A current to the northwest is equivalent to an additional force to the right of the wind, so that a reduction in the current would result in a reduction in turning angle. CTD stations taken during drifts 5 and 6 found warmer surface water ( $0.5\text{--}1.0^\circ \text{C}$ ) and reduced stratification, indicating that the "bulge" in the ice edge that allowed drifts 5 and 6 to be done so far to the southwest corresponded to an excursion of the ice outside the main

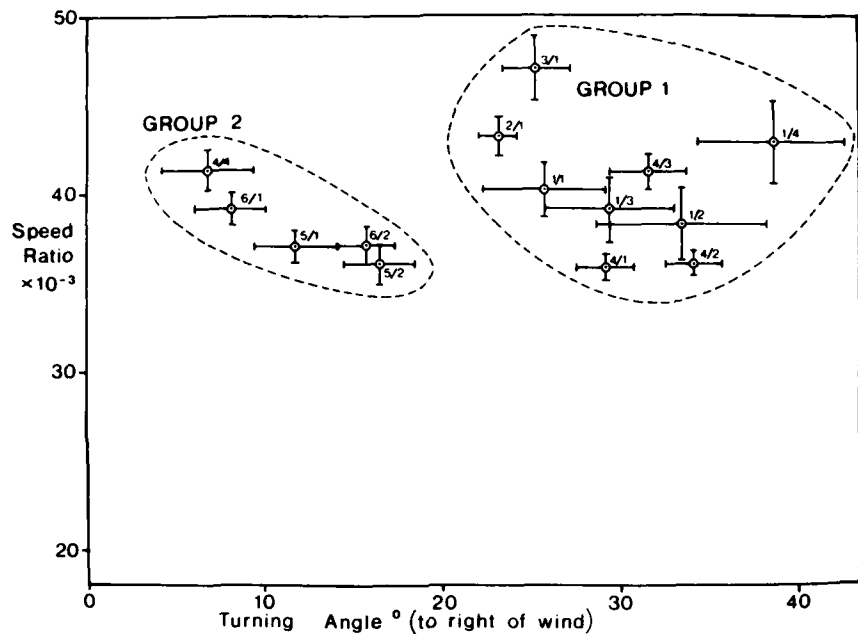


Fig. 23. Plot of average wind response computed from each drift track.  
Labels are experiment number followed by transponder number.

frontal region. This would result in a reduced geostrophic current. Against this should be set the fact that drifts 5 and 6 took place nearer to the shelf break than drifts 1-4, so that the barotropic slope current should be higher.

Variations between turning angles and speed ratios within a single experiment are probably due to variations in ice roughness, which have a disproportionately large effect on small rafted floes on account of the relatively small contribution by skin friction drag.

The experiments in which two transponders were deployed on a single band provide interesting data on relative ice motion within bands. A full analysis of these motions, together with the ice deformation data obtained from the larger arrays, will be presented in a future paper.

#### ACKNOWLEDGMENTS

The party involved in deploying and tracking transponders comprised Dr. P. Wadhams, S.P. O'Farrell, R. Massom (SPRI), G. Rahmani (Calgary, Canada), Dr. R. Bhavarahan (Intera Technologies, Calgary) and D.T. Meldrum (Scottish Marine Biological Association, Oban) aboard *Discoverer* and Dr. V.A. Squire, A.M. Cowan and S.C. Moore (SPRI) aboard *Westwind*. We are grateful to the Office of Naval Research for finan-

cial support under Contract N00014-83-G-0008, and also to the Natural Environment Council of Great Britain and the British Petroleum Co.

#### REFERENCES

- Arya, S.P.S., Contribution of form drag on pressure ridges to the air stress on Arctic sea ice, *J. Geophys. Res.*, 78(30), 7092-7099, 1973.
- Banke, E.G. and S.D. Smith, Measurement of form drag on ice ridges, *AIDJEX Bulletin* 28, 21-28, 1975.
- Banke, E.G., S.D. Smith, and R.J. Anderson, Recent measurements of wind stress on Arctic sea ice, *J. Fish. Res. Bd. Canada*, 33, 2307-2317, 1976.
- Cavalieri, D.J., P. Gloersen and T.T. Wilheit, NASA CV-990 aircraft observations during MIZEX-West, *MIZEX Bulletin VI*, USA Cold Regions Research and Engineering Laboratory, Special Report 85-6, pp. 90-96, 1985.
- Josberger, E.G. and D. Meldrum, Bottom ablation measurements and heat transfer coefficients from MIZEX-West, February 1983, *MIZEX Bulletin VI*, USA Cold Regions Research and Engineering Laboratory, Special Report 85-6, pp. 68-72, 1985.
- Kaiser, J.F., Design for symmetric FIR low pass digital filters with maximally flat pass and stop

bands, in *Programs for Digital Signal Processing*, IEEE Press, 1979.

**McPhee, M.G. and J.D. Smith**, Measurements of the turbulent boundary layer under pack ice, *AID-JEX Bulletin* 29, 49-92, 1973.

**Martin, S., P. Kauffman and C. Parkinson**, The movement and decay of ice edge bands in the winter Bering Sea, *J. Geophys. Res.*, 88(C5), 2803-2812, 1983.

**Martin, S. and A.S. Thorndike**, Ice dispersion in the Bering Sea marginal ice zone. *MIZEX Bulletin VI*, USA Cold Regions Research and Engineering Laboratory, Special Report 85-6, pp. 38-49, 1985.

**Muench, R.D. and J.D. Schumacher**, On the Bering Sea ice edge front, *J. Geophys. Res.*, 1985 (in press).

**Overland, J.E., R.M. Reynolds and C.H. Pease**, A model of the atmospheric boundary layer over the marginal ice zone, *J. Geophys. Res.*, 88(C5), 2836-2840, 1983.

**Reynolds, R.M. and C.H. Pease**, Regional ice drift during MIZEX-West, *MIZEX Bulletin VI*, USA Cold Regions Research and Engineering Laboratory, Special Report 85-6, pp. 31-37, 1985.

**Squire, V.A. and P. Wadhams**, Some wave attenuation results from MIZEX-West, *MIZEX Bulletin VI*, USA Cold Regions Research and Engineering Laboratory, Special Report 85-6, pp. 73-78, 1985.

**Wadhams, P.**, A mechanism for the formation of ice edge bands. *J. Geophys. Res.*, 88(C5), 2813-2818, 1983.

**Weeks, W.F. and W.J. Campbell**, Icebergs as a freshwater source: An appraisal, *J. Glaciol.*, 12, 207-233, 1973.

## Bottom Ablation Measurements and Heat Transfer Coefficients from MIZEX-West, February 1983

EDWARD G. JOSBERGER

*Ice Dynamics Project, United States Geological Survey  
University of Puget Sound, Tacoma, Washington 98416, USA*

DAVID MELDRUM

*Scottish Marine Biological Association  
P.O. Box 3, Oban, Argyll PA34 4AD, Scotland*

### ABSTRACT

During the Bering Sea Marginal Ice Zone Experiment an acoustic and a mechanical ablation gauge measured the bottom ablation of an ice floe near the extreme ice edge for a 48-hour period. Both instruments gave nearly identical results: the melt rate was initially  $7 \text{ mm hr}^{-1}$  and increased to  $28 \text{ mm hr}^{-1}$ . Concurrent measurements of relative ice-water speed and temperature by a current meter suspended 2.5 m below the ice showed that the increased melt rate resulted from an increase in the water temperature and an increase in the relative ice-water speed. The bulk heat transfer coefficient, calculated from the ablation and hourly averaged current meter measurements, remained nearly constant with an average value of  $8 \times 10^{-4}$ .

### INTRODUCTION

Bottom ablation is the fundamental physical process that determines the ice edge position in the Bering Sea marginal ice zone. Overland and Pease (1982) described the sea-ice system as an ice "conveyor belt." Strong northeasterly winds form polynyas on the lee sides of the northern landmasses. The same winds transport the ice towards the ice edge. At the ice edge, the ice is blown out into relatively warm water where it rapidly melts. Bauer and Martin (1980) estimated melt rates of the order of  $1 \text{ m day}^{-1}$ ; however, no detailed observations of the melt rate were made. Josberger (1983) and McPhee (1983) both undertook a theoretical investigation of sea ice melting as a result of the upward oceanic heat flux, but these results lacked observations with which they could be compared.

This paper presents the results of a bottom ablation study performed during MIZEX-West in February 1983. This experiment successfully measured the bottom ablation of an ice floe at the extreme ice edge with an acoustic melt gauge and a mechanical melt gauge.

### THE EXPERIMENT

The experiment took place in the Bering Sea from 20 to 23 February 1983, with equipment deployed from the NOAA ship *Discoverer*. The equipment was placed on a floe that was roughly oval in shape; the major dimension was approximately 38 m and the minor dimension was approximately 20 m. The floe was approximately 30 km from the ice edge at the time of instrument deployment. A sketch map of the floe is given as Fig. 10 in Wadhams and O'Farrell (1985). As a result of strong winds (25 to 30  $\text{km hr}^{-1}$  from 020° true) this floe moved with adjacent floes to the southwest until it reached the edge two days later, and it was near complete destruction when the instrumentation was recovered. During the later part of its drift, the floe became incorporated into a band that broke away from the main portion of the pack.

The acoustic melt gauge determined the bottom ablation by sonically measuring the distance from a transducer deployed under the ice to the ice above. The transducer was on a mast that was deployed through an 8-in. (20-cm) auger hole in the ice; a 1-m-long arm projecting horizontally from the mast held the transducer away from the auger hole. The mast was securely fastened to the electronics box on the upper surface of the ice. Because the air temperature was approximately  $-15^\circ\text{C}$  the

box did not melt into the ice; hence, the transducer remained fixed relative to the ice, yielding accurate measurements of the bottom ablation. A timer turned the device on once an hour for 5 minutes; the power requirements of the system required this short duty cycle.

In addition, a mechanical melt gauge measured the ablation in a less precise manner. This gauge consisted of eight spring-loaded magnetic reed switches and an event recorder. Eight 2-in.-diameter (5-cm) holes were bored to various depths into the ice and a switch was placed into each hole, compressing the spring-loaded switch against the bottom of the hole. When the bottom of the ice melted back to the level of the borehole the switch closed and the event was recorded. The time between events and the vertical distance between the switches then gave an approximation of the melt rate.

Other instrumentation at the ablation site included a current meter, a thermistor to measure the ice temperature, and an anemometer. The current meter was an Interocean savonius rotor type that also measured temperature; it was deployed 2.55 m below the ice, 3 m away from the sonic melt gauge. The thermistor was located 1 m from the sonic melt gauge, in a borehole 0.8 m deep. The anemometer measured only the wind speed, as it lacked a compass, and the air temperature 2 m above the ice. These meteorological data will not be discussed here, as the primary focus of this paper is the bottom ablation and its relation to oceanic parameters.

## RESULTS

Fig. 1 summarizes the bottom ablation measurements from both instruments as a function of time. Both instruments show the same melt characteristics; for the first 24 hours the ablation was small, approximately 0.1 m, while during the second period the ablation was greater than 0.5 m. Hence in two days the ice thinned from 1.7 m to near 1 m, with the majority of the ablation occurring during the last day.

Upon recovery, the record from the sonic device suggested that the instrument did not function properly. Each hourly 5-minute record had a similar shape, and the results shown in Fig. 1 were obtained by taking the maximum reading from each record. The agreement between the sonic melt gauge and the mechanical device confirms that the instrument functioned correctly during a short period of the on-duty cycle. The scatter in the data

Table 1. Melt rates.

	Melt rate (mm hr <sup>-1</sup> )	$r^2$
Section I	2.55	0.96
Section II	7.30	0.98
Section III	28.38	0.96

primarily results from the mast being moved by the current moving past it and by rocking motions of the ice floe. This latter cause probably accounts for the large scatter towards the end of the record. At this time the floe was part of an ice band that had broken away from the ice pack and it was subject to considerable wave action. Also, the floe size had decreased to approximately half its original dimensions, increasing its response to the incident waves.

Of real interest is not the distance as shown in Fig. 1, but its time rate of change, the melt rate. Because the scatter in the data precludes taking the difference between consecutive measurements to give the melt rates, we arbitrarily divided the data into three sections and used a least-squares straight line fit to the data; the resultant slopes then give the melt rates. Table 1 gives the melt rates and the "goodness" of each fit,  $r^2$ .

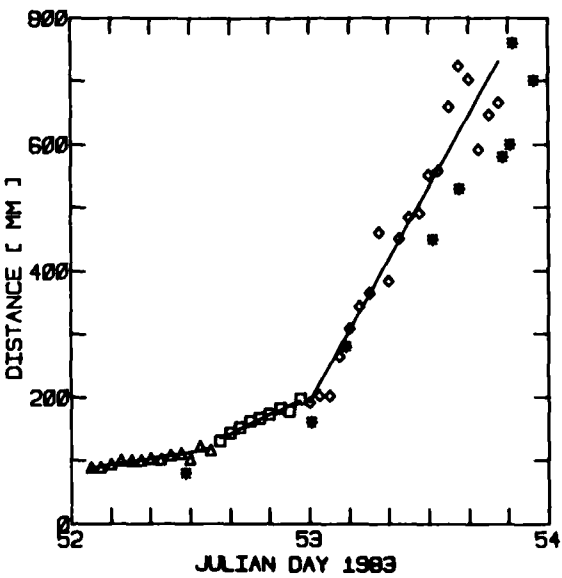


Fig. 1. Distance to the bottom of the ice. The acoustic data were divided into three groups (denoted by the triangles, squares and diamonds); the straight line through each group is the least-squares fit. The asterisks are the data from the mechanical melt gauge.

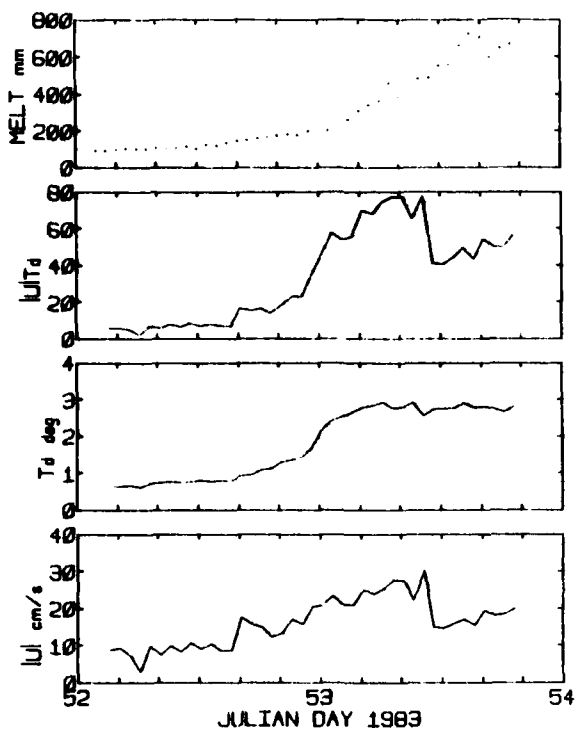


Fig. 2. Data from the current meter suspended 2.55 m below the ice. The bottom panel gives the hourly averaged speed, the second panel from the bottom gives the thermal driving. The third panel from the bottom gives the product of the speed and the thermal driving. The top panel gives the melt data (repeated here for comparison).

Various polynomial fits, up to fourth order, to the entire data set and to portions of the data showed no significant improvement in the following computations. In fact, the wiggles and bumps introduced to the data by the higher order fits produced spurious results in the analysis. Because of this problem and the fact that it was felt that the data, especially at the end of the record, might not contain information beyond a linear fit, the following computations use only the linear approximations.

Fig. 2 gives the hourly averaged current meter data for the experiment. The bottom panel shows the speed only; there are no direction data for the first 24 hours because the vane was not attached. On Julian day 52 at 2200 GMT divers attached the vane. The resulting direction data showed the current to be flowing at a direction of 040° magnetic, with little variation. Conversely, the ice was rapidly moving southwesterly towards the ice edge as a result of strong northeasterly winds. The second panel from the bottom gives the ocean tempera-

ture in terms of the temperature elevation above the ambient freezing point,  $T_d$ . CTD casts in this area show the water to be nearly isohaline at 32.7‰, which corresponds to a freezing point of -1.79°C. Hence, in this case  $T_d$  is just the temperature measured by the current meter with a constant 1.79° added to it. As the data show, the floe was initially in water only 0.5 to 0.75° above its freezing point but then it moved into water nearly 3° above its freezing point; this accounts for the rapid increase in the observed melt rate.

These observations of melt rate, the relative ice-water speed, and the temperature difference between the ice and the water allow for the direct computation of the bulk heat transfer coefficient  $C_h$ , which is defined as

$$C_h = L \rho_i M / [C_p \rho_w |U| T_d] \quad (1)$$

where  $m$  = melt rate,  $\text{mm s}^{-1}$

$L$  = latent heat, adjusted for brine volume

$\rho_i$  = ice density

$\rho_w$  = water density

$U$  = relative ice-water speed

$T_d$  = thermal driving.

Although the ice/water interface temperature is not known, Josberger (1983) showed that this temperature, for oceanic conditions, can be approximated by the ambient freezing point; hence,  $T_d$  becomes the ice-water temperature difference that will be used in these calculations. Because of the relatively high salt content of first-year sea ice, the latent heat must be adjusted to account for the brine volume. Analysis of cores from the instrumented floe shows that the salinity was about 4‰ and the temperature ranged from -1.4°C to -6°C. With a temperature of -2°C and a salinity of 4‰, the results of Frankenstein and Garner (1967) give a brine volume of 10%, which then reduces the latent heat by the proportionate amount.

$C_h$  is simply the proportionality constant that relates the melt rate to the product of the speed and  $T_d$ ,  $|U| T_d$ . The second panel from the top in Fig. 2 shows this product and, for ease of comparison, the top panel of Fig. 2 redisplays the melt data. The melt closely follows  $|U| T_d$ ; however, the scatter in the melt data during the last 9 hours conceals any trend for slower melting when  $|U| T_d$  dropped from near 80  $\text{cm-deg s}^{-1}$  to half this value. Nonetheless the values of  $C_h$  as computed from eq 1 and the three linear fits are remarkably consistent. Fig. 3 shows the  $C_h$  values as calculated from the hourly averaged data. The pattern in these values certainly reflects the combination of

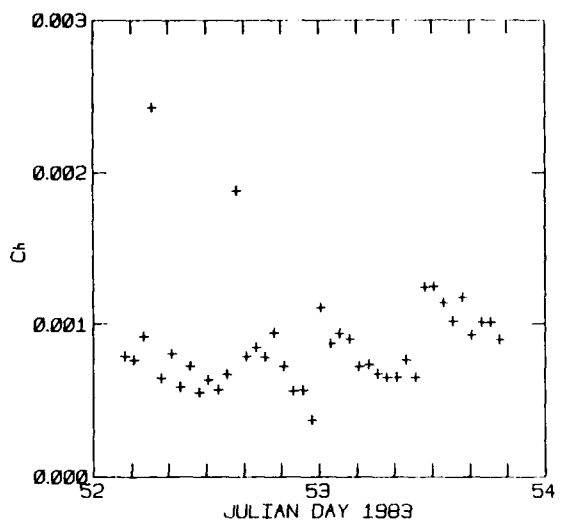


Fig. 3. The values of the heat transfer coefficient  $C_h$  computed from the ablation data and the hourly averaged data.

constant melt rate over periods of time when  $|U|T_d$  varied considerably. The average value of  $C_h$ , excluding the two extraordinarily high values, is  $(8.1 \pm 2.1) \times 10^{-4}$ .

The first high value of  $C_h$  results from the constant melt rate during a period when  $|U|T_d$  dropped to near zero. Close inspection of the melt data shows that during this period little or no melting occurred, a detail that was smoothed over by the linear fit. In this case, the early melt data may warrant a higher order polynomial fit. The second high value of  $C_h$  occurs where the change in approximations to the data takes place; the melt rate shifts to a higher value but  $|U|T_d$  remains low, hence  $C_h$  must be larger.

## DISCUSSION

There are no other direct measurements of the upward heat flux in an ice-covered ocean with which to compare these measurements and resulting heat transfer coefficients; however, as a result of the Reynolds analogy between heat and momentum transfer we can compare these results to measurements of the momentum transfer. The Reynolds analogy states that the turbulent transfer of heat and momentum can be characterized by an equal transfer coefficient for each. Hence, in this case we would expect  $C_d$ , momentum transfer coefficient, to equal  $8 \times 10^{-4}$ . For the central Arctic, Langleben (1980), as part of the AIDJEX program, determined  $C_d$  from measurements 1 m be-

low the ice. The average value of  $C_d$  was found to be  $4.1 \times 10^{-3}$ , roughly five times the value of  $C_h$  found in this study. There are many reasons for this apparent disagreement; first, the ice in the MIZ, as a result of melting, is smoother than the ice in the central Arctic. Second, McPhee (1983) shows that the buoyancy flux generated by the melting ice stabilizes the boundary layer and hence reduces  $C_d$ , although Josberger (1983) shows that the melting may have minimal effect on the boundary layer dynamics. However, ambient stratification in the ocean may reduce the transfer of both heat and momentum to the ice. Finally, Businger et al. (1971) show that for the atmosphere  $C_d$  and  $C_h$  are not equal, even for the neutral case, and their ratio is strongly dependent on the stability.

## ACKNOWLEDGMENTS

We deeply thank the crew of the NOAA ship *Discoverer* for their outstanding assistance in the deployment and recovery of the ablation gear. The diving team headed by G. Lagerloff receives our utmost appreciation for their truly heroic recovery efforts. We also thank the Office of Naval Research for their support of these ablation studies. We thank Dr. Richard Sternberg, University of Washington, for the loan of the sonic melt gauge. Finally, E.G. Josberger extends his thanks and appreciation to all members of the MIZEX-West team for their help in the collection of these data.

## REFERENCES

- Bauer, J. and S. Martin, Field observations of the Bering Sea ice edge properties during March 1979, *Mon. Wea. Rev.*, 108(12), 2045-2056, 1980.
- Businger, J.A., J.C. Wyngaard, Y. Izumi and E.F. Bradley, Flux-profile relationships in the atmospheric surface layer, *J. Atmos. Sci.*, 28(2), 181-189, 1971.
- Frankenstein, G. and R. Garner, Equations for determining the brine volume of sea ice from  $-0.5^{\circ}\text{C}$  to  $-22.9^{\circ}\text{C}$ , *J. Glaciol.*, 6, 943-944, 1967.
- Josberger, E.G., Sea ice melting in the marginal ice zone, *J. Geophys. Res.*, 88(C5), 2841-2844, 1983.
- Langleben, M.P., Water drag coefficient at AIDJEX Station Caribou, in *Sea Ice Processes and Models* (R.S. Pritchard, Ed.), Univ. of Washington Press, Seattle, pp. 464-474, 1980.
- McPhee, M.G., Turbulent heat and momentum transfer in the oceanic boundary layer under melt-

ing pack ice, *J. Geophys. Res.*, 88(C5), 2827-2835, 1983.

**Overland, J.E. and C.H. Pease**, Cyclone climatology of the Bering Sea and its relation to sea ice extent, *Mon. Wea. Rev.*, 110(1), 5-13, 1982.

**Wadhams, P. and S.P. O'Farrell**, The motion of ice edge radar transponders during MIZEX-West, *MIZEX Bulletin VI*, USA Cold Regions Research and Engineering Laboratory, Special Report 85-6, pp. 50-67, 1985.

## Some Wave Attenuation Results from MIZEX-West

VERNON A. SQUIRE AND PETER WADHAMS

*Scott Polar Research Institute, University of Cambridge  
Lensfield Road, Cambridge CB2 1ER, England*

### INTRODUCTION

During the MIZEX-West field experiment in the Bering Sea in February 1983 a wave-measuring program was carried out from both of the ships involved. Two types of experiment were done. The first was a "floe hopping" experimental design, whereby an S-52 helicopter from the U.S. Coast Guard icebreaker *Westwind* visited a number of sites along a line running into the pack, measuring the heave motion of ice at each site using a vertical accelerometer. At the same time the NOAA ship *Discoverer*, working near the ice edge, monitored the incident wave energy at the edge using either an Endeco Wavetrack directional buoy or a Seadisc one-dimensional buoy (an instrument designed by S.C. Moore at SPRI). The second type of experiment was the continuous monitoring of wave energy at a number of stations corresponding to radar transponder buoy sites (see Wadhams and O'Farrell, 1985). The most useful array of sites for this purpose was the first one to be deployed, on 7 February. Here four sites were set out from the *Westwind*, of which three lay along a line almost normal to the ice edge. At each site a Seadisc monitored the wave energy, telemetering data to *Discoverer*, which lay nearby tracking the buoys.

Since wave decay within the marginal ice zone is caused primarily by a scattering mechanism, it is important to measure the ice conditions (floe size distribution, typical floe thickness, ice concentration) along the path of penetration of the waves through the instrument arrays. The intention was that *Westwind*'s helicopter, equipped with a vertical aerial camera, would accomplish this task. In the event, *Westwind* had to penetrate deeply into the ice after 7 February to find suitable conditions for further instrument deployment (see Martin and Thorndike, 1985), so only a single flight over the Seadisc array was possible. Photographic cov-

erage was, however, obtained along the "floe hopping" lines.

Four wave attenuation transects are reported in this paper. The first, on 7 February, which we will call transect A, comprised three Seadisc wavebuoys along a bearing 050° at approximately 6 km separation. The line began 6 km inside the ice edge. These stations are those of the drift experiment described by Wadhams and O'Farrell (1985), with the omission of the most easterly site. Each station was deployed from *Westwind* as she steamed into the interior. After all sites had been deployed, and some equipment and personnel exchanged between the two vessels, an aerial photographic mapping flight was carried out from the *Westwind* by Andrew Cowan. One malfunctioning Seadisc was later revisited before *Westwind* left the area while *Discoverer* continued to record position and wave data from each site. Attenuation data from this transect were selected from the beginning of the experiment and from 12 hours on, before the line of Seadiscs had deformed excessively. Three more attenuation transects (B, C and D) of the "floe hopping" type took place from *Westwind* when she had reached her final position within the interior pack ice. These comprised a line of five stations on 19 February, a line of seven stations on 22 February, and a line of eight stations on 26 February. During the former two experiments a wave buoy was deployed at the ice edge, but conditions were too rough at the edge for this to be done on 26 February.

Apart from the transect of 7 February, which used Seadisc wavebuoys to transmit the vertical motion (acceleration) of each ice floe station directly to *Discoverer*, the wave data were collected by means of accelerometers recording onto a chart recorder. Each record was limited to 20 minutes to allow the maximum number of stations to be visited by the helicopter. During flights the position of the helicopter, marked by its radar transponder,

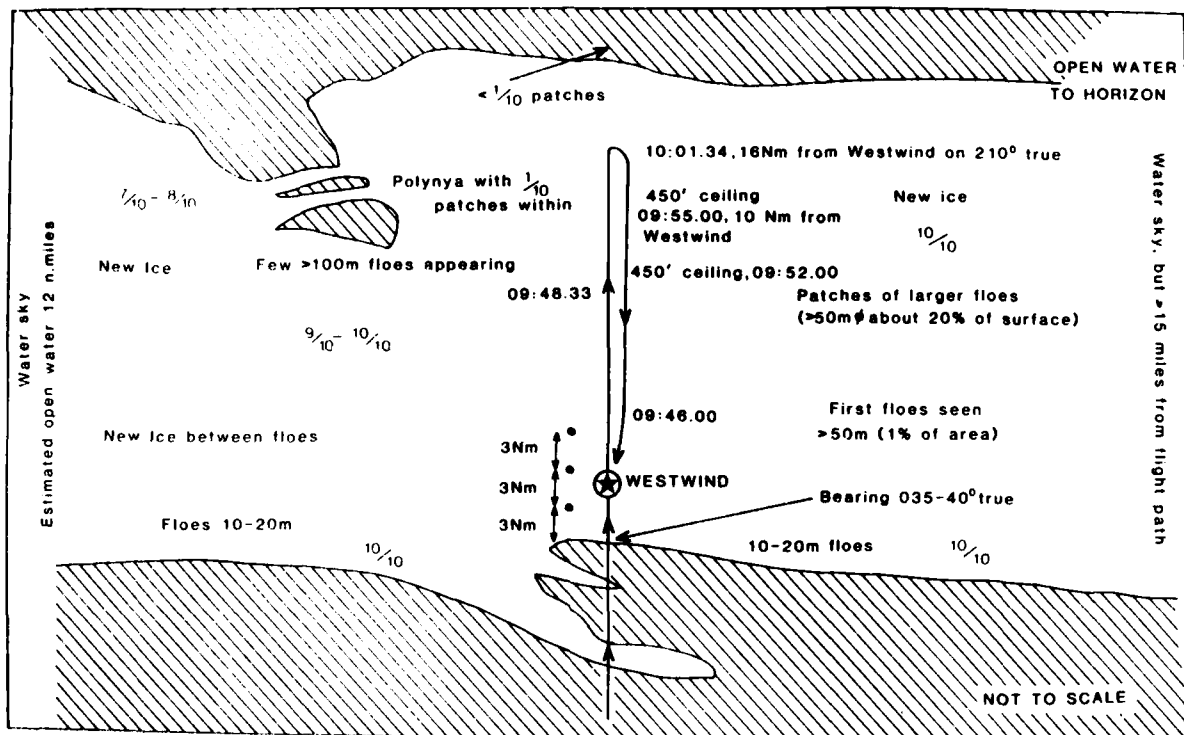


Fig. 1. Sketch of ice conditions observed by helicopter prior to deployment of transect A, 7 February 1983.

was tracked from *Westwind*. This allowed the attenuation line to be accurately charted.

## ICE CONDITIONS

Two types of aerial mapping data are available: Vinten F95 70-mm aerial photography and oblique contextual video. For transect A, all sites were overflowed at 500 ft altitude with camera and video running simultaneously; thus excellent data are available to characterize ice morphology during the experiment. Moreover, in view of the unfavourable ice conditions, a reconnaissance flight to examine the area over a larger scale had preceded deployment. A map drawn during this flight is shown in Fig. 1. Note that the area in which we set out the instruments was suspected of being a wide band of ice that was separated from the main Bering Sea ice pack. This was based on the presence of a "water sky" to the east, west and north, but was later confirmed as *Westwind* steamed into the interior. The band was separated from more consolidated pack by some 20 km of polynya. Sample

aerial photography from the experimental area is shown in Fig. 2, where each image covers an area 100 m square. Locally, within the 18-km stretch of pack ice in which attenuation was measured, the ice conditions were reasonably homogeneous, with many floes only 5 to 10 m across. Concentration was always above  $\frac{1}{10}$  except at the extreme ice edge. The floes chosen for the Seadisc instrumentation were between 10 m and 25 m across, with thickness in the range 0.7 to 1.0 m. However, since thickness was estimated from freeboard, these values may not be accurate. The entire ice edge region, stretching as far as the interior polynya noted above, was in an advanced state of decay.

For transects B and D, Vinten photography and oblique video were collected; for transect C no mapping was possible. Ice conditions were less favourable for attenuation experiments in these three cases, since many polynyas were present and the ice cover was quite diffuse. New ice formed continuously as each polynya opened under the action of divergent stress fields due to wind. Concentration was patchy and varied between  $\frac{1}{10}$  and  $\frac{10}{10}$  among the instrumented sites.

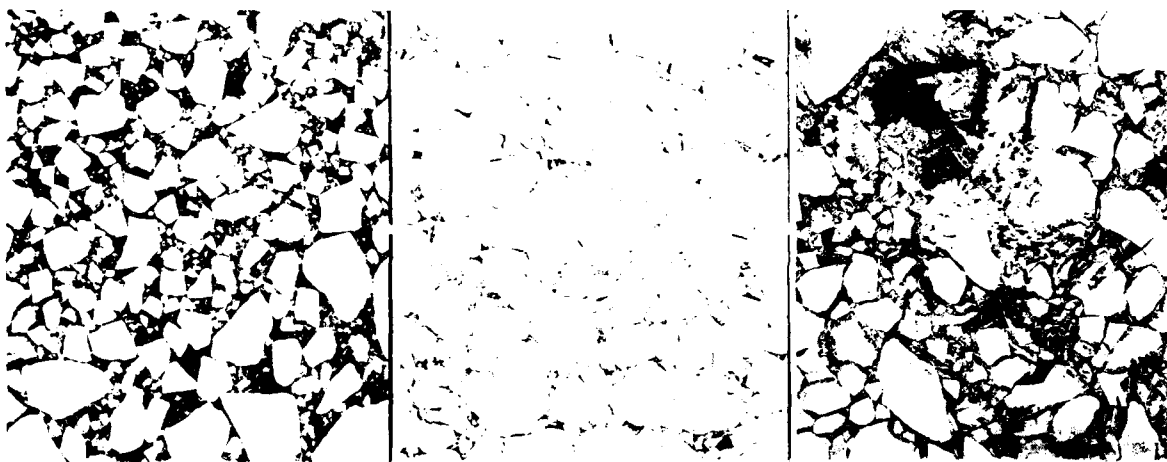


Fig. 2. Three aerial photographs of ice morphology in vicinity of Westwind after transect A was set out. The photographs represent ice near the edge (left), near the first site (middle), and near the furthest interior site (right). Most of the ice was decaying rapidly in this region. Each photograph is 100 m across.

## WAVE ATTENUATION RESULTS

### 7 February

This experiment (transect A) was not intended as an attenuation transect at the time of deployment. Rather, its aim was to study pack deformation as a function of time while monitoring wave energy at each experimental site. Three of the sites, located in a straight line back from the ice edge, can be used to infer attenuation rates for sea and swell entering the ice cover. It must be stressed, however, that three wave stations are not really sufficient for a detailed study of the functional relationship between wave decay, wave period and penetration. Unlike later data, where measurements are offset in time due to helicopter flight time between sites, the measurements of 7 February are truly simultaneous and questions of stationarity do not arise.

Two realizations of wave record from each of the three sites are considered, the first from the beginning of the experiment and the second from 12 hours on. We denote these respectively as experiments 1 and 2. Power spectra with 30 degrees of freedom were computed at each site for both experiments. The spectra allow the energy  $E(\lambda)$  associated with discrete frequencies in a sea-swell range to be found at each site. Then, by assuming a simple exponential decay model for waves penetrating the pack (Wadhams, 1975), a least squares fit to the three energy values from the three stations at every frequency included is carried out for both experiments. Thus attenuation coefficient  $\alpha$ , de-

fined from

$$E(\lambda) = E(0) \exp(-\alpha\lambda), \quad (1)$$

may be plotted as a function of frequency (or period). These values are shown in Fig. 3, where power spectra corresponding to the outermost site have also been plotted. Above about 7 s the attenuation coefficient decreases with period, reaching a platform above 11 s, i.e. long waves are not attenuated as much as short. The data roll over when wave period is less than 7 s, indicating that very short waves might penetrate far into the pack. This is unlikely to be the case, however, since we would expect the scattering mechanism by which energy is lost to be most active at shortest periods. More likely is increased energy at short periods due to local generation of waves by wind. Note also that the spectral energy penetrating the pack is small at these periods, most of the energy being associated with waves of around 11 s period. This may lead to large measurement errors. Error bars on each graph represent the error associated with 30 degrees of freedom (abscissa), and the fractional error in the exponential fit (ordinate).

### 20 February

The attenuation results from transect B are plotted in Fig. 4. In this case five sites were deployed along a bearing of 244°. Measuring from the southernmost station along this line, site positions were 0 km, 4.8 km, 8.2 km, 17.8 km and 19.7 km. Since the ice edge was more than 50 km away only

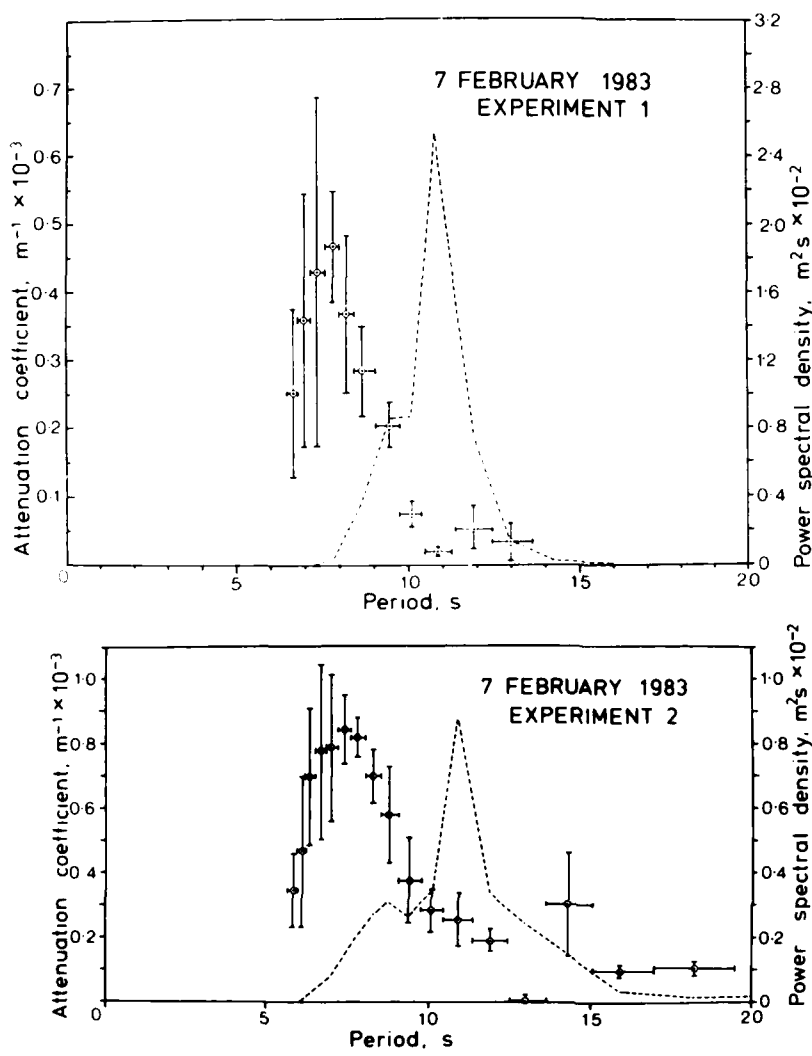


Fig. 3. Attenuation coefficient as a function of period, and wave spectrum from southernmost site for experiments 1 and 2 of transect A.

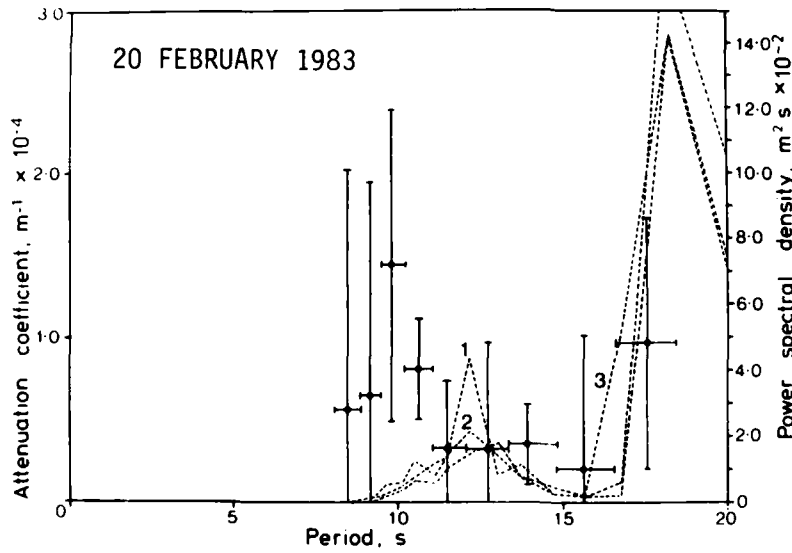


Fig. 4. Attenuation coefficients and three open-sea spectra for transect B.

relatively long waves were expected to penetrate into the experimental zone, the short seas having been attenuated en route. Measurements of wave activity at the extreme ice edge were collected from *Discoverer* using a Seadisc wavebuoy. This allowed the incoming open-sea wave spectrum to be monitored, and thus any alteration in intensity or frequency content was known. These open-sea spectra are plotted alongside the attenuation results of Fig. 4. Within their 95% confidence limits at 30 degrees of freedom, no change in forcing is observed during the 8 hours between recordings 1 and 3, except perhaps for a slight decrease in short period sea, which would not be detected by the sites composing the attenuation transect 50 km in to the pack. The form of the open sea forcing is most surprising since, although the lower peak at 12.5 s is seen by the attenuation array, the peak at 17 s is not. It is likely, therefore, that the direction of propagation of the 17-s swell did not coincide with the bearing of transect B. The attenuation coefficients plotted in Fig. 4 may have large errors due to several factors: the small number of sites involved, their close proximity, and the large drift experienced by *Westwind*.

## 22 February

Seven sites, located at 0 km, 10.3 km, 16.7 km, 25.1 km, 25.5 km, 32.1 km and 36.1 km from the southernmost station on a bearing of 225°, made up transect C. Attenuation coefficients as a function of wave period are plotted in Fig. 5, together with three open-sea spectra obtained by *Discoverer* during the experiment with a free-floating Seadisc wavebuoy. Two swell peaks are apparent, one at about 12 s, the other at 16 s; both were seen in the transect C data. Again a characteristic decrease in attenuation coefficient with increased period is seen, with a roll-over at short periods.

## 26 February

In transect D a total of eight sites were instrumented to measure attenuation in the incoming waves. These were positioned along a line 230° at 0 km, 10.6 km, 20.0 km, 38.8 km, 56.4 km, 62.0 km, 68.6 km and 74.3 km. In this case no measurements of sea state were available near the ice edge, and the spectrum at the most southerly station has been plotted alongside the attenuation coefficients of Fig. 6. Within a central range of 10 to 20 s, the attenuation decreases with increased peri-

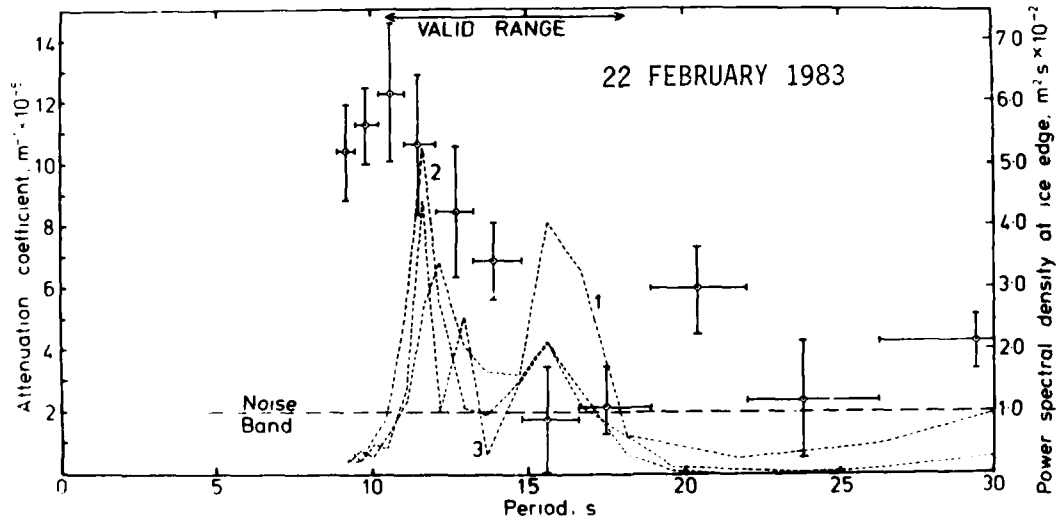


Fig. 5. Attenuation coefficients and three open-sea spectra for transect C.

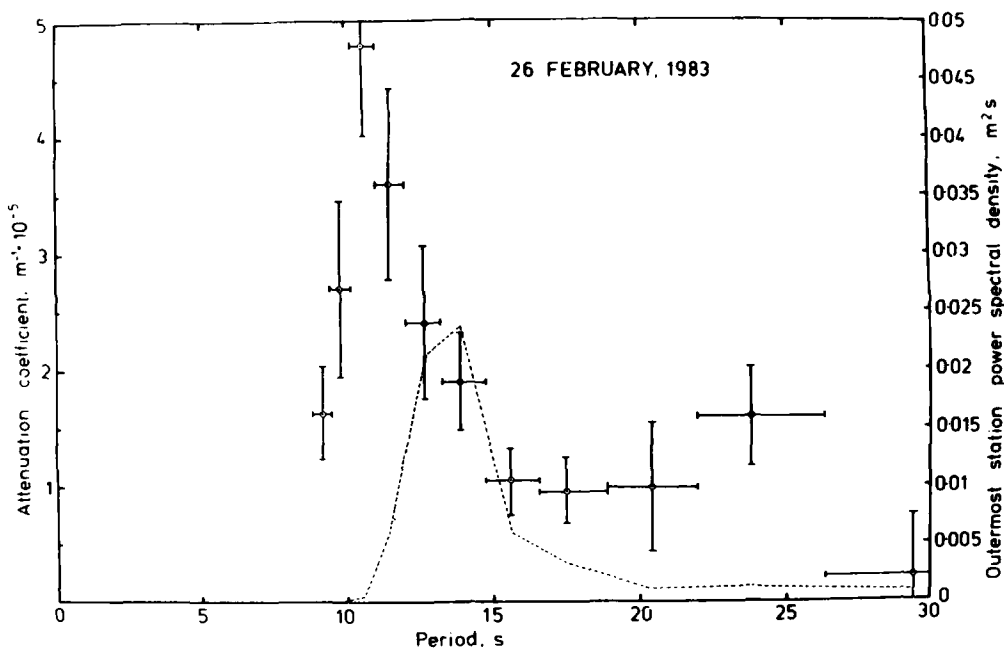


Fig. 6. Attenuation coefficients and southernmost power spectrum for transect D in ice.

od. The incoming spectrum is single-peaked at about 14 s.

## CONCLUSIONS

1. The energy decay experienced by waves traveling through pack ice appears to fit a simple exponential attenuation law with the coefficient a function of frequency and ice conditions.

2. Attenuation is greatest for short period waves and least for long waves. A roll-over seen in the attenuation coefficient at shorter periods still is believed to be either due to wave generation within the ice, or to be an artifact of experimental technique.

3. Values of attenuation coefficient measured during the latter three transects under similar ice conditions are self-consistent. Values measured near the ice edge for transect A in heavier ice are larger.

Detailed comparisons of these data with a theoretical scattering model will appear in a later paper.

## ACKNOWLEDGMENTS

We acknowledge with thanks the financial support of the Office of Naval Research, the Natural Environment Research Council, and British Petroleum Co. Ltd. We are also grateful to Andrew Cowan, Stuart Moore and Rob Massom, who assisted considerably in the collection of data and in the preparation of this brief report.

## REFERENCES

Martin, S. and A.S. Thorndike, Ice dispersion in the Bering Sea marginal ice zone, *MIZEX Bulletin VI*, USA Cold Regions Research and Engineering Laboratory, Special Report 85-6, pp. 38-49, 1985.

Wadhams, P., Airborne laser profiling of swell in an open ice field, *J. Geophys. Res.*, 80, 4520-4528, 1975.

Wadhams, P. and S.P. O'Farrell, The motion of ice edge radar transponders during MIZEX-West, *MIZEX Bulletin VI*, USA Cold Regions Research and Engineering Laboratory, Special Report 85-6, pp. 50-67, 1985.

## Further Aircraft Measurements of Air-Ice Drag Coefficients

JAMES E. OVERLAND AND BERNARD A. WALTER, JR.  
*Pacific Marine Environmental Laboratory/NOAA*  
*Seattle, Washington 98115, USA*

NOAA WP-3D aircraft measurements were obtained over the eastern Bering Sea Shelf during February 1983 in the Marginal Ice Zone Experiment (MIZEX-West). The objective was to obtain measurements of regional winds, heat flux, and air-ice drag coefficients to supplement measurements obtained in 1982 (Walter and Overland, 1984; Walter et al. 1984). Routine weather observations and atmospheric soundings were made on the NOAA ship *Discoverer*, located in the outer MIZ (Fig. 1), and the U.S. Coast Guard ice-breaker *Westwind*, located in first-year ice (Wilson et al., 1984). Two meteorological stations were deployed as part of a 50-km ice deformation array in the vicinity of *Westwind*.

Flight patterns to measure air-ice drag coefficients were flown on 13, 16 and 19 February 1983 (Table 1). A gust probe system on the aircraft measured high-frequency (40 Hz) fluctuations of  $u$ ,  $v$  and  $w$  wind components, air temperature and moisture. The eddy correlation technique was used to calculate mean momentum, heat and moisture fluxes at three or four elevations along individual aircraft tracks of 40 km. These fluxes were used to determine surface fluxes by extrapolation. Walter et al. (1984) discussed the gust probe instrumentation and data analysis in detail. In particular, it is necessary to make repeated measurements over long tracks to correctly sample surface heterogeneity and correctly resolve meso-scale variability of the atmosphere. Air and dew point temperatures and wind were measured at flight level, and downward laser, SLAR and PRT-5 radiation measurements were also made.

During 1-10 February 1983, low sea-level pressure in the southern Bering Sea resulted in winds from easterly to northerly at 3 to 10  $m s^{-1}$ . Air temperatures were  $-4^{\circ}C$  at the ice edge and slightly lower in the ice interior. From 10 to 13 February the easterly winds increased to over 15  $m s^{-1}$  at the *Westwind* in the inner MIZ and to over 18  $m s^{-1}$  at

the *Discoverer* in the outer MIZ. Temperatures decreased to  $-18^{\circ}C$  at the *Westwind* but remained relatively constant at the *Discoverer*. Surface measurements on 13 February 1983 showed winds of 6 to 8  $m s^{-1}$  (at 3-m height) from the northeast and air temperatures of  $-12^{\circ}$  to  $-15^{\circ}C$ .

Crosswind tracks were flown on 13 February at 44, 90, 175 and 344 m in the vicinity of the *Westwind* ( $61.0^{\circ}N$ ,  $171.9^{\circ}W$ ); this pattern was repeated three times. The vertical potential temperature profile from aircraft data (Fig. 2) shows an inver-

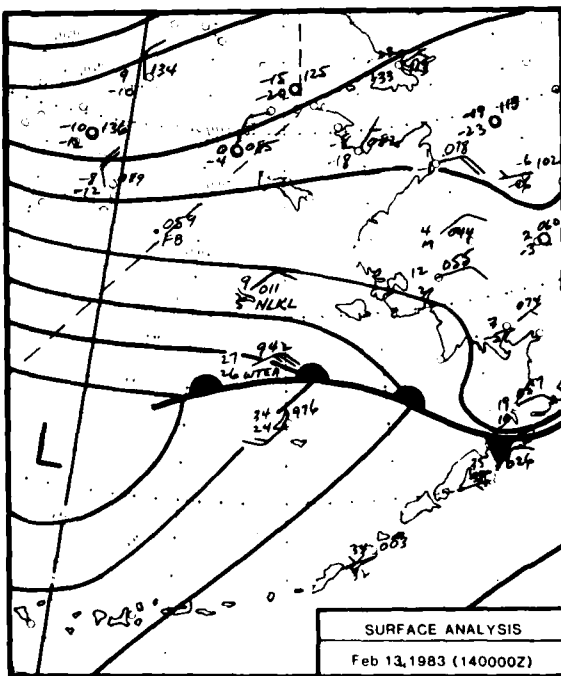
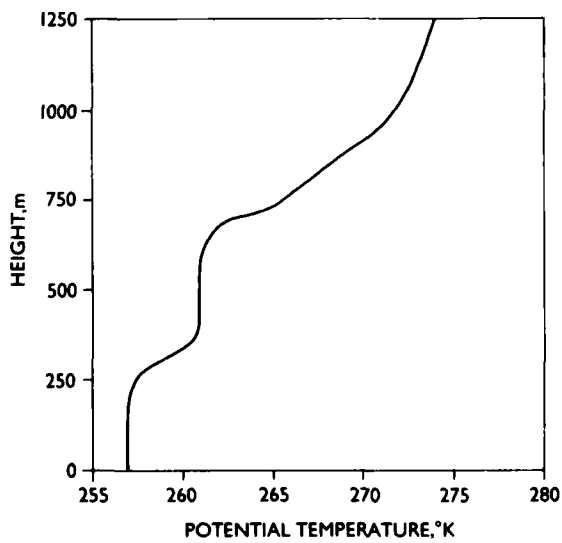


Fig. 1. Sea level analysis for 0000 GMT, 14 February 1983. WTEA indicates the *Discoverer* and NLKL indicates the *Westwind*.

**Table 1. Aircraft-derived drag coefficients and boundary layer parameters.**

	14 Feb 82	13 Feb 83	16 Feb 83	19 Feb 83
$T_o$ (°C)	-16	-11	-11	-13
$U_{10}$ (m s <sup>-1</sup> )	13.9	8.1	10.1	7.5
$u_*$ (m s <sup>-1</sup> )	0.76	0.43	0.50	0.42
$Z_i$ (m)	660.0	260.0	290.0	150.0
$H_o$ (W m <sup>-2</sup> )	62	29	24	17
$L_*$ (m)	-551	-248	-469	-383
$Z_i/L_*$	-1.2	-1.0	-0.6	-0.4
$u_*/fZ_i$	9	13	13	21
$10^3 C_D$	3.0	2.9	2.5	3.1
Roughness (m)				
mean	0.1	0.3	0.3	0.5
extremes	0.5	1.0	0.8	1.3
% open water	12	1	2	8
% thin ice	2	6	4	6

Note: Roughness was computed from laser profiler data on the aircraft; extremes represent 5 to 10 maximum excursions along 40-km tracks. Percent open water and thin ice was determined from downward-looking PRT-5 radiometer measurements along 40-km tracks.



**Fig. 2. Vertical profile of potential temperature for 13 February 1983.**

sion base,  $Z_i$ , at 260 m. The momentum flux profiles (Fig. 3) are defined by

$$\tau_x = -\rho u' w', \quad \tau_y = -\rho v' w', \quad (1)$$

where  $u'$  fluctuations are along the mean planetary boundary layer (PBL) wind direction,  $v'$  fluctuations are normal to the mean PBL wind direction, and  $\rho$  is air density. The highest level (344 m) was above the lower inversion base, therefore only the three lowest levels were used to estimate a surface stress of  $\tau_0 = 0.26 \pm 0.05 \text{ N m}^{-2}$  and a friction velocity of  $u_* = 0.43 \pm 0.04 \text{ m s}^{-1}$ .

The profile of virtual heat flux is shown in Fig. 4. A linear least-squares regression line of the lowest three levels gives a surface buoyancy flux of  $H_o = \rho_o C_p (\bar{T} w')_0 = 29.5 \pm 4.0 \text{ W m}^{-2}$ , where  $C_p$  is specific heat for dry air and the term in parentheses is vertical temperature flux at the surface. Although the magnitude of surface sensible and latent heat fluxes averaged over entire tracks was quite small, fluxes from individual leads along the track were substantial. The value for the Monin-Obukhov length  $L_*$ , based upon track-averaged  $u_*$  and  $H_o$ , was -248 m. This gives a value for the

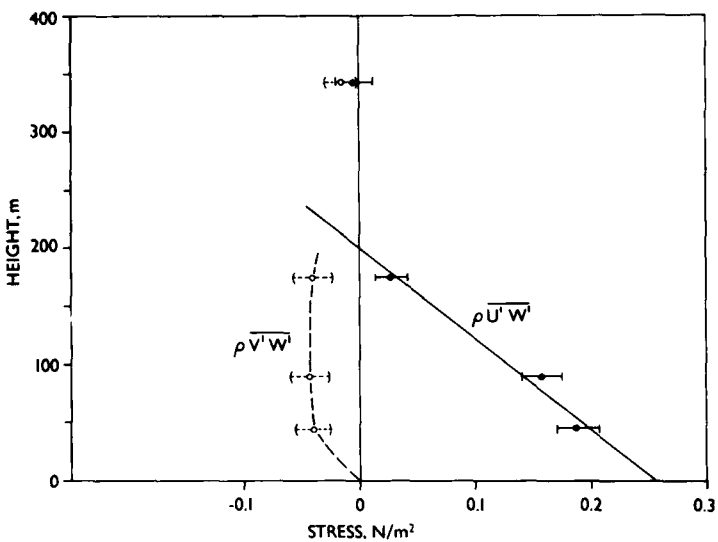


Fig. 3. Vertical profile of stress for 13 February flight.

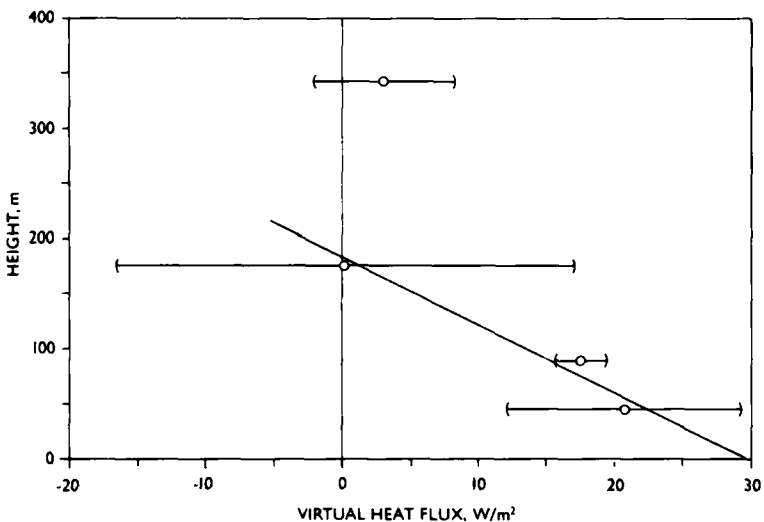


Fig. 4. Vertical profile of virtual temperature flux for 13 February 1983.

boundary layer stability parameter,  $\zeta_* = Z_*/L_*$ , of -1.1, which indicates that the boundary layer was slightly unstable but that convection was not a dominant process.

The 10-m drag coefficient is defined by  $C_d = u_*^2/U_{10}$ , where  $U_{10}$  is the wind at 10 m. The flux profile relations of Dyer and Hicks (1970) were used to reduce wind profiles (Fig. 5) for the three tracks from 44 m to 10 m (Walter et al., 1984), giving  $U_{10}$  of  $8.4 \text{ m s}^{-1}$ . Note that the wind profile in Fig. 5 is not well-mixed since production of turbulence is by vertical shear. Surface-based winds were measured on two 3-m-high towers ( $61.32^\circ\text{N}$ ,  $172.13^\circ\text{W}$  and  $61.02^\circ\text{N}$ ,  $171.9^\circ\text{W}$ ) in the vicinity of

aircraft operations. The average of the two stations during the overflight was  $U_*$  of  $6.7 \text{ m s}^{-1}$ ; extrapolation to 10 m gives a  $U_{10}$  of  $8.1 \text{ m s}^{-1}$ , which is within  $0.3 \text{ m s}^{-1}$  of the aircraft-derived wind speed. The 10-m wind speeds extrapolated from the surface towers are considered more accurate than those extrapolated from flight level estimates, so that surface measurements are used, when available, for drag coefficient estimates. The drag coefficient calculated using  $U_{10}$  derived from the tower winds is  $10^3 C_d = 2.9 \pm 0.6$ .

For a brief period on 14 February 1983 the wind shifted to southerly due to a low pressure center in

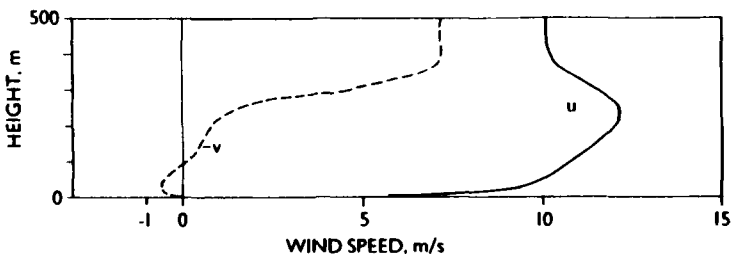


Fig. 5. Vertical profile of velocity for 13 February 1983.

the southwestern Bering Sea. Winds were  $10 \text{ m s}^{-1}$ , and temperature rose to  $0^\circ\text{C}$  at the *Discoverer* and  $-5^\circ\text{C}$  at the *Westwind* during this period of warm air advection. Between 15 and 18 February the North Pacific storm track shifted south of the Aleutian Islands, and winds increased to more than  $18 \text{ m s}^{-1}$  from the northeast. Air temperatures dropped to  $-14^\circ\text{C}$  at the ice edge and  $-24^\circ\text{C}$  in the ice interior. The PBL was defined by a sharp inversion with dry air aloft and deepened from 300 m to 600 m throughout this period at the *Westwind* (Wilson et al., 1984). Winds decreased beginning on 19 February.

On 16 February 1983 aircraft tracks were flown at 54, 102 and 202 m near the *Westwind* ( $61.0^\circ\text{N}$ ,  $172.9^\circ\text{W}$ ); the pattern was flown twice. The vertical profile of potential temperature showed the inversion base at 290 m, so that all three levels for the aircraft measurements were below  $Z_i$ . The surface stress obtained by linear extrapolation was  $\tau_0 = 0.34 \pm 0.03 \text{ N m}^{-2}$  and the friction velocity was  $u_* = 0.50 \pm 0.02 \text{ m s}^{-1}$ .  $H_0$  was  $23.9 \pm 2.9 \text{ W m}^{-2}$ , and the Monin-Obukhov length was  $L_* = -469 \text{ m}$ .  $Z_i/L_*$  was  $-0.6$  and the boundary layer was slightly unstable. Extrapolation of the aircraft wind at 54 m gives  $U_{10} = 11.5 \text{ m s}^{-1}$  and extrapolation of the mean wind from the two 3-m towers during the aircraft flight gives  $U_{10} = 10.1 \text{ m s}^{-1}$ . The drag coefficient derived using the tower wind is  $10^3 C_D = 2.5 \pm 0.2$ . Given the discrepancy in  $U_{10}$ , this value is less reliable than that made on 13 February.

On the third flight, 19 February 1983, only one stack was completed, but it was over the inner MIZ, which had increased open water and was visually rougher than on 13 and 16 February. The inversion base was at 150 m. Tracks at 54 m, 95 m and the near-zero flux value at 200 m were used to estimate surface fluxes of  $\tau_0 = 0.24 \text{ N m}^{-2}$  and  $H_0 = 17.2 \text{ W m}^{-2}$ . Extrapolation of the 54-m wind to 10 m gave a  $U_{10}$  of  $8.7 \text{ m s}^{-1}$ ; extrapolation of the mean of the two surface stations gave a  $U_{10}$  of  $7.5 \text{ m s}^{-1}$  and a drag coefficient estimate of  $10^3 C_D = 3.1$ .

The 13 February 1983 drag coefficient is comparable to the drag coefficient obtained 250 km further north on 14 February 1982 (Walter et al., 1984). The 1983 site was rougher than 1982 and the inversion height was 260 m compared to 660 m in 1982 (Table 1). From plots of cospectra, the horizontal wavelength of maximum vertical transport ( $u'w'$ ,  $v'w'$ ,  $T'w'$ ) at 52 m in 1982 was longer (750 m) than in 1983 (400 m), consistent with the difference in height of the capping inversion.

During MIZEX-West there was a greater percentage of open water on 19 February than on 13 and 16 February, but the surface radiation temperature measured from the aircraft over entire tracks on the 19th was  $2^\circ$  lower than on the 13th and 16th, even though all three days had the same flight level air temperatures. The increase in percent open water on 19 February did not contribute to increased buoyancy flux because of decreased track-averaged surface-air temperature differences, but did contribute to apparent roughness (Table 1).

The three aircraft-derived observations of air-ice drag coefficients from MIZEX-West and the one observation from 1982 can be characterized by three parameters: the stability parameter,  $\zeta_* = Z_i/L_*$ ; an inversion influence parameter,  $Z_* = u_*/fZ_i$  where  $f$  is the Coriolis force; and the surface roughness given by its mean or extremes in Table 1. The stability parameter is small and negative in all cases, indicating that the boundary layer is adiabatic but that convection does not contribute significantly to generation of turbulent kinetic energy or inversion processes compared to mid-latitudes, where  $-\zeta = 100-1000$ . The value of  $Z_*$  is the ratio of the height that this boundary layer would develop by mechanical generation of turbulence to the inversion constrained height. Small values of  $Z_*$  and large values of surface roughness both contribute to large drag coefficients. The 1982 case had the largest inversion height and the lowest surface roughness, while the 19 February

MIZEX-West case over the inner MIZ had the lowest inversion and the greatest roughness. The 13 and 16 February cases are intermediate, with inversion heights of 250 to 300 m, near the climatological mean for the region.

This paper is a contribution to the Marine Services Project at the Pacific Marine Environmental Laboratory and was funded in part by the Arctic Program of the Office of Naval Research. This is PMEL Contribution Number 763.

#### REFERENCES

**Dyer, A.J. and B.B. Hicks**, Flux-gradient relationships in the constant flux layer, *Quart. J. Roy. Met. Soc.*, 96, 715-721, 1970.

**Walter, B.A. and J.E. Overland**, Observations of longitudinal rolls in a near neutral atmosphere, *Mon. Wea. Rev.*, 112, 200-208, 1984.

**Walter, B.A., J.E. Overland and R.O. Gilmer**, Air-ice drag coefficients for first-year sea ice derived from aircraft measurements, *J. Geophys. Res.*, 89, 3550-3560, 1984.

**Wilson, J.G., A.L. Comiskey, R.W. Lindsay and V.L. Long**, Regional meteorology of the Bering Sea during MIZEX-West, February and March 1983, NOAA Special Report, Pacific Marine Environmental Laboratory, Seattle, Washington, 115 pp., 1984.

## Geostrophic Drag of the High Latitude Atmospheric Boundary Layer

JAMES E. OVERLAND

*Pacific Marine Environmental Laboratory/NOAA  
Seattle, Washington 98115, USA*

Sea ice covering the Arctic Ocean and marginal seas consists of floes whose diameters range from a fraction of a meter to tens of kilometers (Rothrock and Thorndike, 1984). Roughness elements in the form of ridges and edges of floes also vary over these scales, locally giving a heterogeneous distribution. In the central Arctic there are large, widely spaced pressure ridges and the roughness is also locally non-isotropic. When strong winds and air temperatures below  $-5^{\circ}\text{C}$  are present, leads, polynyas, and regions of thin ice represent a source of buoyancy to the atmospheric boundary layer (Maykut, 1982). This source of buoyancy acts to increase the coupling between atmosphere and sea ice. A parcel of air will alternately encounter a surface composed of aerodynamically smooth water or new ice serving as a buoyancy source and aerodynamically rough sea ice with near-zero heat flux. In addition to surface effects, the coupling of momentum between the air and ice depends upon the properties of the air mass, in particular the inversion height and stability of the boundary layer. Since there is a distribution of surface roughness and buoyancy, these scales interact so that the turbulence at a specified height over a particular location is the weighted sum of upstream roughness and buoyancy flux and is not necessarily in local equilibrium with the surface.

Because of the inhomogeneity and anisotropy of the surface, it is important to specify the scale of motion of interest in atmospheric/ice momentum exchange. This note defines the scale at greater than 10 km for regional ice forecasting and studying climatic processes. Of concern is the average momentum transfer in response to the distribution of surface properties, i.e. local roughness variations and buoyancy sources, and the distribution of stress and heat flux throughout the atmospheric boundary layer. Atmospheric param-

eters are introduced that characterize such an exchange: a regional stability parameter, an inversion strength parameter and an effective surface roughness. A simplified atmospheric boundary layer model based upon second-order turbulent closure is used to explore the sensitivity of the geostrophic drag coefficient and the surface wind/geostrophic wind turning angle to these parameters.

The influence of stratification, both stable and unstable, on the surface boundary layer is often specified by the Monin-Obukhov length:

$$L = - \frac{u_*^3 \bar{T}_o}{gk(\bar{T}'w')}, \quad (1)$$

where  $u_*$  = the friction velocity equal to the square root of the vertical flux of horizontal momentum at the surface  
 $g$  = gravity  
 $k$  = the von Kármán constant  
 $\bar{T}_o$  = the virtual temperature  
 $(\bar{T}'w')_o$  = the virtual temperature flux at the surface.

When the absolute value of the Monin-Obukhov length  $L$  is large, mechanical mixing is said to dominate buoyancy in the generation of turbulent intensity in the boundary layer.

When considering the response of the entire boundary layer to a horizontal distribution of roughness and buoyancy sources, one must define an effective stability parameter:

$$\xi_* = Z_o/L_o, \quad (2)$$

where  $L_o$  is an effective Monin-Obukhov length, computed from a regional average momentum and heat flux, and  $Z_o$  is the height of the lowest in-

version base (Deardorff, 1972). Aircraft data collected over 40-km tracks of sea ice in winter during strong winds with air temperatures less than  $-5^{\circ}\text{C}$  show that there is a small regional net heat flux from the surface to the air, primarily from regions of thin ice, so that  $L_*$  is a large, negative value. This observation contrasts with measurements made near the surface from towers on large floes; these often show small positive and negative potential temperature gradients with height that vary with a diurnal period, independent of the ambient air temperature (Leavitt, 1980). At high latitudes during strong winds there is normally a low inversion base at 50 to 300 m (Sverdrup, 1933; Carsey, 1980; Wilson et al., 1984), so that  $-\zeta_*$  is of the order 1. This magnitude is dissimilar to convective boundary layers with strong inversions typical of low and mid-latitudes where  $-\zeta_*$  is of the order 100-1000 (Malgarejo and Deardorff, 1974). Production of turbulence in the high latitude atmospheric boundary layer is primarily due to vertical shear of the horizontal wind.

A second relevant parameter (Arya and Wangaard, 1975) for arctic boundary layers dominated by a low inversion during periods of strong winds is

$$Z_* = \frac{u_*}{fZ_i} \quad (3)$$

where  $f$  is the Coriolis parameter.  $Z_*$  is proportional to the ratio of the height that a neutral boundary layer would establish by mechanical mixing in a steady near-neutral atmosphere ( $Z_* \sim 0.3u_*/f$ ) to the inversion-constrained height,  $Z_i$ . The dynamic influence of  $Z_*$  is shown by considering the momentum equation in complex notation for a steady boundary layer:

$$if(\mathbf{V} - \mathbf{G}) = \partial \tau / \partial z \quad (4)$$

where  $\mathbf{V}$  is the horizontal mean wind velocity in complex notation,  $\mathbf{V} = U + iV$ ,  $f\mathbf{G}$  is the pressure gradient force, and  $\tau$  is the turbulent stress (in kinematic units). Boldface denotes vector quantities in complex notation. Introducing non-dimensional scaling,  $\sigma = \tau/u_*^2$ ,  $\mathbf{W} = \mathbf{V}/u_*$ ,  $\mathbf{W}_* = \mathbf{G}/u_*$ , and  $\eta = z/Z_*$ , into eq 4 gives:

$$\frac{u_*}{fZ_i} \frac{d\sigma}{d\eta} = i(\mathbf{W} - \mathbf{W}_*). \quad (5)$$

The solution to eq 5 contains only one non-dimensional dynamic parameter:  $Z_*$ .

The third parameter is based upon the concept

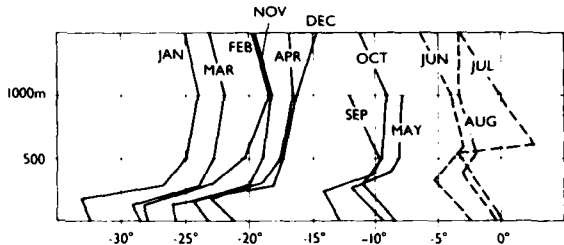


Fig. 1. Vertical temperature distribution in the different months for the Arctic north of eastern Siberia according to results of kite ascents in the years 1923 to 1925 (Sverdrup, 1933).

of effective roughness (Fiedler and Panofsky, 1972), defined as the roughness of a homogeneous terrain that yields the equivalent surface stress for a heterogeneous area:

$$Z_o(m) = 10 \exp(-kC_{D*}^{-1/2}). \quad (6)$$

The regional  $Z_o$  is designated as a capital letter to distinguish it from a local value.  $C_{D*}$  is a 10-m "surface" drag coefficient, which is an equivalent statement of surface roughness. A possible replacement parameter for  $Z_o$  is the non-dimensional  $Z/Z_o$ , but not the surface Rossby number,  $u_*/fZ_o$ , since the latter is valid only for small values of  $Z_o$ .

To evaluate the assumptions of  $Z_*$  scaling for the Arctic, composite temperature soundings are presented (Fig. 1) of the boundary layer over sea ice. These data were collected from the *Maud* (Sverdrup, 1933) north of Siberia in the region between Wrangell Island and the New Siberian Islands over a three-year period (1923-1925). Soundings were made by a kite, with a minimum of 11 soundings per month between October and May. The persistent feature of the composite is the existence of a cold layer near the surface capped by a strong inversion, which was observed in all but three cases:

The average thickness of the cold layer near the ice remains practically constant from November to March and the variation of temperature in the vertical direction is nearly the same in all these months...

For an individual sounding Sverdrup predicated  $Z_*$  scaling to note:

Since the cold layer near the ground is formed by forced mixing by wind, we must expect the thickness of the cold layer to increase with increasing wind velocity.

However,

A very close relationship...cannot be expected because...the altitude up to which the forced mixing

reaches...depends not only on the velocity of the wind but on other factors, especially the life history of the air masses.

Based upon 83 ascents, Sverdrup (1933) showed the arctic boundary layer in November to March to be dominated by a subsiding inversion of  $\Delta T \sim 7^\circ\text{C}$ , which reaches the ground in light winds but forms a nearly adiabatic cold layer when wind speeds are greater than  $6 \text{ m s}^{-1}$  (measured at 4.5 m). The steady inversion height increases with increasing wind speed. Adiabatic conditions occur at lower wind speeds during cloudy conditions due to the change in the radiation balance. For the cold layer in April/May and September/October:

We find the same conditions as before...however,...when the wind velocity and the lapse rate in the inversion are the same, the thickness is much greater than in winter...This indicates that...convection currents...arise when...the ice is heated by radiation...which effectively assist the mixing in the lowest layer.

An analog to the momentum integral method (Brown, 1974) when momentum is not vertically well mixed, since wind shear is necessary for turbulent production in the Arctic, is use of a second-order turbulent-closure boundary-layer model (Lykosov and Gutman, 1970; Mofjeld and Lavelle, 1984; Overland et al., 1984), in which turbulent intensity in the boundary layer is calculated internally from shear production by the wind profile (Appendix). This model will be used to explore the sensitivity of the effective pressure gradient/surface stress relation to  $Z_*$  and  $Z_*$  scaling. The boundary layer momentum equation (eq 4) is

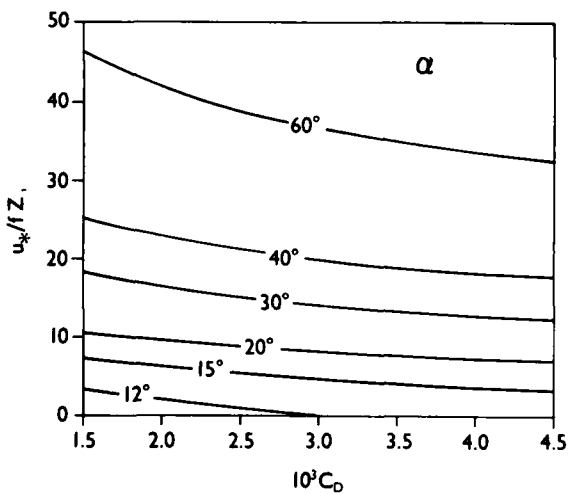


Fig. 3. Second-order closure model results showing dependence of turning angle  $\alpha$  on  $Z_* = u_*/fZ_i$  and  $C_D$ .  $G = 12.5 \text{ m s}^{-1}$ .

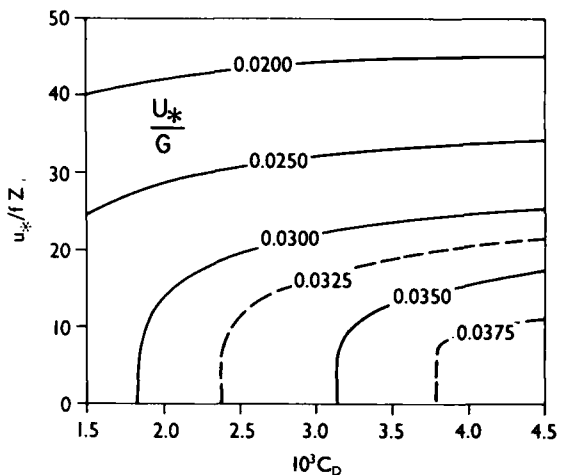


Fig. 2. Second-order closure model results showing dependence of the geostrophic drag coefficient,  $u_*/G$ , on  $Z_* = u_*/fZ_i$  and  $C_D$  referenced to 10 m.  $G = 12.5 \text{ m s}^{-1}$ .

solved subject to boundary conditions of stress approaching zero at  $Z_i$  and horizontal wind approaching zero at  $Z_*$ . Since the model internally calculates  $u_*$  and the 10-m wind  $U_{10}$ , the effective drag coefficient  $C_D$  is not necessarily a function only of  $Z_*$  for larger values of  $Z_*$ . The boundary layer is considered slightly unstable,  $\zeta_* = -1$ , so that the stress and wind profiles are a function only of  $Z_*$  and  $Z_*$ .

Fig. 2 and 3 plot values of constant geostrophic drag coefficient,  $C_r = u_*/G$ , and the turning angle between the surface and geostrophic wind,  $\alpha$ , as a

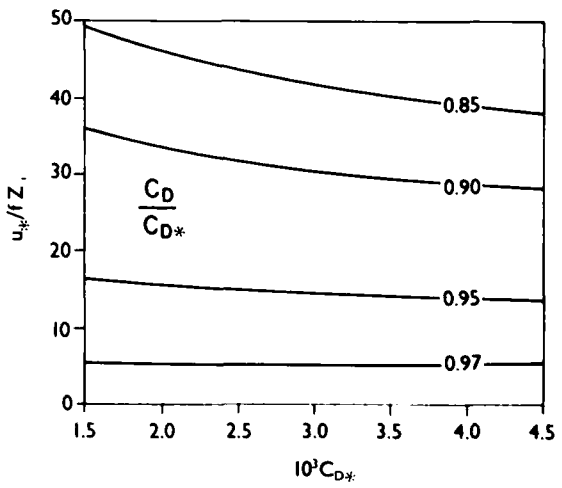


Fig. 4. Second-order closure model results showing dependence of  $C_D/C_D*$  on  $C_D*$ .  $G = 12.5 \text{ m s}^{-1}$ .  $C_D$  is calculated from model-derived  $u_*$  and  $U_{10}$  while  $C_D*$  is a function only of surface roughness.

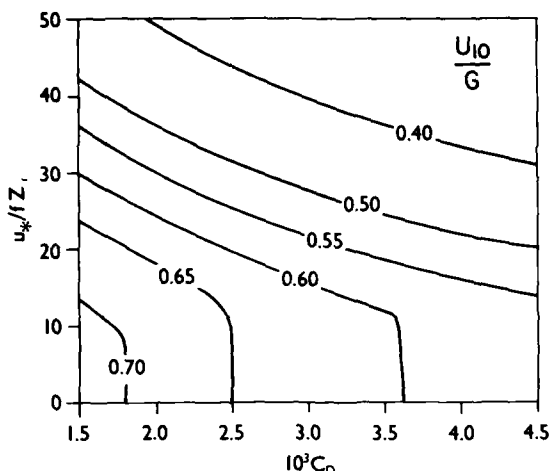


Fig. 5. Second-order closure model results showing dependence of  $U_{10}/G$  on  $Z_*$  and  $C_D$ .  $G = 12.5 \text{ m s}^{-1}$ .

function of  $Z_*$  and  $C_D$ . The drag coefficient on the abscissa corresponds to values that would be obtained from aircraft or other field measurements referenced to 10 m. For  $Z_* < 10$  the boundary layer is unconstrained and there is a nearly linear increase in  $C_s$  with  $C_D^{1/2}$ . With  $Z_* > 10$ ,  $C_s$  is dominated by the inversion and becomes less sensitive to the magnitude of  $C_D$ .  $C_D$  approximately equals  $C_{D*}$  (Fig. 4) for a wide range of  $Z_*$ . The  $U_{10}/G$  ratio varies significantly with both  $C_D$  and  $Z_*$  (Fig. 5). Strong winds in marginal seas are characterized by  $Z_*$  of order 10–15, which has a modest influence on  $C_s$  and  $\alpha$ , compared to unconstrained boundary layers ( $Z_* \sim 3$ ). The winter Arctic is characterized by  $Z_*$  of 20 to 40, maintained by radiational cooling of the surface and persistent large-scale subsidence;  $C_s$  is small, and  $\alpha$  is large (Carsey, 1980).

Three parameters define the high-latitude boundary layer during strong winds,  $\xi_* = Z_*/L_*$ ,  $Z_* = u_*/fZ_*$ , and  $Z_*$ . The stability function  $\xi_*$  is near -1 so the boundary layer is weakly unstable and turbulent production is dominated by wind shear. The effective stability length  $L_*$  differs from tower measurements in the centers of large floes in sign and magnitude. Convection, more typical of lower latitudes, does not play a significant role in inversion processes. In seasonal ice zones the inversion strength parameter  $Z_*$  is of order 10 to 15, so that the wind and stress profiles in high-latitude boundary layers are influenced somewhat by low inversions. Winter Arctic boundary layers, characterized by  $Z_* = 20$  to 40, have a large geostrophic/surface wind turning

angle and a low geostrophic drag coefficient, with low functional dependence on surface roughness.

This paper is a contribution to the Marine Services Project at the Pacific Marine Environmental Laboratory and was funded in part by the Arctic Program of the Office of Naval Research. This is PMEL Contribution Number 764.

## REFERENCES

Arya, S.P.S. and J.C. Wyngaard, Effect of baroclinicity on wind profiles and the geostrophic drag law for the convective planetary boundary layer, *J. Atmos. Sci.*, 32, 767–778, 1975.

Blackadar, A.K., The vertical distribution of wind and turbulent exchange in a neutral atmosphere, *J. Geophys. Res.*, 67, 3095–3120, 1962.

Brown, R.A., A simple momentum integral model, *J. Geophys. Res.*, 79, 4076–4079, 1974.

Carsey, F.D., The boundary layer height in air stress measurements, in *Sea Ice Processes and Models* (R.S. Pritchard, Ed.), pp. 443–451, University of Washington Press, Seattle, Washington, 1980.

Deardorff, J.W., Numerical investigation of neutral and unstable planetary boundary layers, *J. Atmos. Sci.*, 29, 91–115, 1972.

Fiedler, F. and H.A. Panofsky, The geostrophic drag coefficient and the effective roughness length, *Quart. J. Roy. Met. Soc.*, 98, 213–220, 1972.

Leavitt, E., Surface-based air stress measurements made during AIDJEX, in *Sea Ice Processes and Models* (R.S. Pritchard, Ed.), pp. 419–429, University of Washington Press, Seattle, Washington, 1980.

Lykosov, V.N. and L.N. Gutman, The stationary problem of turbulence in the terrestrial planetary boundary layer, *Izv., Atmos. Ocean Phys.*, 6, 1238–1254, 1970.

Malgarejo, J.W. and J.W. Deardorff, Stability functions for the boundary-layer resistance laws based upon observed boundary layer heights, *J. Atmos. Sci.*, 31, 1324–1333, 1974.

Maykut, G.A., Large-scale heat exchange and ice production in the central Arctic, *J. Geophys. Res.*, 87, 7971–7984, 1982.

Mellor, G.L. and T. Yamada, Development of a turbulence closure model for geophysical fluid problems, *Rev. Geophys. Space Phys.*, 20, 851–875, 1982.

Mofjeld, H.O. and J.W. Lavelle, Setting the length scale in a second-order closure model of the

unstratified bottom boundary layer, *J. Phys. Oceanogr.*, 14, 833-839, 1984.  
**Overland, J.E., H.O. Mofjeld and C.H. Pease**, Wind-driven ice drift in a shallow sea, *J. Geophys. Res.*, 89, 6525-6531, 1984.  
**Rothrock, D.A. and A.S. Thorndike**, Measuring the sea ice floe size distribution, *J. Geophys. Res.*, 89, 6477-6486, 1984.  
**Sverdrup, H.U.**, *The Norwegian North Polar Ex-*

*pedition with the "Maud," Vol. II: Meteorology*, Geophysical Institute, Bergen, 331 pp., 1933.  
**Wilson, J.G., A.L. Comiskey, R.W. Lindsay and V.L. Long**, Regional meteorology of the Bering Sea during MIZEX-West, February and March 1983, NOAA Special Report, Pacific Marine Environmental Laboratory, Seattle, Washington, 115 pp., 1984.

## APPENDIX: A DIAGNOSTIC MODEL FOR THE ARCTIC ATMOSPHERIC BOUNDARY LAYER

The steady boundary layer equation in complex notation is

$$if(\mathbf{V} - \mathbf{G}) = \partial \tau / \partial z \quad (A1)$$

where  $\mathbf{V}$  is the horizontal mean wind velocity,  $\mathbf{V} = U + iV$ ,  $i = \sqrt{-1}$ ,  $f\mathbf{G}$  is the pressure gradient force, and  $\tau$  is the turbulent stress (in kinematic units):

$$\tau = A \partial \mathbf{V} / \partial z, \quad (A2)$$

with  $A$  an eddy viscosity coefficient. Boldface denotes vector quantities in complex notation. Equations A1 and A2 are a coupled system of first-order differential equations subject to boundary conditions:

$$\tau = 0 \quad \text{at} \quad z = Z_i$$

$$\mathbf{V} = 0 \quad \text{at} \quad z = Z_o. \quad (A3)$$

One of the simplest differential models of turbulent mixing (Mofjeld and Lavelle, 1984) has  $A$  proportional to the product:

$$A = S_m q l, \quad (A4)$$

where  $S_m$  is a proportionality constant,  $l$  is a prescribed mixing length, and  $q$  is the turbulent intensity determined by the local turbulence balance between shear generation and viscous dissipation:

$$\tau \frac{\partial V}{\partial z} - \frac{q^3}{cl} = 0, \quad (A5)$$

where  $c$  is the dissipation constant. Since the turbulent production represented by the first term in eq A5 cannot depend upon how the turbulence is dissipated (Mofjeld and Lavelle, 1984),  $q$  must be proportional to  $c^{1/3}$ . Substituting the eddy coefficient stress relations A2 and A4 into eq A5 gives

$$q = c^{1/3} l \partial V / \partial z, \quad (A6)$$

and  $S_m = c^{-1/3}$ ; thus

$$A = l^2 \partial V / \partial z. \quad (A7)$$

The form of the mixing length is specified from Blackadar (1962):

$$l = kz(1 + kz/l_o)^{-1}, \quad (A8)$$

with the asymptotic value  $l_o$  given by Mellor and Yamada (1982):

$$l_o = \gamma L_o = \gamma \int_{Z_o}^{Z_i} z q dz \left[ \int_{Z_o}^{Z_i} q dz \right]^{-1}, \quad (A9)$$

where  $L_o$  is the scale height of the turbulent intensity and  $\gamma = 0.3$ , which is at the large end of the observed range, consistent with  $-\zeta_o \approx 1$  (Mofjeld and Lavelle, 1984). The solution integrates eq A1 and A2 downward from  $Z_i$  using a fourth-order Runge-Kutta scheme with 2001 points, where the spacing decreases logarithmically near  $Z_i$  and  $Z_o$ .

# NASA CV-990 Aircraft Observations During MIZEX-West

D.J. CAVALIERI, P. GLOERSEN AND T.T. WILHEIT  
Goddard Laboratory for Oceans, NASA Goddard Space Flight Center  
Greenbelt, Maryland 20771, USA

## INTRODUCTION

During the MIZEX-West Bering Sea experiment in February 1983, the NASA CV-990 airborne laboratory made a series of seven flights in coordination with the NOAA research ship *Discoverer*, the Coast Guard icebreaker *Westwind*, the NOAA WP-3D research aircraft, and the Nimbus 7 spacecraft. The purpose of these flights was first to assess the potential of using an extended range of frequencies for improving passive microwave sea ice observations from spacecraft, and second to provide an overview of the marginal ice zone

(MIZ) for large-scale processes studies. For these purposes, the CV-990 was equipped with both imaging and dual-polarized, fixed-beam passive microwave radiometers spanning a range of frequencies from 10 to 183 GHz. Visual, photographic, and thermal infrared surface observations were also made from the aircraft to complement the microwave measurements. The CV-990 also carried a Rutherford Appleton Laboratory (RAL) radar altimeter in support of the European Space Agency ERS-1 satellite program. A summary of aircraft instrumentation is given in Table 1.

Table 1. NASA CV-990 instrumentation.

Instrument	Frequency (GHz)	View angle	Polarization	Beam width	Resolution (altitude)	
<b>Passive microwave</b>						
Electrically scanned microwave radiometer (ESMR)	19.35	50°L-50°R	H	2.8°	1/20	
Aircraft multichannel microwave radiometer (AMMR)	10.7	45° Rt of nadir	H, V	6°	1/7	
	18.0		H, V	V		
	21.0		H, V			
	37.0		H, V			
Aircraft uplooker	21.0	22° Rt of zenith	—	6°	—	
	37.0					
Advanced microwave moisture sounder (AMMS)	92.0	45°L-45°R	Mixed	2°	1/30	
	183.0 ± 2.0					
	183.0 ± 5.0					
	183.0 ± 9.0					
<b>13.7 GHz Rutherford Appleton Laboratory radar altimeter</b>						
1. Altimeter mode						
2. Scatterometer mode						
<b>10.7-μm nadir viewing infrared radiometer (PRT-5)</b>						
<b>Cartographic cameras</b>						
1. KS-87B, 5-inch format, nadir viewing						
2. KS-87B, 5-inch format, 45° Rt of nadir viewing						

RD-R167 310 MIZEX A PROGRAM FOR MESOSCALE AIR-ICE-OCEAN INTERACTION 2/2  
EXPERIMENTS IN AR. (U) COLD REGIONS RESEARCH AND  
ENGINEERING LAB HANOVER NH P WADHAMS MAY 85

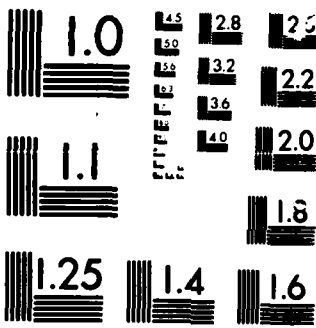
UNCLASSIFIED

CRREL-SR-85-6

F/G 8/12

NL





MICROCOM<sup>®</sup>

CHART

This report presents observations from both the NASA aircraft and the Nimbus 7 satellite for 10 and 21 February, two days that contrast the very different conditions in the MIZ during the experiment period. These two periods also provide a means of assessing the limitations of poor weather conditions on the high frequency microwave imager data. Finally, an analysis of the aircraft data provides a description of the microwave character of several sea ice types, and a comparison is made with data obtained from surface-based radiometric measurements.

## 10 FEBRUARY

During early February, the weather in the region was dominated by an extensive low pressure system located in the southern Bering Sea. Surface analysis charts for this period show easterly and southeasterly winds over the experiment region. The *Discoverer*, located at the ice edge, reported winds from 075° true at 28 knots ( $14.4 \text{ m s}^{-1}$ ). The *Westwind*, located in the pack, reported winds from 055° true at 27 knots ( $13.9 \text{ m s}^{-1}$ ).

Fig. 1a shows the ice concentration distribution for the Bering Sea based on Nimbus 7 SMMR observations for 10 February. On this map, ice concentration contours are drawn every 10% from 25% to 95%. The position of the ice edge is defined by the sharp gradient of contours from 25% to about 65%. Large areas of concentrations greater than or equal to 85% are found in the central basin. Lower concentrations are found to the west of the Alaskan coast and to the northwest of Nunivak, St. Lawrence, and St. Matthew Islands. The positions of the *Discoverer* and the *Westwind* are indicated by D and W respectively. P refers to a large polynya observed from the NASA CV-990. The four parallel lines represent that portion of the aircraft flight pattern designed to obtain contiguous swaths of the MIZ with the aircraft microwave imagers. During the time of the NASA aircraft overflight, the *Westwind* reported  $\frac{1}{10}$  ice cover, which is consistent with the SMMR ice concentration contours in the vicinity of the ship.

Fig. 2a shows the mosaic image produced with the 92-GHz channel of the AMMS instrument from the four CV-990 tracks to the east of St. Matthew Island as shown in Fig. 1a. The location of St. Matthew Island and the position of the *Westwind* during the time of the overflight are indicated. The mosaic is composed of four swaths, each having a width of about 21 km, twice the aircraft altitude. Allowing for some overlap, the mo-

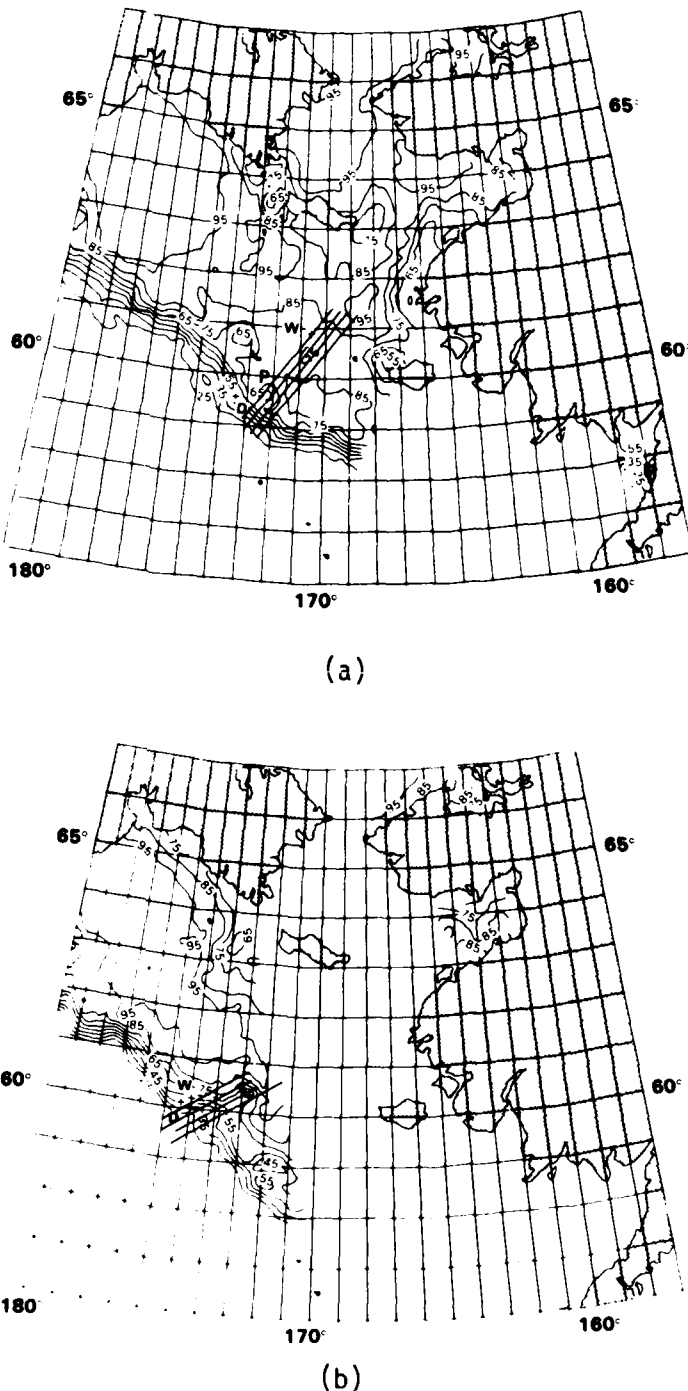


Fig. 1. Nimbus 7 SMMR ice concentration contours for a) 10 February and b) 21 February 1983.

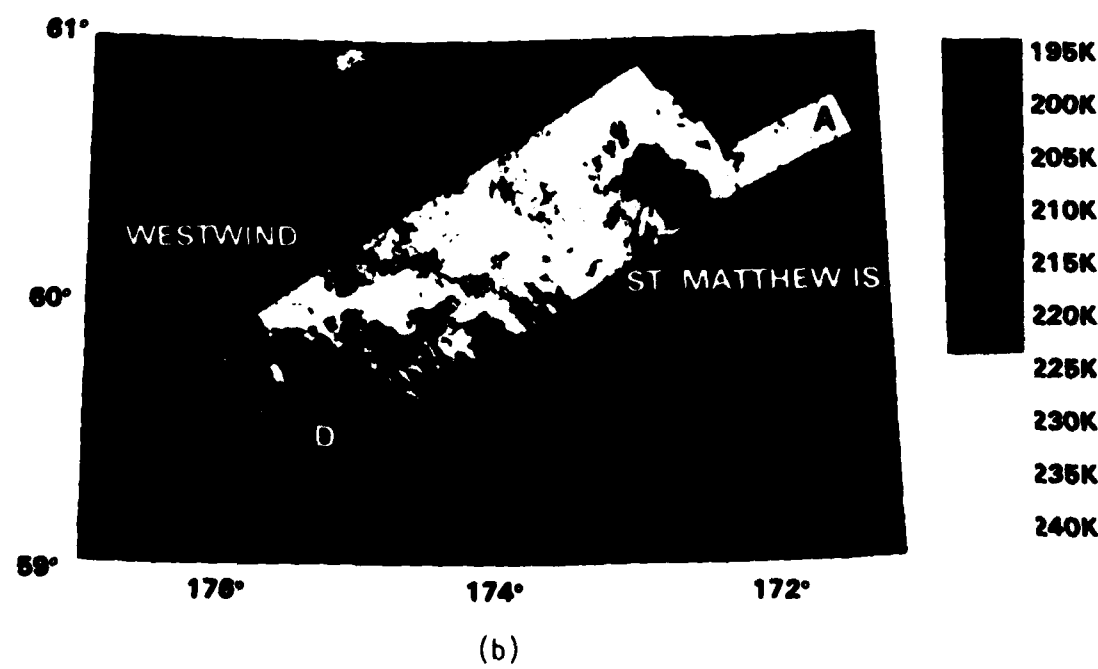
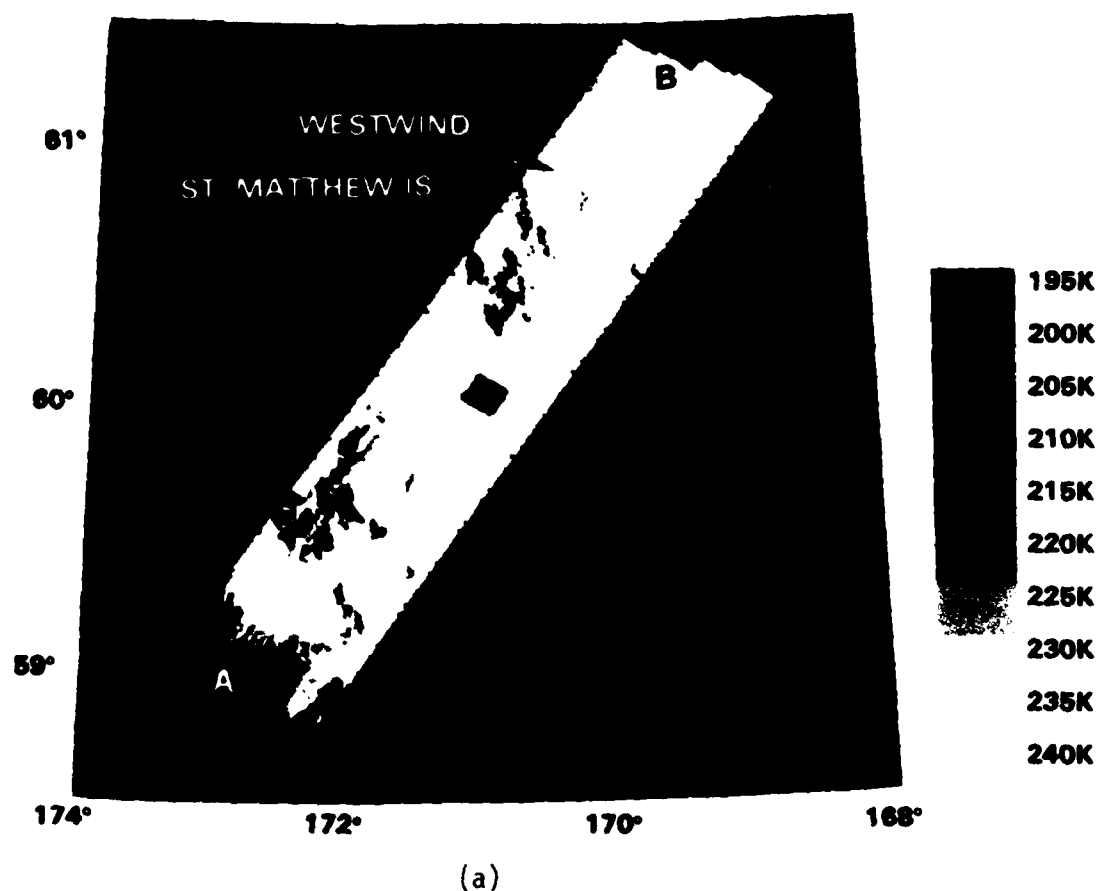


Fig. 2. 92-GHz AMMS mosaic image for a) 10 February and b) 21 February 1983.

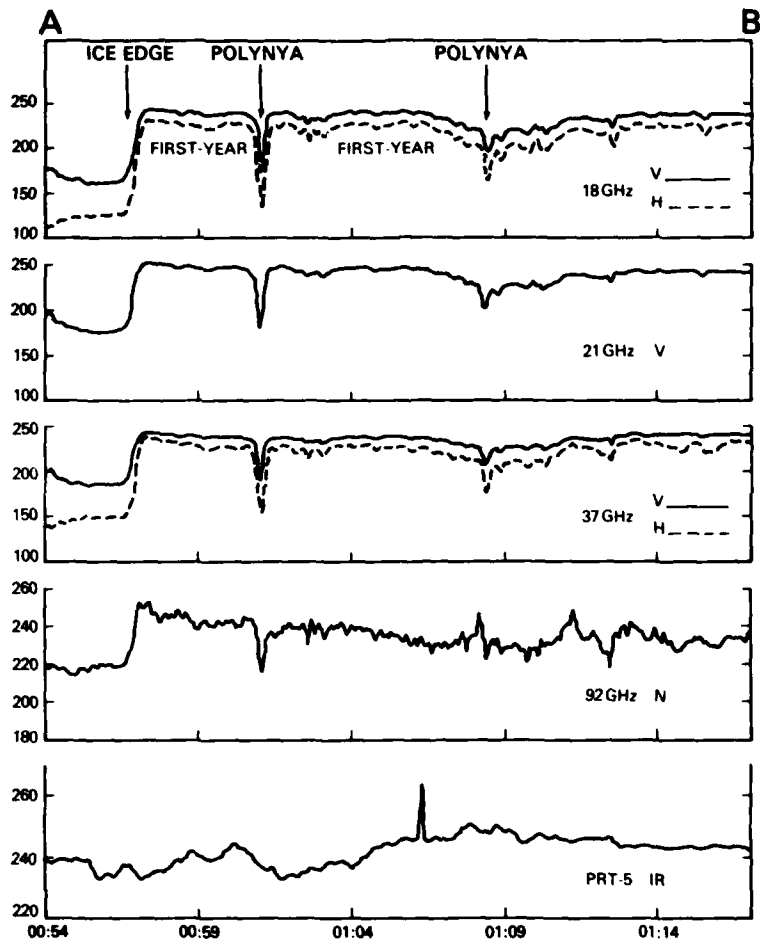


Fig. 3. Microwave and infrared temperatures measured along the third leg (A-B) of the mosaic pattern shown in Fig. 2a.

saic covers an area approximately 70 by 340 km and shows a range in brightness temperature from 210 K over open ocean to 245 K over consolidated pack ice.

Although the heavy cloud cover on 10 February resulted in some loss of ice-water contrast, the mosaic shown in Fig. 2a nevertheless provides good definition of the MIZ character. From this figure, we see that the MIZ is fairly compact, with a few discernible polynyas. Ice streamers are also observed at right angles to the ice edge. The large polynya labeled with the letter P centered at 59.6°N and 172.3°W is oriented in a northeast-southwest direction and is observed in the SMMR ice concentration contour map for 10 February (Fig. 1a) as noted earlier. The orientation of both the polynya and ice streamers is roughly 30° to the right of the wind.

Brightness temperatures obtained with the 18-,

21-, 37- and 92-GHz radiometers, and thermometric temperatures obtained with the PRT-5 IR radiometer, all plotted against GMT time (hr:min) are shown in Fig. 3 for 10 February. The 18- and 37-GHz horizontally and vertically polarized radiances and the 21-GHz vertically polarized radiances are plotted. The 92-GHz AMMS data represent equivalent nadir values at all scan positions and the values plotted were averaged over the 49th and 50th beam positions corresponding to the field of view of the fixed-beam radiometers. All traces shown in the figure were taken along the third leg of the mosaic shown in Fig. 2a, as indicated by the letters A and B in both figures.

All microwave channels clearly show the ice edge indicated by the steep rise in brightness temperature, the large polynya P, and the numerous smaller polynyas further along the track. Visual observations of these features as well as reports on

ice type and concentration were made through occasional openings in the cloud cover. While there is little spectral variation among the three lowest frequencies, the 92-GHz data exhibit far greater variability, which is due in large part to the radiometer's higher resolution. The higher frequency is also more sensitive to surface-related effects as discussed below. The difference between the vertically and horizontally polarized brightness temperatures at 18 and 37 GHz discriminates between open water and compact ice and tracks variations in ice compaction. Except in the vicinity of the polynyas, the ice cover consists of consolidated first-year ice, which is reflected in the fairly uniform brightness temperatures and polarization at 18 and 37 GHz. Because of poor weather conditions, the IR radiometer does not "see" the surface and gives temperatures that are considerably lower than actual surface values.

## 21 FEBRUARY

Between 14 and 19 February there was a marked change in the weather pattern; the high pressure system over Siberia intensified and the Bering Sea low pressure system moved eastward into the Gulf of Alaska. The position of these two centers resulted in a pattern more typical of the Bering winter, with strong, cold winds out of the northeast. 21 February was fairly typical of the weather conditions that dominated the latter half of the experiment. The visibility was generally clear, with northeasterly winds driving the ice to the southwest.

Sea ice concentration contours for 21 February are shown in Fig. 1b. Although the Nimbus 7 SMMR coverage on this day is limited to the western portion of the Bering Sea, it does include the experiment area in the vicinity of St. Matthew Island. As on the map for 10 February, the positions of the *Discoverer* and the *Westwind* are indicated for the time of the SMMR overpass. The *Discoverer*, located at the ice edge, reported winds out of the northeast at 20 knots ( $10.3 \text{ m s}^{-1}$ ). The *Westwind* was well within the ice-edge zone and reported a  $\frac{1}{10}$  ice cover. Examination of Fig. 1b shows the entire MIZ to the east of St. Matthew Island to have extended farther south than in Fig. 1a and to have become considerably more diffuse. The St. Matthew Island polynya, which had been a low ice concentration region to the northwest of St. Matthew Island, is now a well-developed polynya to the southwest as observed in Fig. 1b. Within the interior pack, the low ice concentration southwest

of St. Lawrence Island is associated with a region of high ice divergence south of Anadyr Strait.

Fig. 2b shows the 92-GHz AMMS mosaic for 21 February and includes the location of St. Matthew Island and the position of the *Westwind* during the time of the overflight. The mosaic, which covers an area of about 70 by 220 km, shows a much more diffuse ice edge zone than was observed in the mosaic for 10 February (Fig. 2a). There is also a sharper contrast between open water and ice, resulting from the improved atmospheric conditions. This contrast is 10 to 15 K greater than for 10 February, indicating a decrease of approximately 0.04 to 0.06 in atmospheric opacity at 92 GHz. The variation in brightness temperature observed in this figure is due to a variation in both ice compactness and ice type. The first leg of the mosaic, labeled by the letters A and D, is used to illustrate and interpret this variation. Fig. 4 shows the microwave brightness temperatures and the PRT-5 temperature for this leg. The leg starts northeast of St. Matthew Island, a region of consolidated first-year ice that exhibits the highest brightness temperature at all frequencies, the lowest polarization at 18 and 37 GHz, and a PRT-5 temperature of 254 K. The initial decrease in brightness temperature observed at the lower frequencies between 2226 and 2227 GMT reflects the radiometrically colder surface of the island. Just north of the island, the 92-GHz data show a very different signature. While the reason for this is uncertain, it is possibly related to the shear zone observed north of the island, where there was heavy ridging of thick first-year ice, which is likely to be accompanied by heavy snow accumulation. This observation is coincident with the steep decrease in brightness temperature. The gradual decrease over the island may reflect an additional variation in snow cover.

The area of open water and newly formed ice southwest of the coastline defines the lee shore polynya. By 2228 the new ice driven southward consolidates, forming young ice, and further thickens, forming thin first-year ice that is as radiometrically bright as the thick ice north of the island. At about 2232 the ice edge of the main pack is encountered, followed by numerous ice bands labeled C.

Finally, the microwave polarization (defined by  $(V-H)/(V+H)$ ) was calculated at both 18 and 37 GHz for several sea ice types and open water from the fixed-beam radiometric data obtained with the NASA CV-990 aircraft and from surface radiometric observations obtained by Grenfell (1984). Fig. 5 illustrates the variation in polarization with

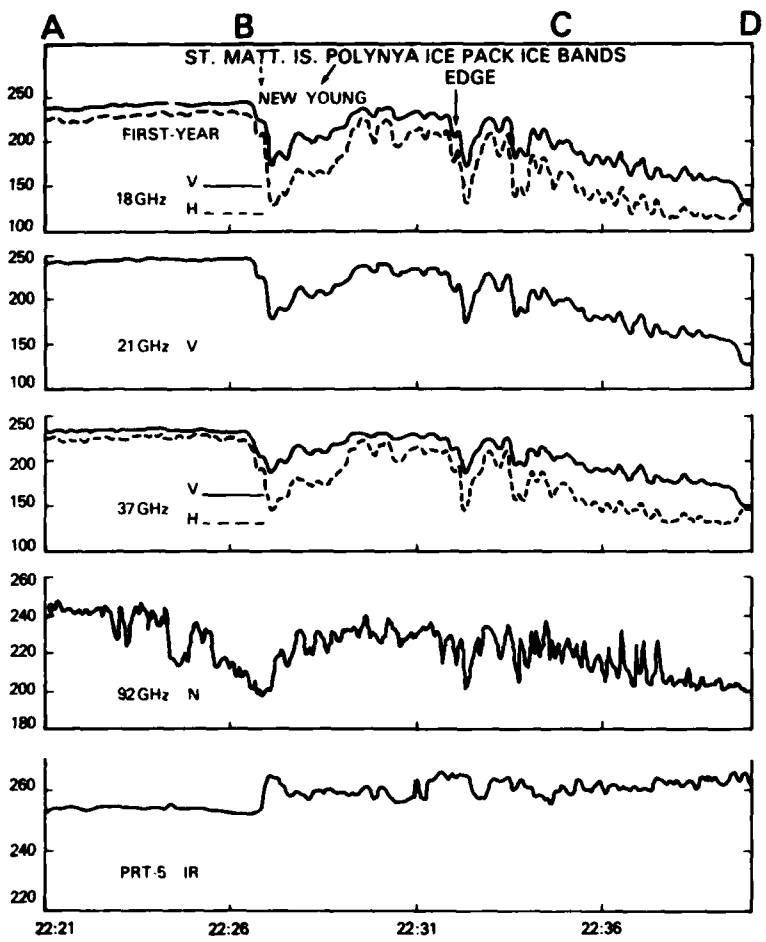


Fig. 4. Microwave and infrared temperatures measured along the first leg (A-D) of the mosaic pattern shown in Fig. 2b.

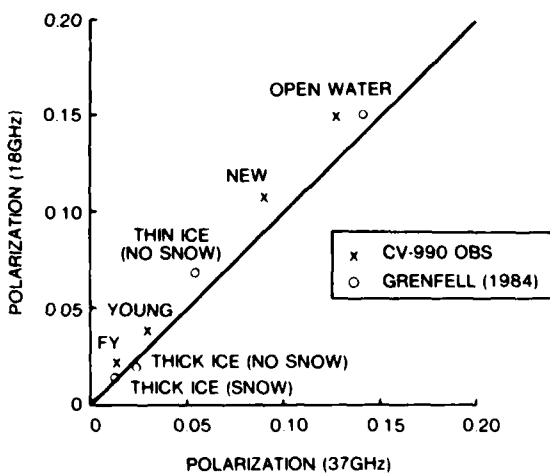


Fig. 5. Comparison of the polarization at 18 and 37 GHz for several sea ice types and open water.

ice type and open water for both data sets. The identification of the CV-990 ice types was made from visual and photographic observations. The first-year ice sample corresponds to snow-covered thick ice, the young ice sample to snow-free grey ice, and new ice to an area of slush and shuga in the polynya south of St. Matthew Island.

#### REFERENCE

**Grenfell, T.C.**, Surface based brightness temperatures of sea ice in the Bering and Greenland Seas, *Proc. IGARSS '84 Symp., Strasbourg, 27-30 Aug.*, 1984.

# Measurement of the Complex Refractive Index of First-Year Sea Ice and Snow Using a Microwave Untuned Cavity

RODNEY J. KNIGHT AND DAVID T. LLEWELLYN-JONES

*Rutherford Appleton Laboratory, Science and Engineering Research Council  
Chilton, Didcot, Oxfordshire OX11 0QX, England*

## ABSTRACT

A microwave untuned cavity has been used to measure the dielectric properties of first-year sea ice and saline snow at frequencies between 9 GHz and 120 GHz. The cavity, approximately 1 m in diameter and 1.2 m high, was located on board the NOAA research ship *Discoverer* during the February 1983 Marginal Ice Zone Experiment (MIZEX-West) in the Bering Sea. Measurements at one frequency, 13.7 GHz, were made to assist in the interpretation of remotely sensed radar altimeter data from concurrent aircraft overflights.

The results show that the absorption index  $k$  is proportional to the salinity, measured from the DC conductivity  $\sigma$ , and to the density  $\rho$ ; the frequency variation has a broad absorption minimum around 60 GHz. The refractive index  $\eta$  increases with salinity and slightly with frequency.

## INTRODUCTION

Ice, snow and water cover more than three-quarters of the earth's surface; knowledge of their spatial and temporal variations is a major input to studies of climatology, oceanography and resource management. The collection of these data on a global scale is only practical by remote sensing from satellites, and thus an understanding of the interaction between electromagnetic radiation and the various constituent parts of the hydro-sphere is essential. The polar regions, in particular, pose special problems in remote sensing. Not only are they significant reservoirs in the global heat budget and the hydrological cycle, but the wide diversity of physical characteristics found in the surface topography makes the analysis of remote sensing data difficult.

One approach to the problem is to establish an empirical relationship between the data and near-

simultaneous ground truth. This requires a lot of physically difficult measurements and means that interpretation of the data from a particular sensor cannot be achieved until an appropriate quantity has been analyzed. Another approach is to model the sensor response to a variety of possible surface characteristics, making use of accumulated statistics. In order to do this, the electromagnetic properties of the surface must be known over a wide range of conditions.

## DIELECTRIC PROPERTIES OF SEA ICE AND SNOW

The optical properties of a material, as a function of frequency  $\nu$  or wavenumber  $v = \nu/c$ , are defined by the complex refractive index

$$\eta = \eta' - ik \quad (1)$$

where the real part  $\eta'$  relates to the phase velocity of propagation in the material and the imaginary part  $k$  is the absorption index. The dielectric properties are defined by the complex relative permittivity

$$\epsilon = \epsilon' - i\epsilon'' \quad (2)$$

where

$$\epsilon = (\eta)^2. \quad (3)$$

The power absorption coefficient  $\alpha$  may be obtained from a measure of the transmission  $T$  of a sample with thickness  $t$ .

$$T = \exp(-\alpha t) \quad (4)$$

where

$$\alpha = 4\pi k v. \quad (5)$$

The loss is sometimes expressed in terms of the loss angle  $\delta$  where

$$\tan \delta = \frac{e''}{e'} = \frac{2\eta k}{\eta^2 - k^2}. \quad (6)$$

The accurate measurement of these quantities traditionally requires precisely formed samples, either to fit into a waveguide for microwave measurements or at higher frequencies for Fourier transform spectroscopy. Untuned cavities can be used with samples in almost any geometric form or state of matter and are thus well-suited to the analysis of naturally occurring substances.

Sea ice has a complicated structure; in a matrix of low loss pure ice is a mixture of high loss brine inclusions, air bubbles and hydrolyzed salts. The composition is temperature- and history-dependent. The ice can be anisotropic, and scattering may be an important part of the losses at some frequencies.

The snow in the Bering Sea initially falls as a low-specific-gravity (s.g.  $\sim 0.1$ ), relatively clean substance, but gradually compacts with time. At the edge of the pack ice, salt spray adds to the snow, increasing its salinity, while seawater washing over the snow causes areas of melting. On refreezing, it is formed into brittle ice of specific gravity around 0.5. Analysis of sea ice is complicated by the drainage of brine from the structure after collection, which alters the density, salinity and electromagnetic properties. There are few existing microwave measurements on naturally occurring sea ice (e.g. Sackinger and Byrd, 1972; Vant, 1974) and none on this form of snow.

## THE UNTUNED CAVITY

The untuned cavity, originally developed for acoustic measurements (Knudsen, 1933), and later used for the measurement of the absorption in moist air (Becker and Autler, 1946), has been successfully exploited for the measurement of losses in irregularly shaped polymers (Llewellyn-Jones et al., 1980). The cavity is an overmoded resonator with linear dimensions of many wavelengths ( $\geq 20\lambda$ ); electromagnetic power is fed into the cavity via a small horn while a rotating paddle stirs the mode pattern of the radiation. The high density of modes excited by this arrangement, and their continual alteration, ensures a structure whose  $Q$  is substantially independent of frequency. A detec-

tor placed anywhere inside the cavity will give an output proportional to the  $Q(S_1)$ . If some absorbing material is introduced into the cavity, the  $Q$  will be degraded and the signal will fall to a level  $S_2$ . It may be shown that (Llewellyn-Jones et al., 1980)

$$\alpha = \left( \frac{S_1}{S_2} - 1 \right) \frac{A_H}{4V\theta} \quad (1)$$

where  $V$  is the sample volume and  $A_H$  a calibration factor for the cavity.  $\theta$ , a dimensionless number of order unity, is a "shape factor" and accounts for self-screening of the sample interior and for multiple paths traversed by radiation in the sample.  $A_H$  can be obtained by introducing a known loss to the system. A hole, which behaves as a perfect absorber to the radiation inside the cavity, has a loss proportional to the hole area.  $A_H$  is then the hole area which loads the cavity by 50% and is therefore equivalent to the internal losses within the cavity. The value of  $A_H$  varies smoothly with frequency, and the cavity is usable over a wide frequency regime. The shape factor is more complicated. For simple shapes, of low loss material (where low loss is defined by  $\alpha \ll 1$ ), it may be computed. When the sample dimensions are more than a few wavelengths the value of  $\theta$  is approximately 1.6. By experiment (Llewellyn-Jones et al., 1980) irregular shapes have the same value of  $\theta$ . When the sample size is small compared to the wavelength  $\theta$  drops to 1. For samples of higher loss, the interior of the sample sees less of the radiation and the value of  $\theta$  falls as the loss or size increases.

Due to the nature of the cavity technique, any scattered radiation from the sample is not lost to the system, and the irradiation of the sample from all directions removes any anisotropic or polarization effects. What is measured, then, is the true dielectric loss  $k$  of the ice and its constituents.

A reflectivity measurement can be performed by covering an aperture in the cavity with the sample. Radiation is reflected back into the cavity, the amount being a function of  $\eta$ ,  $k$ , the frequency  $v$  and the sample thickness  $t$ . For very low loss material the value of  $k$  has little effect on the reflectivity, and  $\eta$  can be obtained, usually by measuring the reflectivity for several values of  $t$  in order to resolve ambiguities. For high loss or thick samples the reflectivity depends only on the properties of one surface and is virtually independent of  $k$ ,  $v$  and  $t$ .

## EQUIPMENT

The untuned cavity, a fibreglass drum 1 m in diameter and 1.2 m high, lined with aluminium foil, was located onboard the NOAA research ship *Discoverer* in a horse-box trailer on the aft deck. An aluminium lid on the cavity supported the microwave sources, the detectors and the stirrer motor. Gunn diode oscillators were used at 9.45 GHz, 13.7 GHz and 25 GHz, with crystal detectors. Impatt oscillators were used at 64.7 GHz, 98 GHz, 110 GHz and 120 GHz with an infrared detector placed at a small aperture in the side of the cavity. The sources were modulated, either on the power supply or by means of a ferrite modulator. The output of the appropriate detector was fed to a lock-in amplifier and from there to a chart recorder. All analysis was from the chart recordings. The trailer provided some protection for the equipment, but as it was unheated, all the measurements were made at ambient temperature. This varied between +1°C and -15°C, depending on the ship's position, but was usually around -5°C. The majority of samples had some measurements made on the day of collection, and were then stored in a deepfreeze at -25°C for further measurements.

## MEASUREMENTS

The type and distribution of ice floes in the marginal ice zone is highly variable, depending upon the recent history of the area. Local weather and ice conditions dictated how and where samples were collected; under good conditions boats were used to transfer people to the larger ice floes where cores and surface samples could be obtained. When the winds were too high for safe boat operations, a volunteer was lowered by the ship's crane to collect samples (Fig. 1). Samples that consisted of snow or crushed ice particles had the absorption loss measured as a function of mass. Larger pieces of ice, cut from cores, were measured for absorption loss and for reflectivity. Densities were measured wherever possible by linear measurement and weighing. For those ice samples whose specific gravity could not be measured, the mean of the measured samples, which varied between 0.70 and 0.85, was used. The specific gravity of the snow increased with time, one sample changing from 0.133 on collection to 0.308 the following morning. The more usual change in specific gravity was about 0.02 day<sup>-1</sup> from a value



Fig. 1. Collection of surface samples from small cakes in bad weather, using cage suspended from *Discoverer*'s crane.

of about 0.3 when collected. Temperature measurements were made with a mercury thermometer, and snow temperatures could be obtained to about  $\pm 0.3^\circ\text{C}$ . Ice samples were assumed to be at the trailer ambient temperature. Samples that had been in the freezer were left in the trailer to allow the temperature to stabilize before they were re-measured.

The salinity of the samples was obtained by measuring the DC conductivity of the melted sample with a conductivity bridge, checked against the ship's salinometer. It was not possible to use the salinometer for routine measurements, as the majority of the samples were of insufficient volume. Brine drainage occurs on all samples once they are removed from the floe, and thus the measured salinity becomes a function of time. The value of rapid, *in situ* measurements is apparent. For all the measurements on snow and crushed ice the actual sample used had the salinity measured the same day. For the large pieces of ice, the surrounding ice was measured on the day of cutting, and the actual sample at the end of the measurement sequence, several days later. The brine drainage was assumed to be linear between these two values to obtain the salinities on intermediate days. Measured conductivities of the ice, which is all first-year, varied between  $3500 \mu\text{mho cm}^{-1}$  and  $20,000 \mu\text{mho cm}^{-1}$  ( $2.1\%$  to  $13.4\%$ ), with a daily change in the range 60 to  $200 \mu\text{mho cm}^{-1}$ . The snow conductivity varied between  $40 \mu\text{mho cm}^{-1}$  and  $14,000 \mu\text{mho cm}^{-1}$ , while some slushy ice samples, collected from small floes where the sea was washing over them, were as high as  $37,500 \mu\text{mho cm}^{-1}$  ( $25.4\%$ ).

## RESULTS

The absorption coefficients of snow and crushed ice were measured as a function of mass for a number of samples at frequencies between 9.45 GHz and 120 GHz. Using eq 7, graphs of  $\alpha\theta$  as a function of mass were obtained (Fig. 2). From a knowledge of the behaviour of  $\theta$ , i.e. rising from 1 to about 1.6 and then decreasing with increasing mass, an empirical relationship between  $\theta$  and mass for samples of different salinity and density could be obtained. This relationship could then be used to obtain values of  $\theta$  for the loss measurements on the ice blocks. The absorption coefficient per unit density is found to be directly proportional to the DC conductivity (Fig. 3, 4). Some of the scatter will be caused by not knowing the density correctly, or by incorrect interpolation of conductivity, and by temperature variations. A summary of the data taken at all frequencies is presented in Table 1, which also indicates the range over which a typical sample can vary. Fig. 5 and 6 show the variation of  $k$  with frequency for some low loss snow samples and for ice pieces cut from one core. As the frequency increases,  $k$  passes through a minimum and then starts to rise.

Because the measurement temperature was not controllable, there is an insufficient range of data to properly characterize the temperature dependence. The general trend, however, was of decreasing absorption with decreasing temperature, as the amount of brine in the ice diminished. There was some indication that at the higher frequencies the absorption rises with decrease of temperature. This may indicate that the losses in the crystallized

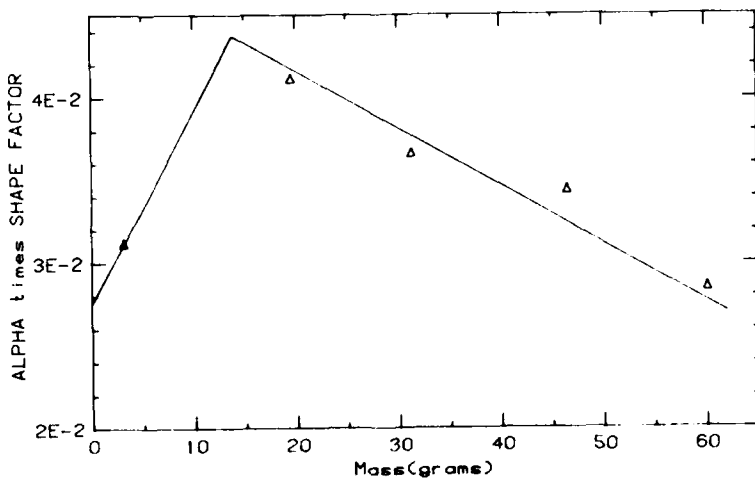


Fig. 2. Typical variation of loss as a function of mass for a uniform snow sample at 25 GHz,  $-5^\circ\text{C}$ .

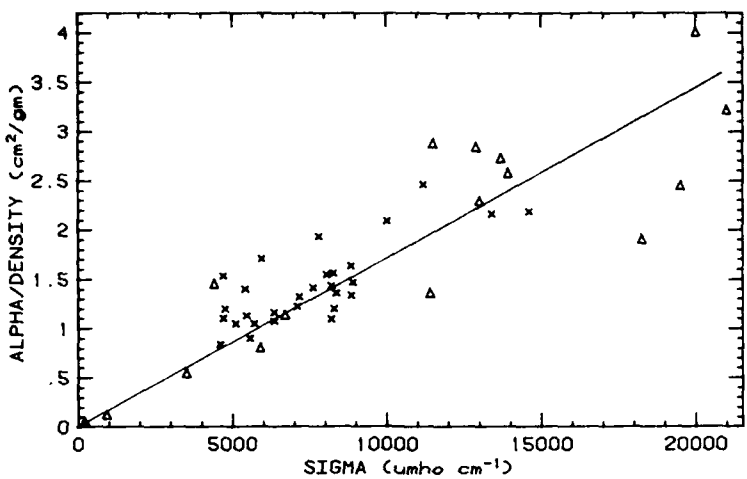


Fig. 3. Comparison of the absorption coefficient measured at 13.7 GHz in the untuned cavity with DC conductivity measurements for both blocks of ice (crosses) and for crushed ice and snow (triangles).

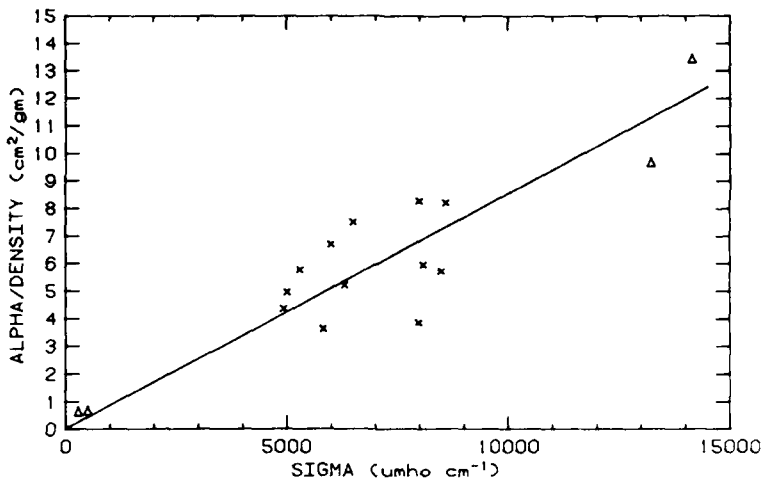


Fig. 4. Comparison of the absorption coefficient measured at 120 GHz in the untuned cavity with DC conductivity measurements for both blocks of ice (crosses) and for crushed ice and snow (triangles).

Table 1. Summary of measurements on first-year sea ice and snow.

Frequency (GHz)	Temp range of sea ice measurements (°C)	Salinity range of sea ice measurements (‰)	Gradients of best fit line attenuation ( $\alpha/\sigma \varrho$ ) ( $\text{cm}^2 \text{g}^{-1} \mu\text{mho}^{-1} \times 10^4$ )	Estimated attenuation range for typical sample of first-year sea ice $\varrho = 0.8$ $s = 4\text{‰}$ ( $\text{cm}^{-1}$ )
9.45	1-5.3	2.8-9.3	$1.529 \pm 0.099$	0.4-1.0
13.7	1-10.5	2.1-14.1	$1.748 \pm 0.082$	0.7-1.4
25	3.5-8	2.7-14.1	$1.949 \pm 0.081$	0.8-1.6
64.7	4-6	2.8-11.8	$3.513 \pm 0.121$	1.7-2.4
98	4.2-4.4	2.9-8.8	$4.363 \pm 0.316$	1.6-2.8
110	4.1-5	2.0-12.0	$5.562 \pm 0.388$	2.1-4.5
120	3.4-3.8	3.1-9.3	$8.512 \pm 0.458$	3.0-6.0

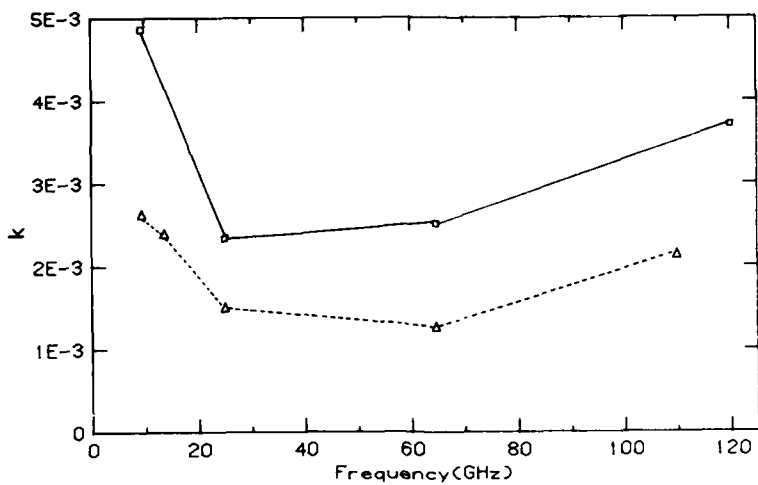


Fig. 5. The variation of  $k$  with frequency for two low loss snow samples, measured at temperatures between  $-2^{\circ}\text{C}$  and  $-7^{\circ}\text{C}$ . The solid line is for a sample with DC conductivity  $\sigma = 500 \mu\text{mho cm}^{-1}$  and the dotted line is for a sample with  $\sigma = 200 \mu\text{mho cm}^{-1}$ .

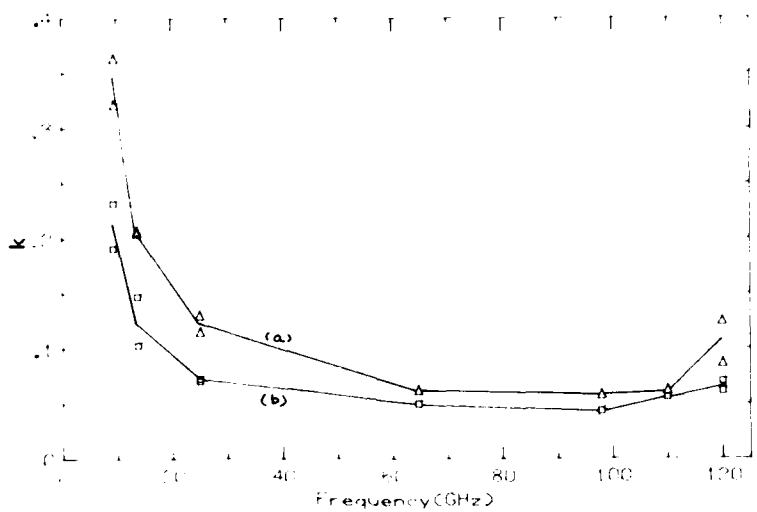


Fig. 6. The variation of  $k$  with frequency for ice cubes cut from one core: a) top 2 cm, salinity =  $5.2\text{\textperthousand}$ ; b) 30-32 cm depth, salinity =  $3\text{\textperthousand}$ . Points are spot measurements on different days and at temperatures between  $-3^{\circ}\text{C}$  and  $-5^{\circ}\text{C}$ .

salts increase with frequency at a rate such that they become comparable, together with the ice that is formed on cooling, with the brine they replace. In Fig. 5, the increase in loss in the snow at high frequency is greater than the corresponding increase in the ice loss (Fig. 6), and may represent the same effect, as the snow salinity will be mainly due to crystalline salt rather than brine.

Reflectivities were measured on various sections of ice core; at the higher frequencies only a small thickness of ice is required to reach the criterion of "high loss" and the reflectivity measurement then gives an unambiguous value of  $\eta$  (Fig. 7). At lower frequencies the rear face of the sample contributes to the reflected radiation and complicates the analysis. Fig. 8 shows the measured refractive in-

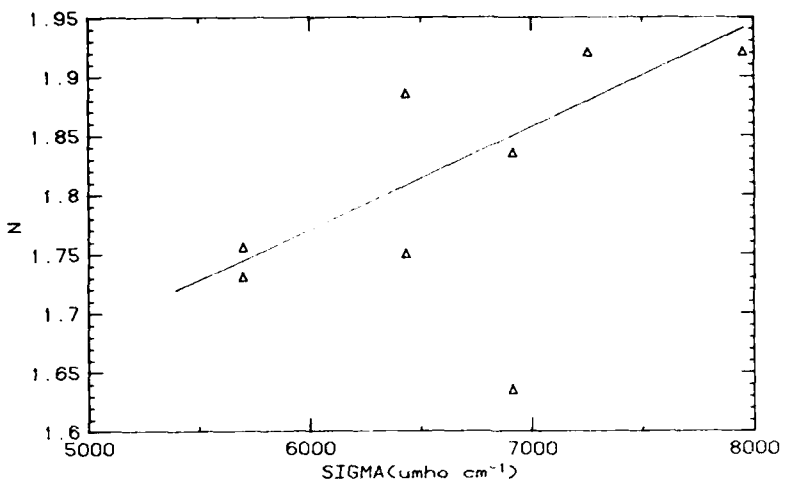


Fig. 7. The real part of the refractive index of sea ice measured at 120 GHz as a function of DC conductivity, and a temperature of -7°C.

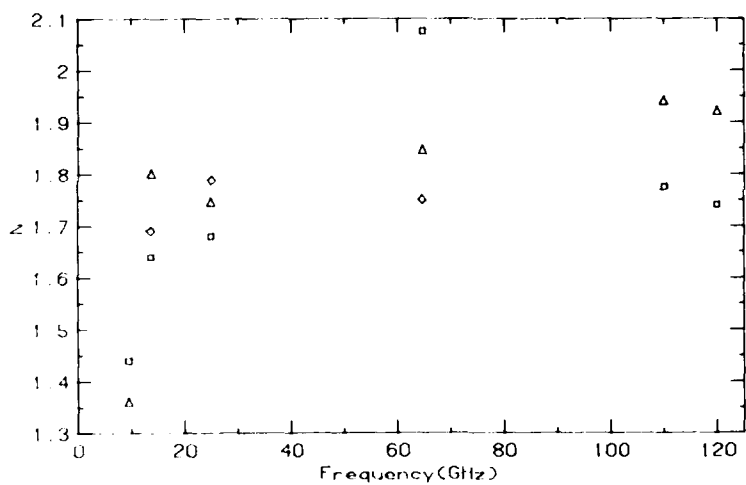


Fig. 8. The real part of the refractive index of three samples of sea ice as a function of frequency, at temperatures between -4.5°C and -9.5°C. triangles:  $\sigma = 6850-7600 \mu\text{mho cm}^{-1}$ ; squares:  $\sigma = 6200-6913 \mu\text{mho cm}^{-1}$ ; diamonds:  $\sigma = 7500-8950 \mu\text{mho cm}^{-1}$ .

dex as a function of frequency for three slabs of ice, where the measurements were spread over a number of days. The 9.45-GHz results appear too low, and probably indicate that the sample size was inadequate for that wavelength.

Table 2 lists those published measurements, both on natural and on artificial sea ice, that fall in this temperature and frequency range. The published data, usually in the form of the dielectric constant, have been converted to  $\eta$ ,  $k$  and  $\alpha$ . The

data on natural sea ice are in good agreement; the 10-GHz data in this paper are at a higher temperature range than those of Vant (1974), so the attenuation would be expected to be higher. Sackinger and Byrd (1972) were only able to measure one polarization at this temperature; the loss tangent for parallel polarization is expected to be greater than for perpendicular. The spread of values on the artificial sea ice is much greater. Bogorodskii and Khokhov (1977) do not quote a salinity

**Table 2. Existing measurements on natural and artificial sea ice.**

Author	Frequency (GHz)	Salinity (‰)	Temp. (°C)	$\eta$	$k$	$\alpha$ (cm <sup>-1</sup> )
<b>Natural sea ice</b>						
Vant (1974)	10	3.2-4.6	2.5-9.3	1.75-2.06	0.24-0.17	0.10-0.69
Sackinger and Byrd (1972) (Perpendicular polarization)	29-37	2.85-7.2	7	1.63-1.88	0.033-0.137	0.52-2.06
<b>Artificial sea ice</b>						
Vant (1974)	34	8	7	1.74	0.03	0.46
Hoekstra and Cappillino (1971)	10 20 23	8 8 8	10 10 9	3.1 3.1 3.1	0.18 0.45 0.58	0.74 3.8 5.6
Bogorodskii and Khokhov (1977)	10	15*	2.5	3.4	0.60	2.5

\* Estimates.

value, but as it is for freshly formed grease ice it is unlikely to be below 10‰ and is probably nearer 20‰. It must be remembered also that measurements of  $\alpha$  in this table will include any losses due to scattering.

## CONCLUSIONS

These preliminary experiments on sea ice, the first to be reported at frequencies above 40 GHz, demonstrate the potential of the untuned cavity for measuring the dielectric properties of complex substances in non-analytic shapes. This feature of the technique is especially valuable for measurements on naturally occurring substances, where the physical changes necessary to make a conventional measurement may alter the electromagnetic properties. The understanding of how the electromagnetic properties of sea ice and snow at various frequencies are related to parameters such as temperature, salinity and density is a necessary part of the analysis of remotely sensed radar echoes and radiometer returns. The correlation of remote sensing with simple in situ measurements can provide realistic physical models, and thus improve the accuracy of interpretation of future satellite data. An accurate knowledge of the fundamental properties of water, salt and brine at frequencies between 10 GHz and 500 GHz is currently lacking (Warren, 1984) and measurements in this region are urgently required.

## REFERENCES

Becker, G.E. and S. Autler, Water vapour absorption of electromagnetic radiation in the centimetre wavelength range, *Phys. Rev.*, 70, 300, 1946.

Bogorodskii, V.V. and G.P. Khokhov, Anisotropy of the microwave dielectric constant and absorption coefficient of Arctic drift ice, *Sov. Phys. Tech. Phys.*, 22, 743, 1977.

Hoekstra, P. and P. Cappillino, Dielectric properties of sea and sodium chloride ice at UHF and microwave frequencies, *J. Geophys. Res.*, 76, 4922, 1971.

Knudsen, V.O., The absorption of sound in air, in oxygen and in nitrogen: Effects of humidity and temperature, *J. Acoust. Soc. Am.*, V, 112, 1933.

Llewellyn-Jones, D.T. et al., New method of measuring low values of dielectric loss in the near millimetre wavelength region using untuned cavities, *Proc. IEEE*, 127A, 535, 1980.

Sackinger, W. and R. Byrd, Backscatter of millimetre waves from snow, ice and sea ice, in *Proceedings, Conference on Propagation of Radio Waves at Frequencies Above 10 GHz*, Institute of Electrical and Electronics Engineers, London, pp. 219-228, 1972.

Vant, M.R., Dielectric properties of fresh and sea ice at 10 and 35 GHz, *J. Appl. Phys.*, 45, 4712, 1974.

Warren, S.G., Optical constants of ice from the ultraviolet to the microwave, *Appl. Optics*, 23, 1206, 1984.

## Fluctuations of Flow Through Bering Strait

J.D. SCHUMACHER AND A.T. ROACH

*Pacific Marine Environmental Laboratory/NOAA  
Bin C15700, 7600 Sand Point Way NE  
Seattle, Washington 98115, USA*

K. AAGAARD

*School of Oceanography, University of Washington  
Seattle, Washington 98195, USA*

### INTRODUCTION

Bering Strait provides the only avenue of exchange between the Pacific and Arctic Oceans. The mean northward transport has been estimated to be of order 1 Sverdrup (Coachman et al., 1975), and this influx is of major consequence for the density structure of the Arctic Ocean (Coachman and Barnes, 1961; Aagaard et al., 1981; Killworth and Smith, 1984) and the nutrient budget (Codispoti, 1979). Recent work also emphasizes the importance of the Bering Strait flow to ice conditions in the Chukchi Sea (Reynolds and Pease, 1984) and to the primary production of this region (Sambrotto et al., 1984). The mean flow appears driven by a sea surface slope downward towards the north of order  $10^{-6}$  (Coachman and Aagaard, 1966), which is probably of steric origin (Coachman et al., 1975; Stigebrandt, 1984). There is, however, substantial evidence of atmospherically forced major variability in the flow, including reversals to southward transport. These reversals can be sufficiently intense and frequent as to significantly reduce the annual mean transport (Coachman and Aagaard, 1981).

In this note, we summarize the recent analysis of current, bottom pressure, and geostrophic wind conducted by Aagaard et al. (in press). These authors show that about two-thirds of the variance of flow in Bering Strait is accounted for by the meridional geostrophic wind. Further, Coachman and Aagaard (1981) have established a relation between transport across the central Chukchi Sea and flow through the eastern channel of Bering Strait ( $r = 0.9$ ).<sup>\*</sup> Thus, reasonable estimates

of transport can be calculated from 37 years of geostrophic wind via the strong correlation with that flow ( $r = 0.8$ ).

### OCEANOGRAPHIC AND METEOROLOGICAL SETTING

North of St. Lawrence Island, the Bering Sea shelf is bounded by the Alaska mainland, Siberia, and the island itself (Fig. 1). Adjoining the northern Bering Sea shelf are three straits; Anadyr Strait and Shpanberg Strait are west and east of St. Lawrence Island respectively, and Bering Strait lies about 250 km to the north. The cross sections of these straits are 75 km by 40 m, 200 km by 25 m, and 85 km by 50 m, respectively. The boundary between this shelf region and Norton Sound proper can be placed at the 20-m isobath. The shelf deepens toward the northwest, attaining maximum depths of 50 to 60 m in the vicinity of Bering Strait. Mean currents in these straits range from about 15 to 25  $\text{cm s}^{-1}$  in Bering Strait to 15  $\text{cm s}^{-1}$  in Anadyr Strait to about 5 to 10  $\text{cm s}^{-1}$  in Shpanberg Strait (Salo et al., 1983). In each of these straits flow is aligned with isobaths and nearly rectilinear, with about 95% of the variance contained in the component directed through the strait.

During winter, geostrophic winds are usually from the northeast, with characteristic long-term means near  $5 \text{ m s}^{-1}$  (Salo et al., 1983). The associated atmospheric pressure pattern is formed by a juxtaposition of the Siberian high and the Aleutian low pressure systems. Their relative positions and strengths control the geostrophic wind velocity and the horizontal scale of the meteorological forcing. When the Aleutian low penetrates far to the north and east, the isobars become tightly

\*  $r$  is the correlation coefficient.

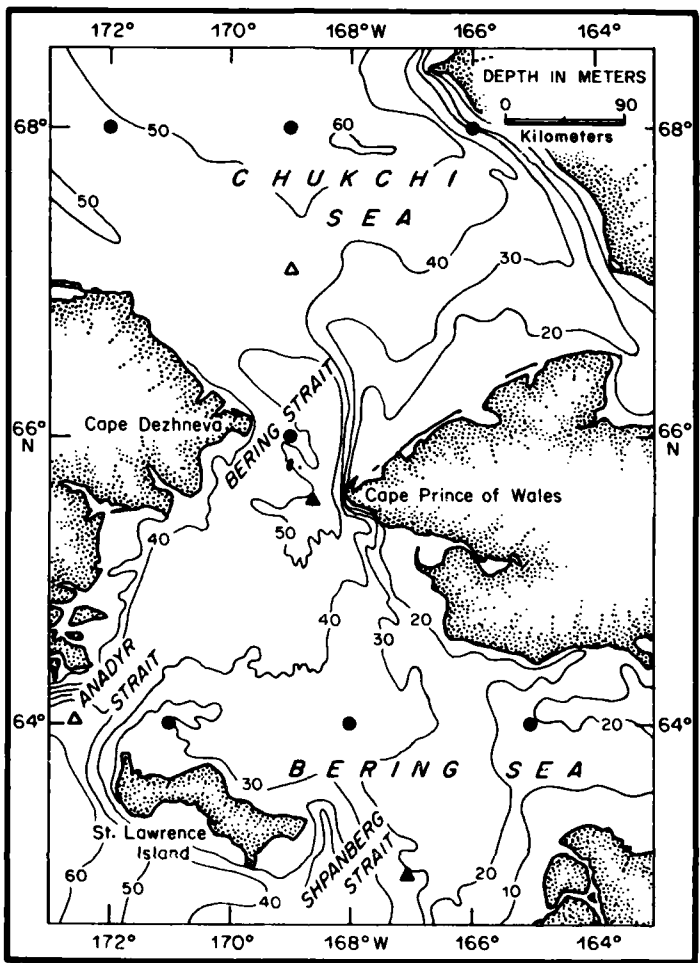


*Fig. 1. Vicinity of Bering Strait. Solid dots show locations of calculated wind series. Open triangles denote pressure gauges. Solid triangles are pressure gauges and current meters.*

packed and aligned nearly north-south. The steep pressure gradient, extending over 400-600 km, generates strong northerly winds that cause flow reversals through Bering Strait (Coachman and Aagaard, 1981).

The region is normally covered by sea ice of varying thickness and concentration from November through May. Recent studies of ice drift in the northern Bering and southern Chukchi seas (Reynolds and Pease, 1984) suggest that in this region ice is normally in nearly free drift, i.e. internal ice stress is dynamically unimportant. A consequence of this would be that the ice does not significantly impede the transfer of momentum from the wind to the ocean in this region.

## SUMMARY OF RESULTS 1981-1982

We summarize the results of Aagaard et al. (in press) as follows (see Fig. 2 and Table 1). There is a strong mean northward flow in Bering Strait, while in Shpanberg Strait the mean is smaller and the relative variability larger, so that the RMS error there is about one-half the mean flow. In both straits, however, the flow is essentially reciprocating along the axis of the strait. Note that reversals in the two straits are not always coincident (e.g. 12-13 January 1982). If the measurements are representative of flow in the respective straits, these times would require continuity to be maintained

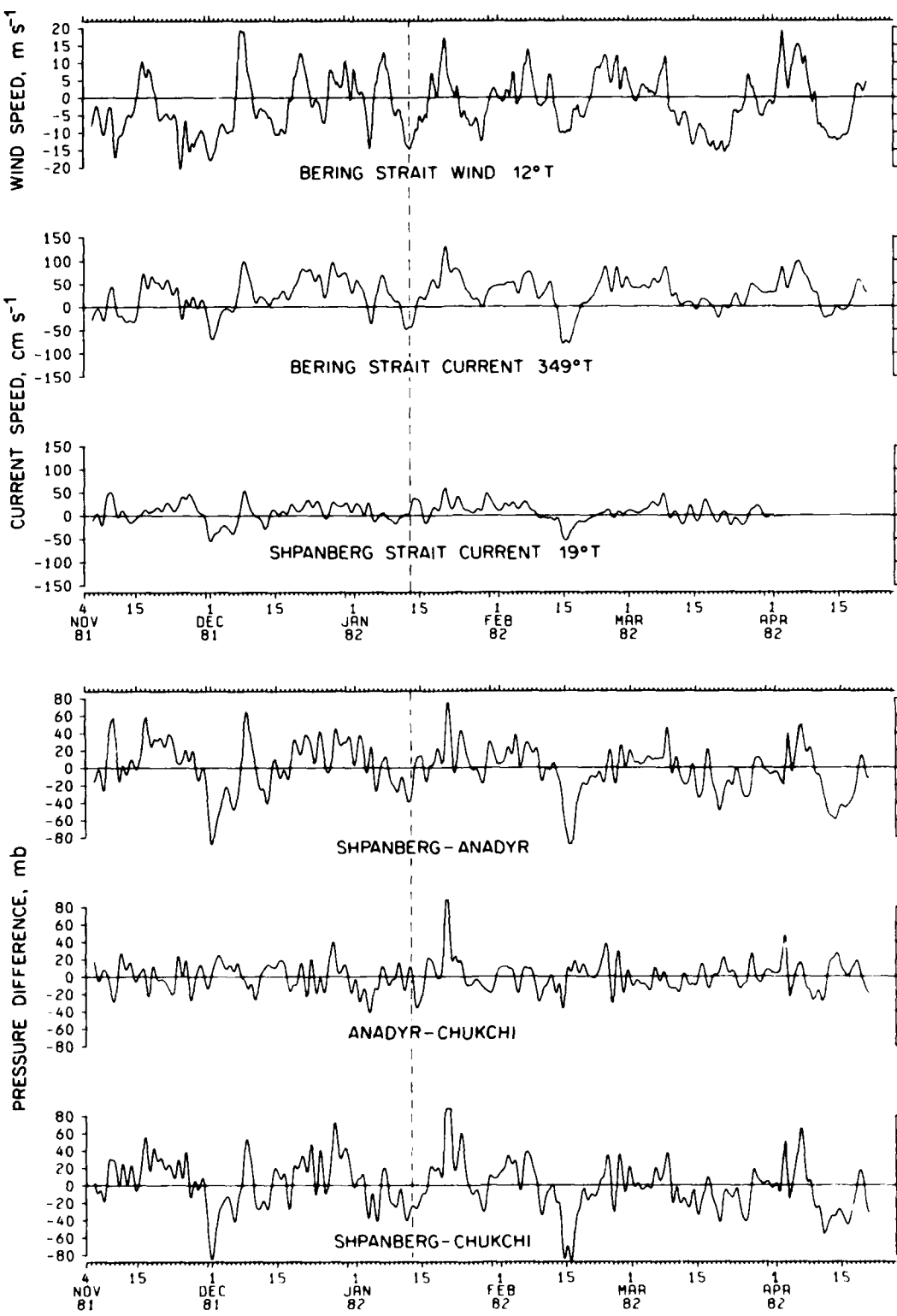


**Fig. 2.** Time series of principal axis components of calculated Bering Strait wind and of current in Bering and Shpanberg Straits. The bottom series are of bottom pressure differences Shpanberg-Anadyr, Anadyr-Chukchi and Shpanberg-Chukchi.

**Table 1. Moored measurements and calculated Bering Strait wind, 2 November 1981 to 24 April 1982.\***

Mooring	Location	Instrument depth (m) (soundings)	Mean velocity (direction)	RMS error <sup>†</sup>	Major axis orientation (fraction of total variance)	Kinetic energy			Pressure variance (mb)
						Total	KE <sub>10</sub> (fraction of total)	KE <sub>2-10</sub> / KE <sub>ind</sub>	
Bering Strait LD10AW	63°35.0' N 168°38.0' W	30 (50)	26.8 cm s <sup>-1</sup> (345°T)	7.4 cm s <sup>-1</sup>	349°T (93%)	701.0 cm <sup>2</sup> s <sup>-2</sup>	484.7 (69%)	187.7 (27%)	5.2 (< 1%)
Shpanberg Strait NC17C	62°52.6' N 167°03.6' W	18 (28)	6.8 cm s <sup>-1</sup> (014°T)	3.6 cm s <sup>-1</sup>	019°T (98%)	294.3 cm <sup>2</sup> s <sup>-2</sup>	128.3 (44%)	79.0 (27%)	76.8 (26%)
Bakun wind, Bering Strait BAK 23	66°N 169°W	Calculated surface wind	3.8 m s <sup>-1</sup> (252°T)	1.1 m s <sup>-1</sup>	192°T (69%)	45.0 m <sup>2</sup> s <sup>-2</sup>	29.1 (65%)	15.2 (34%)	838.2
Anadyr Strait NC19C	64°00.4' N 172°19.6' W	54 (55)							336.0
Chukchi Sea CSRA	67°06.8' N 168°59.1' W	47 (48)							548.9

\* Time base for Shpanberg Strait current is 2 November 1981 to 4 April 1982.

† RMS error =  $\sigma (1/\tau)^{1/2}$ , where  $\sigma$  is the standard deviation along the mean flow axis,  $\tau$  is the record length, and  $\tau$  is the integral scale (area under the autocorrelation function). Error estimate is for 35 hours of filtered data.

by the flow through Anadyr Strait. There would then be a recirculation between St. Lawrence Island and Bering Strait.

Aagaard et al. also examined correlations between current, bottom pressure gradient and wind, with the following results. The correlation between the Bering Strait flow and both the wind ( $r = 0.81$ ) and the pressure gradient components [ $\Delta P$ (NC17C-CS8A,  $r = 0.78$ ) and  $\Delta P$ (NC17C-NC19C),  $r = 0.79$ ] is very high and in phase to within 6 hours (note that the correlations 0.78 and 0.81 are not significantly different at the 95% level). The wind variability can thus account for about two-thirds of the variance of both the Bering Strait flow and the regional oceanic pressure gradient. These statistics are thus consistent with a mean northward flow through Bering Strait, the variability of which is predominantly wind-driven and involving coastal wind set-up sufficient to substantially alter the regional sea level topography. (Since baroclinic effects generally are small through most of the year, sea bottom pressure primarily reflects sea surface topography, supplemented by atmospheric pressure anomalies.) The largest sea level changes apparently occur southeast of Bering Strait, in the vicinity of Norton Sound (compare pressure variances in Table 1). The reason for this is that the south side of the Seward Peninsula constitutes the regionally largest and most effective barrier to a meridional coastal flow regime. During times of strong northerly winds, set-down in this region reverses or weakens the meridional pressure gradient through Bering Strait sufficiently to allow southward flow. The cross-stream pressure gradient component is reversed at the same time.

For many purposes the flow parameter in Bering Strait of most interest is the volume transport, from which heat and material transports can be calculated, subject to various assumptions. Aagaard (in press) used the linear regression from Coachman and Aagaard (1981), together with the LD-10AW record, to estimate the mean transport from November 1981 to June 1982 as 0.63 Sv. This is 50% greater than the corresponding 8-month mean during 1966-67 (0.43 Sv), suggesting considerable interannual variability in transport.

How can we examine the very low frequency variability, given the paucity of direct current measurements? Because of the high correlation between the geostrophic wind and the LD-10AW velocity record (0.8), together with a physically plausible mechanism relating them, Aagaard et al.

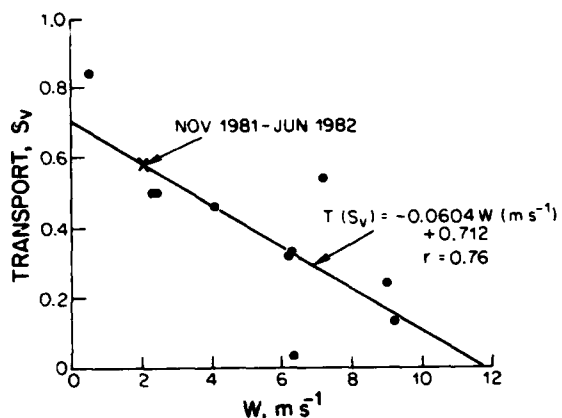


Fig. 3. Correlation between calculated southward wind component in Bering Strait and transport through the Chukchi Sea, September 1976-June 1977.  $\times$  denotes the predicted transport based on the mean wind during November 1981 to June 1982.

(in press) have chosen to use the available 37-year time series of BAK-23 wind as an estimate of transport. Further justification for this is that the correlation between the transport in 1976-77 and the BAK-23 wind was also high (-0.76, Fig. 3), even though BAK-23 was not as representative of the regional wind field during that winter as it was in 1981-82. (The major cyclone tracks did not penetrate as far north during 1976-77, thus creating meridional differences in the wind variance during the two winters.) Note also in Fig. 3 that based on the mean BAK-23 wind ( $2.1 \text{ m s}^{-1}$ ) during November 1981 to June 1982, the regression equation predicts a transport of 0.59 Sv, essentially identical with the 0.63 Sv predicted from the regression equation using current speed in the strait. The statistics are therefore internally consistent, lending further credence to use of the geostrophic wind as a transport index.

We have used the daily averaged component along  $192^{\circ}\text{T}$  of the BAK-23 wind to estimate the Bering Strait transport for 1946-82, based on the linear regression of Fig. 3. Fig. 4 shows the mean monthly transport over the 37 years, bounded by  $\pm 1$  standard deviation. The seasonal signal is clear, with the summer maximum in the mean about 50% greater than the winter values. Fig. 4 also shows the mean monthly transports for 1941-1961 from the summary by Fedorova and Yankina (1964) of Soviet work, but reduced by 50%. Apart from this amplitude disagreement, the similarity in the projected seasonal cycle is striking. At this

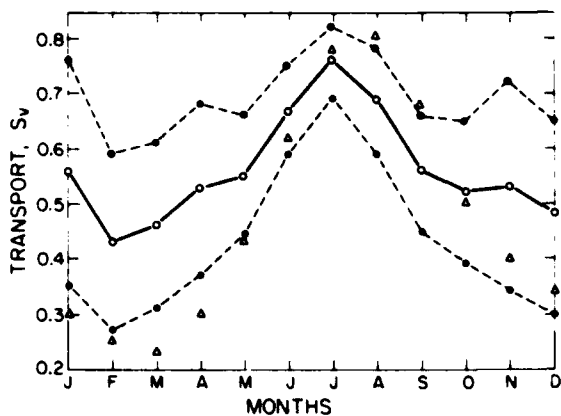


Fig. 4. Mean monthly transport for 1946-1982 based on Bering Strait wind and the correlation of Fig. 3. Dashed lines denote one standard deviation. Triangles show seasonal cycle of Fedorova and Yankina (1964) reduced by 50%.

point it seems safe to conclude that there is a seasonal variation in transport, with a maximum in summer. Note, however, that the variance in winter, particularly, is very large, so that any given year may show a monthly progression very different from the long-term mean.

Transport estimates for the winter period (1 October to 31 March) are shown in Fig. 5. The 35-year mean transport is 0.50 Sv, with a standard deviation of 0.09 Sv, and ranges from +30% to -54% of the mean. This compares favorably with results from Aagaard et al. (in press) for the annual (1 January to 31 December) average transport of 0.56 Sv, with a standard deviation of 0.05 Sv and a maximum deviation from the mean of  $\pm 21\%$ . The differences likely reflect the inclusion in the latter estimates of stronger, less variable

transport during summer. Also shown in Fig. 5 is the northeast Pacific atmospheric pressure index recently defined by Emery and Hamilton (1985) to provide a time series representation of the strength of the atmospheric circulation in the northeast Pacific. (For Fig. 5, we have computed the index for the same months as the transport.) This index is highly dependent on the strength and/or location of the Aleutian low, and thus should be related to atmospheric circulation over the Bering Sea. When this index is below its mean value (13.9 mb), 17 of the 18 transport estimates were above the mean transport. Overall, the two series are well correlated,  $r = -0.84$ .

#### ACKNOWLEDGMENTS

The data were collected and processed through the efforts of R.B. Tripp and P. Moen. Our own work was supported in part by the Bureau of Land Management through interagency agreement with the National Oceanic and Atmospheric Administration, as part of the Outer Continental Shelf Environmental Assessment Program; and in part by the Office of Naval Research. This is Contribution 761 from the Pacific Marine Environmental Laboratory, as part of the Marine Services Project.

#### REFERENCES

Aagaard, K., A.T. Roach and J.D. Schumacher, On the wind-driven variability of the flow through Bering Strait, *J. Geophys. Res.* (in press), 1985.  
 Aagaard, K., L.K. Coachman and E.C. Carmack, On the halocline of the Arctic Ocean, *Deep-Sea Res.*, 29, 529-545, 1981.

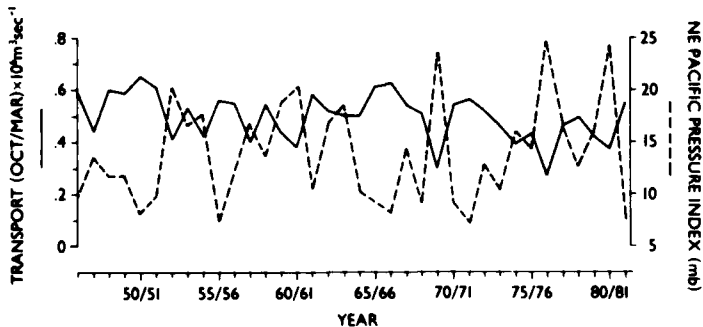


Fig. 5. Mean transport for 1 October to 31 March 1946-1982 based on Bering Strait wind and the correlation of Fig. 4 (solid line). The dashed line shows the northeast Pacific Pressure Index as computed by Emery and Hamilton (1985).

**Coachman, L.K. and K. Aagaard**, On the water exchange through Bering Strait, *Limnol. Oceanogr.*, 11, 44-59, 1966.

**Coachman, L.K. and K. Aagaard**, Reevaluation of water transports in the vicinity of Bering Strait, in *The Eastern Bering Sea Shelf: Oceanography and Resources*, Vol. 1 (D.W. Hood and J.A. Calder, Ed.), pp. 95-110, National Oceanic and Atmospheric Administration, Washington, D.C., 1981.

**Coachman, L.K. and C.A. Barnes**, The contribution of Bering Sea water to the Arctic Ocean, *Arctic*, 14, 147-161, 1961.

**Coachman, L.K., K. Aagaard and R.B. Tripp**, *Bering Strait: The Regional Physical Oceanography*, 172 pp., University of Washington Press, Seattle, 1975.

**Codispoti, L.A.**, Arctic Ocean processes in relation to the dissolved silicon content of the Atlantic, *Mar. Sci. Commun.*, 5, 361-381, 1979.

**Emery, W.J. and K. Hamilton**, Atmospheric forcing of interannual variability in the northeast Pacific Ocean: Connections with El Niño, *J. Geophys. Res.*, 90(C1), 857-868, 1985.

**Fedorova, A.P. and A.S. Yankina**, The passage of Pacific Ocean water through the Bering Strait into the Chukchi Sea, *Deep-Sea Res.*, 11, 427-434, 1964.

**Killworth, P.D. and J.M. Smith**, A one-and-a-half dimensional model for the Arctic halocline, *Deep-Sea Res.*, 31, 271-293, 1984.

**Reynolds, R.M. and C.H. Pease**, Drift characteristics of northeastern Bering Sea ice during 1982, *NOAA Technical Memo ERL PMEL-55*, 135 pp., National Oceanic and Atmospheric Administration, 1984 (PB84-213982).

**Salo, S.A., J.D. Schumacher and L.K. Coachman**, Winter currents on the eastern Bering Sea shelf, *NOAA Technical Memo ERL-PMEL-45*, 53 pp., National Oceanic and Atmospheric Administration, 1983 (PB83-248823).

**Sambrotto, R.N., J.J. Goering and C.P. McRoy**, Large yearly production of phytoplankton in the western Bering Strait, *Science*, 225(4667), 1147-1150, 1984.

**Stigebrandt, A.**, The North Pacific: A global-scale estuary, *J. Phys. Oceanogr.*, 14, 464-470, 1984.

## Theory of Wind-Driven Coastal Polynyas

CAROL H. PEASE

*Pacific Marine Environmental Laboratory/NOAA  
Seattle, Washington 98115, USA*

The Soviet author V.L. Lebedev (1968) had an interesting idea that was largely ignored by western scientists: that wind-generated coastal polynyas attain a maximum size if the air and water are cold enough to produce ice. Although there are some problems with the model formulation that Lebedev proposed, the balance between ice production due to the heat and radiation loss at the polynya surface with the wind-driven divergence of ice from the shore is essentially correct. This effect is caused by the collection of frazil produced over the whole polynya at the downwind side of the polynya (Martin and Kauffman, 1981; Bauer and Martin, 1983) by wind waves or other physical causes. Since the total frazil production is area-dependent, the polynya must reach a size at which it is producing enough ice to maintain a steady-state balance with the advection of the solidified

ice from the shore. Bauer and Martin applied this concept to model a narrow lead for the Arctic. In their model, an initially ice-free lead of constant width gradually fills with ice, which is not conceptually very different from a continuously opening polynya maintaining steady-state production.

The change in polynya width with time ( $dX_p/dt$ ) is proportional to the difference between the advection rate of the solidified ice from the shore ( $V_p$ ) and the production rate ( $F_p$ ) over the width of the polynya ( $X_p$ ) scaled by the collection depth of the grease ice or nilas ( $H_p$ ) (Fig. 1), i.e.

$$dX_p/dt = V_p - X_p F_p / H_p \quad (1)$$

If there is no significant ice production ( $F_p = 0$ ), then eq 1 shows that the polynya will open at a constant rate and the polynya width will be just

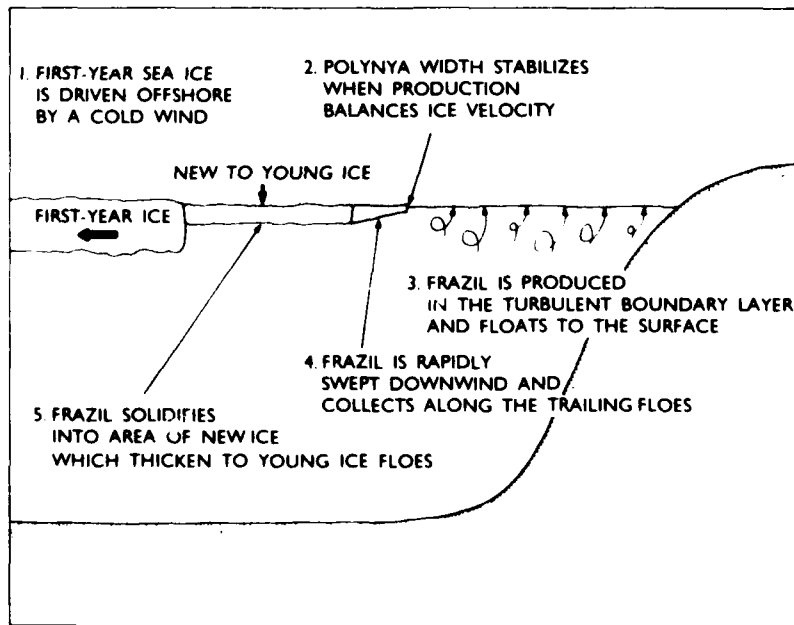


*Fig. 1. Schematic of coastal polynya processes with water at the freezing point and air below freezing.*

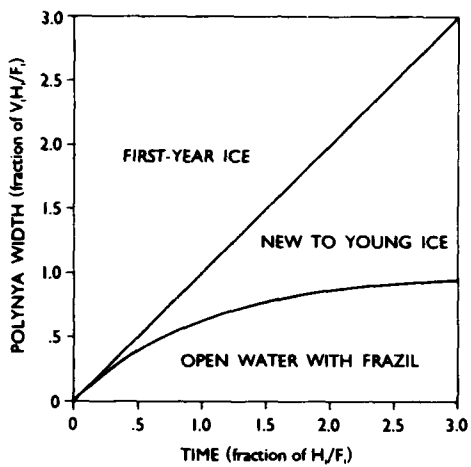


Fig. 2. Wind-driven coastal polynya width as a function of time. For an offshore wind of  $20 \text{ m s}^{-1}$ , air temperature of  $-20^\circ\text{C}$ , and effective frazil collection thickness of  $10 \text{ cm}$ ,  $H/F = 1$  is about 9 hours and  $V.H./F = 1$  is about 19 km.

$V.H./F$ , never reaching equilibrium. However, if the meteorological conditions are steady or at least slowly varying compared to the polynya opening time, and  $V$ ,  $F$ , and  $H$ , are positive, definite and nearly constant, then the linear differential equation (eq 1) has the solution

$$X_p = (V.H./F) + C \exp(-t F/H) \quad (2)$$

where  $C$  is an integration constant to be determined from the boundary condition. If  $X_p = 0$  when  $t = 0$ , then  $C = -V.H./F$ .

$$X_p = (V.H./F)[1 - \exp(-t F/H)] \quad (3)$$

This equation is bounded for very large  $t$ ,

$$X_p(\text{maximum}) = V.H./F \quad (4)$$

which gives the limiting polynya size (Fig. 2).

A time scale for the opening of the polynya can be determined from eq 3 by solving for  $t$  for a given percentage of the maximum size. If we choose  $X_p = 0.95 V.H./F$  (when the polynya reaches 95% of its limiting size) and solve eq 3 for  $t$ , then

$$t_{95} = (H/F) \ln(20) = 3.0 H/F \quad (5)$$

Thus the time scale for reaching maximum size is only dependent on the freezing rate scaled by the collection thickness. For a greater freezing rate,

the polynya will reach maturity faster, that is, the time scale will be smaller.

The freezing rate over the polynya can be estimated from the bulk parameterizations for the vertical heat flux at the air/sea interface. The usual important components of the flux balance are the unreflected shortwave radiation  $[(1-a)Q_s]$ , the downward and upward longwave radiation ( $Q_{ld}$ ,  $Q_{lu}$ ), the sensible or turbulent heat flux ( $Q_r$ ), and the latent heat of evaporation ( $Q_e$ ).

$$-\rho_s L dH/dt = (1-a)Q_s + Q_{ld} - Q_{lu} + Q_r + Q_e \quad (6)$$

where  $\rho_s$  is the density of sea ice,  $L$  is the latent heat of freezing for salt water, and  $dH/dt$  is the area-averaged production rate and is equivalent to  $F$ , above.

From October through February at high northern latitudes, the shortwave radiation contribution is zero to a very small positive value depending on latitude. In the following calculations this term is neglected. At worst, neglecting the shortwave term causes an overestimate of the freezing rate in the polynya and a slight underestimate in the size of the polynya. By spring equinox this assumption is not valid since solar radiation begins to dominate the balance at all latitudes.

For a polynya, the longwave radiation upward ( $Q_{lu}$ ) is equal to  $\sigma e_s T_s^4$  where  $\sigma$  is the Stefan-Boltzmann constant,  $e_s$  is the emissivity of the surface and  $T_s$  is the temperature of the water surface. Since  $T_s$  varies only by a few tenths of a degree proportional to salinity for any given polynya (Schumacher et al., 1983),  $Q_{lu}$  can be assumed constant and equal to  $287 \text{ W m}^{-2}$  for a water temperature of  $-1.8^\circ\text{C}$  and an emissivity of 0.98.

The longwave radiation downward is more problematic and cannot be neglected since it is of the same order of magnitude and of opposite sign as the longwave upward. For this problem I take the simple approximation of  $\sigma e_a T_a^4$ , where  $e_a$  is an emissivity for the air, and  $T_a$  is the air temperature relative to some standard height, which ignores variation in emissivity due to cloud cover. In general, offshore winds in winter are relatively dry and hence clear, so this approximation is better for this case than for a wide range of sea ice modeling problems. In this case  $e_a$  is set to 0.95.

The parametric forms of the sensible and evaporative heat fluxes are

$$Q_r = \rho_s C_p C_r V_a (T_a - T_s) \quad (7)$$

$$Q_e = \rho_s C_p L_r V_a (q_s - q_a) \quad (8)$$

Table 1. Model values for standard case.

Variable	Value	Definition
$T_a$	-20°C	Air temperature
$T_s$	-1.8°C	Water temperature
$V_o$	20 m s <sup>-1</sup>	Offshore wind velocity
$V_i$	3% $V_o$	Ice floe velocity
$H_f$	0.10 m	Frazil collection thickness
$\sigma$	$5.67 \times 10^{-8}$ W m <sup>-2</sup> deg <sup>-4</sup>	Stefan-Boltzmann constant
$e_a$	0.95	Emissivity of the air
$\rho_a$	1.30 kg m <sup>-3</sup>	Air density
$\rho_i$	$0.95 \times 10^3$ kg m <sup>-3</sup>	Ice density
$C_h$	$1.5 \times 10^{-3}$	Sensible heat coefficient
$C_p$	1004 J deg <sup>-1</sup> kg <sup>-1</sup>	Specific heat of air
$Q_{lw}$	287 W m <sup>-2</sup>	Longwave radiation upward
$L$	$3.34 \times 10^5$ J kg <sup>-1</sup>	Latent heat of fusion

where  $\rho_a$  is the density of cold air,  $V_o$  is the wind speed,  $C_p$  is the specific heat for air,  $C_h$  and  $C_s$  are sensible heat and water vapor transfer coefficients,  $T_a$  and  $T_s$  are the air and surface water temperatures, and  $q_o$  and  $q_s$  are the observed and saturated mixing ratios. The transfer coefficients are assumed to be equal and equivalent to the drag coefficient over smooth water.

The candidate model for the sensitivity study includes eq 4 and eq 5, with eq 6 simplified to

$$F = -[\sigma e_a T_a^4 - Q_{lw} + \rho_a C_h C_p V_o (T_a - T_s)] / \rho_a L. \quad (9)$$

In addition,  $V_i$  is assumed to be 3% of the wind speed, a crude but effective order-of-magnitude

estimate for the divergence of first-year ice from the shore. In the following section, this simple model view of a coastal polynya is examined in detail.

To study the sensitivity of a coastal polynya, a standard model case is set up and the independent variables of air temperature and wind speed are varied separately. The values for the parameters and variables for the standard case are given in Table 1. The effective frazil collection thickness is also treated as an independent variable.  $H_f$  is an unknown constant or function assumed constant for lack of knowledge about the frazil collection process. Thus, varying  $T_s$  and  $V_o$  examines the response of the polynya to possible changes in the

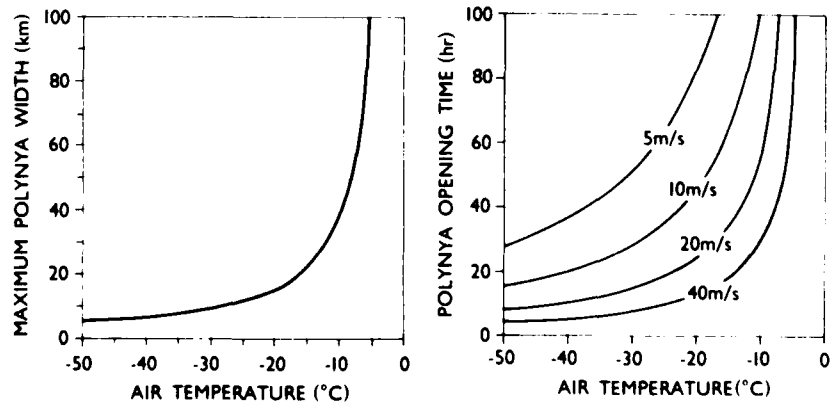


Fig. 3. Variation of maximum polynya width ( $X_p$ ) and opening time ( $t_{op}$ ) with air temperature. Note that coastal polynyas reach a stable size within typical synoptic time scales for low temperatures but not for those approaching freezing. The breakover point is a function of both wind speed and air temperature.

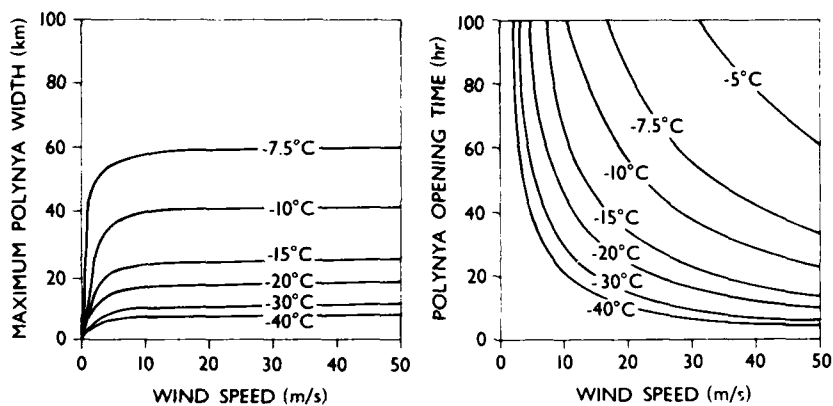


Fig. 4. Variation of maximum polynya width ( $X_p$ ) and opening time ( $t_{05}$ ) with offshore wind speed.

environment, while varying  $H$  looks at the model sensitivity to a poorly understood process.

Fig. 3 gives the variation of maximum polynya width ( $X_p$ ) and opening time ( $t_{05}$ ) with changes in air temperature, and Fig. 4 gives their variation with offshore wind speed. Fig. 3 shows that maximum polynya width is strongly a function of temperature. For air temperatures higher than  $-3^\circ\text{C}$ , maximum polynya widths are more than 100 km (McNutt, 1981). For colder air, the maximum polynya width decreases because frazil production is enhanced. Fig. 4 shows that maximum polynya width is a weak function of wind speed for winds greater than  $5 \text{ m s}^{-1}$ , although the time-dependent polynya width for events younger than  $t_{05}$  is a function of wind speed. The lack of sensitivity of maximum polynya width to the wind is due to a balance between the production rate, which is trying to close the polynya, and the advection rate, which is trying to open the polynya. The linearity of the advection rate of the ice floes from shore may be seen to be an outcome of the assumption that  $V_a = 3\% V_w$ , but most models for ice drift with quadratic or higher-order stress laws give an almost linear ice velocity response with wind speed because wind stress is nearly balanced by current stress, especially for wind velocities higher than  $5 \text{ m s}^{-1}$  (Gaskill et al., 1980; Pease and Overland, 1984).

The opening time for a coastal polynya is a strong function of both wind speed and air temperature. Either higher wind speed or lower air temperature will bring a polynya to its equilibrium point more rapidly. For an air temperature of  $-20^\circ\text{C}$ , a polynya takes about 4 days to open for wind of only  $5 \text{ m s}^{-1}$  or about a half a day to open for a wind of  $40 \text{ m s}^{-1}$ . Similarly, for a wind speed

of  $20 \text{ m s}^{-1}$ , a polynya takes about 4 days to open if the air temperature is  $-7.5^\circ\text{C}$  or about half a day to open if the air is  $-40^\circ\text{C}$ . For a class of light winds and warm temperatures, represented by a product of  $-100^\circ\text{C m s}^{-1}$  or larger, a polynya does not reach equilibrium size within a typical synoptic period of 5 days. Generally, however, winter conditions along the Alaska coast or along the Antarctic coast are characterized by energetic winds and cold air, so polynyas typically reach their maximum size in a day or two during periods of offshore flow.

The model sensitivity to the effective frazil collection thickness is shown in Fig. 5 for  $T_a$  and  $V_w$  held fixed at  $-20^\circ\text{C}$  and  $20 \text{ m s}^{-1}$ . The linearity of the response is caused by the simple form of the assumed model. The frazil collection thickness is probably a function of temperature and wind speed. Lower temperatures freeze the frazil mat more quickly into ice floes, leaving the new floes full of holes. Higher wind speeds may collect frazil more efficiently along the downwind edge of the

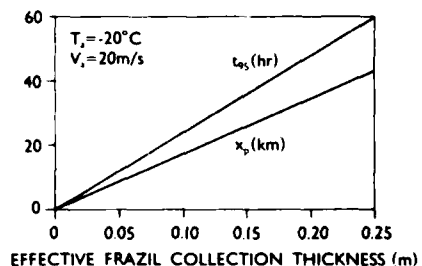


Fig. 5. Sensitivity of opening time ( $t_{05}$ ) and maximum polynya width ( $X_p$ ) to the effective frazil collection thickness ( $H_e$ ).

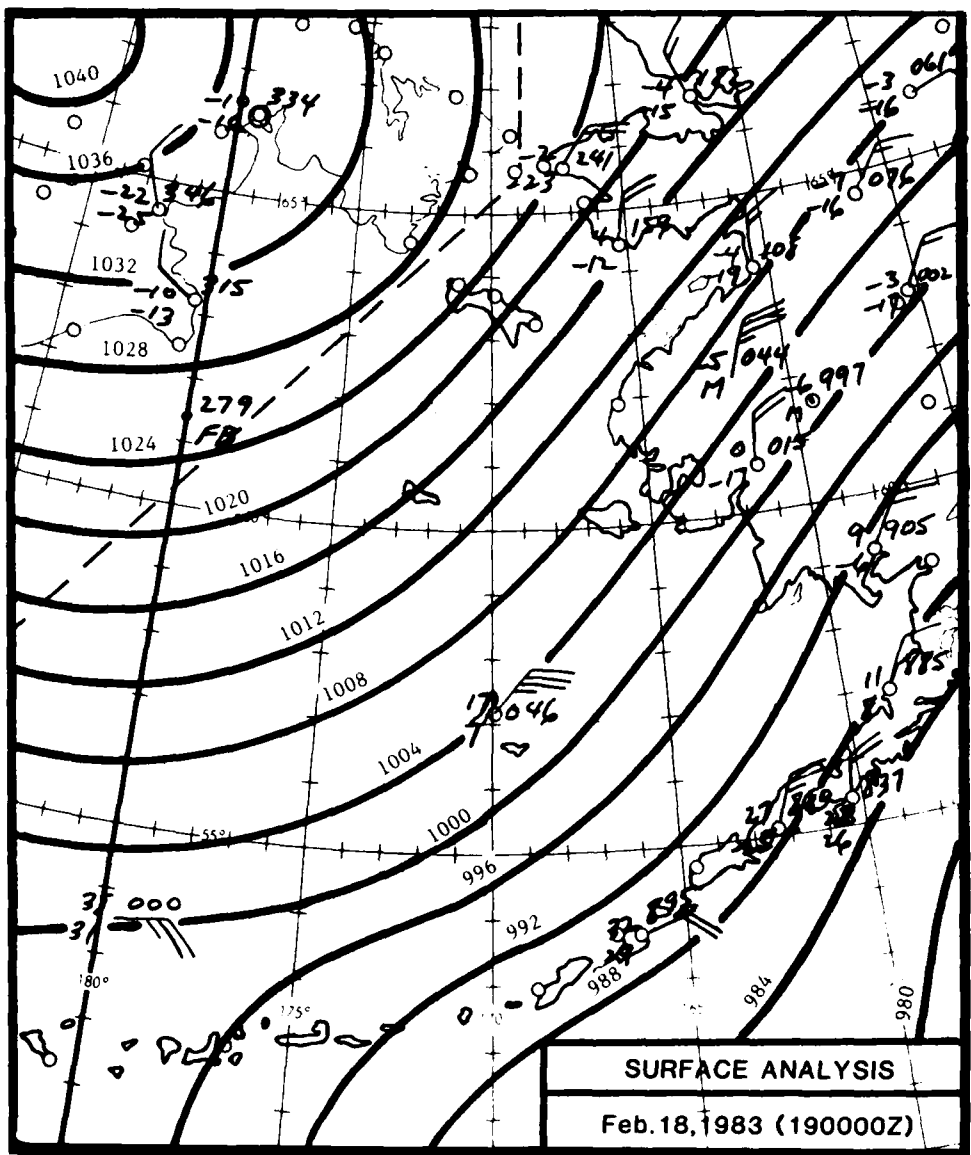


Fig. 6. Surface weather analysis for 0000 GMT, 19 February 1983, with pressure contours in mb and wind barbs in knots.

polynya due to herding by wind waves (Martin and Kauffman, 1981; Bauer and Martin, 1983) and through setting up wind rows along the water surface. These mechanisms have been observed in laboratory studies and from aircraft over polynyas, but have not been studied in detail in the field.

Various measurements were made from the NOAA P-3 aircraft over the St. Lawrence Island polynya during the Marginal Ice Zone Experiment (MIZEX-West) on 18 February 1983. The aircraft was equipped with instruments for measuring flight-level low-frequency atmospheric parameters

and with a gust probe system for measuring turbulent fluxes (Walter et al., 1984). The flight-level data were sampled at 1 Hz and included atmospheric pressure, ambient air temperature, dew point temperature, and winds. Details of the flight-level low-frequency data collection are described in Merceret and Davis (1981). The nominal accuracy of the flight-level winds is  $1 \text{ m s}^{-1}$ . The gust probe system includes a fast-response thermistor, a humidity refractometer, vertical and horizontal strain gauges for velocity fluctuations, and a pitot tube for pressure fluctuations. Filtered, 10-Hz analog signals are digitized and re-

**Table 2. Measurements from NOAA P-3 flight over the St. Lawrence Island polynya on 18 February 1983 (approximately 0000 GMT, 19 February 1983).**

Height (m)	Pressure (mb)	Air temp		Length (s)	Wind speed (m s <sup>-1</sup> )	Wind direction (true)	Plane heading (true)	Flight order
		Ambient (°C)	Potential (°C)					
197	994	-23.8	-23.4	530	23.3	021°	282	2
193	995	-23.5	-23.1	600	17.4	017°	082	5
100	1007	-23.1	-23.6	590	19.1	020°	081	1
100	1007	-22.5	-23.0	400	17.7	017°	282	6
93	1008	-22.4	-23.0	490	17.0	015°	081	7
57	1013	-22.2	-23.1	600	19.7	016°	281	4
52	1014	-22.3	-23.1	590	18.3	015°	081	3
0	1021	-21.7	-23.2 ± 0.2	—	—	017° ± 2°	—	—

sampled at 40 Hz. Details of the data processing are described in Walter et al. (1984).

For the 18 February 1983 flight, the sea-level pressure analysis (19 February 1983, 0000 GMT; Fig. 6) shows a very tight gradient between the Siberian high and Aleutian low pressure centers. Wind conditions were stronger the day before and decreased fairly uniformly during the observation period (Table 2) from about 20 m s<sup>-1</sup> to 17 m s<sup>-1</sup>. This was accompanied by a 5-degree rotation of the wind to a slightly more northerly position during the observations, which held steady for several days thereafter. Air temperatures were nearly constant during the period of the aircraft observations, although the temperature had dropped several degrees just before the flight to -23°C. There was a considerable amount of steam fog over the polynya (Fig. 7) during this flight. The measured sensible heat flux extrapolated to the surface (Table 3) was greater than 300 W m<sup>-2</sup>. An airsonde launched from USCG icebreaker *Westwind*, 250 km south of the polynya (Fig. 7), showed a well-mixed boundary layer of -21°C, capped by an inversion at 800 m, which indicated some warming of the air mass.

The polynya opened on about 16 February 1983 with a maximum width of 10 km and remained open for the rest of the month at nearly constant size. This is in good agreement with the simple model calculation for the observed temperature and wind speed range. We sampled about 3 days after the polynya opened, more an artifact of the amount of time it took to plan a flight once the polynya was observed in satellite images than an effort to sample at some particular time. Argos buoys, tracked on the ice about 300 km south of the island, drifted toward the southwest throughout the period. Also, the polynya shape was canted toward the west, due to the north-northeast orientation of the wind to the coast.

In summary, the size of a wind-driven coastal polynya is a balance between advection of ice floes away from the shore and the ice production rate averaged over the polynya. Since the wind speed affects both the advection rate of floes and the ice production rate, increasing the wind speed above 5 m s<sup>-1</sup> does not increase the maximum size that the polynya can maintain. The effect of air temperature, however, is more one-sided. Cooling the air increases only the freezing rate and therefore reduces the maximum size that the polynya can maintain. Thus for winter conditions at high latitudes with minimal shortwave radiation, air tem-

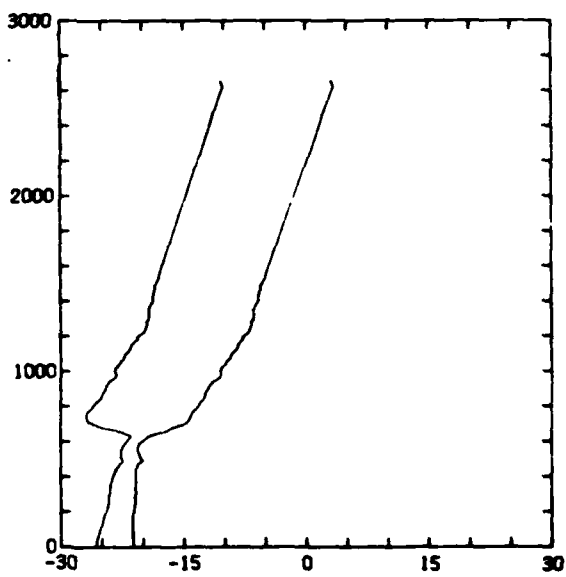


**Fig. 7. Profile of potential (right) and dew point (left) temperatures from an airsonde from USCG icebreaker *Westwind* at 60°39'N, 174°09'W, downwind of the St. Lawrence Island polynya at 2316 GMT, 18 February 1983.**



Fig. 8. Frazil ice in wind rows and steam fog over the St. Lawrence Island polynya on 18 February 1984. The wind direction is from lower (north-northeast) to upper part and the frame width in the foreground is about 70 m across.

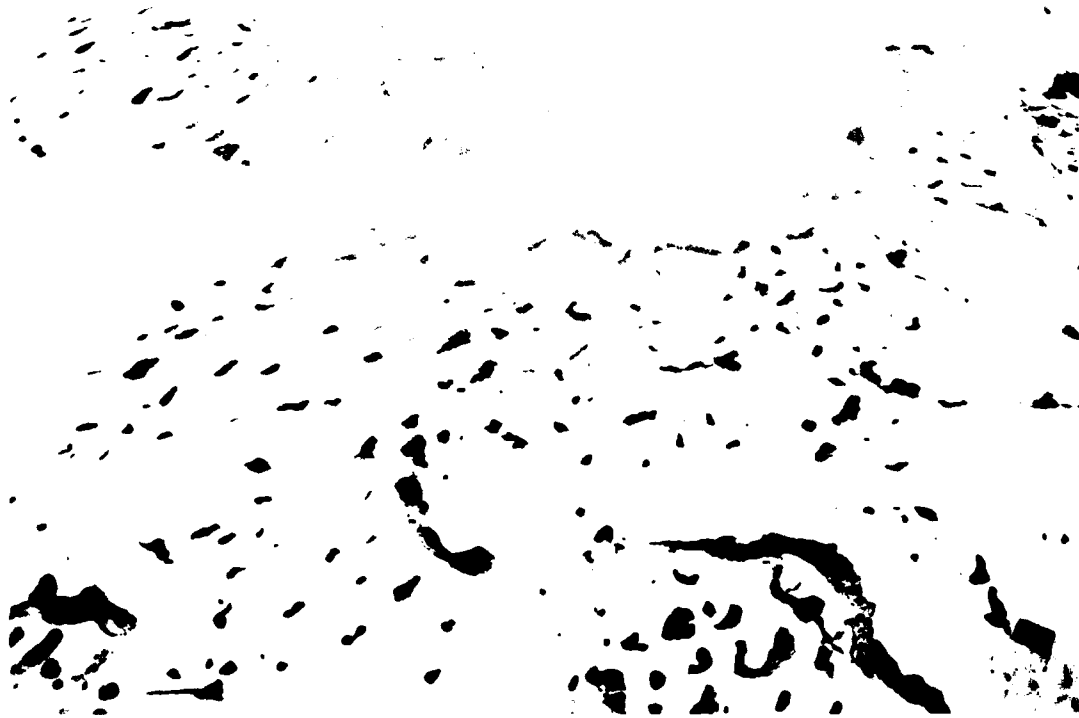


Fig. 9. New ice floes with holes due to inefficient frazil collection about 10 km from the shore of St. Lawrence Island on 18 February 1985. The frame width in the foreground is about 200 m across.

**Table 3. Heat fluxes calculated from gust probe measurements from the NOAA P-3 flight over the St. Lawrence Island polynya on 18 February 1983 (approximately 0000 GMT, 19 February 1983.)**

Height (m)	Avg temp (°C)	Avg wind speed (m s <sup>-1</sup> )	Gust probe fluxes		
			Sensible (W m <sup>-2</sup> )	Evaporative (W m <sup>-2</sup> )	Bowen ratio
197	-23.8	23.3	15	66	0.2
193	-23.5	17.4	-20	108	-0.2
100	-23.1	19.1	118	89	1.3
100	-22.5	17.7	207	82	2.5
93	-22.4	17.0	210	107	2.0
57	-22.2	19.7	276	70	3.9
52	-22.3	18.3	187	74	2.5
0	—	—	334	78 (85)*	4.3 (3.9)*

\* Values in parentheses relate to average evaporative heat flux values for the layer since the trend to the surface was not significant.

perature is the critical determinant for maximum polynya size.

The time required for the polynya to reach 95% of its limiting size is typically 1/2 to 4 days, proportional to the ratio of the frazil-collection thickness and the freezing rate. For a given collection thickness either colder air or higher wind speed will increase the freezing rate and therefore bring the polynya to equilibrium more quickly.

The process of frazil collection into wind rows (Fig. 8) and the formation of ice floes from consolidated frazil (Fig. 9) are not understood in detail. The scale of the numerical results of the model described here depends on the assumed collection thickness. Since the efficiency of frazil collection is probably a function of wind speed and fetch, additional field work and more detailed modeling studies of the process are needed before more than the qualitative results of the present study are achieved.

This study is a contribution to the Marine Services Project at the Pacific Marine Environmental Laboratory of the National Oceanic and Atmospheric Administration and was funded in part by the Arctic Program of the Office of Naval Research. B.A. Walter processed the preliminary aircraft data and A.L. Comiskey reanalyzed the surface weather maps. I thank A. Omstedt for helpful discussions of the physics during his visit to the United States.

## REFERENCES

Bauer, J. and S. Martin, A model of grease ice growth in small leads, *J. Geophys. Res.*, 88, 2917-2925, 1983.

Gaskill, H.S., R.J. Lopez and G.E. Swaters, Free drift of sea ice: A comparison of models, Technical report C-CORE 80-16, St. John's, Newfoundland, 132 pp., 1980.

Lebedev, V.,L., Maximum size of a wind-generated lead during sea freezing, *Oceanology*, 8, 313-318, 1968.

Martin, S. and P. Kauffman, A field and laboratory study of wave damping by grease ice, *J. Glaciol.*, 27, 283-313, 1981.

McNutt, S.L., Ice conditions in the eastern Bering Sea from NOAA and LANDSAT imagery: Winter conditions 1974, 1976, 1977, 1979, *NOAA Technical Memo ERL PMEL-24*, 179 pp., National Oceanic and Atmospheric Administration, 1981 (PB81-220188).

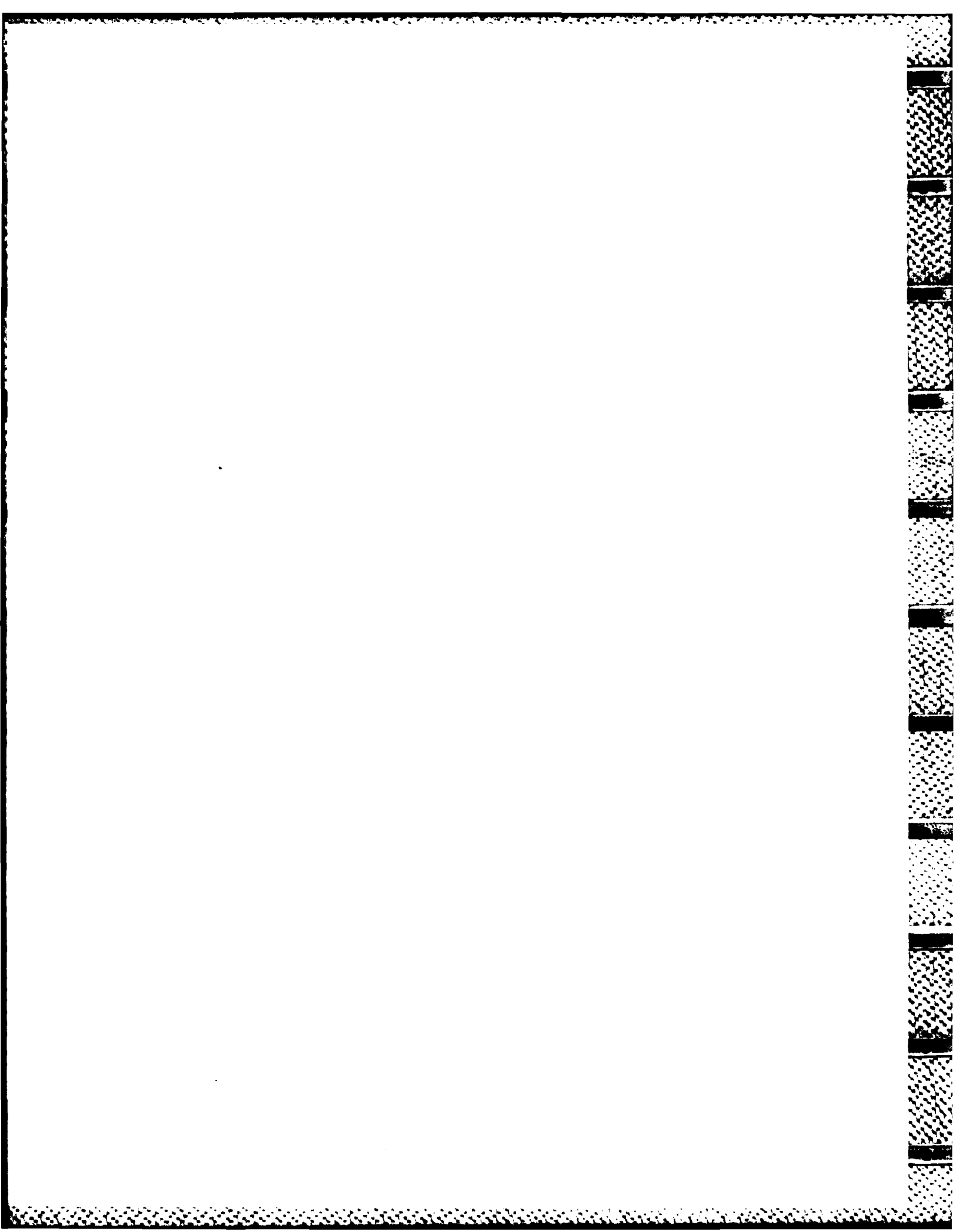
Merceret, F.J. and H.W. Davis, The determination of navigational and meteorological variables measured by NOAA/RFC WP3D aircraft, *NOAA Technical Memo ERL-RFC-7*, 21 pp., National Oceanic and Atmospheric Administration, 1981 (PB81-225468).

Pease, C.H. and J.E. Overland, An atmospherically driven sea-ice drift model for the Bering Sea, *Ann. Glaciol.*, 5, 111-114, 1984.

Schumacher, J.D., K. Aagaard, C.H. Pease and R.B. Tripp, Effects of a shelf polynya on flow and water properties in the northern Bering Sea, *J. Geophys. Res.*, 88, 2723-2732, 1983.

Walter, B.A. Jr., J.E. Overland and R.O. Gilmer, Air-ice drag coefficients for first-year sea ice derived from aircraft measurements, *J. Geophys. Res.*, 89, 3550-3560, 1984.

Wilson, J.G., A.L. Comiskey, R.W. Lindsay and V.L. Long, Regional meteorology during MIZEX-West, February and March 1983, *NOAA Special Report ERL-PMEL*, 115 pp., National Oceanic and Atmospheric Administration, 1985.



E W D

F I L M E D

6-86

D T I C